# Advances in nanocarbon composite materials
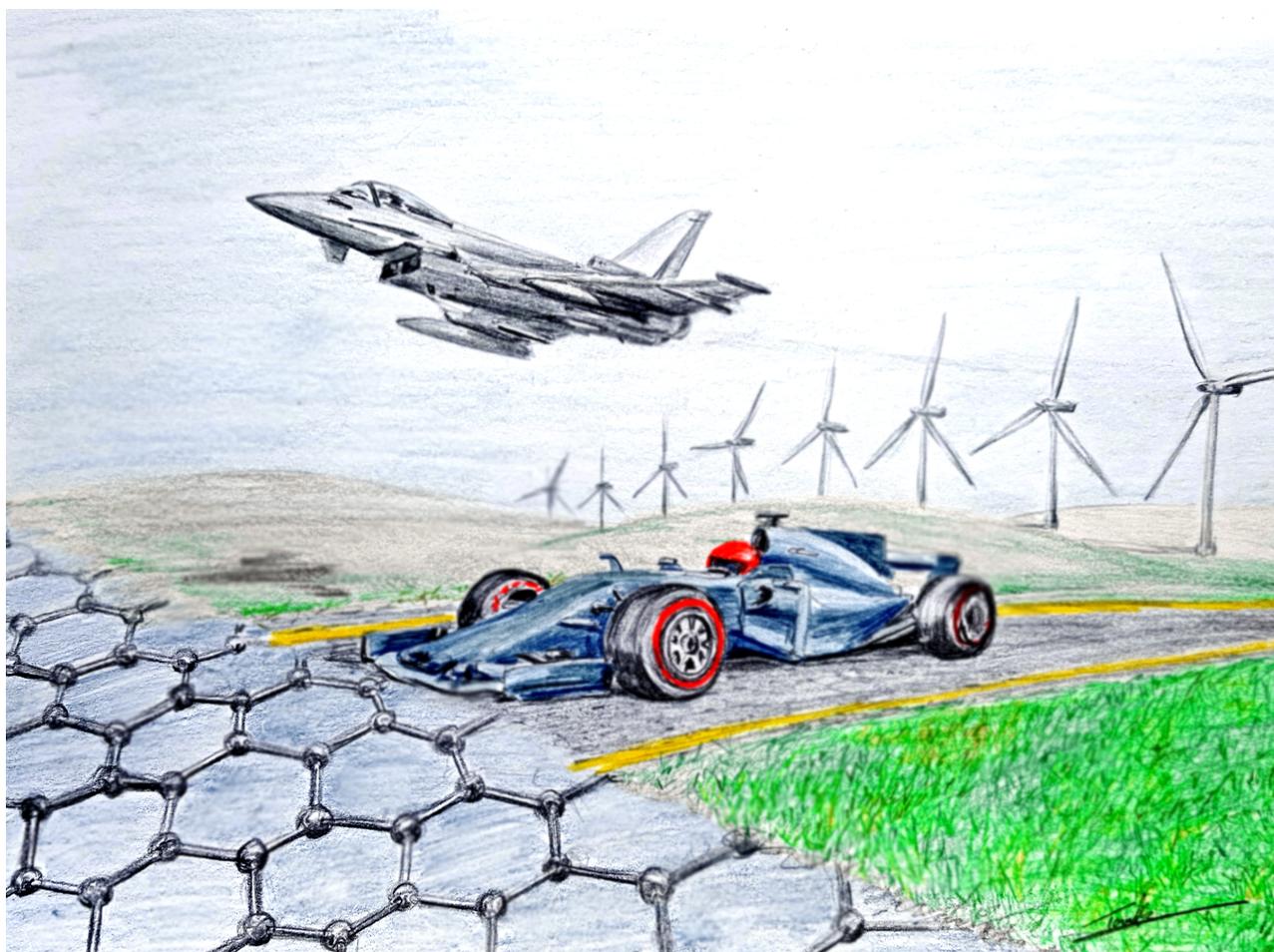
Edited by Sharali Malik, Arkady Krasheninnikov
and Silvia Marchesan

# Imprint

# Advances in nanocarbon composite materials

Sharali Malik[*1], Arkady V. Krasheninnikov[*2,3] and Silvia Marchesan[*4]

## Editorial

Address:
[1]Karlsruhe Institute of Technology, Institute of Nanotechnology, Hermann-von-Helmholtz-Platz 1, 76344 Eggenstein-Leopoldshafen, Germany, [2]Aalto University, Department of Applied Physics, P.O. Box 11100, 00076 Aalto, Finland, [3]Helmholtz-Zentrum Dresden-Rossendorf, Bautzner Landstraße 400, 01328 Dresden, Germany, and [4]University of Trieste, Department of Chemical and Pharmaceutical Sciences, Via L. Giorgieri 1, Trieste 34127, Italy

Email:
Sharali Malik[*] - sharali.malik@kit.edu; Arkady V. Krasheninnikov[*] - arkady.krasheninnikov@aalto.fi; Silvia Marchesan[*] - marchesan.silvia@gmail.com

* Corresponding author

Keywords:
nano-augmented composite materials

Materials have always been crucial to human development, to the point of being used as a reference to name specific stages of development. The first was the Stone Age, then the Bronze Age and then the Iron Age and on to their equivalents in modern times viz. the Plastic Age, the Silicon Age and the Nanomaterials Age. About 70% of all technical innovations (as estimated by the German federal government) can be attributed either directly or indirectly to the properties of the materials used – solutions are being explored on how to interface nanomaterials with other components in the macroscopic world. Therefore, we could reasonably state that we are entering the Composite Age. In particular, nanocarbons display unique properties to innovate in practically all technological sectors and branches of industry. This cutting-edge use of nano-augmented composite materials has the potential to reduce environmental pollution, to conserve resources, to save energy, and generally, to improve the quality of our lives.

Since the discovery of fullerenes over thirty years ago, there has been increasing research in the area of nanocarbon materials.

Research in this field was boosted first by the discovery of carbon nanotubes and then by the advent of graphene and then expanded to the area of two-dimensional materials. This Thematic Series contains reviews and articles spanning diverse areas of research and highlights promising applications for energy transfer composites, coatings, biosensors, diagnostics, biomedicine and advanced nanocarbon materials.

Many of the contributors to this Thematic Series represent a cross-section of research subjects from participants of the European Cooperation in Science & Technology (COST) Action CA15107 "MultiComp". COST is the longest running European framework supporting transnational cooperation amongst researchers, engineers and scholars across Europe. MultiComp is a COST Action designed to bring together theorists, experimentalists, technologists and industrialists in the field of nanocarbon materials technology and currently has over 300 participants from 33 COST countries, along with participants from Belarus, Moldova, Korea, China, Japan, Australia and New Zealand.

This Thematic Series highlights virtually all subfields of advanced nanocarbon materials research, from the longer established fields of carbon nanofibers, graphene oxide (GO) and multiwalled carbon nanotubes (MWCNTs) in composite materials, to the newer areas of nanocarbon materials for use in biomedicine and diagnostics. Energy transfer materials are also well represented with articles and reviews covering aspects of engineering, thermo-mechanical properties, photovoltaics and Li-ion battery materials.

Last but not least, we would like to thank the staff at the *Beilstein Journal of Nanotechnology*, along with all contributors and referees for making this innovative Thematic Series possible.

Sharali Malik, Arkady Krasheninnikov, Silvia Marchesan

Karlsruhe, Aalto, and Trieste, November 2017

## ORCID® iDs

Sharali Malik - https://orcid.org/0000-0003-1057-529X
Silvia Marchesan - https://orcid.org/0000-0001-6089-3873

# Miniemulsion copolymerization of (meth)acrylates in the presence of functionalized multiwalled carbon nanotubes for reinforced coating applications

Bertha T. Pérez-Martínez[1], Lorena Farías-Cepeda[*2], Víctor M. Ovando-Medina[3], José M. Asua[1], Lucero Rosales-Marines[2] and Radmila Tomovska[*1,4]

## Full Research Paper

`Open Access`

Address:
[1]POLYMAT and Departamento de Química Aplicada, Facultad de Ciencias Químicas, University of the Basque Country UPV/EHU, Joxe Mari Korta zentroa, Tolosa Etorbidea 72, Donostia-San Sebastián 20018, Spain, [2]Departamento de Ingeniería Química, Universidad Autónoma de Coahuila, Blvd. V. Carranza e Ing. José Cárdenas V. S/N, Saltillo, Coah, 25280 México, [3]Ingeniería Química, Coordinación Académica Región Altiplano (COARA) Universidad Autónoma de San Luis Potosí, Carretera a Cedral KM 5+600, San José de las Trojes, Matehuala, SLP, 78700 México, and [4]IKERBASQUE, Basque Foundation for Science, Bilbao, Spain

Email:
Lorena Farías-Cepeda[*] - lorenafarias@uadec.edu.mx;
Radmila Tomovska[*] - radmila.tomovska@ehu.es

* Corresponding author

Keywords:
electrical conductivity; hybrid polymers; mechanical properties; miniemulsion polymerization; multiwalled carbon nanotubes

## Abstract

Film forming, stable hybrid latexes made of methyl metacrylate (MMA), butyl acrylate (BA) and 2-hydroxyethyl methacrylate (HEMA) copolymer reinforced with modified multiwalled carbon nanotubes (MWCNTs) were synthesized by in situ miniemulsion polymerization. The MWCNTs were pretreated by an air sonication process and stabilized by polyvinylpyrrolidone. The presence of the MWCNTs had no significant effect on the polymerization kinetics, but strongly affected the polymer characteristics ($T_g$ and insoluble polymer fraction). The performance of the in situ composites was compared with that of the neat polymer dispersion as well as with those of the polymer/MWCNT physical blends. The in situ composites showed the presence of an additional phase likely due to the strong interaction between the polymer and MWNCTs (including grafting) that reduced the mobility of the polymer chains. As a result, a substantial increase of both the storage and the loss moduli was achieved. At 60 °C, which is above the main transition region of the polymer, the in situ composites maintained the reinforcement, whereas the blends behaved as a liquid-like material. This suggests the formation of a 3D network, in good agreement with the high content of insoluble polymer in the in situ composites.

## Introduction

Carbon nanotubes (CNTs) are hollow, fiber-like materials, with a diameter on the nanometer scale and a relatively long length on the micrometer scale, resulting in a very high aspect ratio material. Two types of CNTs exist, those made of a single graphene layer rolled-up into a cylinder (single-walled carbon nanotubes (SWCNTs)) or multiwalled CNTs (MWCNTs) that consist of two or more sheets of graphene concentrically rolled around a hollow core. Due to the excellent electrical, optical, thermal, mechanical, and chemical properties of CNTs, they are considered to be an advanced material that may be useful for multiple applications, one of which is polymer composite synthesis [1-4].

By inclusion of CNTs in polymer matrices, nanostructured materials with improved mechanical, electrical and thermal properties may be synthesized. The interaction between the polymer and the CNTs is crucial to principally determine the distribution of CNTs within the polymer matrix and to obtain the best performance from the nanocomposites [1,2]. One way to improve this interaction is to functionalize the surface of CNTs, either by covalent attachment or through the supramolecular adsorption or wrapping of suitable functionalities and even surface active substances [1,2,4,5].

Various techniques have been developed for the synthesis of CNT–polymer composites, including solution mixing [6,7], melt blending [8-12], latex technology (blends of latexes and CNT dispersions) [13-17], and in situ polymerization [8,12,18-21]. In situ polymerization can be performed in solution, bulk and in dispersed media. Polymerization in dispersed media allows a relatively easy control of the reactor temperature (which is a drawback of bulk polymerization), and when the continuous medium is water, the process is much more environmentally friendly than solution polymerization. Furthermore, this technique has the potential of offering a better distribution of CNTs in the film cast from the dispersion because the CNTs are placed in the interstitial sites between the polymer nanoparticles, which hinders CNT aggregation in the film.

Emulsion polymerization is the most frequently used waterborne polymerization process in industry [22-26]. However, especially for hybrid systems that contain an additional solid phase, miniemulsion polymerization is much more versatile [27-31]. The characteristic feature of this process is that particle formation predominantly occurs by nucleation of the preformed miniemulsion droplets, which minimizes the changes in the system during the particle nucleation period and does not require massive diffusion of the components of the formulation through the aqueous phase. Ham et al. [32,33] used a so-called miniemulsion process in an attempt to cover SWCNTs with

polystyrene nanoparticles, where *n*-pentanol was used as a hydrophobe to minimize Ostwald ripening. However, *n*-pentanol is rather water soluble and it cannot hinder Ostwald ripening. Therefore, it is doubtful that the monomer droplets were stable. Ha et al. [18] polymerized miniemulsions prepared by sonicating a mixture of surfactant-stabilized SWCNTs, monomers (styrene and isoprene) and a costabilizer (hexadecane), finding that the surfactant was transferred to the latex during the reaction; this led to nanotube aggregation. Donescu et al. [34] carried out the miniemulsion polymerization of styrene, styrene/acrylonitrile and methyl methacrylate (MMA) in the presence of MWCNTs. Grafting of the polymer on the MWCNTs was reported. The resulting nanocomposites were foamed with supercritical $CO_2$. The foams showed a decreased pore size, an increased cell density and higher volume expansion when the MWCNT concentration increased. Capek and Kocsisova [35] studied the effect of the type and concentration of surfactant on the kinetics of miniemulsion polymerization of butyl acrylate (BA) in the presence of CNTs.

Waterborne polymer dispersions are mainly used for coatings and adhesives, which involve the formation of films directly cast from the dispersion, usually at ambient temperature [22,24]. This limits the potential application of the dispersions prepared in the works discussed above [18,32-34] because high glass transition temperature ($T_g$) polymers that do not form films at ambient temperature were synthesized. From BA dispersions, the adhesive films might eventually be prepared; however, Capek and Kocsisová [35] did not study this.

The main aim of this work is to produce film-forming waterborne composites for reinforced coating applications, in which the reinforcement is achieved by addition of small amounts of MWCNTs. The synthesis was carried out by miniemulsion co-polymerization of MMA/BA/2-hydroxyethyl methacrylate (HEMA) in the presence of MWCNTs. The minor amount of HEMA in the monomer mixture was added to further improve the interaction between the polymer and the MWCNTs. The disentanglement of the MWCNTs bundles prior to use in polymer composites was performed by ultrapower sonication performed either in water or in air, and afterwards stabilization by polyvinylpyrrolidone (PVP) in dispersion. Air-sonicated MWCNTs allowed for a smooth polymerization reaction, resulting in 20 wt % solids content (s.c.), stable and film-forming latexes with up to 1 wt % MWCNTs incorporated. Important mechanical and thermal reinforcement was achieved due to the 3D network formation of the filler within the polymer matrix and creation of strong interactions (including grafting between the phases).

# Experimental
## Materials

Multiwalled carbon nanotubes (MWCNTs, length = 5–10 μm; diameter = 10–20 nm) were purchased from IoLiTec Nanomaterials Co. (98.5%, Germany). Polyvinylpyrrolidone (PVP) with molar mass of 10,000 g·mol$^{-1}$ was purchased from Sigma-Aldrich (99%). Potassium persulfate (KPS) was used as an initiator and purchased from Fluka. Sodium dodecyl sulfate (SDS) from Sigma-Aldrich (99%) and stearyl acrylate (SA) from BASF (98%), were used as surfactant and costabilizer, respectively. MMA monomer was acquired from Sigma-Aldrich (>98.5%), BA and HEMA were purchased from Fluka (>99%) and used as received. Double deionized water was used throughout the experiment.

## MWCNT pretreatment

MWCNTs were pretreated by sonication in air, after which they were dispersed in water in presence of PVP. The procedure for sonication in air was as follow: 0.35 g of MWCNTs were placed into a 50 mL beaker that had a magnetic stirrer. An ultrasound tip (Branson 450 instrument, Danbury, CT) was introduced into the beaker (keeping a separation between the ultrasound tip and magnetic stirrer of approximately 2 cm and 1 cm separation between the tip and the MWCNTs) and the beaker was sealed. Afterwards, ultrasound was applied for 1.5 h at 70% of power output and 50% duty cycle under magnetic stirring (200 rpm). In addition to disentangling the bundles, sonication is expected to break the MWCNTs.

The aqueous dispersion of MWCNTs used in the composite preparation was prepared by dispersing the treated MWCNTs (0.15 g) in water (50.5 g) in the presence of polyvinylpyrrolidone (PVP, 3 g) and sonicated for 10 min (70% of power output and 50% duty cycle).

## Miniemulsion polymerization of MMA/BA/HEMA in the presence of MWCNTs

Batch miniemulsion polymerization samples were made in a 150 mL glass-jacketed reactor equipped with mechanical stirring (200 rpm). The organic phase contained 20 g of a mixture of MMA/BA/HEMA/SA (47.6/47.6/0.96/3.84 wt/wt or 54.76/43.21/0.6/1.44 mol/mol). SA was used as a costabilizer to prevent the Oswald ripening process.

It is worth pointing out that SA was incorporated into the copolymer; therefore, strictly speaking, a MMA/BA/HEMA/SA copolymer was formed. The aqueous phase was formed by mixing 40 g of water with 0.2 g SDS. The aqueous and the organic phases were mixed under vigorous stirring and this mixture was sonicated under magnetic stirring for 15 min at 9 output control and 80% duty cycle with a Branson 450 instrument (Danbury, CT). Sonication was carried out in an ice bath to avoid overheating. After miniemulsion preparation, it was mixed under stirring (250 rpm, 15 min) with different amounts the aqueous dispersion of PVP-stabilized MWCNTs (0.1, 0.25, 0.5, 0.75 and 1.0 wt % with respect to monomers).

The resulting miniemulsion was bubbled with N$_2$ for 15 min and the temperature was raised to 70 °C. Afterwards, 0.20 g of KPS (1 wt % with respect to monomers) were added to the reactor to start the polymerization. The N$_2$ flow was maintained throughout polymerization.

Blank polymer latexes were synthesized by miniemulsion polymerization using the same organic phase and 40 g of water with 0.2 g of SDS. The mixture was under agitation for 15 min and then sonicated under magnetic stirring for 15 min (80% of duty cycle, 9 output control, Branson 450). Sonication was carried out in an ice bath to avoid overheating. Polymerization was carried out at 70 °C using KPS.

## Films

Films from the hybrid latexes MMA/BA/HEMA/MWCNT and from the blends were cast on Teflon molds and dried in a constant climate chamber (Espec Bench SH-641) at 25 °C and 80% of relative humidity for 3 days. Table 1 presents the nomenclature and characteristics of all the samples investigated throughout this study.

**Table 1:** Preparation method and characteristics of the investigated samples.

| Sample | Preparation method | Weight fraction of MWCNTs (wt %)[a] |
|---|---|---|
| blank polymer | miniemulsion polymerization of neat monomers | 0 |
| in situ 0.5 wt % | miniemulsion polymerization in presence of MWCNTs | 0.5 |
| in situ 1.0 wt % | miniemulsion polymerization in presence of MWCNTs | 1.0 |
| blend 0.5 wt % | mixing of blank polymer + MWCNTs aqueous dispersion | 0.5 |
| blend 1.0 wt % | mixing of blank polymer + MWCNTs aqueous dispersion | 1.0 |
| aged in situ 0.5% | in situ 0.5 wt % film stored for three years | 0.5 |
| aged blend 0.5% | blend 0.5 wt % film stored for three years | 0.5 |

[a]Weight percent based on monomer.

## Characterization

The conversion process was performed gravimetrically [36]. Latex stability was studied by measuring the light backscattered from the dispersions using a Turbiscan Lab expert apparatus scanning the dispersions placed in a vial (55 mm path length) at regular intervals. The particle size was measured by quasielastic light scattering (QLS) with a ZEN1600 apparatus (Malvern Instruments). The samples were prepared by diluting one drop of latex in deionized water. The reported diameters are the average of two subsequent measurements. It should be noted that the content of MWCNTs after dilution is below the detection limit of the apparatus so their presence did not affect the measurements. An insoluble fraction in tetrahydrofuran (THF) of the composite (gel content) was determined by the Soxhlet extraction.

The fractured composite films were prepared under liquid nitrogen and scanning electron microscopy (SEM) images were taken in a Hitachi S-4800. Differential scanning calorimetry (DSC) measurements of films cast from hybrid latexes and blends were carried out in a Q1000, TA Instruments apparatus. 5 mg of each sample were placed in standard aluminum DSC pans and analyzed in air atmosphere at a heating rate of 10 °C/min, starting from cooling to 80 °C and heating to 120 °C. The results of the second heating scan are reported. The conductivity of films was measured using a four-point probe (Digital Lock-In, SR850), and the viscoelastic properties of the films were determined in a dynamic mechanical thermal analyzer (DMTA, Triton Technology, Tritec 2000 DMTA). The scans were performed at a frequency of 1 Hz with a heating rate of 4 °C min$^{-1}$ and the storage and loss moduli were measured. The measurements were run in single-cantilever bending mode with a displacement of 0.005 mm and a length between the clamps of 2 mm.

The mechanical properties of the films were determined by tensile test measurement. The films with an average thickness of 450 μm were prepared by drying in Teflon molds at 25 °C and 80% humidity for 3 days. The measurements were performed in an MTS Insight 10 instrument at a constant strain velocity of 2 mm·s$^{-1}$ at two different temperatures, 25 °C and 60 °C.

## Results and Discussion
### Miniemulsion polymerization kinetics and properties of the hybrid latexes

In situ miniemulsion polymerization at 20 wt % solid content was performed in the presence of various amounts of air-sonicated MWCNTs (0–1 wt % with respect to monomer) stabilized by PVP. All the latexes had a dark blue color and were very stable (Figure S1, Supporting Information File 1), presenting less than 1 wt % coagulum after the reaction.
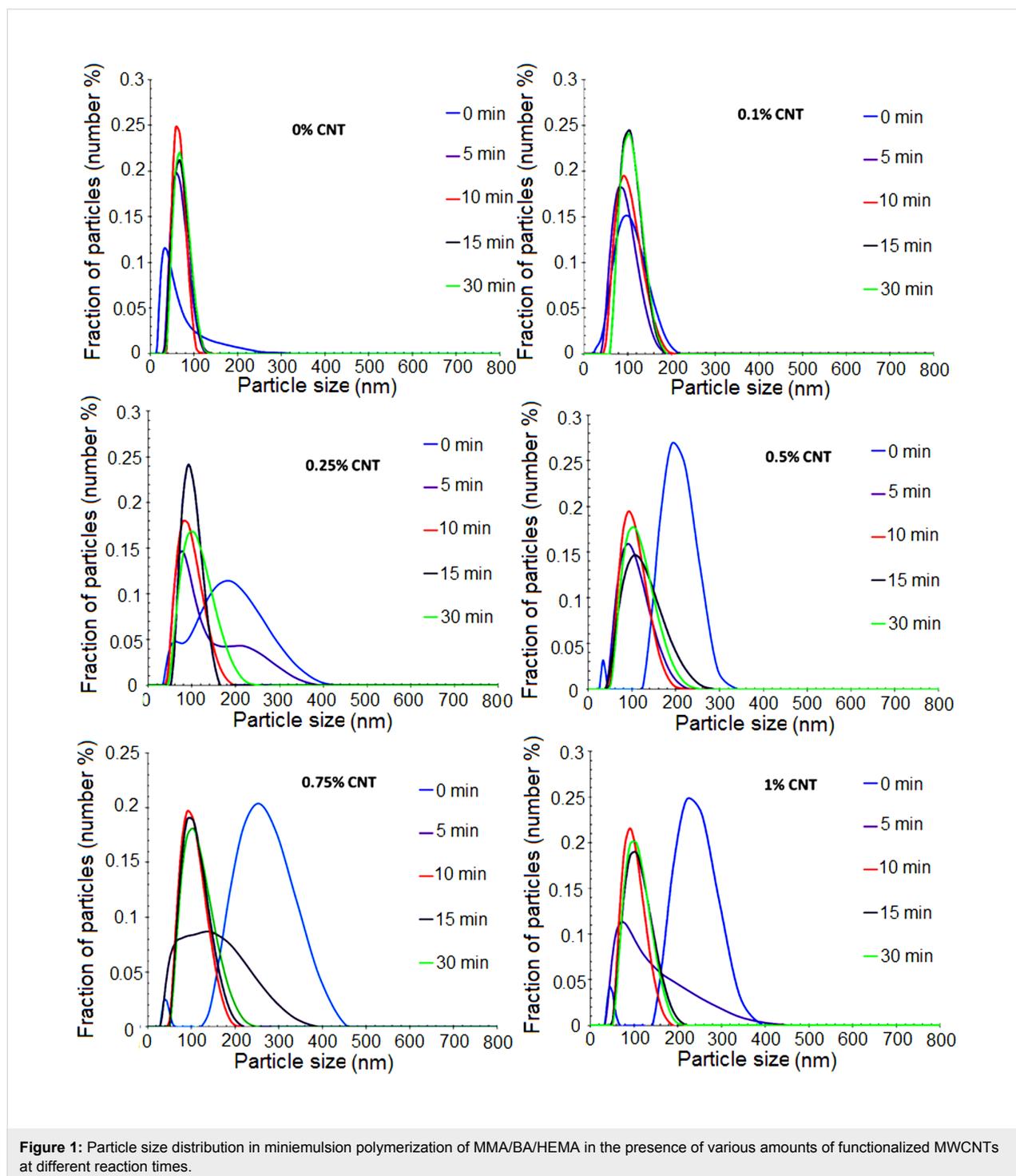
Table 2 presents the characteristics of the miniemulsions and the corresponding in situ latexes prepared with air-sonicated MWCNTs. It can be seen that the droplet size increased with increased MWCNT concentration. A possible reason for this finding is that, as the total amount of surfactant (SLS and PVP) used in these experiments was constant, the amount of surfactant available for droplet stabilization decreased as the MWCNT concentration increased. The concentration of MWCNTs may also have an influence on the miniemulsification process, which is sensitive to changes in viscosity [37,38].

The comparison between the droplet and particle diameters (Table 2) may shed some light on the relative importance of these effects. It can be seen that a significant secondary nucleation occurred and that the final particle size was not affected by the concentration of MWCNTs. This suggests that the number of polymer particles was controlled by the surfactant available, which was independent of the MWCNT concentration, indicating that the presence of MWCNTs reduced the efficiency of the miniemulsification by increasing the viscosity of the system. In Figure 1, the evolution of the particle size distribution per number of particles during the miniemulsion polymerization of MMA/BA/HEMA in the presence of various quantities of MWCNTs (0.1–1%) is presented.

It can be seen that, except for the 0.1 wt % MWCNT sample, most of the particles were formed by secondary nucleation

**Table 2:** Droplet *z*-average diameter ($d_d$) and particle *z*-average diameter ($d_p$), number of particles ($N_p$), and gel content in the final latexes obtained in the miniemulsion polymerization of MMA/BA/HEMA with different MWCNT concentrations.

| MWCNT (wt %) | $d_d$ (nm) | $d_p$ (nm) | $N_p$ (number/$L$) | Weight fraction of insoluble polymer (%) |
|---|---|---|---|---|
| 0 | 40 | 70 | $1.11 \times 10^{18}$ | 0 |
| 0.10 | 100 | 101 | $3.71 \times 10^{17}$ | 13 |
| 0.25 | 210 | 102 | $3.60 \times 10^{17}$ | 21 |
| 0.50 | 246 | 97 | $4.20 \times 10^{17}$ | 30 |
| 0.75 | 261 | 98 | $4.06 \times 10^{17}$ | 45 |
| 1.0 | 283 | 99 | $3.94 \times 10^{17}$ | 85 |

**Figure 1:** Particle size distribution in miniemulsion polymerization of MMA/BA/HEMA in the presence of various amounts of functionalized MWCNTs at different reaction times.

likely due to the combined effect of the presence of a highly water soluble monomer (HEMA) that promoted the formation of oligomers in the aqueous phase, and the large droplet size that reduced the total surface area of the droplets and consequently their ability to capture oligomers from the aqueous phase. For the 0.1 wt % sample, the particle size was similar to the droplet size, likely because the smaller droplets had a larger

surface area, and hence they were more efficient capturing radicals from the aqueous phase.

Figure 2 presents the kinetics of the miniemulsion polymerizations carried out with different air-sonicated MWCNT loads. In all cases, final conversion yields between 96% and 100% were obtained after 30 min of polymerization. It can be seen that,

after the initial stages, all the reactions carried out in the presence of MWCNTs presented almost the same polymerization rate (slope of the curve conversion vs time), which agrees with the similar number of particles. The polymerization carried out in the absence of MWCNTs showed a higher polymerization rate that agrees well with a higher number of polymer particles. The discrepancies at shorter process times are common in batch processes carried out using technical monomers (monomers containing inhibitors).
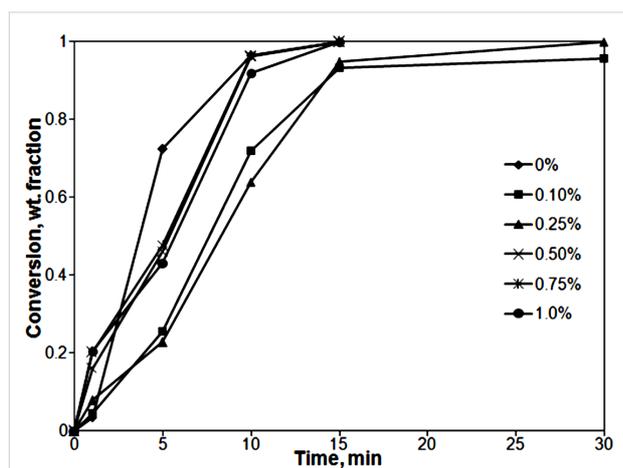


**Figure 2:** Conversion vs time curves for the MMA/BA/HEMA miniemulsion polymerizations with different MWCNT concentrations. Continuous lines are a guide to the eye.

Table 2 also shows that the fraction of insoluble polymer in THF (often called gel) increased with the concentration of MWCNTs, reaching values as high as 85% for 1 wt % CNTs. In this regard, it is worth pointing out that this fraction was measured in films, not in individual particles. On the other hand, the blank experiment (first row in Table 2) shows that, in agreement with previous results [39], no gel was obtained for the monomer composition used.

The substantial increase in the fraction of insoluble polymer with slight increase of MWCNT load could be explained by two

different processes. On one hand, polymer chains may be grafted onto either the PVP or the surface of MWCNTs, as it has been reported in the emulsion polymerization of styrene initiated with KPS in the presence of MWCNTs [40] and in the emulsion polymerization of MMA/BA with graphene filler [41]. The second reason for such a high gel content may be the H-bonding created between the PVP-stabilized MWCNTs and the OH groups of the polymer (due to presence of HEMA) upon film formation.

## Characterization of films cast from hybrid latexes

SEM images of the fractured surface of the composite films cast from hybrid latexes at different air-sonicated MWCNT loads are presented in Figure 3, where MWCNTs appear as white structures embedded within a dark polymer matrix. A homogeneous dispersion of the MWCNTs within the matrix is evident at all MWCNT loadings and the presence of larger aggregates may be observed for 1 wt % MWCNTs in Figure 3c,d d (indicated by white arrows in Figure 3d, under higher magnification).

In Table 3, the glass transition temperatures ($T_g$) of the neat polymer and the polymer composites determined by DSC are presented. The neat polymer and simple blends of the neat polymer and the air-sonicated MWCNTs were used as reference samples. In all the samples, three main transition regions were observed, which are the result of the heterogeneous composition of the polymer formed in the batch polymerization of monomers with different reactivity ratios ($r_{MMA} = 2.02 \pm 0.36$, $r_{BA} = 0.26 \pm 0.14$) [42] that yield a MMA-rich polymer ($T_g = 90$ ºC) at the beginning of the process and an acrylate-rich copolymer at the end. The $T_g$ of this copolymer was close to −70 ºC, which indicates that it is a copolymer of BA (−54 ºC) and SA ($T_g = -111$ ºC).

The broad peak from 40 ºC to about 50 ºC for the neat polymer (Figure S2, Supporting Information File 1) corresponds to the change of the copolymer composition during polymerization. In

**Table 3:** Glass transition temperatures of films made of in situ and blends of poly(MMA/BA/HEMA) polymers at different air-sonicated MWCNT concentrations.

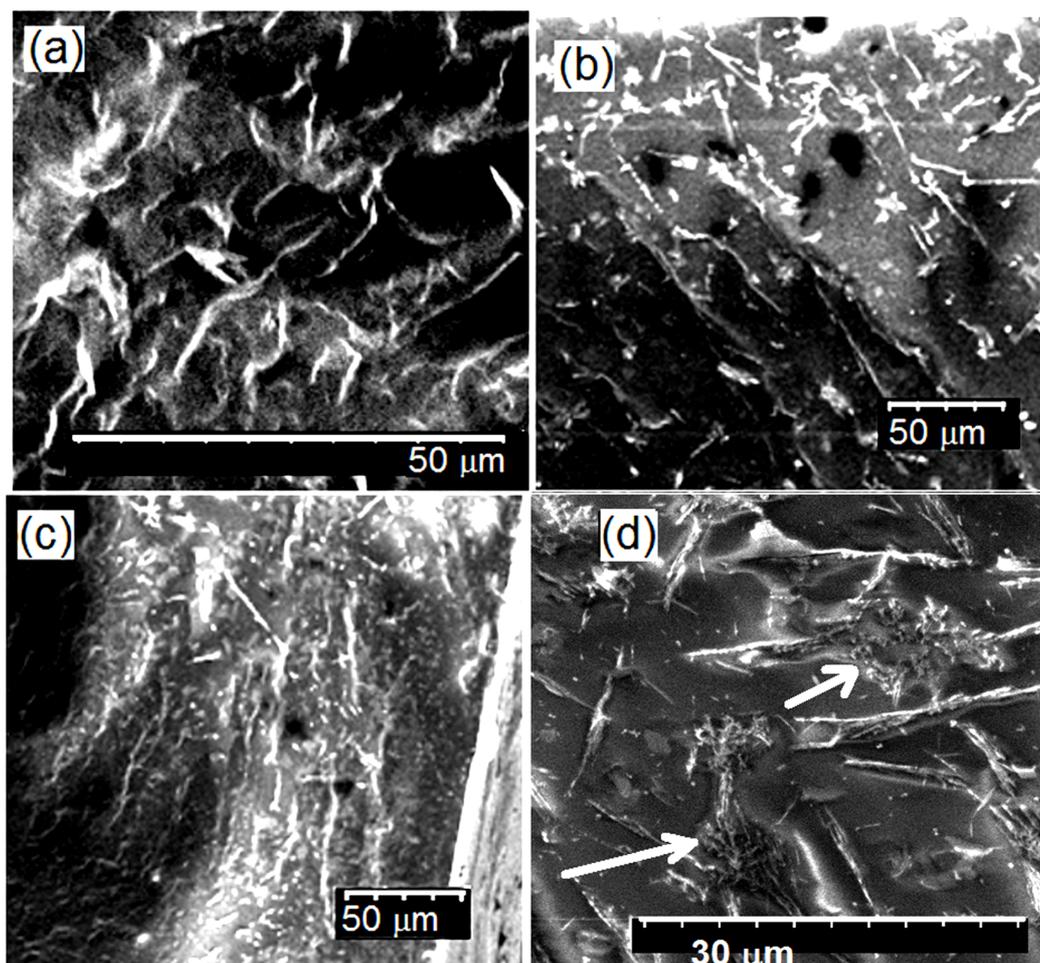| MWCNT content | $T_{g1}$ region | $T_{g2}$ region | $T_{g3}$ region |
|---|---|---|---|
| 0% | −70 °C | −40 to 50 °C | 93 °C |
| blend 0.50% | −71 °C | −45 to 60 °C | 92 °C |
| blend 1.0% | −71 °C | −45 to 60 °C | 90 °C |
| in situ 0.50% | −71 °C | −45 to 75 °C (additional $T_g$ at about 50 °C ) | 90 °C |
| in situ 1.0% | −69 °C | −45 to 75 °C (additional $T_g$ at about 50 °C ) | 90 °C |

**Figure 3:** SEM images of the fractured surface of films made of MMA/BA/HEMA/MWCNT in situ hybrid latexes at different air-sonicated MWCNT loadings: (a) 0.1 wt % MWCNT; (b) 0.5 wt % MWCNT; (c,d) 1 wt % MWCNT under different magnifications.

the case of the blends, this broad peak shifted 10 ºC towards higher temperatures, which denotes that the mobility of the polymer chains was influenced by the presence of the MWCNTs. This, in turn, suggests significant mutual interaction. The PVP used to stabilize the MWCNTs may play a key role in those effects as it is expected to develop π–π interactions with the MWCNTs and hydrogen bonding with the O–H functionalities of the polymer.

In the in situ produced composites, the broad, middle peak shifted to an even higher temperature with the new peak centered at about 50 ºC. This indicates the presence of a new phase that was attributed to grafted polymer, which also contributed to the high fraction of insoluble polymer (see above). The stronger interaction between the polymer and the MWCNTs for in situ composites is further supported by the fact that aging did not vary the results of the DSC measurements, whereas for the neat polymer samples and blends, the 90 ºC

peak disappeared through microphase mixing (Figure S2, Supporting Information File 1).

Figure 4a shows that the addition of MWCNTs (0.5 wt %) to the polymer resulted in an augmentation of the storage modulus (i.e., stiffness) over the entire temperature range. In addition, the loss modulus of the composites was also higher than that of the blank polymer (Figure 4b), namely the energy dissipation as heat was promoted. This may be due to an additional energy dissipation mechanism when the MWCNTs slide at the interface with polymer in presence of PVP, as previously reported in case of organic/inorganic hybrids [43].

The strong polymer–MWCNT interaction substantially improves the mechanical properties of the in situ composites, particularly at high temperatures. Figure 4 shows that, whereas in the glassy state ($T < 20$ °C) there was no difference between the blends and in situ composites, in the rubbery region, both the
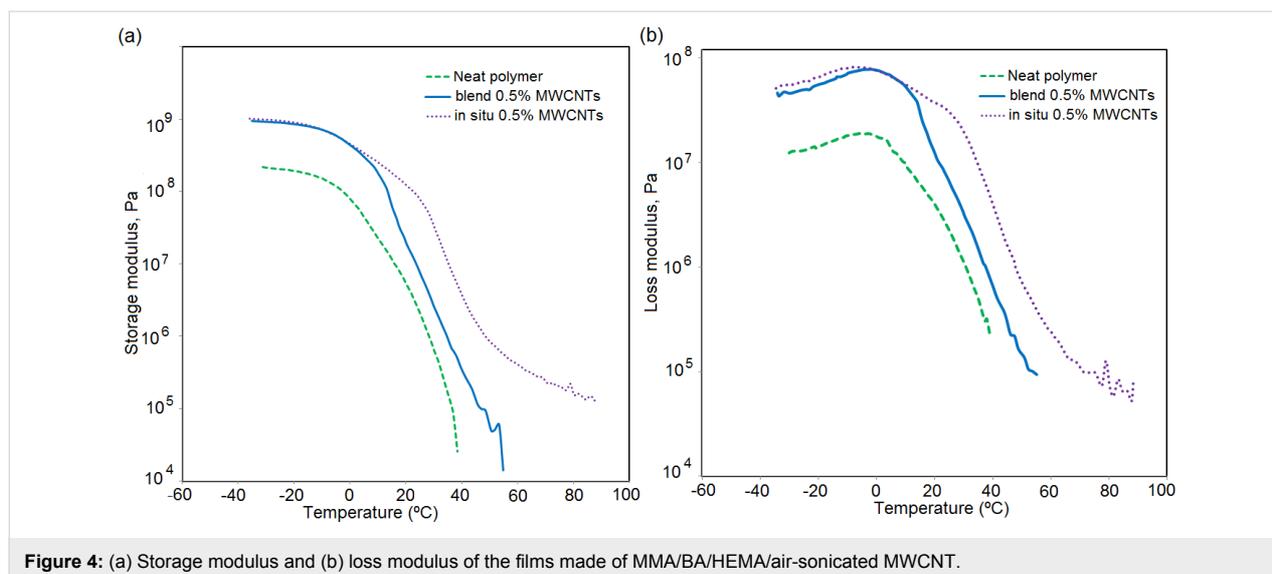
**Figure 4:** (a) Storage modulus and (b) loss modulus of the films made of MMA/BA/HEMA/air-sonicated MWCNT.

storage and the loss moduli were higher for the in situ composite. The effect was particularly noticeable above 60 °C. The high moduli of the in situ composites in the high temperature region suggest the formation of 3D networks of the filler within the polymer matrix and significant crosslinking between the both phases [18].

In order to gain deeper insight into the reinforcement effect of the MWCNTs in these composites, stress–strain testing of the films was performed at 25 °C and at 60 °C (Figure 5).

At 25 °C, the addition of MWCNTs led to a substantial reinforcement of the polymer with significant differences between blends and in situ composites. Whereas the blends showed a high Young's modulus followed by a softening after the yield point, the in situ components presented a lower Young's

modulus with a gradual transition from elastic to plastic behavior. In addition, they had a much higher stress at break.

The differences between blends and in situ composites were more acute in the tensile tests carried out at 60 °C, where the in situ composites maintained the reinforcement, but the neat polymer and the blends behaved as liquid-like materials. As the amount of MWCNTs is the same in the blend and in the in situ composites, the reinforcement was clearly due to the improved interaction between MWCNTs and the polymer, and due to the formation of the 3D reinforcing network of MWCNTs within the matrix.

## Conclusion

Film-forming polymer–MWCNT composite dispersions were synthesized in situ by miniemulsion polymerization of MMA/
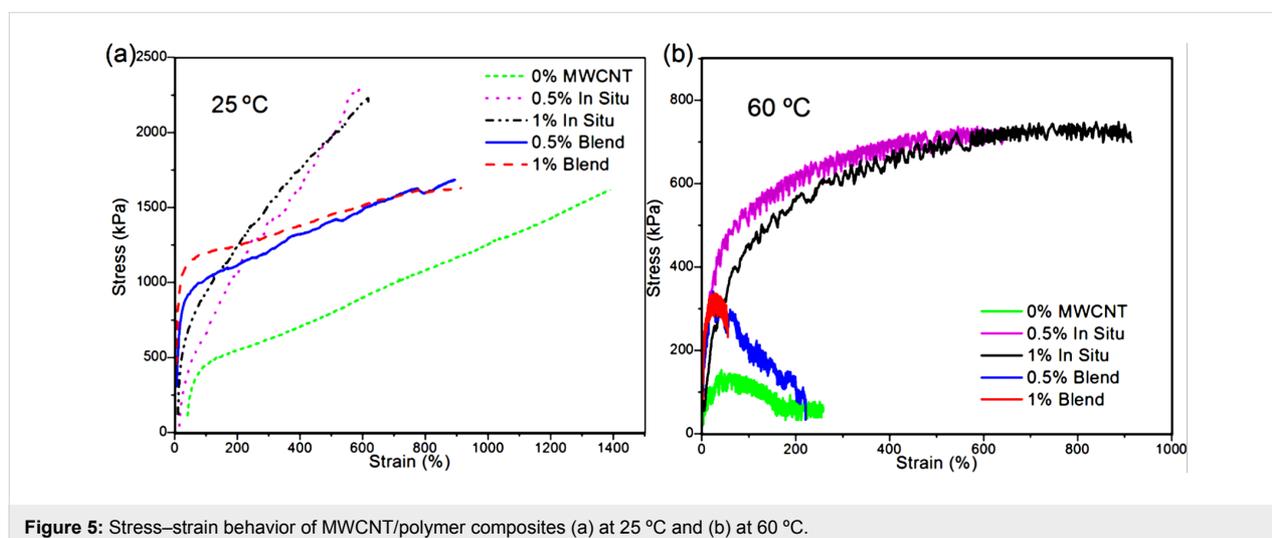


**Figure 5:** Stress–strain behavior of MWCNT/polymer composites (a) at 25 °C and (b) at 60 °C.

BA/HEMA/SA in the presence of varying amounts of air-sonicated MWCNTs, stabilized in aqueous dispersions by means of PVP. The reactions proceeded smoothly and resulted in stable, colloidal, hybrid latexes without coagulum. The presence of the MWCNTs had no significant effect on polymerization kinetics, but strongly increased the fraction of insoluble polymer that was attributed to the interaction between the OH groups of the copolymer and the PVP-stabilized MWCNTs and as well to the possible grafting of polymer chains onto MWCNTs. Because monomers with different reactivity ratios were polymerized in batch, a heterogeneous copolymer showing different $T_g$ values was obtained. The in situ composites showed the presence of an additional phase likely formed as a result of the strong interactions between polymer and MWNCTs (including grafting) that reduced the mobility of the polymer chains.

The MWCNTs were homogeneously dispersed within composite films formed from the hybrid latexes up to a load of 1 wt % MWCNTs, where the presence of larger aggregates was noticed. The performance of the in situ composites was compared with that of the neat polymer dispersion, as well as with those of polymer/MWCNT physical blends. The addition of MWCNTs resulted in a substantial increase of both the storage and the loss moduli. At 60 ºC, which is above the main transition region of the polymer, the in situ composites maintained the reinforcement, whereas the blends behave as a liquid-like material. This suggests the formation of a 3D network in good agreement with the high content of insoluble polymer in the in situ composites.

## Supporting Information

### Supporting Information File 1
Colloidal stability of the latexes and the aging effect on the stability of the composite films.
Colloidal stability of polymer and hybrid (in situ 1 wt % MWCNT) latexes, measured by light backscattered from the dispersions, is shown. Differential scanning calorimetry (DSC) results for neat polymer and composite in situ and blend with 0.5 wt % MWCNT are presented for as-received and aged latexes (for three years).
[http://www.beilstein-journals.org/bjnano/content/supplementary/2190-4286-8-134-S1.pdf]

## Acknowledgements

## References

1. Ma, P.-C.; Siddiqui, N. A.; Marom, G.; Kim, J.-K. *Composites, Part A* **2010,** *41,* 1345–1367. doi:10.1016/j.compositesa.2010.07.003
2. Balasubramanian, K.; Burghard, M. *Small* **2005,** *1,* 180–192. doi:10.1002/smll.200400118
3. Park, S.; Vosguerichian, M.; Bao, Z. *Nanoscale* **2013,** *5,* 1727–1752. doi:10.1039/c3nr33560g
4. Wang, X. J.; Liu, Z. *Chin. Sci. Bull.* **2012,** *57,* 167–180. doi:10.1007/s11434-011-4845-9
5. Karousis, N.; Tagmatarchis, N.; Tasis, D. *Chem. Rev.* **2010,** *110,* 5366–5397. doi:10.1021/cr100018g
6. Bryning, M. B.; Milkie, D. E.; Islam, M. F.; Kikkawa, J. M.; Yodh, A. G. *Appl. Phys. Lett.* **2005,** *87,* 161909. doi:10.1063/1.2103398
7. Sundararajan, P. R.; Singh, S.; Moniruzzaman, M. *Macromolecules* **2004,** *37,* 10208–10211. doi:10.1021/ma048269g
8. Araujo, R. S.; Oliveira, R. J. B.; Marques, M. d. F. V. *Macromol. React. Eng.* **2014,** *8,* 747–754. doi:10.1002/mren.201400012
9. Jin, Z.; Pramoda, K. P.; Xu, G.; Goh, S. H. *Chem. Phys. Lett.* **2001,** *337,* 43–47. doi:10.1016/S0009-2614(01)00186-5
10. Kim, J. Y.; Kim, S. H. *J. Polym. Sci., Part B: Polym. Phys.* **2006,** *44,* 1062–1071. doi:10.1002/polb.20728
11. Zhang, Q.-H.; Chen, D.-J. *J. Mater. Sci.* **2004,** *39,* 1751–1757. doi:10.1023/B:JMSC.0000016180.42896.0f
12. Annala, M.; Lahelin, M.; Seppälä, J. *eXPRESS Polym. Lett.* **2012,** *6,* 814–825. doi:10.3144/expresspolymlett.2012.87
13. Grossiord, N.; Loos, J.; Regev, O.; Koning, C. E. *Chem. Mater.* **2006,** *18,* 1089–1099. doi:10.1021/cm051881h
14. Jurewicz, I.; Keddie, J. L.; Dalton, A. B. *Langmuir* **2012,** *28,* 8266–8274. doi:10.1021/la301296u
15. Jurewicz, I.; Worajittiphon, P.; King, A. A. K.; Sellin, P. J.; Keddie, J. L.; Dalton, A. B. *J. Phys. Chem. B* **2011,** *115,* 6395–6400. doi:10.1021/jp111998p
16. Wang, T.; Lei, C.-H.; Dalton, A. B.; Creton, C.; Lin, Y.; Fernando, K. A. S.; Sun, Y.-P.; Manea, M.; Asua, J. M.; Keddie, J. L. *Adv. Mater.* **2006,** *18,* 2730–2734. doi:10.1002/adma.200601335
17. Wang, T.; Lei, C.-H.; Liu, D.; Manea, M.; Asua, J. M.; Creton, C.; Dalton, A. B.; Keddie, J. L. *Adv. Mater.* **2008,** *20,* 90–94. doi:10.1002/adma.200700821
18. Ha, M. L. P.; Grady, B. P.; Lolli, G.; Resasco, D. E.; Ford, W. T. *Macromol. Chem. Phys.* **2007,** *208,* 446–456. doi:10.1002/macp.200600521
19. Lahelin, M.; Vesterinen, A.; Nykänen, A.; Ruokolainen, J.; Seppälä, J. *Eur. Polym. J.* **2011,** *47,* 873–881. doi:10.1016/j.eurpolymj.2011.02.020
20. Nie, M.; Xia, H.; Wu, J. *Iran. Polym. J.* **2013,** *22,* 409–416. doi:10.1007/s13726-013-0141-7
21. Xia, H.; Qiu, G.; Wang, Q. *J. Appl. Polym. Sci.* **2006,** *100,* 3123–3130. doi:10.1002/app.22934
22. Takamura, K.; Urban, D. *Polymer Dispersions and Their Industrial Applications;* Willey-VCH: London, U.K., 2002.

23. van Herk, A. M.; Gilber, R. G. Emulsion Polymerisation. In *Chemistry and Technology of Emulsion Polymerisation;* van Herk, A. M., Ed.; John Wiley & Sons Ltd., 2013; pp 43–74. doi:10.1002/9781118638521.ch3

24. Daniel, J.-C. Aspects industriels. Les grandes familles de produits et de procédés industriels. In *Les Latex Synthétiques. Élaboration, Propriétés, Applications;* Daniel, J.-C.; Pichot, C., Eds.; Lavoisier: Paris, 2006; pp 319–329.

25. Barandiaran, M. J.; de la Cal, J. C.; Asua, J. M. Emulsion Polymerization. In *Polymer Reaction Engineering;* Asua, J. M., Ed.; Blackwell Publishing Ltd.: Oxford, U.K., 2007; pp 233–272. doi:10.1002/9780470692134.ch6

26. Tomovska, R.; de la Cal, J. C.; Asua, J. M. Reactions in heterogeneous media: emulsion, miniemulsion, microemulsion, suspension, and dispersion polymerization. In *Monitoring Polymerization Reactions: From Fundamentals to Applications;* Reed, W. F.; Alb, A. M., Eds.; John Wiley & Sons: Hoboken, New Jersey, 2014. doi:10.1002/9781118733813.ch4

27. Asua, J. M. *Prog. Polym. Sci.* **2002,** *27,* 1283–1346. doi:10.1016/S0079-6700(02)00010-2

28. Schork, F. J.; Luo, Y.; Smulders, W.; Russum, J. P.; Butti, A.; Fontenot, K. *Adv. Polym. Sci.* **2005,** *175,* 129–255. doi:10.1007/b100115

29. Weiss, C. K.; Landfester, K. *Adv. Polym. Sci.* **2010,** *233,* 185–236. doi:10.1007/12_2010_61

30. Asua, J. M. *Prog. Polym. Sci.* **2014,** *39,* 1797–1826. doi:10.1016/j.progpolymsci.2014.02.009

31. Paulis, M.; Asua, J. M. *Macromol. React. Eng.* **2016,** *10,* 8–21. doi:10.1002/mren.201500042

32. Ham, H. T.; Choi, Y. S.; Chee, M. G.; Chung, I. J. *J. Polym. Sci., Part A: Polym. Chem.* **2006,** *44,* 573–584. doi:10.1002/pola.21185

33. Ham, H. T.; Choi, Y. S.; Jeong, N.; Chung, J. *Polymer* **2005,** *46,* 6308–6315. doi:10.1016/j.polymer.2005.05.062

34. Donescu, D.; Corobea, M. C.; Petcu, C.; Spataru, C. I.; Ghiurea, M.; Somoghi, R.; Gabor, R.; Thomassin, J.-M.; Alexandre, M.; Jerome, C. *J. Appl. Polym. Sci.* **2014,** *131,* 41148. doi:10.1002/app.41148

35. Capek, I.; Kocsisová, T. *Polym. J.* **2011,** *43,* 700–707. doi:10.1038/pj.2011.50

36. Goldwasser, J. M.; Rudin, A. *J. Polym. Sci., Polym. Chem. Ed.* **1982,** *20,* 1993–2006. doi:10.1002/pol.1982.170200803

37. Manea, M.; Chemtob, A.; Paulis, M.; de la Cal, J. C.; Barandiaran, M. J.; Asua, J. M. *AIChE J.* **2008,** *54,* 289–297. doi:10.1002/aic.11367

38. López, A.; Chemtob, A.; Milton, J. L.; Manea, M.; Paulis, M.; Barandiaran, M. J.; Theisinger, S.; Landfester, K.; Hergeth, W. D.; Udagama, R.; McKenna, T.; Simal, F.; Asua, J. M. *Ind. Eng. Chem. Res.* **2008,** *47,* 6289–6297. doi:10.1021/ie701768z

39. González, I.; Asua, J. M.; Leiza, J. R. *Polymer* **2007,** *48,* 2542–2547. doi:10.1016/j.polymer.2007.03.015

40. Shaffer, M. S. P.; Koziol, K. *Chem. Commun.* **2002,** *18,* 2074–2075. doi:10.1039/b205806p

41. Arzac, A.; Leal, G. P.; Fajgar, R.; Tomovska, R. *Part. Part. Syst. Charact.* **2014,** *31,* 143–151. doi:10.1002/ppsc.201300286

42. Roos, S. G.; Müller, A. H. E.; Matyjaszewski, K. *Macromolecules* **1999,** *32,* 8331–8335. doi:10.1021/ma9819337

43. Daniloska, V.; Keddie, J. L.; Asua, J. M.; Tomovska, R. *ACS Appl. Mater. Interfaces* **2014,** *6,* 22640–22648. doi:10.1021/am506726f

# Luminescent supramolecular hydrogels from a tripeptide and nitrogen-doped carbon nanodots

Maria C. Cringoli[1], Slavko Kralj[1,2], Marina Kurbasic[1], Massimo Urban[1]
and Silvia Marchesan[*1]

## Abstract

The combination of different components such as carbon nanostructures and organic gelators into composite nanostructured hydrogels is attracting wide interest for a variety of applications, including sensing and biomaterials. In particular, both supramolecular hydrogels that are formed from unprotected D,L-tripeptides bearing the Phe-Phe motif and nitrogen-doped carbon nanodots (NCNDs) are promising materials for biological use. In this work, they were combined to obtain luminescent, supramolecular hydrogels at physiological conditions. The self-assembly of a tripeptide upon application of a pH trigger was studied in the presence of NCNDs to evaluate effects at the supramolecular level. Luminescent hydrogels were obtained whereby NCND addition allowed the rheological properties to be fine-tuned and led to an overall more homogeneous system composed of thinner fibrils with narrower diameter distribution.

## Introduction

Carbon nanodots (CNDs) are quasi-spherical nanoparticles with a diameter less than 10 nm. They are a very interesting class of nanocarbons because of their excellent water solubility, ease of functionalization, high chemical stability and resistance to photo-bleaching. In particular, CNDs have attracted particular interest in light of their biocompatibility, combined with their fascinating fluorescence properties, such as excitation-dependent emission range. Their properties allow them to have an important impact in biological and environmental applications as

alternatives to traditional, toxic, semiconductor-based quantum dots (QDs). They can be employed as biosensors in bioimaging, drug delivery, and in the photoreduction of metals, since they have electron transfer and redox properties. There are two main methods to synthesize CNDs: top-down (e.g., laser ablation, electrochemical synthesis) and bottom-up (e.g., combustion, microwave irradiation) [1,2]. In particular, the use of microwave (MW) irradiation is an interesting synthetic approach, which allows several molecular precursors to be employed,

such as amino acids in aqueous solution [3]. As an example, L-tyrosine was used to form hydrophobic CNDs able to sense ions and silver nanoparticles [4]. Arginine or cysteine have also been efficiently employed as starting materials through a hydrothermal route [5]. Alternatively, in a convenient MW-based method, arginine was shown to be a useful starting material towards highly fluorescent nitrogen-doped CNDs (NCNDs) that were chosen for the present study (Scheme 1) [6].

Several works have reported incorporation of CNDs into hydrogels as an interesting method to control fluorescence quenching upon application of a specific trigger, and to introduce new physical and optical properties of interest [7,8]. Such systems can be useful in several applications, such as bacteria detection [9], sensing of reactive oxygen species (ROS) and screening for apoptotic activity of 5-fluorouracil [10]. Hydrogels containing CNDs reported thus far are mainly composed of cross-linked macro-polymer networks, such as poly-(*N*-vinylcaprolactam) (PVCL) [11] or poly(*N*-isopropylacrylamide) (PNIPAM), which is a thermoresponsive polymer suitable for biomedical and environmental applications [12,13]. Carbohydrates such as chitosan [14,15], alginate [16], and agarose [7,17] hydrogels have also been used to incorporate CNDs.

Only a very few studies have incorporated CNDs into supramolecular hydrogels obtained from low-molecular-weight gelators (LMWGs). Relative to gelling polymers, LMWGs have many advantages including well-defined chemical composition, and the possibility to achieve reversible gelation upon application of a specific trigger. Thus, smart, soft materials that can adapt to the environment can be obtained, mimicking natural biological tissues to address demanding therapeutic challenges [18]. In 2015, Steed et al. reported CND–hydrogel hybrids obtained from bis(urea) derivatives used as LMWGs [19] that displayed considerable fluorescence enhancement relative to CNDs alone and showed promising performance in silver ion selective determination [20]. In 2016, the interesting hydrogelation ability of guanosine 5′-monophosphate (5′-GMP)-derived CNDs was also

reported [21]. To the best of our knowledge, the addition of CNDs to peptide-based hydrogels has not yet been investigated, despite this being an interesting class of supramolecular soft materials.

Peptide self-assembled hydrogels are inherently biocompatible and biodegradable and thus are promising biomaterials for cell culture, regenerative medicine, tissue engineering, and drug delivery applications [22]. The identification of self-assembling peptides that are as short as possible is highly useful due to the low cost and simplicity of synthesis, as opposed to longer peptides that require solid-phase-peptide synthesis [23]. The most typical approach employs *N*-capped short peptides, especially whereby the *N*-capping group is a hydrophobic, aromatic moiety that assists self-assembly in water [24]. In 2012, the first systems of uncapped tripeptides were reported to self-assemble into nanostructured hydrogels at physiological conditions and without the need for organic solvents. These tripeptides were heterochiral, that is, composed of both D- and L-amino acids, and they formed hydrogels following a pH change, while their homochiral stereoisomers did not.

In particular, the tripeptide DLeu-Phe-Phe, which was chosen for the present study, immediately formed a self-supporting hydrogel [25]. In a typical protocol, the tripeptide was first dissolved as an anion in an alkaline buffer thanks to electrostatic repulsion between molecules. Then, the addition of a second buffer was used to lower the pH to neutral. This tripeptide proved to be a strong gelator able to co-assemble into nanostructured hydrogels with aromatic small molecules. In this manner, it yielded a useful vehicle for the sustained release of the poorly soluble antibiotic ciprofloxacin [26]. Fluorescent hydrogels were formed from co-assembly with a dye into nanostructures of different morphology, depending on whether the dye was added initially to the peptide in the alkaline buffer solution, or later to the second buffer that triggered self-assembly, thus showing different outcomes depending on the protocol used [27].
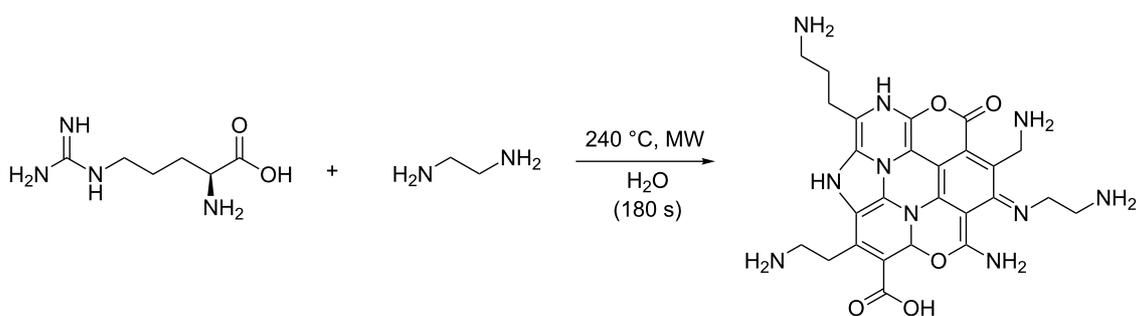


**Scheme 1:** Microwave-assisted formation of nitrogen-doped carbon nanodots from arginine [6].

In this study, we report for the first time two different protocols for NCND incorporation into supramolecular hydrogels composed of an uncapped tripeptide, [D]Leu-Phe-Phe, and characterize the system by rheometry, fluorescence, circular dichroism (CD), FTIR spectroscopy, transmission electron microscopy (TEM), and differential scanning calorimetry (DSC). Given that this tripeptide is capable of forming a hydrogel with mild antimicrobial activity and a lack of cytotoxicity in vitro [26], this new system could be valuable for the development of wound healing applications [28], whereby luminescence could be advantageous to visually track the presence of the hydrogel and the ability of its components to penetrate through the derma [29]. In addition, peptide hydrogels based on the Phe-Phe motif [30,31] and bearing unnatural D-amino acids [32,33] are attractive biomaterials that may display higher durability relative to traditional peptide counterparts, in addition to better biocompatibility and the possibility to incorporate bioactive motifs relative to non-peptide hydrogels. Therefore, in the long term, a supramolecular hydrogel composed of a peptide and luminescent nanodots could be valuable for tissue regeneration based on a bioactive scaffold that can be also visualized in vivo by fluorescence microscopy. Alternatively, other potential applications could be developed in the future for drug delivery and even sensing, if the nanodots were suitably derivatized to release a drug or undergo fluorescence quenching upon binding of a specific target molecule.

## Results and Discussion
### Peptide self-assembly in the presence of NCNDs
The incorporation of carbon nanostructures into hydrogels is a useful approach to introduce additional properties to soft materials. In the case of self-assembling peptides, non-covalent π–π interactions between the nanocarbon and aromatic residues of the peptide offer a convenient means to bring the two components together into a supramolecular system [34]. This rationale

could also be applied to NCNDs and the tripeptide [D]Leu-Phe-Phe, which were evaluated for co-assembly into hydrogels following a pH trigger from alkaline to neutral. Different scenarios were envisaged: the presence of the NCNDs 1) could promote peptide self-assembly by acting as a nucleation agent, 2) could hinder self-assembly of the peptide, or 3) might not interact with the peptide. To verify the effects of NCNDs on the supramolecular behavior of the tripeptide, a series of experiments were performed as outlined in Table 1, with different amounts of each component dissolved in either buffer or together in the alkaline buffer.

It is apparent that the presence of NCND hindered peptide supramolecular organization, and even more so when peptide and NCND were dissolved together prior to self-assembly (i.e., NCND and peptide were both added to the alkaline buffer). Increasing the peptide concentration up to nearly its solubility limit (i.e., for a final peptide concentration of 15 mM in the hydrogel) progressively increased the amount of NCND that could be tolerated by the peptide to achieve self-assembly, up to a maximum of 1 mg/mL or 15% w/w relative to [D]Leu-Phe-Phe (highlighted in Table 1). In this case, self-supportive hydrogels were formed regardless of the protocol used (i.e., addition of the NCNDs to either alkaline or acidic buffer), as shown in Figure 1. Both conditions were further investigated since peptide nanostructure morphology may change significantly upon co-assembly with other molecular components, depending onto whether the latter were added either to the alkaline or the acidic buffer [27].

### Rheological properties of NCND–peptide hydrogels
The rheological properties of the hydrogels were assessed by means of oscillatory rheometry (Figure 2). In all cases, gelation was so rapid that the monitoring of the sol-to-gel transition was not possible. Time sweep experiments (Figure 2a,c,e) revealed

**Table 1:** Experiments to probe the effects of NCND presence on peptide self-assembly (SA).

| Peptide final concentration[a] | NCND concentration (relative to the peptide) | Hydrogel formation? NCND prior to SA[b] | Hydrogel formation? NCND during SA[c] |
|---|---|---|---|
| 5 mM | 0.02 mg/mL (1% w/w) | No | Yes |
| 5 mM | ≥0.05 mg/mL (2.5% w/w) | No | No |
| 10 mM | 0.04 mg/mL (1% w/w) | No | Yes |
| 10 mM | 0.1 mg/mL (2.5% w/w) | No | Yes |
| 10 mM | 0.2 mg/mL (5% w/w) | No | Yes |
| 10 mM | ≥0.4 mg/mL (10% w/w) | No | No |
| 15 mM | 0.7 mg/mL (10% w/w) | Yes | Yes |
| **15 mM** | **1.0 mg/mL (15% w/w)** | **Yes** | **Yes** |
| 15 mM | ≥1.4 mg/mL (20% w/w) | No | No |

[a]The peptide alone forms hydrogels already at 5 mM. [b]NCNDs are dispersed in the alkaline buffer. [c]NCNDs are dispersed in the acidic buffer.

(G'') moduli were significantly reduced, yielding softer hydrogels (G' of 3 kPa within 1 h). Instead, when the NCNDs were added to the peptide during the pH trigger, gelation kinetics were slowed down. However, over 1 h, the hydrogel had already reached an elastic modulus of 10 kPa, thus yielding a stiffer material relative to the former case (Figure 2e). In any case, at any given time point, the hydrogels containing NCNDs displayed a lower elastic modulus G' relative to the peptide alone. This phenomenon could be compatible with the presence of thinner bundles of fibers.

Stress sweeps (Figure 2b,d,f) were employed to monitor variations in the hydrogel resistance to applied stress. Relative to the peptide alone (Figure 2b), NCND addition (Figure 2d,f) increased the linear viscoelastic region, thus improving the material stability to external forces, especially when NCNDs were added to the acidic buffer. This observation was compatible with better interconnected networks of fibrils in the presence of NCND. Frequency sweep experiments confirmed in all cases a hydrogel nature with G' > G'' and both G' and G'' indepen-



**Figure 1:** Hydrogels obtained from $^D$Leu-Phe-Phe (15 mM) and NCNDs at 1 mg/mL (15% w/w relative to the peptide) dissolved either in alkaline buffer with the peptide prior to self-assembly (left), or in acidic buffer that was added to the peptide alkaline solution to trigger self-assembly (right).

that relative to the peptide alone, which reached an elastic modulus G' of 20 kPa within 1 h (Figure 2a), the addition of NCNDs to the peptide prior to self-assembly (Figure 2c) did not slow down gelation kinetics. Both the elastic (G') and viscous
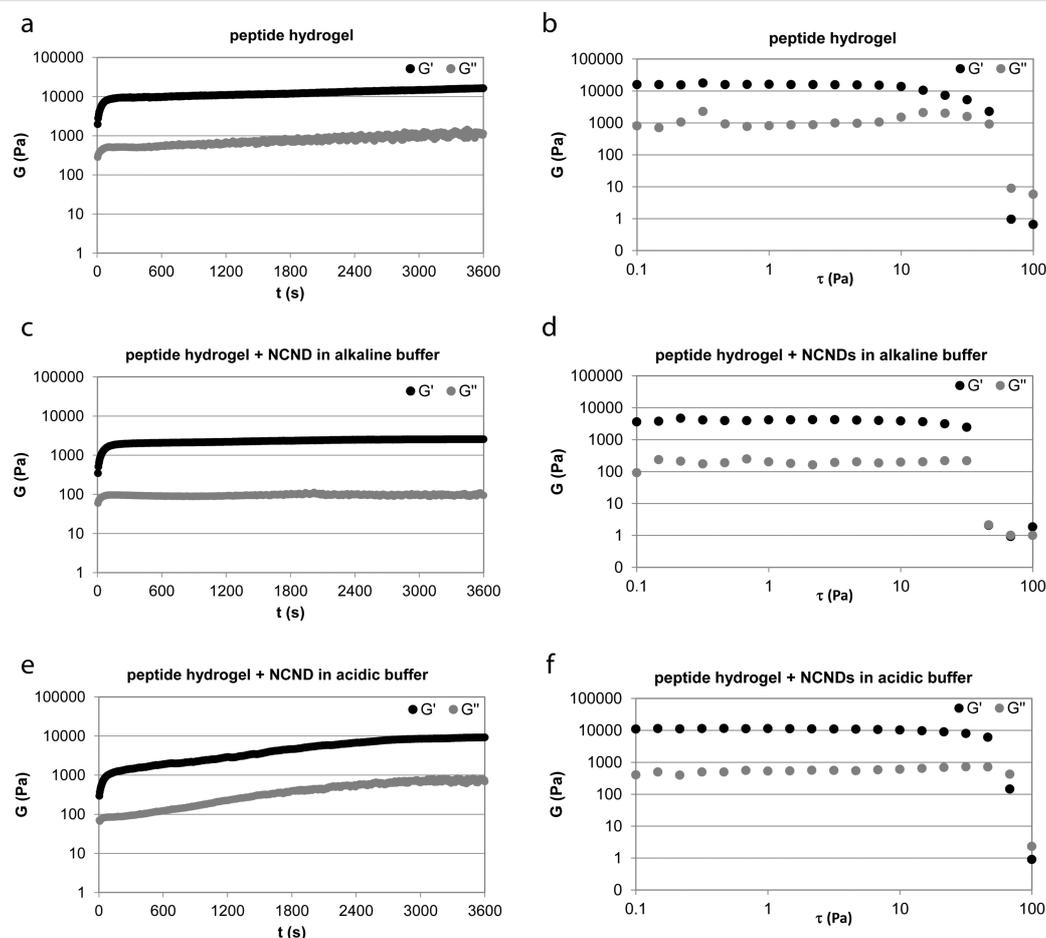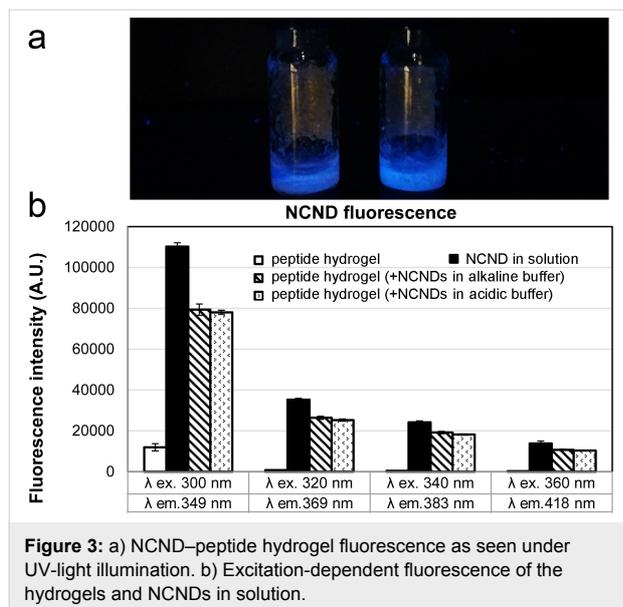


**Figure 2:** Oscillatory rheometric data for the hydrogels. Time sweeps (left) and stress sweeps (right) for the hydrogel composed of the peptide alone (a,b), and with NCNDs added either to alkaline buffer (c,d) or to acidic buffer (e,f).

dent of the applied frequency (see Supporting Information File 1).

Overall, from a rheological point of view, the addition of NCNDs increased the peptide hydrogel stability to applied stress and offered the opportunity to fine-tune stiffness or gelation kinetics, depending on the protocol used to prepare the material.

## Fluorescence properties of NCND–peptide hydrogels

The excitation-dependent fluorescence emission range of the NCNDs was probed within the hydrogel structure (Figure 3). As expected, the peptide hydrogel showed negligible fluorescence properties at the wavelengths explored, while the NCNDs displayed intense fluorescence, especially in the UV region [6]. Relative to NCNDs in solution, their incorporation within the hydrogel matrix resulted in a decrease of their fluorescence emission intensity, accounting for nearly 30% upon excitation at 300 nm, and 20–25% upon excitation at longer wavelengths. Nevertheless, the hydrogels were intensely luminescent as seen under UV-light illumination (Figure 3a). No significant difference was observed between the materials prepared according to the two different protocols. Importantly, upon incorporation into the hydrogel matrix, no shift in NCND fluorescence emission spectra was registered, and the NCND fluorescence stability was not affected over a 7-day period.



**Figure 3:** a) NCND–peptide hydrogel fluorescence as seen under UV-light illumination. b) Excitation-dependent fluorescence of the hydrogels and NCNDs in solution.

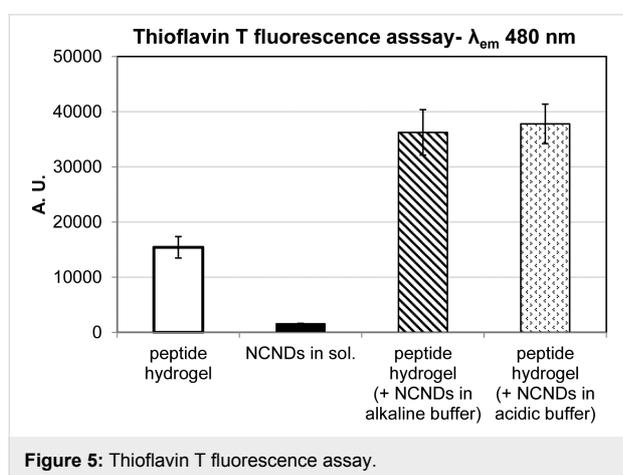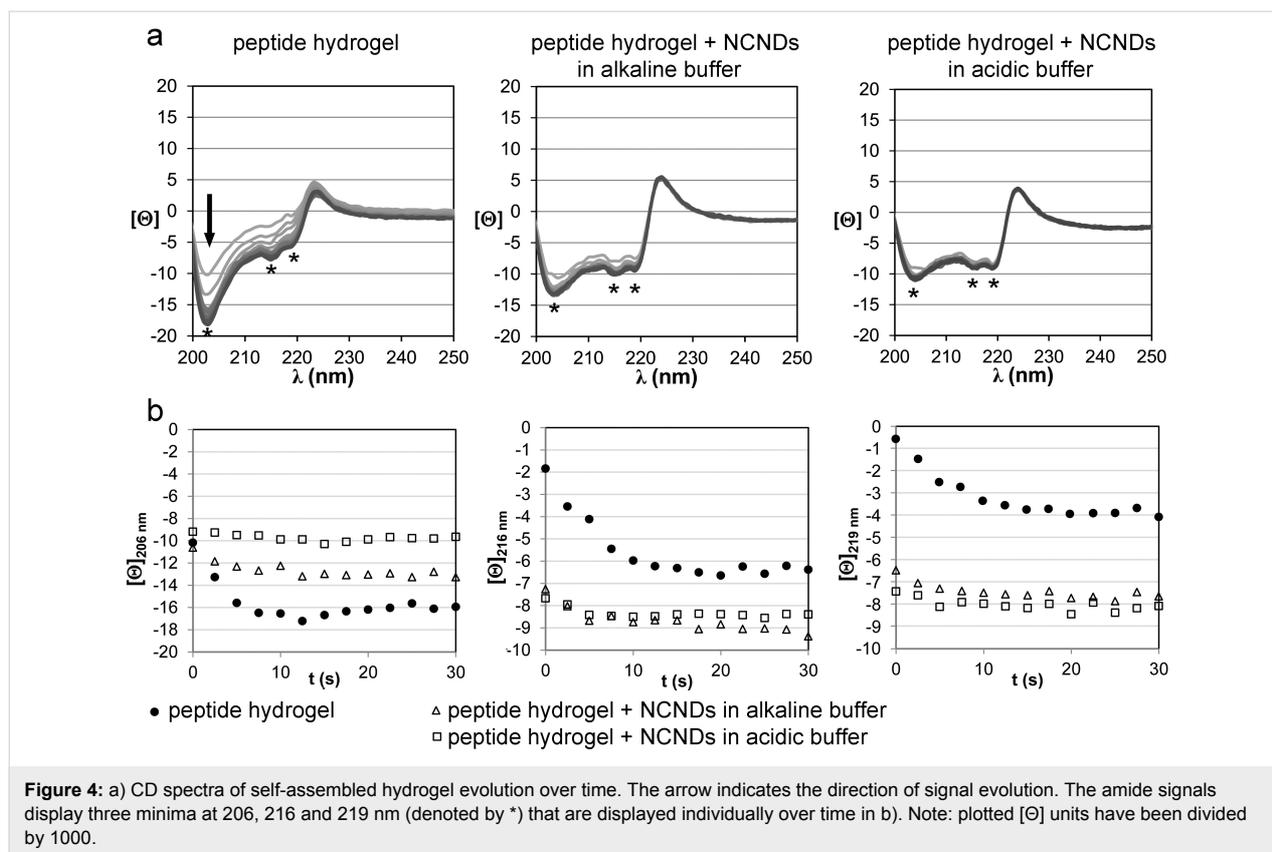## Peptide conformation in the presence of NCNDs

Peptide conformation was assessed by means of circular dichroism (CD), FTIR spectroscopy, and thioflavin T fluorescence.

CD was used to monitor self-assembly over one hour (Figure 4). In all cases, self-assembly led to a spectrum that was very distinctive of the supramolecular structure and markedly different to the peptide in solution (see Supporting Information File 1). Overall, the main features of the peptide hydrogel CD spectra were maintained after NCND addition with quantitative rather than qualitative differences observed. Signal evolution occurred mainly during the initial 10 minutes, with only minor variations over time for the NCND-containing hydrogels.

The 200–220 nm region, which is attributed to amide signals and is thus related to peptide conformation, was characterized by negative minima that were compatible with supramolecular beta-sheets. In particular, three minima were present: one at 206 nm that was more intense for the peptide hydrogel, and another two at 216 and 219 nm that were more intense after addition of NCNDs. In particular, the intensity of the latter was nearly doubled in the presence of NCNDs (Figure 4b). FTIR spectroscopy did not reveal significant differences in the amide I signal between samples (see Supporting Information File 1), suggesting that NCND addition did not significantly affect overall peptide conformation (e.g., from beta-sheets to random coil or else). This hypothesis was further supported by the CD spectrum of the peptide in solution that was unchanged in the presence of NCNDs (see Supporting Information File 1).

Thioflavin T fluorescence was thus used to further understand NCND effects on the peptide supramolecular structure. Thioflavin T is a dye that binds to hydrophobic grooves formed by at least four consecutive beta-strands, leading to fluorescence that is used to assess the peptide amyloid character [35]. Fluorescence arises from the limited rotation of a single bond between two aromatic rings composing the dye, namely the benzothiazole and the dimethylanilino units [36]. Although its fluorescence can also be increased by an increase of solvent viscosity [36], in aqueous environments, it is effectively and universally used as an amyloid marker thanks to its ability to laterally bind to the surface of peptide fibrils [37]. This interaction has been the subject of numerous studies that overall elucidated that an increase in fluorescence intensity linearly correlates to amyloid fibril concentration [38].

In the presence of the dye, the NCNDs showed negligible fluorescence at the wavelength probed, in contrast with the self-assembled peptide, which is in agreement with the literature [25]. Unexpectedly, the addition of NCNDs to the hydrogel led to an over a two-fold increase in thioflavin T fluorescence, regardless of the protocol used (Figure 5). Considering that the addition of NCNDs reduced the overall viscosity of the hydrogel systems, as revealed by rheometry, it is unlikely that the noted increase in fluorescence is to be ascribed to viscosity

**Figure 4:** a) CD spectra of self-assembled hydrogel evolution over time. The arrow indicates the direction of signal evolution. The amide signals display three minima at 206, 216 and 219 nm (denoted by *) that are displayed individually over time in b). Note: plotted [Θ] units have been divided by 1000.



**Figure 5:** Thioflavin T fluorescence assay.

variations. Overall, while NCNDs did not modify peptide conformation, they appeared to favor the formation of supramolecular extended beta-sheets that could bind thioflavin T. This resulted in more intense CD minima at 216 and 219 nm and more intense thioflavin T fluorescence.

## Nanostructure morphology of NCND–peptide hydrogels

Transmission electron microscopy (TEM) was used to assess the nanostructure of the hydrogels (Figure 6). Once self-assem-

bled, the tripeptide formed elongated fibrils that bundled into thicker fibers, forming a three-dimensional network that entrapped water. Typical hydrogel samples composed of peptide alone under TEM imaging appeared as networks of fibers of highly heterogeneous thickness, with a wide distribution ranging from individual fibrils to thick bundles that grow in thickness over time [25]. The TEM imaging performed in the present study confirmed the presence of the anisotropic structures in all cases, with no significant difference in individual fibril diameter upon addition of NCNDs (i.e., $9 \pm 3$ nm for the peptide alone, and $10 \pm 2$ nm upon addition of NCNDs, regardless of the protocol used). In all cases, there was a high density of fibrils with length exceeding the field-of-view of several micrometers, thus hindering the possibility to quantify minor differences in fibril number or length. However, the number of fibrils running in parallel, reflecting their tendency to bundle, appeared higher in the absence of NCNDs, which may play a role in explaining the thioflavin T fluorescence data. Indeed, the presence of higher numbers of thinner and less bundled fibrils could result in a higher accessible surface area for thioflavin T binding.

Due to their small diameter (<2 nm), the NCNDs could not clearly be discerned individually by TEM. However, their presence was compatible with less dense areas in between fibrils, in
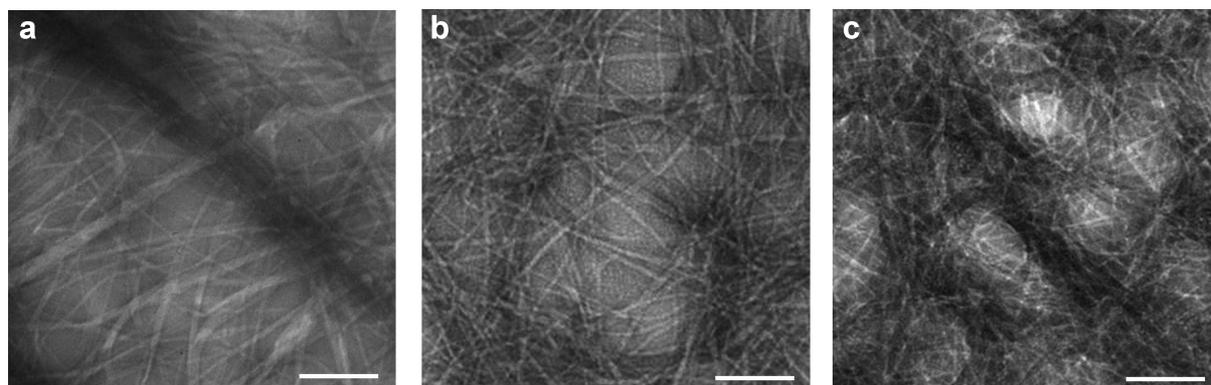
**Figure 6:** TEM micrographs of hydrogels containing peptide (a) and NCNDs added to either alkaline (b) or acidic (c) buffer. Scale bar = 200 nm for all images.

agreement with a lack of a strong interaction of the peptide. However, it was not possible to identify whether NCNDs were also present within the peptide fibrils, giving scope for future investigations to elucidate these systems in further detail.

In a separate set of experiments, a gradual pH change was also investigated to monitor the effects on nanofibril morphology. Briefly, the samples were prepared as previously described, but the acidic buffer was added dropwise to achieve the desired pH. During sample preparation, it was evident that as soon as each drop of the second buffer was added to the system, peptide self-assembly immediately occurred locally before the system could be homogenized by mixing. As a result, all samples displayed a heterogeneous nature, with gel mass and liquid phase around it until gelation was complete. Such a heterogeneous nature was also present at the nanoscale, as revealed by TEM, with wide distribution of fiber diameters in all samples, with and without NCNDs (see Supporting Information File 1). These observations are not surprising since it is well known that the nanostructure outcome of self-assembly is greatly influenced by experimental conditions and gelation kinetics [39,40].

## Thermal stability of NCND–peptide hydrogels

The NCND–peptide hydrogels were assessed for their thermal stability by means of differential scanning calorimetry (DSC) and circular dichroism (CD) with a heating ramp from room temperature up to complete disappearance of the CD signal (see Supporting Information File 1).

DSC did not reveal major differences in the gel-to-sol transition temperature amongst samples. In all cases a first, a wide and asymmetric endotherm was observed, whose minimum relative to $T_m$ was displayed at approximately 77–82 °C. A second, narrow endotherm with a minimum just above 100 °C

could be ascribed to the evaporation of residual buffer solution. It is worth noting that the DSC data of similar peptides and amyloids often display multiple minima that are not always discernible and result in wide, asymmetric endotherms; besides the gel-to-sol transition, other minima in the range of 80–85 °C can be ascribed to aggregates formed during heating [41,42]. It is thus possible that the wide endotherm observed in this work is the sum of all such different components. As a result, minor differences in the thermal stability of the systems with or without NCNDs may have been masked. Indeed, the small DSC sample volumes include as little as 19 µg of NCNDs.

For this reason, we next performed CD with a heating ramp until complete disappearance of the UV signal that monitors specifically peptide conformation and the resulting supramolecular chiral environment. The peptide hydrogel samples displayed progressive reduction of the CD signal until 80 °C, in agreement with DSC data. The samples containing NCNDs in either buffer displayed an anticipated loss of the supramolecular chiral environment that was complete at 70 °C (see Supporting Information File 1). Such reduction in thermal stability is compatible with the thinner fibers observed by TEM upon addition of NCNDs. A minor discrepancy between the absolute values obtained with the two techniques could also be ascribed to sample holder geometries that differ in their surface-to-volume ratios (which is much higher in the CD cell), as well as different heat transfer systems for the two instruments.

## Conclusion

For the first time we reported herein two convenient protocols for the rapid preparation of luminescent supramolecular hydrogels formed by a tripeptide in the presence of NCNDs at physiological conditions. It was shown that relative amounts of peptide and NCNDs needed optimization to allow self-assembly

and gelation, which occurred with up to 15% w/w of NCNDs relative to the peptide. Nevertheless, rheometric analyses revealed that NCNDs increased the linear viscoelastic region of the hydrogel, thus resulting in increased stability of the soft material to applied stress. Importantly, the addition of NCNDs offered the opportunity to fine-tune the gelation kinetics as well as the stiffness of the final material, thus opening new windows of use depending on the intended final application.

Interestingly, neither the beta-sheet peptide conformation nor the individual fibril nanostructure in the hydrogel were significantly changed by the presence of NCNDs. However, both circular dichroism and thioflavin T fluorescence revealed signs of interaction between the two components at the supramolecular level that were compatible with increased concentration of thinner fibres, as opposed to thick bundles, with higher surface area available for thioflavin T binding. As a result, the hydrogels containing NCNDs displayed a narrower fiber diameter distribution with overall thinner structures that were better interconnected, which was in agreement with the rheological observations discussed above. Importantly, NCND addition not only provided luminescence to the hydrogels, but also allowed control over the well-known issue of heterogeneous thickness of supramolecular peptide fibers, resulting in improved viscoelastic properties of the final materials.

# Experimental

All chemicals were purchased from Sigma-Aldrich. All solvents were from Merck. High purity Milli-Q water (MQ water) with a resistivity greater than 18 MΩ·cm was obtained from an in-line Millipore RiOs/Origin system.

## Synthesis and characterization

The tripeptide [D]Leu-Phe-Phe was synthesized according standard Fmoc solid phase peptide synthesis and purified by RP-HPLC, as previously described [25]. The peptide identity and purity was verified by ESI–MS, ^{1}H NMR and ^{13}C NMR. The as-produced NCNDs were synthesized and purified following a reported procedure [6].

## Sample preparation

Tripeptide hydrogels were prepared in phosphate buffer as previously described [25] at the desired concentration as described in Table 1. Briefly, the peptide was dissolved in a 0.1 M solution of sodium phosphate at pH 11.8 (alkaline buffer), and then an equal volume of 0.1 M solution of sodium phosphate buffer at pH 5.8 (acidic buffer) was added to reach a final pH of 7.3 ± 0.1, as verified with a pH meter. For the preparation of the peptide hydrogels containing NCNDs, NCNDs were dispersed either in the alkaline buffer (with the peptide) or in the acidic buffer, at various concentrations as described in Table 1.

## Rheometry

The dynamic time sweep rheological analysis was conducted on a Malvern Kinexus Ultra Plus rheometer with a 20 mm stainless steel parallel plate geometry. The temperature was maintained at 25 °C using a Peltier temperature controller. The samples were prepared in situ and immediately analyzed with a gap of 1.00 mm. Time sweeps were recorded for 1 h using a frequency of 1.00 Hz and a controlled stress of 5.00 Pa. After 1 h, the frequency sweeps were recorded using a controlled stress of 5.00 Pa and then stress sweeps were recorded using a frequency of 1 Hz.

## Circular dichroism (CD) spectroscopy

A 0.1 mm quartz cell was used on a Jasco J815 spectropolarimeter, with 1 s integration time, 1 accumulation, and a step size of 1 nm with a bandwidth of 1 nm over a wavelength range of 200–250 nm. The samples were freshly prepared directly in the CD cell and the spectra were immediately recorded. The spectra were recorded at 25 °C or with a heating ramp up to 80 °C and 5 °C steps. The control samples with only NCNDs in buffer solutions (without peptide) did not show any signal in the region analyzed.

## Fluorescence assay

Gel precursor solutions were prepared as described above and 100 μL of each buffer were immediately put on wells of Greiner 96 U Bottom Black Polystyrene. The controls were used in 200 μL total volume. After 1 h, the fluorescence emission spectra were acquired using a Tecan Infinite M1000 pro, with a bandwidth of 10 nm, selecting the following excitation (ex.) and emission (em.) wavelengths: ex. 300 nm and em. 325–499 nm (maximum at 349 nm); ex. 320 nm and em. 345–499 nm (maximum at 369 nm); ex. 340 nm and em. 365–499 nm (maximum at 383 nm); ex. 360 nm and em. 385–520 nm (maximum at 418 nm). Each condition was repeated at least twice in triplicate. The average and standard deviations were calculated and plotted.

## Thioflavin T fluorescence assay

Gel precursor solutions were prepared as described above and 100 μL of each buffer were immediately put on wells of Greiner 96 U Bottom Black Polystyrene. The controls were used in 200 μL total volume. After 1 h, 20 μL of a solution of thioflavin T (22.2 μM in 20 mM glycine/NaOH pH 7.5, filtered with a 0.2 μm filter) were added in the wells. After 15 min, the fluorescence emission was analyzed using a Tecan Infinite M1000 pro, selecting an excitation wavelength of 446 nm and an emission wavelength range from 470 to 560 nm, with a bandwidth of 10 nm. Each condition was repeated at least twice in triplicate. The average and standard deviations were calculated and plotted.

## TEM imaging

TEM micrographs were acquired on a Jeol, JEM 2100 instrumen (Japan) at 100 kV. TEM grids (copper-grid-supported lacey carbon film) were first exposed to a UV-ozone cleaner (UV-Ozone Procleaner Plus) for 45 mins to make the grid surface more hydrophilic. Then, the six-hour-aged gels were precisely deposited on a TEM grid, dried for 15 min at room temperature, and contrasted by an aqueous tungsten phosphate solution (pH 7.4). The average size or cross-section diameter of the nanostructures was determined by taking into account at least 100 individual nanostructures.

## Supporting Information

The supporting information includes FTIR methods and spectra, additional rheometry and CD data, DSC data, and additional TEM images for the gradual pH change experiments.

### Supporting Information File 1

Additional experimental information.
[http://www.beilstein-journals.org/bjnano/content/supplementary/2190-4286-8-157-S1.pdf]

## Acknowledgements

## References

1. Baker, S. N.; Baker, G. A. *Angew. Chem., Int. Ed.* **2010,** *49,* 6726–6744. doi:10.1002/anie.200906623
2. Miao, P.; Han, K.; Tang, Y.; Wang, B.; Lin, T.; Cheng, W. *Nanoscale* **2015,** *7,* 1586–1595. doi:10.1039/C4NR05712K
3. Jiang, J.; He, Y.; Li, S.; Cui, H. *Chem. Commun.* **2012,** *48,* 9634–9636. doi:10.1039/c2cc34612e
4. Gude, V. *Beilstein J. Nanotechnol.* **2014,** *5,* 1513–1522. doi:10.3762/bjnano.5.164
5. Marinovic, A.; Kiat, L. S.; Dunn, S.; Titirici, M.-M.; Briscoe, J. *ChemSusChem* **2017,** *10,* 1004–1013. doi:10.1002/cssc.201601741
6. Arcudi, F.; Đorđević, L.; Prato, M. *Angew. Chem., Int. Ed.* **2016,** *55,* 2107–2112. doi:10.1002/anie.201510158
7. Gogoi, N.; Barooah, M.; Majumdar, G.; Chowdhury, D. *ACS Appl. Mater. Interfaces* **2015,** *7,* 3058–3067. doi:10.1021/am506558d
8. Nguyen, C. T.; Tran, T. H.; Lu, X.; Kasi, R. M. *Polym. Chem.* **2014,** *5,* 2774–2783. doi:10.1039/C3PY01636F
9. Bhattacharya, S.; Nandi, S.; Jelinek, R. *RSC Adv.* **2017,** *7,* 588–594. doi:10.1039/C6RA25148J
10. Bhattacharya, S.; Sarkar, R.; Nandi, S.; Porgador, A.; Jelinek, R. *Anal. Chem.* **2017,** *89,* 830–836. doi:10.1021/acs.analchem.6b03749
11. Sun, W.; Wu, P. *Phys. Chem. Chem. Phys.* **2017,** *19,* 127–134. doi:10.1039/C6CP06862F
12. Li, P.; Huang, L.; Lin, Y.; Shen, L.; Chen, Q.; Shi, W. *Nanotechnology* **2014,** *25,* 055603. doi:10.1088/0957-4484/25/5/055603
13. Wang, H.; Yi, J.; Mukherjee, S.; Banerjee, P.; Zhou, S. *Nanoscale* **2014,** *6,* 13001–13011. doi:10.1039/C4NR03748K
14. Baruah, U.; Konwar, A.; Chowdhury, D. *Nanoscale* **2016,** *8,* 8542–8546. doi:10.1039/C6NR01129B
15. Sachdev, A.; Matai, I.; Gopinath, P. *Colloids Surf., B* **2016,** *141,* 242–252. doi:10.1016/j.colsurfb.2016.01.043
16. Hu, S.; Zhao, Q.; Dong, Y.; Yang, J.; Liu, J.; Chang, Q. *Langmuir* **2013,** *29,* 12615–12621. doi:10.1021/la402647t
17. Liu, C.; Li, F.; Yang, J.; Tian, F.; Sun, J. *J. Controlled Release* **2015,** *213,* e16–e17. doi:10.1016/j.jconrel.2015.05.023
18. Zhou, J.; Li, J.; Du, X.; Xu, B. *Biomaterials* **2017,** *129,* 1–27. doi:10.1016/j.biomaterials.2017.03.014
19. Cayuela, A.; Kennedy, S. R.; Soriano, M. L.; Jones, C. D.; Valcárcel, M.; Steed, J. W. *Chem. Sci.* **2015,** *6,* 6139–6146. doi:10.1039/C5SC01859E
20. Cayuela, A.; Soriano, M. L.; Kennedy, S. R.; Steed, J. W.; Valcárcel, M. *Talanta* **2016,** *151,* 100–105. doi:10.1016/j.talanta.2016.01.029
21. Ghosh, A.; Parasar, B.; Bhattacharyya, T.; Dash, J. *Chem. Commun.* **2016,** *52,* 11159–11162. doi:10.1039/C6CC05947C
22. Dasgupta, A.; Mondal, J. H.; Das, D. *RSC Adv.* **2013,** *3,* 9117–9149. doi:10.1039/c3ra40234g
23. Adams, D. J. *Macromol. Biosci.* **2011,** *11,* 160–173. doi:10.1002/mabi.201000316
24. Du, X.; Zhou, J.; Shi, J.; Xu, B. *Chem. Rev.* **2015,** *115,* 13165–13307. doi:10.1021/acs.chemrev.5b00299
25. Marchesan, S.; Waddington, L.; Easton, C. D.; Winkler, D. A.; Goodall, L.; Forsythe, J.; Hartley, P. G. *Nanoscale* **2012,** *4,* 6752–6760. doi:10.1039/c2nr32006a
26. Marchesan, S.; Qu, Y.; Waddington, L. J.; Easton, C. D.; Glattauer, V.; Lithgow, T. J.; McLean, K. M.; Forsythe, J. S.; Hartley, P. G. *Biomaterials* **2013,** *34,* 3678–3687. doi:10.1016/j.biomaterials.2013.01.096
27. Marchesan, S.; Waddington, L.; Easton, C. D.; Kushkaki, F.; McLean, K. M.; Forsythe, J. S.; Hartley, P. G. *Bionanosci.* **2013,** *3,* 21–29. doi:10.1007/s12668-012-0074-1
28. Loo, Y.; Wong, Y.-C.; Cai, E. Z.; Ang, C.-H.; Raju, A.; Lakshmanan, A.; Koh, A. G.; Zhou, H. J.; Lim, T.-C.; Moochhala, S. M.; Hauser, C. A. E. *Biomaterials* **2014,** *35,* 4805–4814. doi:10.1016/j.biomaterials.2014.02.047
29. Lademann, J.; Lange-Asschenfeldt, S.; Ulrich, M.; Darvin, M. E.; König, K.; Meinke, M. C.; Lange-Asschenfeldt, B. Application of Laser Scanning Microscopy in Dermatology and Cutaneous Physiology. In *Non Invasive Diagnostic Techniques in Clinical Dermatology;* Berardesca, E.; Maibach, H. I.; Wilhelm, K.-P., Eds.; Springer: Berlin, Germany, 2014; pp 101–113. doi:10.1007/978-3-642-32109-2_10
30. Marchesan, S.; Vargiu, A. V.; Styan, K. E. *Molecules* **2015,** *20,* 19775–19788. doi:10.3390/molecules201119658

31. Yan, X.; Zhu, P.; Li, J. *Chem. Soc. Rev.* **2010,** *39,* 1877–1890.
    doi:10.1039/b915765b
32. Melchionna, M.; Styan, K. E.; Marchesan, S. *Curr. Top. Med. Chem.*
    **2016,** *16,* 2009–2018. doi:10.2174/1568026616999160212120302
33. Wang, H.; Feng, Z.; Xu, B. *Adv. Drug Delivery Rev.* **2017,** *110–111,*
    102–111. doi:10.1016/j.addr.2016.04.008
34. Iglesias, D.; Bosi, S.; Melchionna, M.; Da Ros, T.; Marchesan, S.
    *Curr. Top. Med. Chem.* **2016,** *16,* 1976–1989.
    doi:10.2174/1568026616666160215154807
35. Wu, C.; Biancalana, M.; Koide, S.; Shea, J.-E. *J. Mol. Biol.* **2009,** *394,*
    627–633. doi:10.1016/j.jmb.2009.09.056
36. Amdursky, N.; Erez, Y.; Huppert, D. *Acc. Chem. Res.* **2012,** *45,*
    1548–1557. doi:10.1021/ar300053p
37. Biancalana, M.; Koide, S. *Biochim. Biophys. Acta, Proteins Proteomics*
    **2010,** *1804,* 1405–1412. doi:10.1016/j.bbapap.2010.04.001
38. Xue, C.; Lin, T. Y.; Chang, D.; Guo, Z. *R. Soc. Open Sci.* **2017,** *4,*
    160696. doi:10.1098/rsos.160696
39. Cardoso, A. Z.; Alvarez Alvarez, A. E.; Cattoz, B. N.; Griffiths, P. C.;
    King, S. M.; Frith, W. J.; Adams, D. J. *Faraday Discuss.* **2013,** *166,*
    101–116. doi:10.1039/c3fd00104k
40. Raeburn, J.; Zamith Cardoso, A.; Adams, D. J. *Chem. Soc. Rev.* **2013,**
    *42,* 5143–5156. doi:10.1039/c3cs60030k
41. Marchesan, S.; Styan, K. E.; Easton, C. D.; Waddington, L.;
    Vargiu, A. V. *J. Mater. Chem. B* **2015,** *3,* 8123–8132.
    doi:10.1039/C5TB00858A
42. Kar, K.; Wang, Y.-H.; Brodsky, B. *Protein Sci.* **2008,** *17,* 1086–1095.
    doi:10.1110/ps.083441308

# Two-dimensional carbon-based nanocomposites for photocatalytic energy generation and environmental remediation applications

Suneel Kumar, Ashish Kumar, Ashish Bahuguna, Vipul Sharma and Venkata Krishnan[*]

## Abstract

In the pursuit towards the use of sunlight as a sustainable source for energy generation and environmental remediation, photocatalytic water splitting and photocatalytic pollutant degradation have recently gained significant importance. Research in this field is aimed at solving the global energy crisis and environmental issues in an ecologically-friendly way by using two of the most abundant natural resources, namely sunlight and water. Over the past few years, carbon-based nanocomposites, particularly graphene and graphitic carbon nitride, have attracted much attention as interesting materials in this field. Due to their unique chemical and physical properties, carbon-based nanocomposites have made a substantial contribution towards the generation of clean, renewable and viable forms of energy from light-based water splitting and pollutant removal. This review article provides a comprehensive overview of the recent research progress in the field of energy generation and environmental remediation using two-dimensional carbon-based nanocomposites. It begins with a brief introduction to the field, basic principles of photocatalytic water splitting for energy generation and environmental remediation, followed by the properties of carbon-based nanocomposites. Then, the development of various graphene-based nanocomposites for the above-mentioned applications is presented, wherein graphene plays different roles, including electron acceptor/transporter, cocatalyst, photocatalyst and photosensitizer. Subsequently, the development of different graphitic carbon nitride-based nanocomposites as photocatalysts for energy and environmental applications is discussed in detail. This review concludes by highlighting the advantages and challenges involved in the use of two-dimensional carbon-based nanocomposites for photocatalysis. Finally, the future perspectives of research in this field are also briefly mentioned.

# Review

## Introduction

The problems of global energy shortage and environmental pollution are continuously increasing and various research groups are working to develop an alternative for the depleting fossil fuel reserves to effectively address the energy crisis and other environmental issues [1,2]. Moreover, the immense industrialization and rapid population increase has generated more demand for clean water sources all over the world. This demand has been continuously increasing due to the inevitable discharge of pollutants into the natural water cycle from various pharmaceutical and food industries [3]. Hence, there is an urgent need to develop green (ecologically-friendly), sustainable and technologically promising approaches to generate clean energy as well as to completely degrade pollutants into $CO_2$ and $H_2O$. Hydrogen seems to be a promising solution as a sustainable, clean and renewable energy source to overcome this energy crisis [4]. Hydrogen is mainly present in fossil fuels, such as natural gas and coal, from which it can be produced through steam reforming, partial oxidation, coal gasification and other processes [4]. However, these methods are mainly restricted due to carbon dioxide emission into the environment and high costs [4,5]. As hydrogen is an abundant element and present in nature in the form of water, its production from water using solar energy is therefore an area of immense interest for researchers because of its potential to fulfil the global energy demand and related environmental issues [5].

For the first time, photoelectrochemical (PEC) hydrogen production was achieved in 1972 by Fujishima and Honda on a $TiO_2$ anode and Pt cathode under ultraviolet (UV) light irradiation [6]. After this, research interest in exploring semiconductors for hydrogen production has grown significantly and many research groups have focussed their studies in this direction [7-10]. Hence, in the recent decade, heterogeneous photocatalysis has been widely explored for the conversion of solar energy into chemical energy and for pollutant removal from water [11,12]. Up to now, various interesting semiconductors such as $TiO_2$, ZnO, $WO_3$, CdS, $Bi_2O_3$, $Fe_2O_3$, $SnO_2$, $BiVO_4$, etc. have been investigated for hydrogen evolution reactions and environmental remediation applications [13-19].

In the last 25 years, the emergence of carbon-based nanomaterials has opened new ways of harvesting solar energy and generation of clean energy in the form of hydrogen [20,21]. Carbon is one of the most abundant elements on the earth. In the past two decades, carbon-based materials such as graphene, graphitic carbon nitride (g-$C_3N_4$), fullerenes and carbon nanotubes (CNTs) have been explored for various applications such as Li-ion batteries [22], supercapacitors [23], energy storage [24],

biosensors [25], molecular imaging [26], fuel cells [27] and catalysis [28]. The non-toxicity, abundance and the environmentally benign nature of these carbon-based materials makes them a remarkable class of materials with unique electrical and optical properties for diverse applications.

In recent times, carbon-based materials and semiconductor nanocomposites have attracted great attention and significant progress has been achieved in the field of photocatalysis. In this regard, much of the pioneering work on nanocarbon–semiconductor interface engineering has been reported by D. Eder and M. Prato for environmental remediation and energy generation applications [29-32]. Semiconductor nanocomposite-based photocatalytic reactions are generally initiated by absorbing light energy equal to or more than the band gap of semiconductor photocatalyst [4]. This leads to the excitation of electrons from the valence band (VB) of the semiconductor to their empty conduction band (CB), resulting in the electron–hole pair generation [4]. This photoexcitation process leaves a hole in the VB of the photocatalyst, which can oxidize water of $OH^-$ at its surface to produce hydroxyl radical ($OH^*$), which is a powerful oxidizing agent and can degrade organic pollutants [12]. Moreover, the pollutants may also be directly oxidized by the holes ($h^+$) due to their oxidizing nature, but the detailed reaction mechanism is still under debate. In addition, photoexcited electrons in the CB of a semiconductor can reduce $H^+$ ions in aqueous solution to generate hydrogen, or it can produce a superoxide radical anion ($O_2^{-*}$) by reacting with the dissolved oxygen, hydroperoxide radical ($^*OOH$) upon reaction with $H^+$ ions [4]. These reactive radical species also have potential to accomplish complete mineralization of the pollutants into $H_2O$ and $CO_2$ [12]. But the main drawback of this process is the instability of the photogenerated species, which can readily recombine with other processes and lose the absorbed energy in the form of heat leading to low photocatalytic efficiency [33]. Therefore, various strategies have been adopted by the scientific community such as heteroatom doping [34], noble metal doping [35], coupling with semiconductors [36] and nanocomposite formation with carbon-based materials, such as graphene [37] and g-$C_3N_4$ [38], to enhance the photocatalytic efficiency. Among the various types of nanocomposites, the materials based on two-dimensional (2D) nanocomposites have attracted particular interest because of their improved properties [39]. It is noteworthy to mention here that various groups have reported zero-dimensional (0D) and one-dimensional (1D) nanocarbon–semiconductor hybrids with excellent photocatalytic efficiency towards pollutant removal and energy generation [29-32]. Hence, the carbon-based nanocomposites with different morphologies have made substantial contribution as promis-

ing materials for diverse applications in the field of materials chemistry.

It has been well-reported in the literature that nanocomposite formation of semiconductors with such 2D materials effectively improves the photocatalytic processes. In addition, these 2D materials possess several extraordinary properties, which makes them more advantageous over other materials as summarized below [39]:

1. high specific surface area with a large number of active sites on the surface to boost photocatalytic reactions as compared to their bulk counterpart;
2. π-conjugated structures, which lead to fast electron transfer and promote the separation of electron−hole pairs on the photocatalyst surface; and
3. excellent support matrix for metals, metal oxide semiconductors and other nanomaterials, which can form efficient heterojunction with intimate contact between them, such as, point-to-face contact (0D-2D), line-to-face contact (1D-2D) and face-to-face contact (2D-2D) as presented in Figure 1. This is more beneficial for the rapid charge transfer and better catalytic dispersion to enhance the photocatalytic activity.



**Figure 1:** Schematic diagram of interfaces of (a) 0D-2D (b) 1D-2D, and (c) 2D-2D materials.
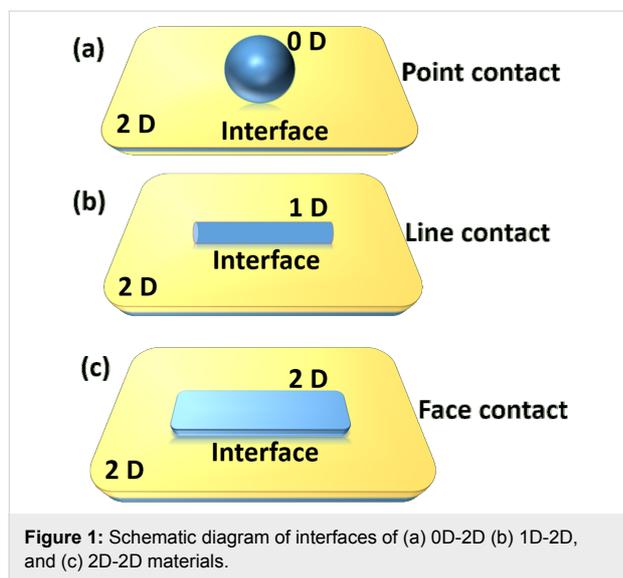
The 2D carbon-based nanomaterials combine several of the above-mentioned advantages of both 2D and carbon-based materials, and have shown great prospects as catalysts for various applications. As this is currently an area of immense research, we decided to write a review article on these materials, especially summarizing the recent developments. Since the scope of 2D carbon-based materials for various applications is very broad as per recent reports on their advances by M. Strano and N. Coleman [40,41], we have focussed our review on only two of the 2D morphology of carbon materials, graphene and g-C$_3$N$_4$, and their nanocomposites for photocatalytic energy generation and environmental remediation applications. In this review, we firstly discuss the synthetic procedures and salient properties of these two 2D carbon materials, followed by a detailed discussion on what makes them suitable for photocatalysis applications and the different roles played by them during the photocatalysis process. Subsequently, we discuss the use of graphene and g-C$_3$N$_4$ based nanocomposites for photocatalytic energy generation and environmental remediation applications, along with several recent citations. We then conclude by highlighting the advantages and challenges involved in the use of 2D carbon-based nanocomposites for photocatalysis. Lastly, the future perspectives of research in this field (way ahead) are also briefly discussed.

## Carbon-based 2D materials
### Graphene

Since the discovery of graphene in 2004, it has attracted great attention because of its fascinating electrical, thermal, optical and mechanical properties. Basically, graphene consists of a single layer of sp$^2$ hybridized carbon atoms densely packed into an atomically thin layer to form a 2D hexagonal honeycomb-like structure [42]. The π-conjugated structure in graphene provides ultrafast electron transfer (200,000 cm$^2$·V$^{-1}$·s$^{-1}$), very high specific surface area (2600 m$^2$·g$^{-1}$), and high thermal conductivity (5000 W·w$^{-1}$·K$^{-1}$) [43]. In addition to this, graphene possesses high transparency, high elastic modulus (≈1 TPa), high mechanical strength (≈1060 GPa), and optical transmittance (≈97.7%) [44]. These superior properties of graphene make it a potential candidate for technological application such as such as optical electronics [45], photosensors [46] and photocatalysis [47]. As graphene is a zero band gap material and susceptible to oxidative reactions, it is often combined with other semiconductors and metallic nanostructures to form composite materials suitable for various applications, including photocatalysis. Furthermore, due to the exceptional electrical, thermal, optical and mechanical properties, graphene helps to enhance the photocatalytic performance by acting as excellent electron acceptor and transporter in nanocomposites. Moreover, enhanced pollutant adsorption on the surface of graphene is an additional advantage, which accelerates the photocatalytic degradation of adsorbed pollutants [48]. Several chemical and physical methods have been developed for the synthesis of graphene and graphene-based nanocomposites. One of the well-known methods for graphene oxide synthesis is Hummers' method, which includes chemical oxidation of graphite flakes to form graphene oxide (GO) [49]. GO contains carboxyl, epoxides and hydroxyl groups covalently attached to the graphene sheet. This leads to the loss of electrical conduc-

tivity and limits the application of GO in many areas. However, the presence of polar functional groups in GO makes it hydrophilic in nature and it is responsible for the easy dispersal in many solvents such as water, which is helpful for the formation of various composites [50]. The reduction of GO in various reducing conditions forms reduced graphene oxide (RGO) in which electrical conductivity is partly revived. This RGO is also known as chemical-modified graphene [51]. The schematic illustration of RGO preparation from graphite is shown in Figure 2. The composite formation of graphene with semiconductor materials has been reported by various methods, such as hydrothermal/solvothermal [52], sol−gel [53], self-assembly [54], precipitation [55], and photo-reduction [13]. The hydrothermal/solvothermal method for the synthesis of graphene-based nanocomposites involves the treatment of its precursor in a confined volume, teflon-lined autoclave at elevated temperature, wherein high pressure is generated. This method is very important for the synthesis of inorganic nanocrystals and gives rise to highly crystalline nanostructures and also reduces GO to RGO. As the name suggests, water is the main solvent in hydrothermal synthesis method and major advantage of water as the solvent is its abundance in nature as well as its non-toxic, non-carcinogenic and non-flammable nature. However, other sol-

vents like ethanol can also be used as the main solvent in solvothermal method. Hence this method involves a very simple and ecologically-friendly process for the synthesis of nanostructures. By controlling some other parameters, such as concentration, temperature, reaction time, etc., nanocomposites with various exposed crystal facets can be obtained by hydrothermal/solvothermal methods.

The sol–gel method is another widely explored method for the synthesis of graphene-based nanocomposites [53]. The precursor material undergoes a series of reactions, mainly controlled hydrolysis and condensation, to form the desired photocatalyst. The major advantage of using the sol–gel method is the in situ growth of nanostructures so that the various functional groups on the surface of GO sheets are available to provide reactive and anchoring sites for the growth of nanoparticles and hence the resultant photocatalytic materials are chemically bonded with each other [53]. This method has been successfully used in the in situ preparation of various graphene–semiconductor nanocomposites, such as $TiO_2$ on GO sheets [57].
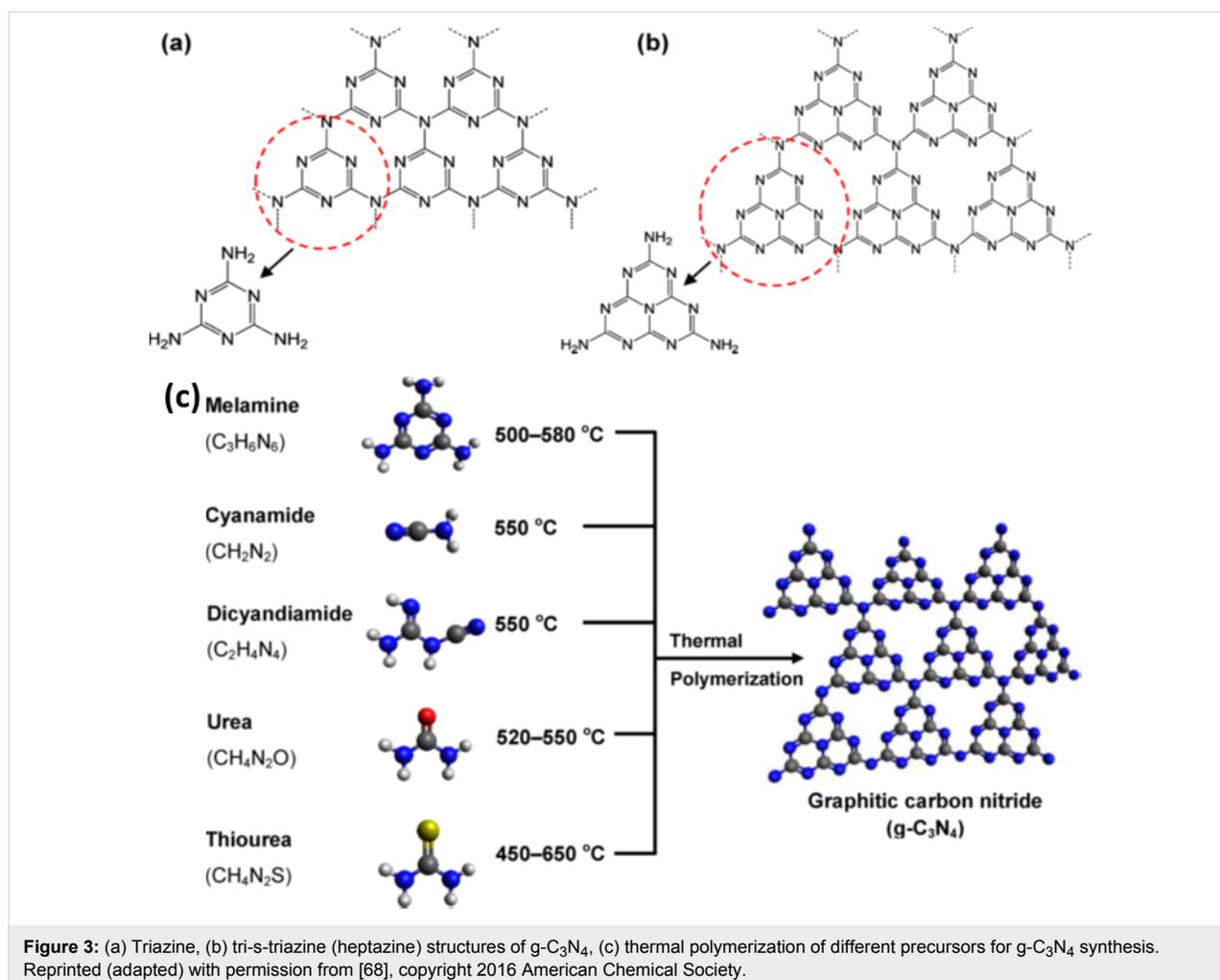
Self-assembly is a very important method, wherein micro- and nanostructures assemble spontaneously by supramolecular



**Figure 2:** Schematic illustration of the preparation of reduced graphene oxide (RGO) from graphite. Reprinted with permission from [56], copyright 2011 Wiley-VCH.
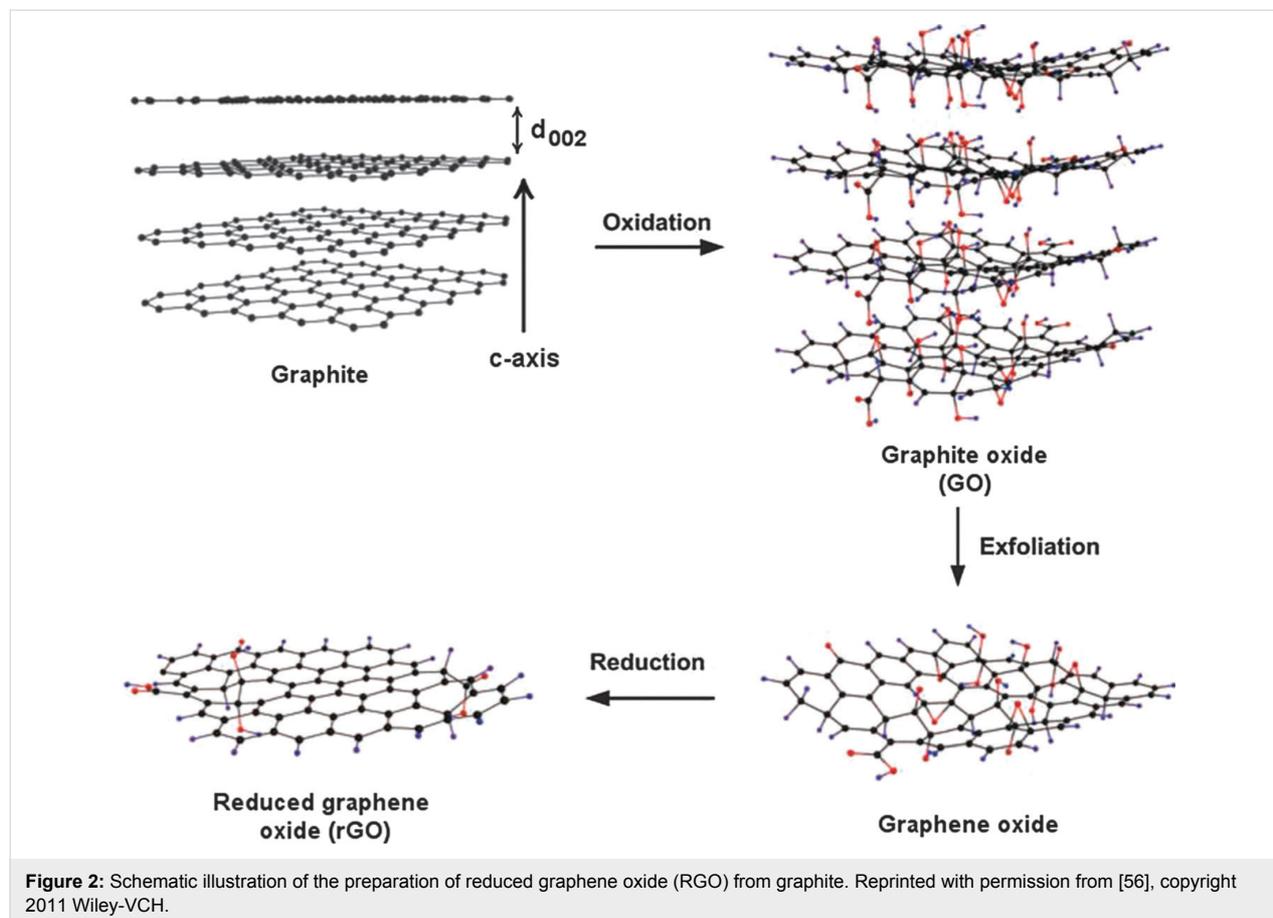
interactions to form larger functional units [58]. This self-assembly of nanoparticles is very useful for various applications. In the surfactant-assisted ternary self-assembly of metal oxides with functionalized graphene sheets, an anionic surfactant gets adsorbed on the surface of graphene sheets and helps in the dispersion of graphene sheets. Then, the surfactant micelles with graphene sheets bind with metal cations and hence act as building block for self-assembly of metal oxides. Finally metal oxides become crystallized between alternating layers of graphene to form fine layered nanostructures. Self-assembly is also a widely used method for constructing a new class of layered nanostructures with stable, ordered and crystalline structure [58]. In layer-by-layer self-assembly of functionalized graphene nanoplatelets, the electrostatic interactions between graphene nanoplatelets are responsible for self-assembly of graphene sheets. In addition to the above-mentioned methods, there are also other efficient methods for synthesis of graphene–metal oxide hybrid nanocomposites, such as solution mixing [59], UV-assisted reduction [13], microwave irradiation [60] and so on.

## Graphitic carbon nitride

The covalent carbon nitride ($C_3N_4$) was discovered by Berzelius with heptazine units as basic structural units [61]. It is reported that $C_3N_4$ possesses seven different phases, viz., $\alpha$-$C_3N_4$, $\beta$-$C_3N_4$, cubic-$C_3N_4$, pseudocubic-$C_3N_4$, g-h-triazine, g-h-heptazine and g-o-triazine, which exhibit the band gaps of 5.49, 4.85, 4.30, 4.13, 2.97, 2.88 and 0.93 eV, respectively [62]. Among these seven phases, the $\beta$-$C_3N_4$ crystalline phase possess similar hardness as compared to that of diamond, and the pseudocubic-$C_3N_4$ and g-h-triazine-$C_3N_4$ possess direct band gap structure, while other five phases have indirect band gaps in their bulk structures [62]. It is noteworthy to mention here that the polymeric graphitic carbon nitride (g-$C_3N_4$) has been reported as the most stable, highly ordered polymeric structure with pendant amino groups and tri-s-triazine ($C_6N_7$) as the building structural units (Figure 3a,b) [63]. g-$C_3N_4$ was first reported by Wang et al. in 2009 as an interesting, metal free, n-type semiconductor, polymeric photocatalytic material for the water splitting reaction to evolve $H_2$ and $O_2$ [64]. The unique optical, electrical and physiochemical properties of g-$C_3N_4$



**Figure 3:** (a) Triazine, (b) tri-s-triazine (heptazine) structures of g-$C_3N_4$, (c) thermal polymerization of different precursors for g-$C_3N_4$ synthesis. Reprinted (adapted) with permission from [68], copyright 2016 American Chemical Society.

makes it a multifunctional photocatalytic material [64]. Therefore, g-C$_3$N$_4$ has attracted immense attention mainly for photocatalytic hydrogen generation reactions and pollutant removal by harvesting visible light due to its suitable band gap energy (≈2.7 eV) [65,66]. Hence this material possesses high photocatalytic efficiency under visible light, which constitutes about 43% of the solar energy spectrum as compared to ultraviolet light (5%). Moreover, the CB and VB of g-C$_3$N$_4$ are suitably positioned with appropriate potential (CB = −1.13 eV, VB = 1.57 eV), which favours various photocatalytic reactions but mainly hydrogen evolution reactions [67].

The lattice structure of g-C$_3$N$_4$ is composed of C–N with short interlayer distances and amino functional groups with larger periodic vacancies [67]. In addition to this, g-C$_3$N$_4$ possesses excellent chemical and thermal stability, unique surface properties with unsaturated N-atoms for anchoring active sites [69]. Furthermore, the stacked 2D layered structure of g-C$_3$N$_4$ consists of single-layer nitrogen heteroatom-substituted graphite nanosheets, formed through sp$^2$ hybridization of C and N atoms, and various layers are bound together by van der Waals forces [69]. Thus it is clear that the lattice structure of g-C$_3$N$_4$ consists only of two abundant elements, C and N (C/N molar ratio = 0.75), which are earth abundant and nontoxic in nature [61]. More surface active sites, nontoxicity, natural abundance and good thermal stability of g-C$_3$N$_4$ makes it a multifunctional, sustainable photocatalytic material. The main drawback from which pure g-C$_3$N$_4$ suffers is poor light absorption and fast recombination of photogenerated electron–hole pairs, which leads to low photocatalytic efficiency and limits its applications [61]. To date, various attempts have been made to improve the light absorption of g-C$_3$N$_4$ and retard the recombination of photogenerated charge carriers to improve the photocatalytic efficiency. These strategies involve doping with metal atoms [70], non-metal doping [71], coupling with other carbon-based materials [72], and heterojunction formation by coupling with semiconductor materials such as TiO$_2$ [73], ZnO [74], CdS [75], SnO$_2$ [76], CeO$_2$ [77], WO$_3$ [78], Fe$_2$O$_3$ [79], Ag$_3$PO$_4$ [80], Ag$_3$VO$_4$ [81], ZnWO$_4$ [82], SrTiO$_3$ [83], BiVO$_4$ [84], Bi$_2$WO$_6$ [85], BiOX [86,87], etc. These heterojunction formations have proved to be an effective method to improve the separation rate of photogenerated charge carriers to enhance the quantum yield. Notably, such heterojunction formation with semiconductors also enhances the light absorption efficiency of photocatalysts from UV to visible region of the solar energy spectrum.

Furthermore, it is noteworthy to mention here that the surface physicochemical properties of g-C$_3$N$_4$ can be tuned by introducing impurities into the crystal lattice of polymeric g-C$_3$N$_4$. Mainly the hydrogen impurities can produce the basic primary

and secondary amines on its layer edges [68]. The presence of such basic groups (=NH, −NH$_2$) on the surface of g-C$_3$N$_4$ can remove toxic acidic molecules through electrostatic interactions [68]. The surface hydrophobicity of g-C$_3$N$_4$ can be changed by chemical oxidation by introducing various hydroxyl and carbonyl groups, which eventually lead to good dispersion during catalytic process. The layered g-C$_3$N$_4$ exhibit excellent chemical stability and is insoluble in various kinds of acid, base and organic solvents like toluene and THF [68]. The good chemical and thermal stability of carbon nitride permits its use in PEC cells even under oxygen atmosphere [63]. Furthermore, the chemical inertness and insolubility of g-C$_3$N$_4$ in most of the known solvents is one main hurdle for easy synthesis of its g-C$_3$N$_4$ based nanocomposites. Recently, layered g-C$_3$N$_4$ based nanocomposites have attracted much attention because of reports on some simple synthesis methods [68]. The g-C$_3$N$_4$ and its nanocomposites with semiconductors and carbon-based materials can be easily designed and synthesized by thermal condensation of several low cost, solid precursor materials such as urea, thiourea, dicyandiamide, cyanamide and guanidine hydrochloride at high temperature (500–600 °C) in air or inert atmosphere (Figure 3c) [88-90]. It is noteworthy to mention here that by using different precursor materials, some of the properties, such as microstructure, adsorption affinity and isoelectric point of g-C$_3$N$_4$ can be tuned [91]. It is known that catalysis is a surface phenomenon, which is affected by the surface structure and morphology of catalytic material. Therefore the fabrication of g-C$_3$N$_4$ with different microstructures is expected to show different surface properties and ability to enhance the photocatalytic performance. As per one of the reports by Zhu et al., g-C$_3$N$_4$ synthesized by using melamine, thiourea, or urea as precursor, exhibited different microstructure and isoelectric points [91]. The g-C$_3$N$_4$ prepared by the thermal condensation method generally exhibit low surface area, which can limit its practical applications, as high specific surface area of catalyst is highly desirable for enhanced photocatalytic activity [92]. Therefore, the preparation of exfoliated thin g-C$_3$N$_4$ nanosheets is becoming one of interesting areas for further exploration of the potential of g-C$_3$N$_4$ in various photocatalytic applications [65]. In addition to the thermal condensation method, there are also some other strategies reported for the preparation of g-C$_3$N$_4$ based nanocomposites, which includes molecular self-assembly [93], microwave assisted heating [38], molten salt synthesis [94] and ionic liquid strategy [95].

## 2D carbon-based nanocomposites as photocatalysts
### 2D graphene-based photocatalysts for energy generation
Photocatalytic H$_2$ production through solar water splitting has been widely explored as it has several advantages like easy and

abundant availability of raw materials, tunable electronic structure and the fact that combustion of hydrogen in air produces water; hence, this method is ecologically-friendly [96]. Moreover the $H_2$ production has attracted great attention as a renewable, sustainable energy source due to growing environmental issues [96,97]. Therefore photocatalytic water splitting has been extensively studied using various semiconductor-based materials and many new semiconductor-based photocatalysts have been successfully developed and investigated recently [4,98,99]. In 1972, Fujishima and Honda achieved photoelectrocatalytic water splitting using a $TiO_2$ electrode [6]. $TiO_2$ was irradiated with UV light and electrons and holes are generated in the CB and VB, respectively. The $TiO_2$ electrode acts as an anode and is connected to a Pt cathode. The photogenerated electrons reduce $H^+$ ions to generate $H_2$ on the Pt electrode while holes oxidize water to form $O_2$ on $TiO_2$ electrode, as illustrated in the Figure 4a. After this discovery, semiconductor-based materials with suitable band gaps have attracted much attention in this field. In order to efficiently utilize the solar energy, many photoelectrochemical cells have been developed for hydrogen production [100,101]. Basically, in the process of photocatalytic water splitting, photons with energy greater than the band gap energy of the chosen semiconductor material result in the formation of photogenerated electrons and holes in the conduction band (CB) and the valence band (VB), respectively. These photogenerated electron–hole pairs are responsible for the reduction and oxidation reactions, i.e., reduction of $H^+ \rightarrow H_2$ in CB and oxidation of $H_2O \rightarrow O_2$ in the VB, as illustrated in Figure 4b [4,102].

The most important point in achieving water splitting is the position of the VB and CB in semiconductor materials. The bottom level of the CB must be more negative than the redox potential of $H^+ \rightarrow H_2$ (0 V vs NHE, where NHE refers to the normal hydrogen electrode), while the top level of the VB must be more positive than the oxidation potential of $H_2O \rightarrow O_2$ (1.23 V vs NHE) [4]. Therefore 1.23 eV is the minimum band gap for water splitting and this band gap corresponds to light at 1008 nm (near-infrared region). According to standard literature [4], the wavelength and eV are related to each other as, band gap (eV) = 1240 / λ (nm). Hence a suitable band gap value plays a crucial role in order to make the catalytic material active in the visible region of light to generate $H_2$ and $O_2$ by water splitting. The band gap of some semiconductor materials with band positions are summarized in Figure 5 [103].

As it is well known, the band gap and wavelength are directly related to each other, and suitable band gap engineering is required to make photocatalysts active in the visible light region of the spectrum. The overall water splitting reaction on the surface of a semiconductor material occurs in three main steps, (1) absorption of light, (2) charge separation, (3) redox reactions on the catalyst surface.

The first step involves the absorption of light by the photocatalyst and generation of electron–hole pairs in the CB and VB. The second step involves the charge separation and migration of charge carriers to the surface. Higher crystallinity and smaller size of particles play a significant role in enhancing the photocatalytic activity by decreasing the recombination probability of photogenerated charge carriers [4]. It is well known that higher crystallinity leads to enhanced photocatalytic activity. Finally, the third step involves the reduction and oxidation of adsorbed species at the different reaction sites, wherein hydrogen production takes place by the reduction of $H^+$ ions in the CB. Hydrogen evolution by water splitting is promoted by the presence of cocatalysts, such as Pt, Rh, NiO, and $RuO_2$. These cocatalysts are mainly helpful to introduce the active sites on the photocata-
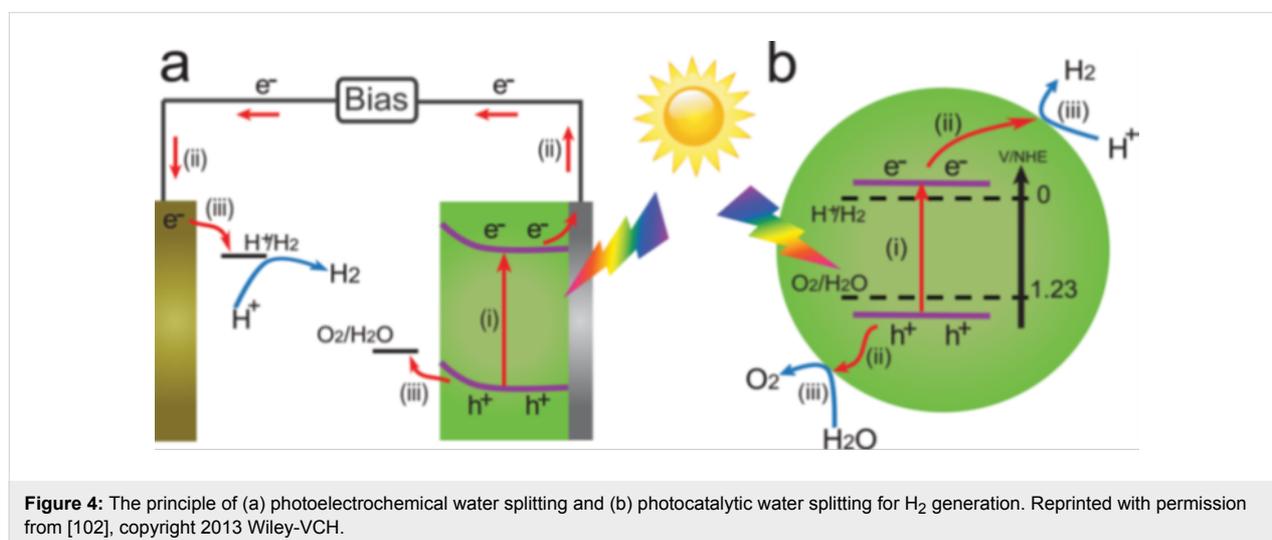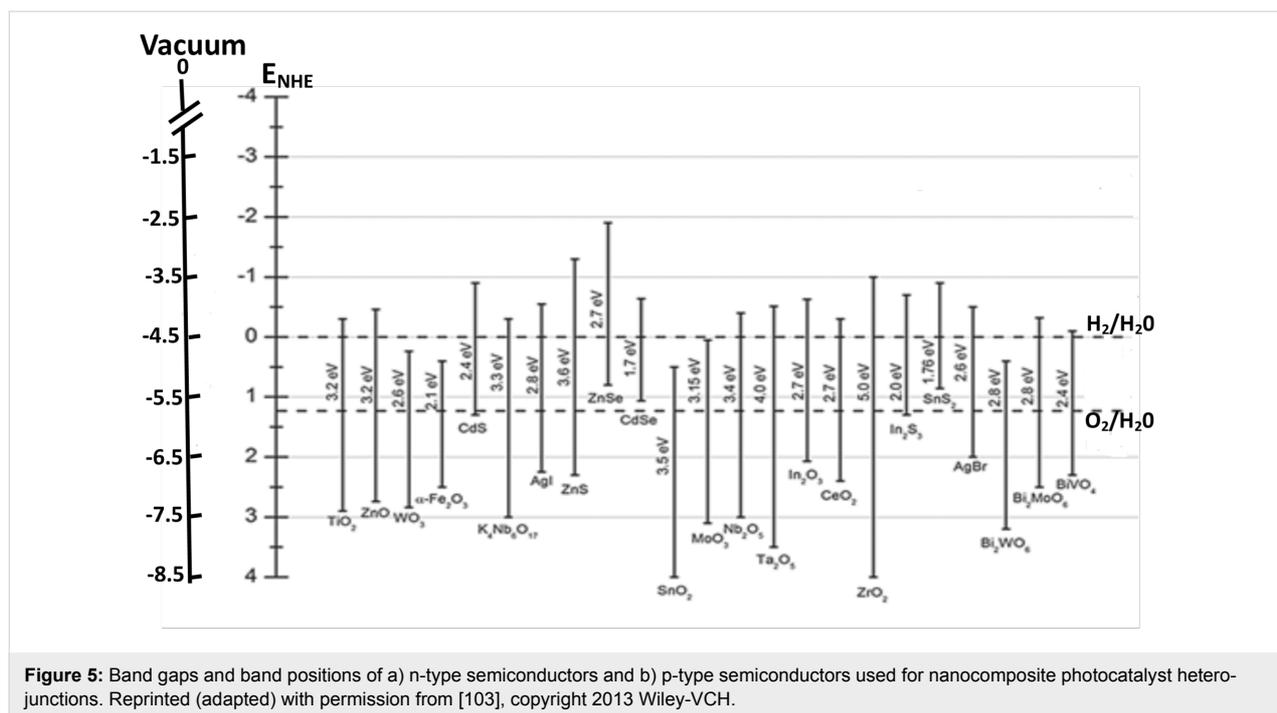


**Figure 4:** The principle of (a) photoelectrochemical water splitting and (b) photocatalytic water splitting for $H_2$ generation. Reprinted with permission from [102], copyright 2013 Wiley-VCH.

**Figure 5:** Band gaps and band positions of a) n-type semiconductors and b) p-type semiconductors used for nanocomposite photocatalyst hetero-junctions. Reprinted (adapted) with permission from [103], copyright 2013 Wiley-VCH.

lyst surface, to facilitate the electron transfer from the CB of excited semiconductor, and hence, to enhance the process of $H_2$ generation [11]. However, the sacrificial agents (methanol, ethanol, sodium sulphide, sodium sulphite, etc.) are always employed in photocatalytic water splitting reactions to scavenge holes and hence suppress photogenerated charge recombination effectively. When graphene-based nanocomposites are used as photocatalysts for energy generation through the water splitting reaction, the graphene in the nanocomposite plays different roles, such as photocatalyst, cocatalyst, electron acceptor/transporter and photosensitizer. These roles are described in detail in the following sections.

## Graphene as a photocatalyst

A photocatalyst is a substance which produces the catalytic activity using energy from light without undergoing any change in itself [104]. The photocatalytic activity depends on the generation of electron–hole pairs in the catalyst under the influence of light energy [105]. These photogenerated charge carriers then generate free radicals such as hydroxyl, superoxide, hydroperoxide, which migrate to the surface of the catalyst and undergo secondary reactions [106]. Due to the superior properties of 2D layered materials, particularly high specific surface area, ultrafast electron transfer and better dispersion, such materials have been investigated in detail by various research groups. Hence, a new class of photocatalysts with significantly suppressed charge recombination and fast interfacial charge transfer have been developed using these materials with extraordinary $H_2$ evolution capability.

Yeh et al. [107] demonstrated graphite oxide as a photocatalyst for hydrogen generation from water without using any noble metal as a cocatalyst. They used moderately oxidized GO with a band gap in the range 2.4–4.3 eV, which can absorb visible light. The oxidation of graphite introduces many oxygen-containing functional groups such as carboxyl, epoxide and hydroxyl groups on its surface, which make GO hydrophilic. Thus GO is easily dispersible in water and hence it has more exposed area in aqueous solutions and effectively catalyses the water splitting reaction. In addition, the band gap of GO can be tuned with its degree of reduction. The variation of the band gap of GO with increasing degree of reduction has been illustrated in Figure 6. Its electrical conductivity decreases with increasing oxidation level, meaning fully oxidized GO acts as an insulator and partially oxidized GO acts as a semiconductor [108]. The conduction band edge of GO is mainly formed by the anti-bonding $\pi^*$ orbital which has a higher energy level of $-0.52$ eV. Thus, due to the more negative anti-bonding $\pi^*$ orbital, which is needed for hydrogen generation, GO can act as a photocatalyst. Also, the VB edge of GO is mainly composed of O 2p orbitals and may not be positive enough to oxidize water but it varies with the reduction degree. It has been observed that the band gap of GO decreases with the reduction. It is well-reported in the literature that for GO with 12.5% of the oxygen atoms, the top energy level of the VB is not high enough to oxidize water for $O_2$ evolution; but at the same time, for GO having 25% coverage of oxygen atoms, the energy level of the CB is high enough for $O_2$ evolution from water [109,110]. Hence, by tuning the electronic properties of GO, it can act as a promising
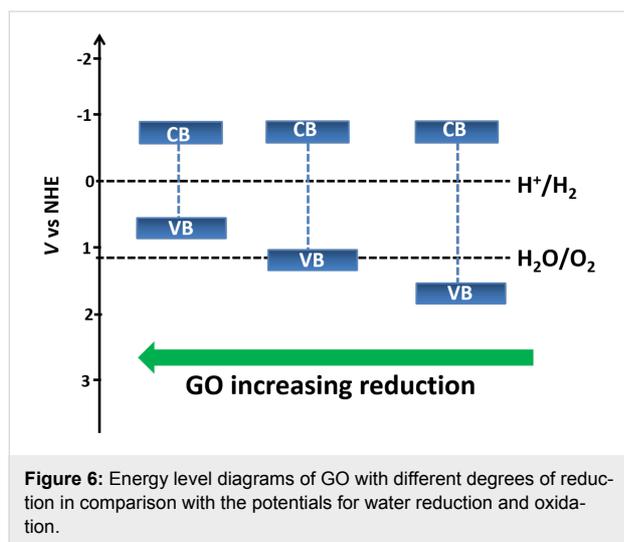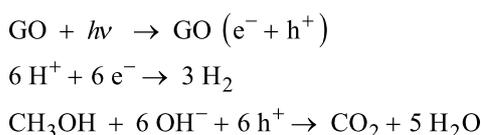
**Figure 6:** Energy level diagrams of GO with different degrees of reduction in comparison with the potentials for water reduction and oxidation.

material for $H_2$ generation from water without any cocatalyst. The possible mechanism of water splitting with GO as a photocatalyst, using methanol as hole scavenger, can be summarized as [107],

$$GO + h\nu \rightarrow GO\left(e^- + h^+\right)$$

$$6\,H^+ + 6\,e^- \rightarrow 3\,H_2$$

$$CH_3OH + 6\,OH^- + 6\,h^+ \rightarrow CO_2 + 5\,H_2O$$

Eda et al. have investigated the insulator → semiconductor → semimetal transition in RGO with degree of reduction [111]. They found that the energy gap even approaches zero with the extensive degree of reduction. Therefore, this possibility of band gap engineering of RGO is always an area of interest for its implementation in various applications. Yeh et al. [112] also demonstrated the photocatalytic activity of GO in hydrogen and oxygen evolution from water with different oxidation levels. They showed that the band gap energy of GO increases with the increasing oxidation level of GO, which limits the light absorption. This, instead of the fact that GO has a narrow band gap energy, is the main contributor to the poor photocatalytic activity. It was also observed that during the photocatalytic reaction, the $H_2$ evolution rate was constant. This is mainly because the GO band gap decreases during the reaction, leading to the upward shift of the VB. Teng et al. [113] have shown the functional engineering of GO for tuning its band gap by its treatment with ammonia and have explored its photocatalytic activity in water splitting reactions under visible light irradiation. Ammonia-modified GO (NGO) shows n-type conductivity due to the introduction of nitrogen functionality. The band gap of NGO is narrowed due to the removal of various epoxy and carboxyl groups and it further acts as a promising photocatalyst towards the $H_2$ and $O_2$ generation from water splitting.

## Graphene as a cocatalyst

A cocatalyst is a substance which assists the catalyst in a chemical reaction and hence enhances the activity of the catalyst [114]. Cocatalysts are generally loaded on the surface of semiconductors as a dispersion of nanoparticles and accelerate the photocatalytic rate by introducing more reaction sites and promoting charge separation in semiconductors [115]. In water splitting reactions, generally noble metals (e.g., Pt, Rh) and some metal oxides (e.g., NiO) act as the cocatalyst and these are loaded on the surface of photocatalysts to produce more reactive sites and to reduce the activation energy for $H_2$ and $O_2$ gas evolution. Cocatalysts also enhances the charge separation in photocatalytic materials because of their high work function. This high work function of noble metals and some metal oxides accelerates the transfer of electrons from the CB of excited semiconductors to the cocatalyst and results in the formation of a Schottky barrier, which efficiently decreases the recombination of charge carriers [102]. Hence cocatalysts play a crucial role in the enhancement of photocatalytic activity by providing abundant reaction sites for $H_2$ evolution, increasing interfacial charge transfer and reducing the recombination probability of photogenerated electron–hole pairs [116]. However, the high cost of noble metals limits their use as cocatalysts on a large scale. Graphene has been demonstrated to be one of the best alternatives for noble metals. Graphene acts as a promising cocatalyst in $H_2$ evolution reactions due to its high work function (4.42 eV) [117], and the reduction potential of graphene/graphene$^-$ is reported to be −0.08 eV, which is more negative than reduction potential of $H^+ \rightarrow H_2$ [52]. It is noteworthy to mention here that the work function of any material is an important parameter for many technical applications, mainly device fabrication as it decides contact properties with foreign material and charge transfer direction in nanocomposites. The work function of carbon-based materials, graphene, GO, carbon nanotubes (CNT) and g-$C_3N_4$ has been presented in Table 1.

**Table 1:** Work function of carbon-based materials.

| Sl. no. | Material | Work function (eV) | Ref. |
|---------|----------|--------------------|------|
| 1 | graphene oxide | 3.7–5.1 | [118] |
| 2 | reduced graphene oxide | 4.5 | [119] |
| 3 | graphene | 4.8–5.1 | [120] |
| 4 | graphitic carbon nitride | 4.4–4.7 | [121] |
| 5 | carbon nanotubes | 4.7–4.9 | [122] |

The role of graphene as a cocatalyst has been investigated by various research groups. Peng et al. [123] reported graphene oxide (GO)–CdS nanocomposites for photocatalytic hydrogen evolution by using $Na_2S$ and $Na_2SO_3$ as sacrificial agents, where GO acts as a supporting matrix for the CdS nanoparti-

cles, which are about 10 nm in size. Due to the narrow band gap CdS is active in the visible region. They observed the highest $H_2$ production rate of 314 µmol h$^{-1}$ for the composition having 5 wt % of GO, as can be seen in Figure 7a. Herein, GO functions as an excellent electron acceptor and transporter from the CB of excited CdS to reaction sites. Thus graphene reduces the recombination rate of photogenerated charge carriers and improves the interfacial charge transfer process, which is ultimately responsible for the enhanced activity of the photocatalyst. The general mechanism for this reaction has been illustrated in Figure 7b. A similar binary nanocomposite has been reported by Xiang et al., which consists of graphene-modified $TiO_2$ nanosheets [124]. This composite shows excellent $H_2$ production rate of 736 µmol h$^{-1}$ with 1 wt % of graphene content. Here graphene also plays a key role as the cocatalyst to enhance the $H_2$ production.

Furthermore, Lv et al. [125] demonstrated the cocatalytic function of metal-doped graphene (Cu-doped graphene–$TiO_2$ composites). They found the $H_2$ generation efficiency of Cu-graphene cocatalyst is about five times higher than pure graphene cocatalyst. Similarly some other groups have also investigated the cocatalytic role of graphene, for example Ye et al. [116] have reported CdS–$MoS_2$–graphene nanocomposites, which is active in visible light for hydrogen generation. They reported the hydrogen evolution rate of 1.8 mmol h$^{-1}$ in lactic acid solution at 420 nm, which is much higher than that of the Pt–CdS system in the same solution. This high $H_2$ evolution rate was mainly achieved because of the excellent cocatalytic function of $MoS_2$–graphene, which leads to the higher number of reaction sites and fast charge transfer. Moreover, in nanometer-sized $MoS_2$, exposed S atoms have strong affinity to $H^+$ ions in solution, which are reduced to $H_2$ by transferred electrons

from the CB of CdS. Similarly, a noble-metal-free, ternary nanocomposite of $TiO_2$–$MoS_2$–graphene has been reported by Yu et al. for $H_2$ generation [126]. This composite prepared by a two-step hydrothermal process lead to uniform dispersion of $TiO_2$ nanopartilces over layered $MoS_2$–graphene (MG), as shown in Figure 8. Herein, the MG hybrid plays a crucial role for charge separation in UV-excited $TiO_2$ nanoparticles and the observed hydrogen production rate was 165 µmol h$^{-1}$ for the composition having 0.5 wt % of MG hybrid. Figure 9 presents the proposed mechanism for the enhanced electron transfer in the $TiO_2$–MG system under UV irradiation showing the photoexcited electron transfer from the CB of $TiO_2$ to the $MoS_2$ nanosheets, followed by transfer to graphene sheets, wherein $H_2$ is produced from $H^+$ ions.

## Graphene as a photosensitizer

Apart from the photocatalytic and cocatalytic role of graphene, it is worth to discuss the photosensitizer role played by graphene in many nanocomposite materials. A photosensitizer is a light-absorbing substance which mediates reactions either in living cells or in chemical systems [127]. So far graphene–semiconductor-based composites have been widely explored for $H_2$ generation in which mainly graphene acts as the electron acceptor and transporter, and hence, enhances the life span of photogenerated charge carriers, which leads to improved $H_2$ evolution. Besides this, graphene can act as an excellent photosensitizer for semiconductors in nanocomposites [128]. The role of graphene as a photosensitizer has been proved theoretically as well as experimentally [128,129].

The photosensitizer role of graphene has been demonstrated by Du et al. [129] on graphene–titania hybrid nanocomposites and explained as the interfacial charge transfer by using density
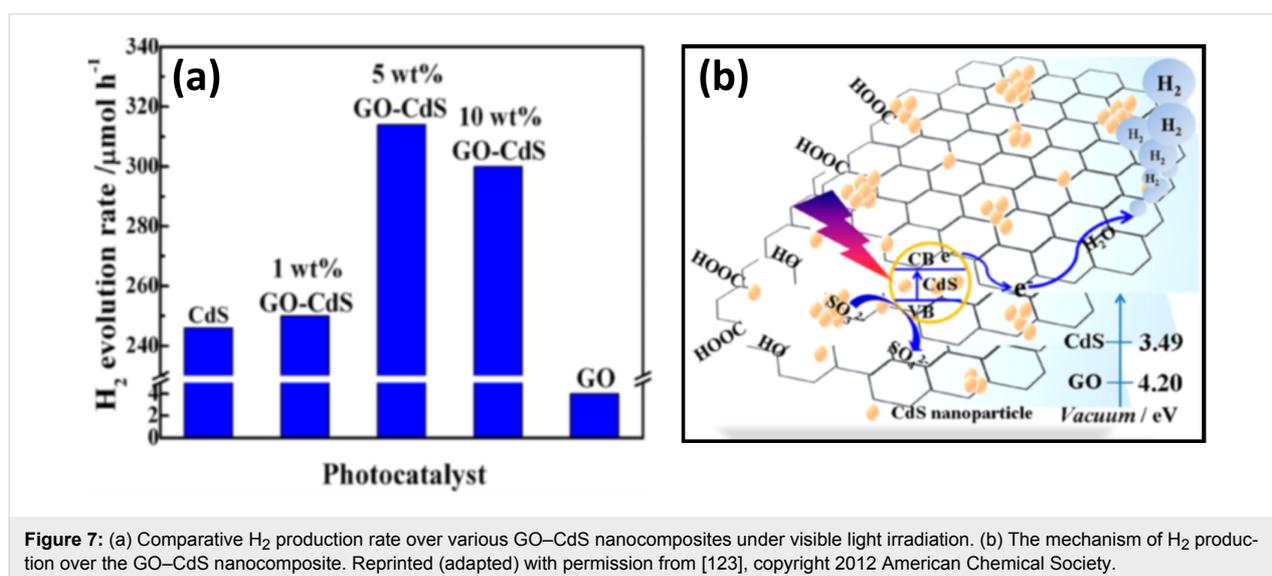


**Figure 7:** (a) Comparative $H_2$ production rate over various GO–CdS nanocomposites under visible light irradiation. (b) The mechanism of $H_2$ production over the GO–CdS nanocomposite. Reprinted (adapted) with permission from [123], copyright 2012 American Chemical Society.
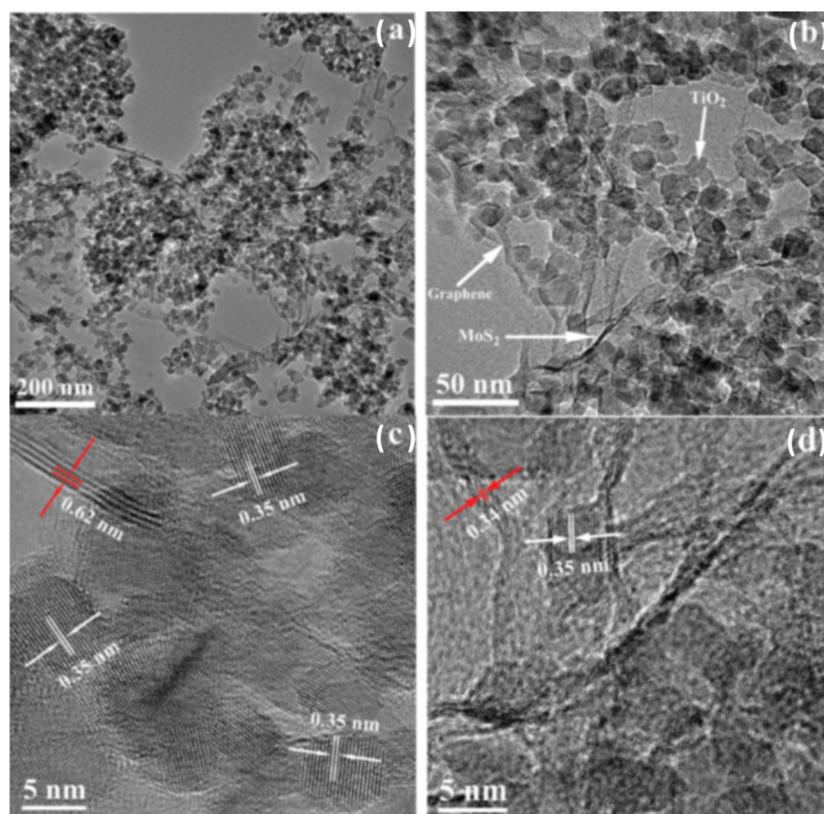
**Figure 8:** (a,b) TEM images of TiO$_2$–MoS$_2$–graphene composites and (c,d) high-resolution TEM images of TiO$_2$–MoS$_2$–graphene composites. Reprinted with permission from [126], copyright 2012 American Chemical Society.
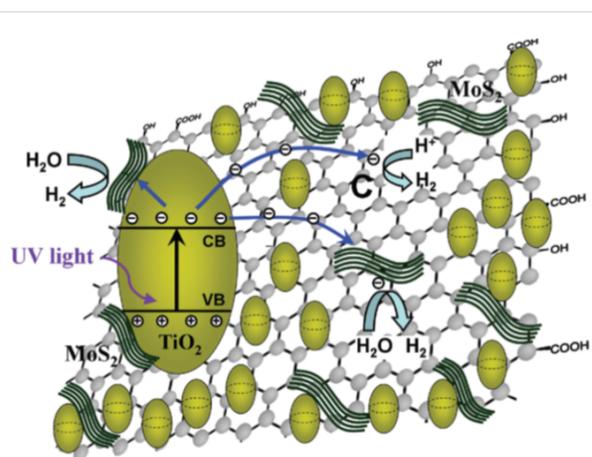


**Figure 9:** Proposed mechanism for the photocatalytic H$_2$ generation over TiO$_2$–MoS$_2$–graphene composite. Reprinted with permission from [126], copyright 2012 American Chemical Society.

functional calculations. They demonstrated the formation of a charge transfer complex at the interface of graphene and titania due to the work function difference of both materials and upon visible light irradiation, the electrons in the upper VB of graphene can be excited to the CB of titania. As TiO$_2$ is inac-

tive under visible light irradiation, the photoactivity was mainly attributed to the photosensitizer, graphene, which absorbs light to generate the charge carriers, which are then utilized to reduce the adsorbed species on the surface of photocatalyst. Zhang et al. [130] also explored the photosensitizer role of graphene by reporting the nanometer-sized assembly of ZnS on graphene sheets and the interfacial contact between them. They formulated a new photocatalytic mechanism for this visible-light-based activity of this nanocomposite. As ZnS is not active under visible light, the light must be absorbed by graphene to produce photogenerated electrons, which gets transferred to the CB of ZnS, thereby making the wide band gap semiconductor visible light active. Peng et al. fabricated TiO$_2$–graphene binary nanocomposites by a simple hydrothermal method and demonstrated the high visible-light-based H$_2$ evolution from water [131]. Herein, they claimed graphene as the photosensitizer and efficient interfacial charge transfer was observed upon visible light irradiation. Hence, on the basis of all the above-mentioned reports, it can be concluded that besides acting as an electron reservoir to capture and shuttle the electrons, graphene also act as a photosensitizer and transform the UV-active semiconductors into visible light responsive materials. This photosensitization by graphene has opened many new paths in fabricating

novel graphene–semiconductor-based nanocomposites for various photocatalytic applications. In addition to the reports cited above, several graphene-based nanocomposites have been successfully developed and utilized for photocatalytic energy generation applications. Some of the noteworthy recent ones have been summarized in Table 2.

## 2D g-C$_3$N$_4$-based photocatalysts for energy generation

The development of g-C$_3$N$_4$-based photocatalysts for water splitting reactions requires several important factors to be taken into account. First of all, the enhanced light absorption capability and effective heterojunction is used to separate electron–hole pairs during photocatalytic process. Next, the CB and VB potentials of the semiconductor should be appropriately positioned to favour H$_2$ evolution and O$_2$ evolution by water splitting reaction, by charge transfer as per favoured potential. Since it is not possible for a bare g-C$_3$N$_4$ to fulfil all these requirements, nanocomposite formation with metal oxide semiconductors, metals and other carbon-based materials is always a preferable route for designing photocatalytic materials

with desired properties. The nanocomposite heterojunctions can drastically enhance the photocatalytic efficiency by enhanced light absorption in combination with narrow band gap semiconductors, cocatalytic effect, which results in and the formation of a p–n heterojunction or Schottky junction, which can effectively suppress the photogenerated charge carrier recombination and facilitate their transfer.

As mentioned earlier, g-C$_3$N$_4$ was first investigated as a photocatalyst by Wang et al. [64] in 2009 for visible-light-based water splitting reactions to generate clean, renewable energy in the form of H$_2$. They found and explained the appropriate band gap structure of g-C$_3$N$_4$ to absorb visible light and evolve H$_2$ and O$_2$ by reduction and oxidation reactions during the photocatalytic process. After this report, several research groups performed dedicated studies on g-C$_3$N$_4$ and its nanocomposites to generate H$_2$ by photocatalytic process. Recently, the coupling of g-C$_3$N$_4$ with various metal oxides/sulfides, composite oxides, BiOX halides (X = Cl, Br, I), AgX, noble metals and graphene has attracted great attention for the formation of heterojunctions with excellent light absorption and charge transfer

**Table 2:** Photocatalytic energy generation using graphene-based nanocomposites. GR – graphene; RGO – reduced graphene oxide; LED – light emitting diode; SS – solar simulator; TEOA – triethanolamine.

| Sl no. | Photocatalyst | Synthesis route | Light source | Sacrificial reagents | H$_2$ production | Ref. (year) |
|---|---|---|---|---|---|---|
| 1 | RGO–TiO$_2$ | sol–gel | 500 W Xe lamp | Na$_2$S and Na$_2$SO$_3$ | 8.6 µmol h$^{-1}$ | [57] (2013) |
| 2 | GR–TiO$_2$ | sol–gel | 500 W Xe lamp | Na$_2$S and Na$_2$SO$_3$ | 17.2 µmol | [53] (2010) |
| 3 | RGO–TiO$_2$ | hydrothermal | UV | Na$_2$S and Na$_2$SO$_3$ | 20 µmol h$^{-1}$ | [132] (2011) |
| 4 | RGO–TiO$_2$ (P25) | hydrothermal | 200 W Xe arc lamp | – | 74 µmol h$^{-1}$ | [13] (2011) |
| 5 | GR–CdS | solvothermal | 350 W Xe lamp | lactic acid | 1.12 mmol h$^{-1}$ | [133] (2011) |
| 6 | RGO–Cu$_2$O | in situ growth | 150 W Xe lamp | methanol | 264.5 µmol h$^{-1}$ g$^{-1}$ | [134] (2012) |
| 7 | GR–Cu–TiO$_2$ | hydrothermal and photodeposition | 300 W Hg lamp | – | 10.2 mmol | [125] (2012) |
| 8 | GO–CdS | precipitation process | 300 W Xe lamp | Na$_2$S and Na$_2$SO$_3$ | 314 µmol h$^{-1}$ | [123] (2012) |
| 9 | RGO–Zn$_x$Cd$_{1-x}$S | coprecipitation - hydrothermal reduction | SS (AM 1.5 G) | Na$_2$S and Na$_2$SO$_3$ | 1824 µmol h$^{-1}$ g$^{-1}$ | [52] (2012) |
| 10 | RGO–MoS$_2$ | hydrothermal | 300 W Xe lamp | TEOA | 83.8 µmol h$^{-1}$ | [135] (2012) |
| 11 | RGO–CdS–ZnO | solid state | 500 W tungsten halogen lamp | Na$_2$S and Na$_2$SO$_3$ | 751 µmol h$^{-1}$ 0.2 g$^{-1}$ | [136] (2012) |
| 12 | GR–TiO$_2$–MoS$_2$ | hydrothermal | UV | ethanol | 165.3 µmol h$^{-1}$ | [126] (2012) |
| 13 | RGO–N–TiO$_2$ | hydrothermal | UV–visible | methanol | 716 µmol h$^{-1}$ g$^{-1}$ 112 µmol h$^{-1}$ g$^{-1}$ | [137] (2013) |
| 14 | GR–MoS$_2$–CdS | hydrothermal | 300 W Xe lamp | lactic acid | 2.32 mmol h$^{-1}$ | [138] (2014) |
| 15 | GR–MoS$_2$–CdS | hydrothermal | 300 W Xe lamp | Na$_2$S and Na$_2$SO$_3$ | 1.8 mmol h$^{-1}$ | [116] (2014) |
| 16 | GR–Au–TiO$_2$ | microwave-assisted hydrothermal | LED lamp (420 nm) | – | 296 µmol h$^{-1}$ g$^{-1}$ | [139] (2014) |
| 17 | GR–MoS$_2$–ZnS | hydrothermal | 300 W Xe lamp | Na$_2$S and Na$_2$SO$_3$ | 2258 µmol h$^{-1}$ g$^{-1}$ | [140] (2014) |
| 18 | GR–Au–TiO$_2$ | hydrothermal and Photodeposition | 450 W Hg lamp | methanol | 1.34 mmol | [141] (2014) |
| 19 | GO-reduced TiO$_2$ | laser ablation in liquid | SS (AM 1.5G) | – | 16 mmol h$^{-1}$ g$^{-1}$ | [142] (2016) |
| 20 | GR–CdS | solvothermal | 300 W Xe lamp | – | 175 µmol h$^{-1}$ | [143] (2016) |
| 21 | RGO–Pt–TiO$_2$ | step-wise | SS (AM 1.5G) | TEOA | 1075.68 µmol h$^{-1}$ g$^{-1}$ | [144] (2017) |

kinetics, which is discussed in the following sections of this article.

## g-C$_3$N$_4$-oxide/sulfide nanocomposites

Jing et al. [145] reported the cocatalyst-free boron-doped g-C$_3$N$_4$–TiO$_2$ (BCN-T) nanocomposite for H$_2$ generation from CH$_3$OH under visible light irradiation. The boron doping in g-C$_3$N$_4$ nanosheets introduces the impurity near to the VB top level, which traps holes and hence the photoinduced electrons were transferred from the CB of g-C$_3$N$_4$ to the CB of TiO$_2$ as per their band potentials (Figure 10), which further leads to the photocatalytic reaction for fuel production. Hence the synergetic effect of boron doping and heterojunction formation with TiO$_2$ results in the greatly enhanced, photogenerated charge transfer results with a 29-fold higher H$_2$ production as compared to the bare g-C$_3$N$_4$. Thus this study demonstrates the fabrication of low cost, highly efficient g-C$_3$N$_4$ nanosheet-based nanocomposites with improved light absorption and charge transfer to generate clean energy.
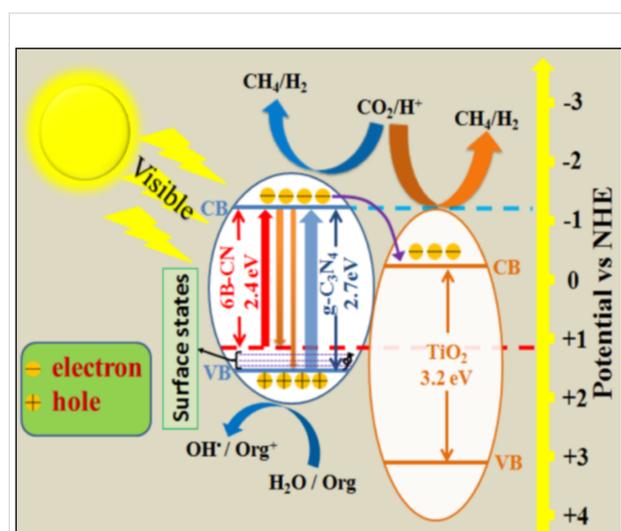


**Figure 10:** Proposed mechanism of BCN-T system under visible irradiation for H$_2$ generation, pollutant removal and carbon dioxide reduction. Reprinted with permission from [145], copyright 2015 American Chemical Society.

Shi et al. reported the visible-light responsive g-C$_3$N$_4$-InVO$_4$ nanocomposite heterojunction by in situ growth of InVO$_4$ nanoparticles onto the surface of g-C$_3$N$_4$ nanosheets by a hydrothermal synthesis process [146]. The g-C$_3$N$_4$ nanosheet serves as an excellent support matrix for the in situ growth of nanoparticles, which were 20 nm in diameter and the interface formation between the two semiconductors improves charge transfer across the interface by inhibiting recombination. The H$_2$ evolution rate of 212 μmol h$^{-1}$ g$^{-1}$ was achieved with this nanocomposite material.

Feng et al. reported novel CdS quantum dot (QDs) coupled with g-C$_3$N$_4$ photocatalysts by a chemical impregnation method [16]. The reported photocatalyst was used for visible-light-based H$_2$ evolution from an aqueous methanol solution with Pt as a cocatalyst. The effect of CdS loading was optimized to be 30 wt % of the photocatalyst. The optimized catalyst achieved about a nine times higher H$_2$ evolution rate of 17.27 μmol h$^{-1}$, as compared to pure g-C$_3$N$_4$. The improved photocatalytic H$_2$ evolution by the CdS–g-C$_3$N$_4$ nanocomposite has been attributed to the synergistic effect of g-C$_3$N$_4$ and CdS QDs, which leads to the efficient separation of the photogenerated charge carriers and thereby enhances the visible light photocatalytic H$_2$ production activity of the nanocomposite.

As discussed in the introduction section regarding the significance of 2D materials in photocatalytic applications, Chen et al. [147] reported a highly efficient 2D–2D heterojunction of a ternary metal sulfide CaIn$_2$S$_4$ with g-C$_3$N$_4$ nanosheets with intimate interfacial contact obtained by facile two-step hydrothermal method. The as-prepared heterojunction exhibits face-to-face contact of CaIn$_2$S$_4$ nanosheets with g-C$_3$N$_4$ nanosheets in which the interfacial contact area is very large as compared to other heterojunctions, such as point-to-line contact (OD-1D), point-to-face contact (0D-2D), line-to-line contact (1D-1D) and line-to-face contact (1D-2D). The optimized 30% CaIn$_2$S$_4$-g-C$_3$N$_4$ nanocomposite showed a H$_2$ evolution rate of 102 μmol g$^{-1}$ h$^{-1}$, which was about 3-fold higher than pristine CaIn$_2$S$_4$ (Figure 11b). This enhanced H$_2$ evolution was attributed to high interfacial contact between CaIn$_2$S$_4$ and g-C$_3$N$_4$ and suitable energy bands alignments, which facilitate separation of photogenerated charge carriers to reaction sites (Figure 11a). Moreover the catalyst shows excellent stability and the original phase was retained even after five reusability cycles. The H$_2$ evolution mechanism was demonstrated on the basics of suitable band potentials of both the semiconductors. Under visible-light illumination, the photogenerated electron–hole formation takes place in the CB and VB of both semiconductors. As electrons transfer always takes place down potential, and holes always move up potential, the photoexcited electrons from the CB of g-C$_3$N$_4$ transfers to the CB of CaIn$_2$S$_4$, while holes from the VB of g-C$_3$N$_4$ also transfer to the VB of CaIn$_2$S$_4$. Pt serves as an excellent cocatalyst and accepts the photoexcited electrons due to its high work function, which finally reduce the H$^+$ ions to generate H$_2$.

## g-C$_3$N$_4$-composite oxide nanocomposites

The composite oxide-based heterojunctions include very interesting nanocomposites, such as g-C$_3$N$_4$–Ag$_3$PO$_4$, g-C$_3$N$_4$–Ag$_3$VO$_4$, g-C$_3$N$_4$–ZnWO$_4$, g-C$_3$N$_4$–SrTiO$_3$, g-C$_3$N$_4$–BiWO$_4$, and g-C$_3$N$_4$–Bi$_2$WO$_6$. Such kinds of nanocomposites have been widely explored with remarkably en-
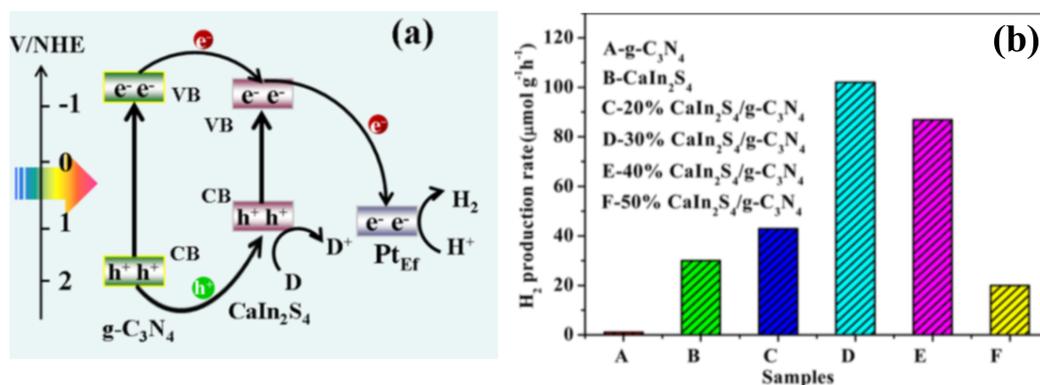
**Figure 11:** (a) Schematic illustration of the photocatalytic $H_2$ production over $CaIn_2S_4$/g–$C_3N_4$ catalysts and (b) comparison of photocatalytic $H_2$ production over various photocatalysts, under visible-light irradiation. Reprinted (adapted) with permission from [147], copyright 2015 American Chemical Society.

hanced photocatalytic performance as compared to their respective bare counterparts. Recently, Woo et al. [84] reported their investigation on a sulfur-doped g-$C_3N_4$ (SCN)-$BiVO_4$ nanocomposite for water oxidation reaction. Bismuth vanadate ($BiVO_4$) is one of the most fascinating photocatalysts with a suitable direct band gap (2.4 eV), which is excited by visible light energy and suitably positioned CB and VB edge potentials, which are favorable for various photocatalytic reactions. However, a very high exciton recombination rate limits the photocatalytic efficiency of $BiVO_4$. Hence, to overcome this issue, the heterojunction formation with an ideal material like g-$C_3N_4$ is one of the promising strategies. The sulfur-doped g-$C_3N_4$-$BiVO_4$ nanocomposite was fabricated by a one-pot impregna-

tion co-precipitation method as shown in Figure 12a. The S doping was introduced to narrow the band gap of g-$C_3N_4$ by stacking its 2p orbitals on the valence band of bare g-$C_3N_4$ which eventually contributes to increase the efficiency. Furthermore, the sulfur doping facilitates the surface oxidation of g-$C_3N_4$ during the impregnation method, and consequently, the $VO_4^{3-}$ tetrahedron is formed on the oxidized site of g-$C_3N_4$. A very interesting electron transfer mechanism has been discussed in the case of g-$C_3N_4$-$BiVO_4$ nanocomposite in terms of a Z-scheme, wherein excited electrons from $BiVO_4$ favorably combine with VB holes of g-$C_3N_4$, which is placed between the CB and VB of $BiVO_4$. The high rate of $O_2$ evolution (328 μmol $h^{-1}$ $g^{-1}$) has been achieved with an optimized g-$C_3N_4$-$BiVO_4$
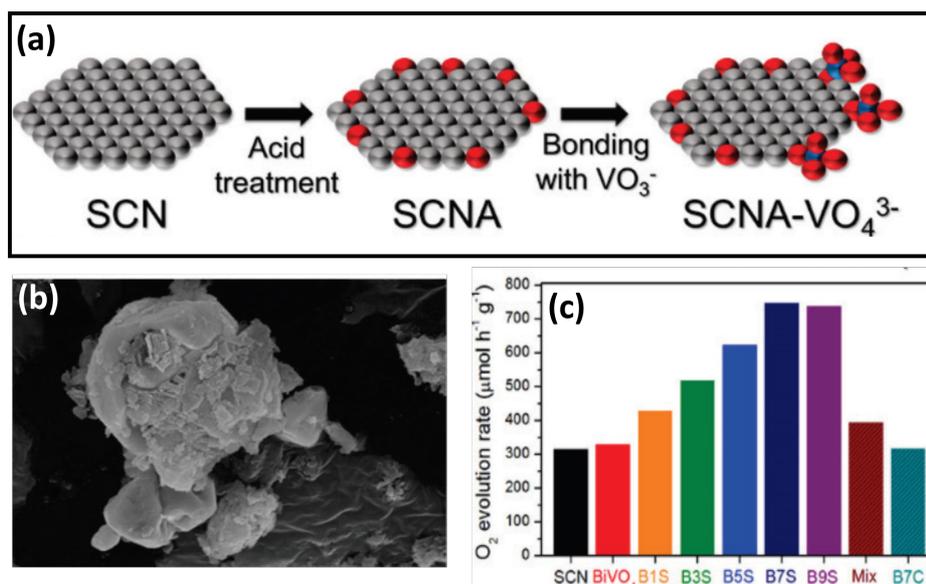


**Figure 12:** (a) Schematic diagram showing the effect of SCN acid treatment that leads to the formation of a composite between SCN and $BiVO_4$ (gray for SCN, red for oxygen, and blue for vanadium atom), (b) morphology of prepared photocatalyst, and (c) photocatalytic activity of the prepared photocatalysts. Reprinted (adapted) with permission from [84], copyright 2016 American Chemical Society.

nanocomposite, which is 2-fold higher than pristine $BiVO_4$. Figure 12 b,c presents SEM images of the g-$C_3N_4$–$BiVO_4$ nanocomposite and the comparative rate of rate of $O_2$ evolution for various prepared catalysts along with control samples.

It is well known that perovskite-type oxides ($ABO_3$) constitute one of the promising classes of materials with diverse properties [148]. The main advantage of using the perovskite-type cubic structure is the flexibility to tune the composition of the A and B sites to form substituted materials [148]. Strontium titanate ($SrTiO_3$) is an important dielectric material, with a band gap energy of 3.2 eV. The $SrTiO_3$ has been explored as an ideal photocatalytic material for water splitting reactions for $H_2$ fuel generation [149]. It is worth to mention here that $SrTiO_3$ provides a higher potential as compared to $TiO_2$ and facilitates the formation of hydrogen and oxygen. Li et al. [150] have reported the synthesis of cubic $SrTiO_3$ by a polymerized complex method (solid state milling), for $H_2$ evolution by water splitting under UV irradiation. It is very interesting to note that they tune the $SrTiO_3$ nanoparticle size depending on the synthesis parameters. The $SrTiO_3$ nanoparticles prepared by this polymerized complex route exhibit the best photocatalytic hydrogen evolution rate of 3.2 mmol $h^{-1}$ $g^{-1}$. This enhanced photocatalytic $H_2$ evolution by water splitting of $SrTiO_3$ nanoparticles could be attributed to the small particle size and hence large surface area. Small particles offer numerous active sites exposed on the surface of the catalyst. These active sites may absorb more water molecules, which are reduced by photogenerated electrons to evolve $H_2$ gas. Moreover, small particles facilitate the diffusion distance from the interior to the surface of the catalyst for photogenerated charge carriers. Taking inspiration from water splitting capabilities of $SrTiO_3$, various reports came on interesting nanocomposite materials based on $SrTiO_3$. Subsequently, in order to enhance the photocatalytic $H_2$ evolution and make $SrTiO_3$ active in visible light, Irvine et al. [83] reported a unique and highly stable g-$C_3N_4$-coated $SrTiO_3$ photocatalyst, which can absorb visible light for energy generation. This highly efficient photocatalyst based on g-$C_3N_4$-coated $SrTiO_3$ has been synthesized in a facile manner by decomposing urea in the presence of $SrTiO_3$ at 400 °C. The catalytic activity was demonstrated by photocatalytic water splitting reaction for $H_2$ production and a high rate of evolution of 440 µmol $h^{-1}$ $g^{-1}$ has been achieved under visible light irradiation. The enhancement in photocatalytic activity could be attributed to the intimate interfacial interaction between g-$C_3N_4$ and $SrTiO_3$, where photogenerated electrons and holes are effectively separated and transferred to reaction sites.

## g-$C_3N_4$-bismuth oxyhalide nanocomposites

Recently, bismuth oxyhalides, BiOX (X = Cl, Br, I) have attracted much attention as layered materials with excellent pho-

tocatalytic properties, since the first report on the high photocatalytic activity of BiOCl in 2009 [151]. The layered structure of BiOX composed of $[Bi_2O_2]^{2+}$ blocks, and the internal electric field formed in BiOX semiconductors is very effective for separation of photoexcited charge carriers to enhance the photocatalytic activity [152]. Hence, it is very interesting to couple such material with g-$C_3N_4$ to get remarkable photocatalytic enhancements. It is noteworthy to mention here that most of the p-type narrow band gap semiconductors, which have shown excellent photocatalytic activity under visible light irradiation, belong to the family of BiOX. Among them, BiOI is an attractive, p-type, visible-light responsive semiconductor due to its narrow band gap energy (1.78 eV) and is a potential to sensitize wide band gap semiconductors [153]. It is known that BiOI-based heterojunctions exhibit enhanced photocatalytic performance under visible light irradiation. Xie et al. [153] reported the synthesis of n-type porous g-$C_3N_4$ with p-type nanostructured BiOI to form a novel BiOI–g-$C_3N_4$ p–n heterojunction photocatalyst and demonstrated its efficient photocatalytic activity. The results show that the BiOI–g-$C_3N_4$ heterojunction photocatalyst exhibits superior photocatalytic activity compared to bare BiOI and g-$C_3N_4$. The visible-light photocatalytic activity enhancement of BiOI–g-$C_3N_4$ heterostructures has been attributed to the strong absorption in the visible region by both the semiconductors and improved charge transfer due to significantly suppressed recombination rate of the electron–hole pairs because of the heterojunction formed between BiOI and g-$C_3N_4$.

BiOBr is another semiconductor from the bismuth oxyhalides family that has recently gained attention in solar energy conversion due to its high photocatalytic activity and stability under UV and visible light irradiation. BiOBr is a lamellar-structured p-type semiconductor with an intrinsic indirect band gap that provides it with fast carrier mobility and prolonged electron life time [154]. However, the band gap energy of BiOBr is around 2.9 eV, indicating that it cannot absorb a significant part of visible light above 430 nm. Sun et al. [154] adopted a very interesting strategy to enhance photocatalytic activity by constructing a 2D–2D heterojunction of a BiOBr semiconductor with g-$C_3N_4$ nanosheets. This 2D–2D heterojunction exhibited enhanced photocatalytic performance due to face-to-face contact, which facilitates efficient charge transfer. They investigated the electronic coupling between the (001) plane of BiOBr and the (002) plane of g-$C_3N_4$. The favorable coupling of the crystal planes and matching band energies between BiOBr and g-$C_3N_4$ promotes the efficient transportation of photogenerated electrons and holes to reaction sites.

## g-$C_3N_4$-noble metal nanocomposites

The noble metal nanoparticles (NPs), mainly Au, Pt, Pd, and Ru, are of great interest because of their unique electronic,

optical, and magnetic properties [155]. In particular, Au NP are employed to facilitate efficient charge separation, thus serving as a Schottky barrier, wherein the charge transfer takes place from one component to another in order to align the Femi energy levels which effectively reduces the electron-hole pair recombination [155]. Moreover, the surface plasmon resonance (SPR) effect in noble metals increases the visible light utilization in nanocomposites, which leads to the improved performance [156]. Furthermore, the synthesis of nanoparticles with exposed high-energy or active facets has attracted considerable attention because they usually exhibit fascinating interfacial behaviour and have been applied in many fields including catalysis [157], sensors [158], photovoltaics [156], and energy storage applications [159]. In addition, the decoration of noble metal particles on certain substrates such as g-$C_3N_4$ is highly beneficial for enhancing the performance in many photocatalytic reactions. In particular, the use of Au NPs has proved to be extremely effective in promoting photocatalytic reactions within a wide spectral range because of size effects and the surface plasmon resonance (SPR) effect from Au NPs, leading to visible-light responsive materials. Moreover, the interfacial loading of noble metals nanoparticles on g-$C_3N_4$ could largely increase the migration of photoelectrons, which can promote the separation of electrons and holes, and thus play an important role to enhance the photocatalytic activity.

Parida et al. [160] explored the nanocomposite prepared by Au NP deposition on g-$C_3N_4$ by a facile deposition/precipitation method. They systematically studied the effect of Au loading on nanocomposites for visible-light-based photocatalytic $H_2$ evolution. Upon exposing the nanocomposite to visible light, the electron–hole pairs are generated, resulting in the formation of a Mott–Schottky junction at the interface of the Au NP and g-$C_3N_4$ (Figure 13 a). This results in the electron transfer from the CB of g-$C_3N_4$ to the Au NP, which increases the electron density on the Au NP. Furthermore, the interaction between Au NPs and g-$C_3N_4$ results in a significant band gap reduction of g-$C_3N_4$, making it more active in visible light. The high electron density on the surface of Au NPs results in the reduction of water molecules to generate $H_2$ fuel (Figure 13 b). The 1 wt % Au loaded nanocomposite was found to be the optimized composition and displayed the highest $H_2$ evolution of 532 μmol, which was about 23 times higher than pure g-$C_3N_4$ along with a high photocurrent density of 49 mA cm$^{-2}$.

Similarly, Zhu et al. reported visible-light responsive plasmonic composites of Ag@g-$C_3N_4$ having a core–shell architecture [161]. In addition to self-catalysis by noble metals, localized surface plasmon resonance (LSPR) generates local electromagnetic fields, which can be used to tune the absorption wavelength of the composites. Moreover, the core–shell composites exhibit 3D contact between the metal core and semiconductor shell, which highly facilitates the plasmonic energy transfer process. This also provides stability by preventing metals from corrosion and aggregation. These Ag@g-$C_3N_4$ core–shell composites have shown excellent activity for $H_2$ evolution by water splitting under visible light irradiation. The photoluminescence (PL) emission spectra of Ag@g-$C_3N_4$ core–shell composites was broadened and quenched with increasing Ag content. This is indicative of charge transfer processes from the CB of g-$C_3N_4$ to Ag and efficiently suppresses the recombination. Furthermore, the Ag@g-$C_3N_4$ material exhibits about a 4-fold higher photocurrent density than bare g-$C_3N_4$, signifying the charge separation process in the core–shell composite with a
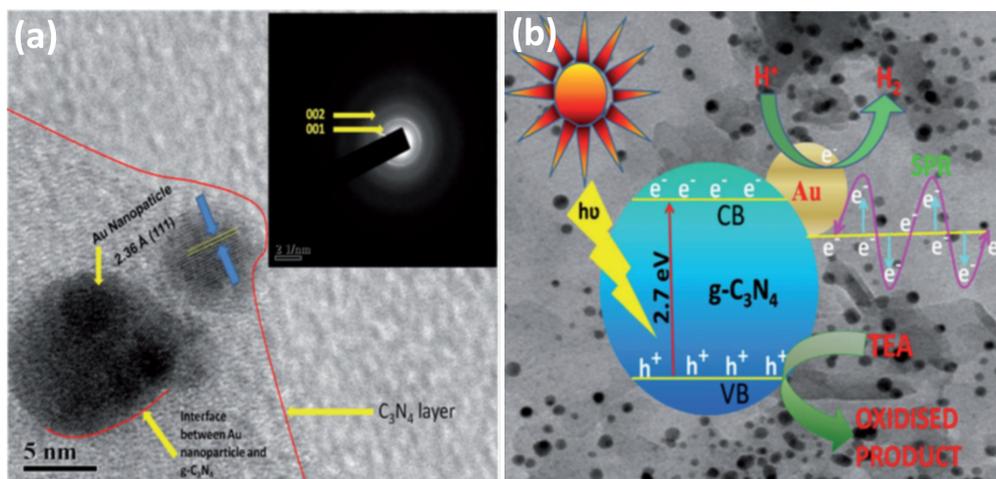


**Figure 13:** (a) HRTEM image of 1 wt % Au–g-$C_3N_4$ nanocomposite where the inset presents the corresponding SAED pattern. (b) Proposed mechanism of photocatalytic $H_2$ production and SPR of Au in a Au–g-$C_3N_4$ nanocomposite. Reprinted (adapted) with permission from [160], copyright 2014 Wiley-VCH.
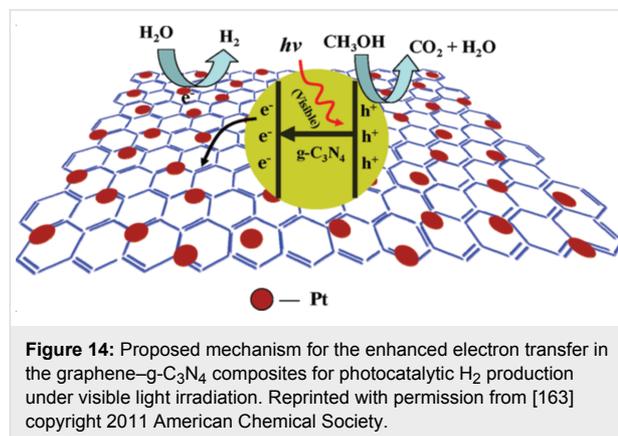
prolonged life time of the photogenerated charge species. Hence with the synergistic effect of LSPR of Ag and the facilitated charge transfer across the core–shell due to the large area interfacial contact, the optimized Ag@g-$C_3N_4$ composite exhibits about a 30-fold higher photocatalytic $H_2$ evolution as compared to g-$C_3N_4$.

## g-$C_3N_4$-other carbon-based material nanocomposites

In the past few years, the development of noble-metal-free, highly efficient photocatalysts have been the thrust area of research in scientific community as the very high cost of noble metals restricts their use on a large scale [72]. Thus research has taken a pathway towards the development of a carbon conductive support with proper electronic structure with ultrafast electron transfer and with high concentration of active sites on their surface [162]. It has been reported that graphene also acts as an excellent electron-donating modifier for g-$C_3N_4$ due to the layered structure similar to g-$C_3N_4$ and their suitable electronic, mechanical, thermal and chemical properties [162]. Thereby, combining the two related structures of carbon-based materials would integrate their respective properties together, with remarkable or unique properties in the resulting nanocomposites. For instance, graphene–g-$C_3N_4$ nanocomposites exhibit significantly improved charge transfer kinetics because of the intimate contact between graphene–g-$C_3N_4$, wherein photogenerated electron−hole transfer takes place, which eventually plays vital role in improving the photocatalytic performance. Hence for such 2D–2D nanocomposites, the enhanced photocatalytic performance could be attributed to high catalytic surface area, abundant reaction sites and formation of well-defined electron−hole puddle at the interface of the 2D materials.

Recently, Xiang et al. reported on an intriguing nanocomposite of g-$C_3N_4$ coupled with graphene as one of the most promising metal-free visible-light active photocatalysts for $H_2$ evolution [163]. The effect of graphene concentration on photocatalytic $H_2$ evolution activity has been investigated and the optimum content of graphene was found to be 1 wt %. The optimized catalyst shows a $H_2$ evolution rate of 451 μmol h$^{-1}$ g$^{-1}$ and 2.6% apparent quantum efficiency, which was about 3-fold higher than pure g-$C_3N_4$. The reported photocatalytic mechanism for the $H_2$ evolution reaction can be seen in Figure 14. It is clear that in g-$C_3N_4$ structures, N 2p orbitals constitute the VB, whereas the C 2p orbitals form the CB. Upon visible light irradiation, electrons are excited from the VB to CB of g-$C_3N_4$, which results in the formation of photogenerated electron–hole pairs. The holes from the VB are scavenged by methanol, while electrons participate in the photocatalytic reduction reaction to generate $H_2$ fuel. However, the electrons are transferred from g-$C_3N_4$ to graphene sheets in the case of layered nanocomposites of graphene–g-$C_3N_4$. The transferred electrons reduce H$^+$ in aqueous solution to release $H_2$ as graphene acts as a conductive channel to separate the photogenerated charge carriers. The proposed photocatalytic mechanism has been further supported by photoluminescence and photocurrent studies.



**Figure 14:** Proposed mechanism for the enhanced electron transfer in the graphene–g-$C_3N_4$ composites for photocatalytic $H_2$ production under visible light irradiation. Reprinted with permission from [163] copyright 2011 American Chemical Society.

In order to overcome the poor light absorption and fast recombination of charge carriers in g-$C_3N_4$, Dong et al. [164] reported a unique, metal-free, isotopic heterojunction nanocomposite with a prolonged life time of the photogenerated electrons for photocatalytic reactions by utilizing more visible light energy. They fabricated layered g-$C_3N_4$–g-$C_3N_4$ isotope heterojunctions with molecular composite precursors, urea and thiourea, which were treated under the same thermal conditions. Owing to the fact that both the precursors, urea and thiourea all possess different band structures, this gave rise to the layered g-$C_3N_4$–g-$C_3N_4$ heterojunction. Hence a facile, economic and ecologically-friendly method with earth-abundant precursors was utilized for the preparation of this isotopic heterojunction. The precursors show lattice fringes with a *d*-spacing of 0.323 nm (g-$C_3N_4$, thiourea) and 0.327 nm (g-$C_3N_4$, urea). Visible-light irradiation results in the generation of photogenerated charge carriers which tend to transfer from g-$C_3N_4$, thiourea (CN-T) to g-$C_3N_4$, urea (CN-U) driven by a CB offset of 0.10 eV, whereas the photogenerated holes transfer from CN-U to CN-T driven by a VB offset of 0.40 eV. The potential difference is considered to be the main driving force for efficient charge separation and transfer across the heterojunction. Thus the down-potential and up-potential movement of photogenerated electrons and holes, respectively, drastically reduces their recombination, which is of great significance for enhancing photocatalytic activity. Furthermore, the significance of the isotopic heterojunction was justified by photoelectrochemical (PEC) and photoluminescence (PL) studies. In the case of CN-U, a strong PL emission at 450 nm was observed, indicating the fast recombination of charge carriers, which was greatly inhibited by the heterojunction formation with CN-T. This isotopic heterojunc-

tion formation results in the redistribution of electrons on one side and holes on the other side of the heterojunction as per their band offsets. Hence intrinsic limitations have been overcome by heterojunction formation to improve quantum efficiency and construct a new class of photocatalysts materials. In addition to the works presented above, many more g-$C_3N_4$-based nanocomposites have been investigated by several researchers for photocatalytic energy generation applications. Some of the important recent reports have been summarized in Table 3.

## Photocatalysts for environmental remediation applications

Over the years, it has been observed that substantial research efforts have been devoted to the design and development of functional nanomaterials, which can utilize maximum light energy and remove various kinds of organic and inorganic pollutants from water. It has been noticed that most of these pollutants cannot be removed completely by biological or conventional treatment methods because of their high chemical stability or strong resistance to mineralization [182]. As environmental pollution, and especially water contamination, has

surpassed the threshold of the natural purification process due to rapid industrialization, there is an urgent need to develop low cost, environmentally benign methods, which can effectively remove pollutants from contaminated water. The chemical oxidation of pollutant dyes, such as methylene blue (MB), methyl orange (MO), rhodamine B (RhB) can lead to their complete mineralization [183]. This oxidation process involves the in situ generation of highly reactive oxidative species, such as hydroxyl radicals ($^*OH$), superoxide radicals ($O_2^{-*}$) and holes ($h^+$) during photocatalytic reaction [12]. These highly oxidative species react with target molecules (pollutants) and bring about their complete mineralization. The heterogeneous photocatalysis has turned out to be one of the most appealing options for pollutant removal due to its potential to mineralize pollutants by utilizing the solar energy spectrum [12]. Carbon-based 2D materials (mainly graphene and g-$C_3N_4$) have been extensively employed as nanocomposites because of their high specific surface area, which can adsorb large quantities of pollutants. Therefore, more adsorption of pollutants over the catalyst surface is one of the crucial parameters in addition to a low recombination rate and fast charge transfer to generate active oxidative species during oxidative degradation processes.

**Table 3:** Photocatalytic $H_2$ evolution over g-$C_3N_4$-based nanocomposites. LED – light emitting diode; TEOA – triethanolamine; QDs – quantum dots.

| Sl no. | photocatalyst | synthesis route | light source | sacrificial agent | $H_2$ production | ref. (year) |
|--------|---------------|-----------------|--------------|-------------------|------------------|-------------|
| 1 | g-$C_3N_4$–SrTiO$_3$ | co-precipitation I and calcination | 250 W UV–vis lamp | – | 440 µmol h$^{-1}$·g$^{-1}$ | [83] (2011) |
| 2 | g-$C_3N_4$–SrTiO3:Rh | solid state reaction | 300 W Xe lamp | methanol | 223.3 µmol·h$^{-1}$ | [165] (2012) |
| 3 | g-$C_3N_4$–NiS | hydrothermal | visible light | TEOA | 48.2 µmol·h$^{-1}$ | [166] (2013) |
| 4 | g-$C_3N_4$–MoS$_2$ | impregnation | visible light | lactic acid | 20.6 µmol·h$^{-1}$ | [167] (2013) |
| 5 | g-$C_3N_4$–CdS | solvothermal and chemisorption | 350 W Xe arc lamp | – | 4152 µmol h$^{-1}$·g$^{-1}$ | [168] (2013) |
| 6 | g-$C_3N_4$–Cu$_2$O | reduction | 300W Xe lamp | TEOA | 241.3 mol h$^{-1}$·g$^{-1}$ | [169] (2014) |
| 7 | g-$C_3N_4$–SnO$_2$ | chemical synthesis | 300W Xe lamp | TEOA | 900 µmol h$^{-1}$·g$^{-1}$ | [170] (2014) |
| 8 | g-$C_3N_4$–N-TiO$_2$ | electrospinning | 300 W Xe arc lamp | methanol | 8931.3 µmol h$^{-1}$·g$^{-1}$ | [171] (2015) |
| 9 | g-$C_3N_4$–C-N-TiO$_2$ | solvothermal | 300 W Xe lamp | TEOA | 39.18 µmol h$^{-1}$·g$^{-1}$ | [172] (2015) |
| 10 | g-$C_3N_4$–CdS QD | thermal polymerization | 300W Xe lamp | TEOA | 601 µmol·h$^{-1}$ | [173] (2015) |
| 11 | g-$C_3N_4$–Au–CdS | in situ reduction and photodeposition | visible light | TEOA | 277 µmol·h$^{-1}$ | [174] (2015) |
| 12 | g-$C_3N_4$–N-CeOx | annealing | 300 W Xe lamp | TEOA | 292.5 µmol· h$^{-1}$·g$^{-1}$ | [175] (2015) |
| 13 | g-$C_3N_4$–MgFe$_2$O$_4$ | sol−gel and auto combustion | 300 W Xe lamp | TEOA | 30.09 µmol·h$^{-1}$ | [176] (2015) |
| 14 | g-$C_3N_4$–InVO$_4$ | hydrothermal | 300 W Xe arc lamp | methanol | 212 µmol h$^{-1}$·g$^{-1}$ | [146] (2015) |
| 15 | g-$C_3N_4$–TiO$_2$ | solvothermal | UV LED (3 W, 420 nm) | methanol | 5.6 µmol·h$^{-1}$ | [177] (2016) |
| 16 | g-$C_3N_4$–TiO$_2$ | calcination and solvothermal | AM1.5 solar power system | methanol | 186.9 µmol·h$^{-1}$ | [178] (2016) |
| 17 | g-$C_3N_4$–Ni@NiO-CdS | reduction | 300 W Xe lamp | TEOA | 1258.7 µmol·h$^{-1}$·g$^{-1}$ | [179] (2016) |
| 18 | g-$C_3N_4$@TiO$_2$–CdS | hydrothermal | UV LED (3 W, 420 nm) | – | 75.2 µmol·h$^{-1}$ | [180] (2017) |
| 19 | g-$C_3N_4$–Ca$_2$Nb$_2$TaO$_{10}$ | thermal condensation and polymerization | 300 W Xe arc lamp | TEOA | 43.54 µmol·h$^{-1}$ | [181] (2017) |

Generally, the photocatalytic degradation mechanism over semiconductor-based nanocomposites can be summarized as the following [12]:

$$\text{semiconductor nanocomposite} + h\nu \rightarrow \text{h}^+ + \text{e}^-$$

$$O_2 + \text{e}^- \rightarrow O_2^{-*}$$

$$O_2^{-*} + H^+ \rightarrow {}^*OOH$$

$${}^*OOH \rightarrow O_2 + H_2O_2$$

$$H_2O_2 + h\nu + \text{e}^- \rightarrow 2{}^*OH$$

$$\text{h}^+ + H_2O \rightarrow {}^*OH + H^+$$

$$\text{pollutant} + \text{h}^+ + O_2^{-*} + {}^*OH \rightarrow \text{degradation products}$$
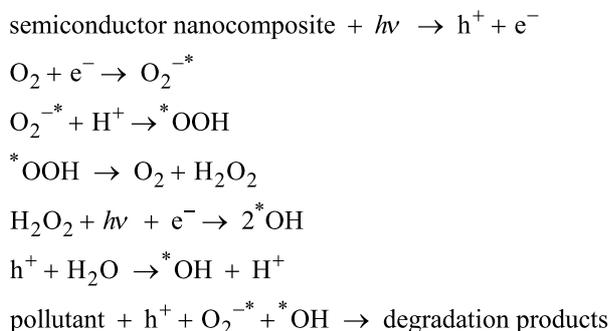
It is clear from the above reactions that when a photocatalyst is subjected to light, electron–hole pair formation takes place after absorption of photon energy ($h\nu$) is equal to or greater than the band gap of the semiconductor. Then, photogenerated electrons in the CB of the semiconductor and the holes in its VB migrate to the surface of the semiconductor photocatalyst. This is followed by the in situ generation of active oxidative species, hydroxyl radicals ($^*OH$), superoxide radicals ($O_2^{-*}$) and holes ($\text{h}^+$). The $^*OH$ radicals are primary oxidative species in photocatalytic reactions to degrade pollutants, which are formed in aqueous solution by two routes. Initially, water is photooxidized by $\text{h}^+$ followed by reaction of $O_2^{-*}$ with protons ($H^+$) to form $^*OOH$, which in turn generates $O_2$ and $H_2O_2$ that finally decomposes to form $^*OH$. Furthermore, the photogenerated $\text{h}^+$ also have the tendency to degrade organic pollutants directly depending on oxidative conditions. In order to increase the efficiency of photocatalytic reactions, the use of hole scavengers is always preferred, which effectively suppresses the photogenerated carrier recombination.

## Graphene-based binary nanocomposites for environmental remediation

As explained in a previous section, the extraordinary optical and electrical properties of graphene makes it a perfect material for various practical applications. It is anticipated that bulk graphene can preserve its extraordinary properties. However, the strong van der Waals interactions result in restacking of graphene sheets and its conductivity is partly revived after reduction from graphene oxide to the reduced form which diminishes its accessible surface area [184]. Extensive studies have been devoted to tackle this problem. One of the effective ways is nanocomposite formation with metal sulfide/oxide semiconductors, noble metals etc., which can effectively avoid re-stacking of individual graphene sheets. This retains the high conductivity and high specific surface area availability for practical applications such as photocatalytic pollutant removal.
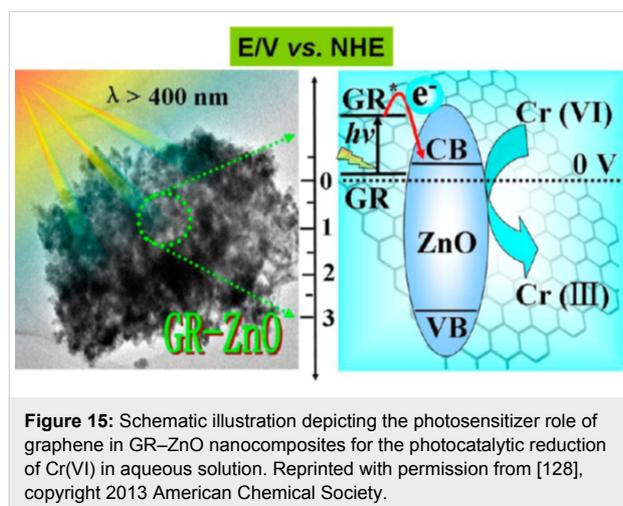
Graphene–semiconductor-based binary nanocomposites with excellent visible-light response have been explored widely for pollutant degradation because of their extraordinary performance. Based on the visible-light response, the narrow band gap semiconductors, mainly $MoS_2$ ($E_g = 1.86$ eV) in nanocomposite with graphene, have been intensively studied. Pan et al. [185] reported binary nanocomposites of $MoS_2$–reduced graphene oxide prepared by a microwave-assisted method. The graphene oxide was reduced to RGO with $MoS_2$ precursor thioacetamide solution during microwave treatment. This binary nanocomposite was tested for visible-light-based photocatalytic degradation of MB as a model pollutant. The results indicate about 99% degradation occurred within 60 min of visible-light irradiation for nanocomposites optimized at 0.5 wt % RGO in the photocatalyst. This enhanced photocatalytic performance has been attributed to excellent dye adsorption on RGO and improved charge transfer between $MoS_2$ and RGO. Subsequently, Chen et al. also reported similar binary $MoS_2$–graphene oxide (GO) nanocomposites by hydrothermal method for solar-light-based degradation of MB. The $MoS_2$ content was systematically varied in the nanocomposites and composition where 10 wt % of $MoS_2$ proved to be best composition for enhanced photocatalytic performance for MB removal [186].

Furthermore, visible-light responsive catalysts, such as CdS, have been explored by Wang et al. [187] who reported visible-light active CdS–graphene nanocomposites prepared by hydrothermal methods for dye degradation. Interestingly, the loading of graphene onto CdS further decreases the band gap of CdS, which signifies the strong interaction between both the components in binary nanocomposites and has been supported by the diffuse reflectance UV–vis spectroscopy. Moreover, the transient photocurrent response studies further confirm the CdS–graphene heterojunction formation and excellent photogenerated charge separation, which leads to more 95% degradation of MO in only 60 min of irradiation.

Besides acting as an excellent electron acceptor/transporter, the role of graphene as a photosensitizer has also been reported. Zhu et al. [188] have reported the $ZnWO_4$–graphene nanocomposite and the photocatalytic activity was demonstrated both under UV and visible light for MB degradation. The visible-light responsive activity of $ZnWO_4$–graphene nanocomposites was about 7-fold higher than bare $ZnWO_4$, which could be ascribed to the generation of $^*OH$ and $O_2^{-*}$ because of charge transfer from graphene (LUMO) to the CB of $ZnWO_4$. The transferred electrons in the CB of $ZnWO_4$ reduce the dissolved $O_2$ to generate $O_2^{-*}$. This explains the photosensitizer role of graphene in which photogenerated electron–hole pair formation by promotion of electrons from HOMO to LUMO. In addition to this, $ZnWO_4$ is UV-excited as per its band gap energy

(3.08 eV), which also results in photogenerated charge carrier formation. However, this work does not exclude the possibility of dye sensitization which could lead to fast charge transfer and enhanced photocatalytic activity. There are many reports available [189,190], which explain the significance of dye sensitization to enhance photocatalytic activity.

Thus, to avoid self-induced photosensitization of the reaction substrate, Xu et al. reported graphene–ZnO-based nanocomposites with strong interfacial bonding by in situ growth of graphene (GR) sheets on ZnO [128]. This nanocomposite has been utilized for photocatalytic reduction of Cr(VI) to Cr(III) in aqueous solution under visible-light irradiation. The band gap of ZnO is about 3.37 eV, hence it cannot absorb visible light and this excludes the possibility of photocatalytic activity because of ZnO excitation. Thus upon visible-light irradiation, electron promotion from HOMO (GR) to LUMO (GR) takes place, from where photogenerated electrons are transferred to the CB of ZnO and further participate in the reduction reaction as presented in Figure 15.



**Figure 15:** Schematic illustration depicting the photosensitizer role of graphene in GR–ZnO nanocomposites for the photocatalytic reduction of Cr(VI) in aqueous solution. Reprinted with permission from [128], copyright 2013 American Chemical Society.

## Graphene-based ternary nanocomposites for environmental remediation

In addition to the binary nanocomposites, graphene-based ternary nanocomposites have also attracted much attention for environmental remediation applications. In order to further improve the photocatalytic performance, heterojunction construction of ternary nanocomposites with suitable energy band alignments have been explored. Such ternary heterojunctions could benefit the charge transfer across the interface as per suitable band potentials to facilitate the separation of photogenerated charge carriers efficiently. In addition to the improved charge transfer kinetics, ternary nanocomposites showed excellent light absorption owing to the presence of a three-component system, which can better utilize a wide range

of the solar energy spectrum in comparison to binary nanocomposites. Recently, our group reported the synergetic effect of $MoS_2$–RGO doping of ZnO nanoparticles to enhance its photocatalytic performance for pollutant removal [191]. The ZnO–$MoS_2$–RGO ternary nanocomposites were prepared by a facile hydrothermal method with varying content of $MoS_2$–RGO nanosheets. Firstly, $MoS_2$–RGO nanosheets were prepared and then its suspension with zinc acetate dihydrate, $Zn(CH_3COO)_2 \cdot 2H_2O$, sodium hydroxide (NaOH) was made and treated hydrothermally to afford the final ternary nanocomposites exhibiting intimate contact between ZnO–$MoS_2$–RGO. The photocatalytic activity of the prepared ternary nanocomposites was examined by the studying the degradation of a coloured pollutant, MB dye, and a colourless pollutant, carbendazim, a hazardous fungicide under natural sunlight irradiation. The enhanced photocatalytic activity of as-prepared ternary nanocomposites, as compared to bare ZnO nanoparticles, has been attributed to the synergetic effect between $MoS_2$–RGO. The charge transfer occurs as per the CB and VB potentials of ZnO and $MoS_2$. The CB of ZnO (−0.31 eV vs NHE) is more negative than that of $MoS_2$ (−0.13 eV vs NHE), which favours the photogenerated electron transfer from the CB of ZnO to the CB of $MoS_2$. Furthermore, $MoS_2$ has a more negative CB than RGO, which has Fermi level at −0.08 eV vs NHE, facilitating the charge transfer to RGO. These transferred electrons form reactive oxidative species $^*OH$, which degrade both the coloured and colourless pollutants during the photocatalytic process. The high surface area of $MoS_2$–RGO nanosheets adsorb pollutants effectively thereby contributing to their efficient degradation.

To further prove the role of graphene as an excellent electron accepting/shuttling system with high pollutant adsorption ability, our group reported another ternary nanocomposite composed of CdS–ZnO–RGO for degradation of MO under visible light and natural sunlight irradiation [192]. More than 90% of the dye was removed from water in 60 min under natural sunlight irradiation, while it took about 90 min under visible-light irradiation. Under natural sunlight irradiation, both of the semiconductors (CdS and ZnO) are photoexcited and charge transfer takes place from the more negative CB of CdS (−0.66 eV vs NHE) to the CB of ZnO (−0.31 eV vs NHE). The photogenerated electrons from the CB of ZnO are readily transferred to RGO because of the high work function value of ZnO (5.2–5.3 eV) as compared to RGO (4.5 eV). Simultaneously, the transfer of the holes takes place up-potential from the VB of ZnO to the VB of CdS. As the Fermi level of RGO is −0.08 eV vs NHE, which is more positive than the redox potential of $O_2/O_2^{-*}$ (−0.13 V), $O_2^{-*}$ cannot be formed but $H_2O_2$ formation was favoured as per its redox potential ($O_2/H_2O_2$ = +0.695 eV vs NHE). This $H_2O_2$ further decomposed to form $^*OH$. Thus photogenerated electron–hole pairs are effectively separated,
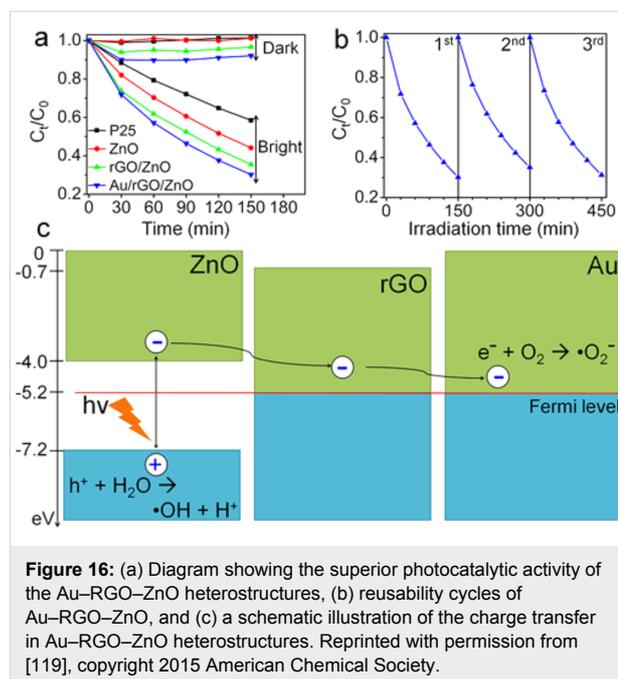
which improves the efficiency of the reaction. Holes along with *OH resulted in the degradation of adsorbed MO on the photocatalyst surface.

Many research groups have utilized the SPR effect of noble metals like Au and Ag to utilize the visible region of the solar energy spectrum by the formation of a Schottky barrier for facile charge transfer to fabricate ternary nanocomposites with promising photocatalytic activity. Hahn et al. [119] fabricated Au NP-decorated, reduced graphene oxide (RGO)-wrapped, ZnO hollow spheres. The unique structure of the ZnO hollow spheres provided a very high charge transfer of around 87 ps, which is better than other nanostructures like nanorods (128 ps), nanoparticles (150 ps), etc. Au-decorated heterostructures showed an improved charge transfer efficiency of 68% as compared to their binary counterpart (RGO–ZnO) at only 40.3%. These high charge transfer kinetics resulted in improved photocatalytic activity of nanocomposites towards MB degradation as can be seen from Figure 16a,b. In addition, the high surface area of the Au–RGO–ZnO heterostructures (28.9 $m^2g^{-1}$), as compared to RGO–ZnO (17.9 $m^2g^{-1}$) and ZnO (12.7 $m^2g^{-1}$) resulted in excellent adsorption of MB, which is readily degraded. The photocatalytic degradation mechanism of the Au–RGO–ZnO nanocomposite is presented in Figure 16c. Upon UV light irradiation, electron−hole pairs are generated in the ZnO. The photogenerated electrons from the CB of ZnO are transferred to RGO due to the suitable work function value of RGO (4.5 eV) as compared to 5.2–5.3 eV for ZnO and 5.1 eV for Au nanoparticles. These transferred photogenerated electrons react with dissolved $O_2$ to form $O_2^{\bullet-}$ while photogenerated holes can generate *OH by reacting with water. These oxidative reactive species finally result in the mineralization of pollutants.

In addition to these binary and ternary graphene-based nanocomposites, there are many reports available in literature on the use of other graphene-based nanocomposites for environmental remediation application. Some of the noteworthy recent reports have been summarized in Table 4.

## g-$C_3N_4$-based nanocomposites for environmental remediation

g-$C_3N_4$ is an important material of interest for environmental remediation applications in the form of nanocomposites [95,216]. The structure of g-$C_3N_4$ is composed mainly of C–N bonds, which makes it a mildly basic catalytic material. Furthermore, the replacement of C by N in the six-membered ring leads to more basicity, which is beneficial for reactions like the nitrogen monoxide (NO) decomposition [217]. NO is a hazardous pollutant that causes various environmental issues such as acid rain, photochemical smog, etc. The direct decom-



**Figure 16:** (a) Diagram showing the superior photocatalytic activity of the Au–RGO–ZnO heterostructures, (b) reusability cycles of Au–RGO–ZnO, and (c) a schematic illustration of the charge transfer in Au–RGO–ZnO heterostructures. Reprinted with permission from [119], copyright 2015 American Chemical Society.

position reaction of NO into $N_2$ and $O_2$ is not feasible due to various issues in real conditions [218]. Moreover, atmospheric $O_2$ prevents adsorption of NO on active sites of the catalyst surface and hence decreases the activity. The basic groups on the surface of g-$C_3N_4$ provide resistance to $O_2$, the polar groups C–N–C favours adsorption of NO on its surface. Therefore g-$C_3N_4$ is an ideal catalyst for the NO decomposition reaction [217].

Recently, Zhang et al. [217] reported n–n type nanocomposites of $CeO_2$–g-$C_3N_4$ by an in situ pyrolysis method with enhanced photocatalytic activity for phenol and NO removal under visible-light irradiation. The optimized $CeO_2$–g-$C_3N_4$ catalyst with 8% $CeO_2$ in the nanocomposite shows the best photocatalytic performance. The photocatalysts having more $CeO_2$ content show decreased activity due to agglomeration of $CeO_2$ over g-$C_3N_4$ nanosheets, which can destruct interfacial contact and hence the charge transfer across it. This optimized 8% $CeO_2$–g-$C_3N_4$ photocatalyst exhibited a high photocurrent (0.35 µA) as compared to bare $CeO_2$ (0.06 µA) and g-$C_3N_4$ (0.14 µA), which clearly signify the high interfacial charge separation and suppressed recombination rate of the photogenerated charge carriers. The CB potential of g-$C_3N_4$ (−1.09 eV) is more negative as compared to $CeO_2$ (−0.79 eV) which favours the photogenerated electron transfer down-potential to the CB of $CeO_2$ from the CB of g-$C_3N_4$. This is followed by hole transfer from the VB of $CeO_2$ to the VB of g-$C_3N_4$. Hence photogenerated charge species are effectively separated from each other at intimate interfacial contact between $CeO_2$ and g-$C_3N_4$. The density of holes increases in the VB of g-$C_3N_4$,

**Table 4:** Graphene-based nanocomposites for environmental remediation. MCM 41 – mesoporous silica; $H_2TCPP$ – *meso*-tetrakis(4-carboxyphenyl)porphyrin; RGO – reduced graphene oxide; GR – graphene; EE2 – 17α-ethinylestradiol.

| Sl no. | photocatalyst | light source | pollutant (concentration) | $t_{completion}$ (min) | ref. (Year) |
|---|---|---|---|---|---|
| 1 | $GO–TiO_2$ | visible light 1000 W Xe lamp | MO (12 mgL$^{-1}$) | 180 min | [193] (2010) |
| 2 | $GR–TiO_2–MCM41$ | 100 W Hg lamp | 2-propanol (2.6 mmol L$^{-1}$) | – | [194] (2010) |
| 3 | RGO–ZnO | UV light | MB (5 mg L$^{-1}$) | 260 min | [195] (2011) |
| 4 | GO–Ag–AgX (X = Cl, Br) | 500 W Xe arc lamp | MO (15 mg L$^{-1}$) | 40 min | [196] (2011) |
| 5 | $GR–ZnFe_2O_4$ | 500 W Xe lamp | MB (20 mg L$^{-1}$) | 90 min | [197] (2011) |
| 6 | $GR–TiO_2$ | 150 W high-pressure Xe lamp | MB (1 mg · L$^{-1}$) | 180 min | [198] (2011) |
| 7 | $GR–InNbO_4$ | 500 W Xe lamp | MB (5 mg L$^{-1}$) | 90 min | [199] (2011) |
| 8 | $GR–Bi_2WO_6$ | 500 W Xe lamp | RhB (10$^{-5}$ M) | 16 min | [200] (2011) |
| 9 | $GR–TiO_2$ | UV light, mercury lamp solar light | RhB (0.5 × 10$^{-5}$ M) | 40 min | [201] (2012) |
| 10 | $RGO–SnO_2$ | 350 W Xe lamp | MB (2.7 × 10$^{-5}$ M) | 360 min | [202] (2012) |
| 11 | RGO@ZnO | simulated solar light | RhB | 120 min | [48] (2012) |
| 12 | RGO–ZnO | 12 W UV lamp | MB (5.0 × 10$^{-5}$ M) | 130 min | [203] (2012) |
| 13 | $GR–TiO_2$ | UV light, 40 W cylindrical black light bulb | MB (0.01 mM) | – | [204] (2012) |
| 14 | $GR–Fe^{3+}–TiO_2$ | UV–vis light | MB (4.5 ppm), formaldehyde (3000 ppmV) | 150 min, 90 min | [205] (2013) |
| 15 | $RGO–SnS_2$ | 500 W Xe lamp | Rh B (10 mg L$^{-1}$), phenol (10 mg L$^{-1}$) | 120 min, ≈240 min | [206] (2013) |
| 16 | $RGO–MoS_2$ | visible light, 5 W white LED | MB (60 mg L$^{-1}$) | 60 min | [185] (2014) |
| 17 | $GR–TiO_2$ | UV light, 100 W mercury lamp | MO (10$^{-4}$ mol L$^{-1}$) | 240 min | [207] (2014) |
| 18 | $GR–CaTiO_3$ | 15 W low-pressure mercury lamp | MO (1 mg L$^{-1}$) | 60 min | [208] (2014) |
| 19 | $RGO–TiO_2–ZnO$ | 300 W Xe lamp | MB (0.3 mg L$^{-1}$) | 120 min | [209] (2015) |
| 20 | $RGO–KTaO_3$ | visible light | phenol (0.21 mM) | 60 min | [210] (2015) |
| 21 | $RGO–H_2TCPP–TNT$ | halogen lamp | MB (10 mg L$^{-1}$) | 120 min | [211] (2016) |
| 22 | $RGO–Pt–TiO_2$ | 300 W Xe lamp irradiation | nitrobenzene (0.01M) | 480 min | [212] (2016) |
| 23 | $RGO–Ag–Bi_2MoO_6$ | 300 W halogen tungsten lamp | phenol (10 mg L$^{-1}$) | 300 min | [213] (2016) |
| 24 | $RGO–Ag–ZnFe_2O_4$ | 300 W Xe lamp | EE2 (2.0 mg L$^{-1}$) | 240 min | [214] (2016) |
| 25 | $RGO–Pd–Bi_2MoO_6$ | 300 W halogen tungsten lamp | phenol (10 mg L$^{-1}$) | 300 min | [215] (2017) |

which causes the mineralization of pollutants because of its strong oxidizing power. On the other hand, electrons from the CB of $CeO_2$ react with the dissolved $O_2$ to form $O_2^{-*}$, contributing to the degradation of the pollutants.

A highly efficient $g$-$C_3N_4$–$Ag_3PO_4$ nanocomposite for MO removal under visible light was reported by Katsumata et al. [219]. $Ag_3PO_4$ is one of the more interesting semiconductors with a 2.45 eV band gap and high oxidative power for pollutant degradation. The in situ precipitation method was employed for $g$-$C_3N_4$–$Ag_3PO_4$ nanocomposite synthesis, during which Ag nanoparticle formation on the surface of catalysts plays a crucial role in photocatalytic activity. The charge transfer in this nanocomposite takes pace through the Z-scheme process. As is clear from Figure 17, visible-light irradiation results in the formation of photogenerated electrons in the CB and holes in the VB of both the semiconductors. The photogenerated electrons from the CB of $Ag_3PO_4$ migrate to the Ag nanoparticles through the Schottky barrier due to the more positive Fermi level of Ag. Moreover, the Fermi level of Ag is more negative
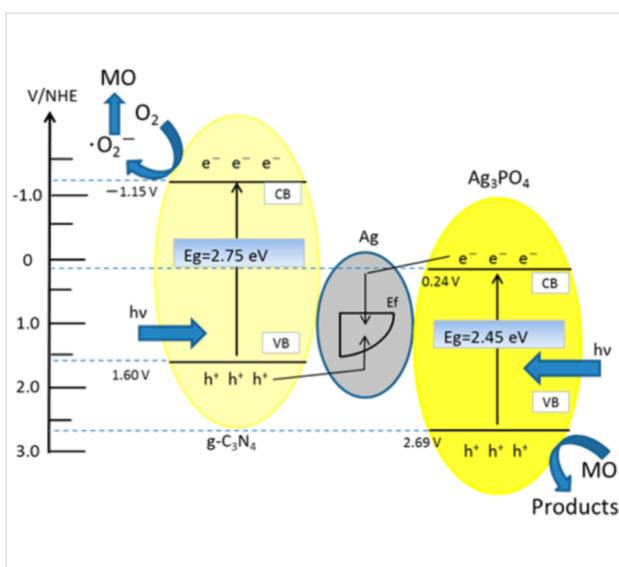


**Figure 17:** Z-scheme photocatalytic mechanism of the $g$-$C_3N_4$–$Ag_3PO_4$ hybrid photocatalyst under visible-light irradiation (>440 nm). Reprinted with permission from [219], copyright 2014 American Chemical Society.

than the VB potential of g-$C_3N_4$, which leads to the hole migration from the VB of g-$C_3N_4$ to Ag. Hence Ag nanoparticles at the interface of g-$C_3N_4$–$Ag_3PO_4$ acts as a charge separator and oxidative species are formed by CB electrons in g-$C_3N_4$, which brings about pollutant degradation. Holes from the VB of $Ag_3PO_4$ itself oxidize the pollutants. The g-$C_3N_4$–$Ag_3PO_4$ nanocomposite was able to degrade MO dye in just 5 min of irradiation, which illustrates the high efficiency of the photocatalyst. This excellent photocatalytic activity could be attributed to the efficient photogenerated charge separation by the Z-scheme process, wherein Ag nanoparticles as charge separation centers leads to fast charge transfer across interface in g-$C_3N_4$–$Ag_3PO_4$ nanocomposites.

Zhao et al. [220] reported a very interesting study on the band gap tuning of g-$C_3N_4$-RGO nanocomposites. They reported that by controlling the reduced graphene oxide (RGO) content in the nanocomposite, its band gap can be easily tuned. The g-$C_3N_4$–RGO nanocomposite exhibits a considerably reduced band gap as compared to bare g-$C_3N_4$. It was very interesting that an optimized RGO content in the nanocomposite led to a positive shift of the VB edge potential, thereby increasing its oxidation power. The decrease in the band gap energy of the nanocomposite was ascribed to the covalent bond formation of C–O–C between g-$C_3N_4$ and RGO, which has been confirmed by Fourier transform infrared (FTIR) and X-ray photoelectron spectroscopy (XPS). This nanocomposite exhibits improved photocatalytic activity for the degradation of rhodamine B and 4-nitrophenol under visible light irradiation, which could be attributed to the enhanced visible light absorption by band gap narrowing, high oxidation power and the excellent electron conductivity across the g-$C_3N_4$–RGO interface. Many g-$C_3N_4$ nanocomposites based on heterojunction formation with graphene have been reported with high quantum efficiency for various photocatalytic applications.

Huang et al. [221] reported a novel ternary nanocomposite composed of g-$C_3N_4$–Ag–$TiO_2$ with enhanced photocatalytic activity for pollutant removal. The Ag was photodeposited as an interlayer between g-$C_3N_4$ and $TiO_2$ and this ternary nanocomposite was demonstrated for visible-light-based photocatalytic activity. The visible-light response of the nanocomposite was enhanced due to the SPR effect of Ag and the interface formation between Ag–g-$C_3N_4$–$TiO_2$. The photocatalytic mechanism has been discussed on the basis of CB and VB edge potentials in this ternary g-$C_3N_4$–Ag–$TiO_2$ nanocomposite. The CB and VB edge potentials of g-$C_3N_4$ were at −1.23 and +1.52 eV, while those of $TiO_2$ were at −0.30 and +2.92 eV, respectively. Under visible-light irradiation, only g-$C_3N_4$ was excited because of its suitable band gap. The photoexcited electron transferred to the CB of $TiO_2$ because of the more negative CB

potential of g-$C_3N_4$. Furthermore, Ag NPs in the interlayer of the two semiconductors played a crucial role as an electron-conduction bridge. Moreover the Schottky barrier formation takes place at the interface of the Ag and $TiO_2$ nanoparticles, which facilitates this electron transfer in addition to enhanced visible-light response due to its SPR effect.

The nanocomposites of g-$C_3N_4$ with other cabon-based materials, such as graphene, have been investigated thoroughly as efficient, low cost and metal-free photocatalysts for removal of various pollutants. The development of such nanocomposites is generally based on some nanoparticle/nanorod/nanosheet heterostructure, which are nowadays a very common strategy explored on a large scale. In this regard, recently, Jiang et al. [222] explored a very effective 3D porous aerogel based on g-$C_3N_4$ and GO nanosheets for photocatalytic environmental remediation. This aerogel was prepared by the hydrothermal co-assembly method and utilized for MO dye removal under visible-light irradiation. The GO nanosheets with porous structure and high pollutant adsorption capability were utilized for nanocomposite formation with g-$C_3N_4$ . The main advantage of the 3D porous structure is that it can inhibit the stacking of nanosheets and make more active sites available for catalytic reaction. The g-$C_3N_4$ acts as a photocatalyst and electron–hole pairs are generated by visible light absorption. GO makes a 3D porous structure and facilitates the charge transfer process at the large coherent interface to generate reactive oxidative species, which can mineralize the MO dye effectively. More than 90% of MO was removed by a porous aerogel of g-$C_3N_4$ and GO nanosheets in 4 h of irradiation, which is about 6-fold higher than bare g-$C_3N_4$.

In the past few years, g-$C_3N_4$-based nanocomposites with semiconductors and metals have been successfully prepared and employed for environmental remediation applications for various harmful pollutant degradation. Some of the notable recent reports have been presented in Table 5.

## Conclusion

The combination of excellent properties and the easy availability have made carbon-based materials one of the most promising materials for catalysis. Solar energy harvesting for energy generation from water is one of the attractive and challenging field in photocatalysis. Due to the huge specific surface area, graphene acts as an excellent 2D support material for metals, metal oxides and other materials. The tunable optical and electronic properties of these materials have made them a versatile material, particularly graphene, which can act as cocatalyst, photocatalyst and photosensitizer, and even exhibit the property of hydrogen evolution (energy generation) by itself. On similar note, a wide range of g-$C_3N_4$-based nanocomposites

**Table 5:** g-$C_3N_4$-based nanocomposites for environmental remediation. CQDs – carbon quantum dots; CNTs – carbon nanotubes; MO – methyl orange; MB – methylene blue; DCP – dichlorophenol; PNP – p-nitrophenol; RhB – rhodamine B; BF – fuchsin; 4-NP – 4-nitrophenol.

| SI no. | photocatalyst | light source | pollutant (concentration) | $t_{completion}$ (min) | ref. (Year) |
|---|---|---|---|---|---|
| 1 | g-$C_3N_4$–Au | 500 W Xe lamp | MO (10 mg L$^{-1}$) | 150 min | [223] (2013) |
| 2 | g-$C_3N_4$–$Bi_2WO_6$ | 300 W Xe lamp | MO (5 mg L$^{-1}$), 2,4-DCP (20 mg L$^{-1}$) | 120 min | [224] (2013) |
| 3 | g-$C_3N_4$–$Ag_2O$ | 300 W Xe lamp | MO, phenol (20 mg L$^{-1}$) | 30 min, 180 min | [225] (2013) |
| 4 | g-$C_3N_4$–Ag | 300 W Xe lamp | MO, PNP (10 mg L$^{-1}$) | 120 min | [226] (2013) |
| 5 | g-$C_3N_4$–C–ZnO | 300 W Xe lamp | MB (10 mg L$^{-1}$) | 120 min | [74] (2014) |
| 6 | g-$C_3N_4$–N–ZnO | 300 W Xe lamp | RhB (5 mg L$^{-1}$) | 60 min | [227] (2014) |
| 7 | g-$C_3N_4$–ZnO | 500 W Xe lamp | MB (0.04 mM) | 150 min | [228] (2014) |
| 8 | g-$C_3N_4$–$WO_3$ | 500 W Xe lamp | MB (0.9 × 10$^{-5}$ mol), BF (1.0 × 10$^{-5}$ mol) | 60 min | [229] (2014) |
| 9 | g-$C_3N_4$–$WO_3$ | 500 W Xe lamp | RhB (0.01 M) | 120 min | [230] (2014) |
| 10 | g-$C_3N_4$–N–$SrTiO_3$ | 300 W Xe lamp | RhB, 4-chlorophenol (5 mg L$^{-1}$) | 60 min | [231] (2014) |
| 11 | g-$C_3N_4$–CdS | PLS-SXE 300 lamp | MO (5 mg L$^{-1}$) | 16 min | [232] (2014) |
| 12 | g-$C_3N_4$–$C_{60}$ | 500 W Xe lamp | RhB (1.0 × 10$^{-5}$ mol L$^{-1}$) | 60 min | [233] (2014) |
| 13 | g-$C_3N_4$–$C_{60}$ | 500 W Xe lamp | MB (0.01 mM), phenol (5 ppm) | 180 min | [234] (2014) |
| 14 | g-$C_3N_4$–$TiO_2$ | 100 W mercury lamp, 300 W halogen lamp | MO, RhB (0.2 wt %) | 50 min, 300 min | [235] (2014) |
| 15 | g-$C_3N_4$–$SnO_2$ | 300 W Xe lamp | MO (10 ppm) | 180 min | [170] (2014) |
| 16 | g-$C_3N_4$–$SnS_2$ | 300 W Xe lamp | Cr(VI) (50 mg L$^{-1}$) | 50 min | [236] (2014) |
| 17 | g-$C_3N_4$–Ag | 500 W Xe lamp | MB (0.01 mM) and phenol (10 ppm) | – | [161] (2014) |
| 18 | $C_3N_4$–CQD | IR source | MO (4 mg L$^{-1}$) | 240 min | [237] (2015) |
| 19 | g-$C_3N_4$–Au–CNT | visible light source | RhB | 50 min | [238] (2015) |
| 20 | g-$C_3N_4$ –$TiO_2$ | LED 3 W | MO, phenol (10 mg L$^{-1}$) | 80 min | [239] (2015) |
| 21 | g-$C_3N_4$ –$Ti^{3+}$–$TiO_2$ | 300 W Dy lamp | RhB (20 mg L$^{-1}$) | 120 min | [240] (2015) |
| 22 | g-$C_3N_4$–$Ag_2CO_3$ | 300 W Xe lamp | MO, RhB (10 mg L$^{-1}$) | 30 min | [241] (2015) |
| 23 | g-$C_3N_4$–AgBr | 35 W metal halide lamp | MO (10 mg L$^{-1}$) | 120 min | [242] (2015) |
| 24 | g-$C_3N_4$–$Bi_2WO_6$ | Xe lamp | RhB (10 mg L$^{-1}$) | 50 min | [243] (2015) |
| 25 | g-$C_3N_4$–$CeO_2$ | 300 W Xe lamp | MB (10 mg L$^{-1}$) | 210 min | [244] (2015) |
| 26 | g-$C_3N_4$–$Fe_2O_3$ | 300 W Xe lamp | RhB (20 mg L$^{-1}$) | 90 min | [245] (2015) |
| 27 | g-$C_3N_4$–$AgVO_3$ | visible light | MO (10 mg L$^{-1}$) | 60 min | [246] (2017) |
| 28 | g-$C_3N_4$–Ag–$Fe_3O_4$ | visible light | MB (10 ppm) | 120 min | [247] (2017) |
| 29 | Na–g-$C_3N_4$–$DyVO_4$ | tungsten/halogen linear lamp (500 W) | RhB (0.02 mM), 4-NP (0.143 mM) | 80 min, ≈360 min | [248] (2017) |
| 30 | g-$C_3N_4$–$TiO_2$–CdS | 500 W Xe lamp | phenol (10 mg L$^{-1}$) | 300 min | [249] (2017) |

with non-metal, metal oxide semiconductors, composite oxide semiconductors, and noble metals have been reported with enhanced light absorption and accelerated charge transfer kinetics for energy generation applications. Furthermore, these two-dimensional carbon-based nanocomposites have shown promising results in the case of photocatalytic environmental applications as well, as described in detail in this review article.

Despite all the excellent results obtained with carbon-based nanocomposites for photocatalytic applications, there are also some challenges for improving its utilization.

(1) First of all, the water splitting reaction is a thermodynamically unfavourable reaction as the Gibbs free energy is positive for this reaction. Hence, making this reaction feasible and preventing the back reaction of hydrogen and oxygen to form

water using economic and ecologically-friendly catalysts is a big challenge.

(2) The oxidation of graphite flakes introduces various functional groups in graphene oxide, which disrupt its electronic structure by several orders of magnitude as compared to pristine graphene. The conductivity is revived when graphene oxide is reduced but various defects remain. Thus, the fabrication of novel graphene-based nanocomposites with improved catalytic performance is still a challenge. Moreover, large-scale production of graphene-based nanocomposites with controlled morphology and high performance is a challenging task.

(3) The role of graphene as a photocatalyst and photosensitizer is also complex in a mechanistic way, because generally it has been reported that the enhanced photogenerated charge carrier

separation, and then charge transfer to the CB of semiconductor, is responsible for the activity of the catalyst. However, many research groups have demonstrated that electrons can be transferred from the upper VB of graphene to the semiconductor, as graphene can act as photosensitizer. Such a mechanism is still not fully understood and detailed investigations are needed for this particularly interesting interfacial charge transfer in graphene-based nanocomposites.

(4) The multicomponent graphene-based nanocomposites have shown remarkable enhancement in the photocatalytic performance towards energy generation and pollutant removal due to improved charge transfer kinetics and well-defined intimate contact between constituent materials. Therefore, more of the facile synthetic strategies need to be developed in order to control morphology and design such multicomponent nanocomposites.

(5) In photocatalytic water splitting, it is predominantly the hydrogen evolution which contributes to the energy generation. This evolved hydrogen needs to be stored in an efficient and safe manner for future consumption. Hence, hydrogen storage is also a big issue in order to use it as fuel.

(6) Although a huge number of carbon-based photocatalysts have been explored for energy generation by solar water splitting, the significant breakthrough in harvesting energy by utilizing the full solar spectrum still needs to be achieved.

(7) Most of the photocatalytic water splitting reactions for $H_2$ generation are carried out in the presence of sacrificial agents as hole scavengers, such as methanol, ethanol, triethanolamine, sodium sulfide, sodium sulphite, etc. Keeping in view the energy efficiency, environmental benignity and sustainability, the use of such sacrificial agents needs to be avoided in future.

(8) The synthesis of g-$C_3N_4$-based complex nanocomposites with proper architecture and a rational charge cascading process for real life applications is full of challenges as the mechanism of photocatalytic enhancement by g-$C_3N_4$ nanocomposites is still unclear.

(9) The most important concern with g-$C_3N_4$-based complex nanocomposites is stability, which is not well addressed to date. The photocatalytic stability is one of the crucial parameters that decides commercial application of catalysts.

(10) The detailed mechanistic pathways leading to the mineralization of pollutants using these carbon-based nanocomposites as photocatalysts is not fully understood and entails detailed investigations on the intermediates formed during the process.

Finally, the rapid development of materials science and nanotechnology in the past few years has invented a new class of functional materials for photocatalytic applications. The fascinating properties of these materials could be further explored for understanding the mechanisms in photocatalytic reactions to effectively address the various global issues in the future. Hence, it requires more effort from scientific community for better understanding of physicochemical properties of the nanocomposites based on these two-dimensional carbon-based materials to develop novel functional materials for sustainable chemistry.

## Acknowledgments

## References

1. Asif, M.; Muneer, T. *Renewable Sustainable Energy Rev.* **2007,** *11,* 1388–1413. doi:10.1016/j.rser.2005.12.004
2. Li, Y.; Wang, H.; Xie, L.; Liang, Y.; Hong, G.; Dai, H. *J. Am. Chem. Soc.* **2011,** *133,* 7296–7299. doi:10.1021/ja201269b
3. Khin, M. M.; Nair, A. S.; Babu, V. J.; Murugan, R.; Ramakrishna, S. *Energy Environ. Sci.* **2012,** *5,* 8075–8109. doi:10.1039/C2EE21818F
4. Kudo, A.; Miseki, Y. *Chem. Soc. Rev.* **2009,** *38,* 253–278. doi:10.1039/B800489G
5. Qu, Y.; Duan, X. *Chem. Soc. Rev.* **2013,** *42,* 2568–2580. doi:10.1039/C2CS35355E
6. Fujishima, A.; Honda, K. *Nature* **1972,** *238,* 37–38. doi:10.1038/238037a0
7. Carpetis, C. *Int. J. Hydrogen Energy* **1982,** *7,* 287–310. doi:10.1016/0360-3199(82)90123-9
8. Khan, S. U.; Akikusa, J. *J. Phys. Chem. B* **1999,** *103,* 7184–7189. doi:10.1021/jp990066k
9. Khan, S. U. M.; Al-Shahry, M.; Ingler, W. B., Jr. *Science* **2002,** *297,* 2243–2245. doi:10.1126/science.1075035
10. Zhao, W.; Wang, Z.; Shen, X.; Li, J.; Xu, C.; Gan, Z. *Int. J. Hydrogen Energy* **2012,** *37,* 908–915. doi:10.1016/j.ijhydene.2011.03.161
11. Maeda, K.; Domen, K. *J. Phys. Chem. Lett.* **2010,** *1,* 2655–2661. doi:10.1021/jz1007966
12. Dong, S.; Feng, J.; Fan, M.; Pi, Y.; Hu, L.; Han, X.; Liu, M.; Sun, J.; Sun, J. *RSC Adv.* **2015,** *5,* 14610–14630. doi:10.1039/C4RA13734E
13. Fan, W.; Lai, Q.; Zhang, Q.; Wang, Y. *J. Phys. Chem. C* **2011,** *115,* 10694–10701. doi:10.1021/jp2008804
14. Lu, X.; Wang, G.; Xie, S.; Shi, J.; Li, W.; Tong, Y.; Li, Y. *Chem. Commun.* **2012,** *48,* 7717–7719. doi:10.1039/C2CC31773G
15. Phuruangrat, A.; Ham, D. J.; Hong, S. J.; Thongtem, S.; Lee, J. S. *J. Mater. Chem.* **2010,** *20,* 1683–1690. doi:10.1039/B918783A
16. Ge, L.; Zuo, F.; Liu, J.; Ma, Q.; Wang, C.; Sun, D.; Bartels, L.; Feng, P. *J. Phys. Chem. C* **2012,** *116,* 13708–13714. doi:10.1021/jp3041692
17. Naik, B.; Martha, S.; Parida, K. M. *Int. J. Hydrogen Energy* **2011,** *36,* 2794–2802. doi:10.1016/j.ijhydene.2010.11.104

18. Derbal, A.; Omeiri, S.; Bouguelia, A.; Trari, M. *Int. J. Hydrogen Energy* **2008,** *33,* 4274–4282. doi:10.1016/j.ijhydene.2008.05.067

19. Xie, M.; Fu, X.; Jing, L.; Luan, P.; Feng, Y.; Fu, H. *Adv. Energy Mater.* **2014,** *4,* 1300995. doi:10.1002/aenm.201300995

20. MamathaKumari, M.; Kumar, D. P.; Haridoss, P.; DurgaKumari, V.; Shankar, M. V. *Int. J. Hydrogen Energy* **2015,** *40,* 1665–1674. doi:10.1016/j.ijhydene.2014.11.117

21. Beltram, A.; Melchionna, M.; Montini, T.; Nasi, L.; Fornasiero, P.; Prato, M. *Green Chem.* **2017,** *19,* 2379–2389. doi:10.1039/c6gc01979j

22. Reddy, A. L. M.; Srivastava, A.; Gowda, S. R.; Gullapalli, H.; Dubey, M.; Ajayan, P. M. *ACS Nano* **2010,** *4,* 6337–6342. doi:10.1021/nn101926g

23. Zhang, L. L.; Zhou, R.; Zhao, X. S. *J. Mater. Chem.* **2010,** *20,* 5983–5992. doi:10.1039/C000417K

24. Pumera, M. *Energy Environ. Sci.* **2011,** *4,* 668–674. doi:10.1039/C0EE00295J

25. Shao, Y.; Wang, J.; Wu, H.; Liu, J.; Aksay, I. A.; Lin, Y. *Electroanalysis* **2010,** *22,* 1027–1036. doi:10.1002/elan.200900571

26. Sun, X.; Liu, Z.; Welsher, K.; Robinson, J. T.; Goodwin, A.; Zaric, S.; Dai, H. *Nano Res.* **2008,** *1,* 203–212. doi:10.1007/s12274-008-8021-8

27. Qu, L.; Liu, Y.; Baek, J.-B.; Dai, L. *ACS Nano* **2010,** *4,* 1321–1326. doi:10.1021/nn901850u

28. Zheng, Y.; Jiao, Y.; Ge, L.; Jaroniec, M.; Qiao, S. Z. *Angew. Chem.* **2013,** *125,* 3192–3198. doi:10.1002/ange.201209548

29. Cherevan, A. S.; Gebhardt, P.; Shearer, C. J.; Matsukawa, M.; Domen, K.; Eder, D. *Energy Environ. Sci.* **2014,** *7,* 791–796. doi:10.1039/C3EE42558D

30. Melchionna, M.; Beltram, A.; Montini, T.; Monai, M.; Nasi, L.; Fornasiero, P.; Prato, M. *Chem. Commun.* **2016,** *52,* 764–767. doi:10.1039/C5CC08015K

31. Melchionna, M.; Prato, M.; Fornasiero, P. *Catal. Today* **2016,** *277,* 202–213. doi:10.1016/j.cattod.2016.04.024

32. Moya, A.; Cherevan, A.; Marchesan, S.; Gebhardt, P.; Prato, M.; Eder, D.; Vilatela, J. J. *Appl. Catal., B: Environ.* **2015,** *179,* 574–582. doi:10.1016/j.apcatb.2015.05.052

33. Malato, S.; Fernández-Ibáñez, P.; Maldonado, M. I.; Blanco, J.; Gernjak, W. *Catal. Today* **2009,** *147,* 1–59. doi:10.1016/j.cattod.2009.06.018

34. Sathish, M.; Viswanathan, B.; Viswanath, R. P.; Gopinath, C. S. *Chem. Mater.* **2005,** *17,* 6349–6353. doi:10.1021/cm052047v

35. Murdoch, M.; Waterhouse, G. I. N.; Nadeem, M. A.; Metson, J. B.; Keane, M. A.; Howe, R. F.; Llorca, J.; Idriss, H. *Nat. Chem.* **2011,** *3,* 489. doi:10.1038/NCHEM.1048

36. Kim, H.-i.; Kim, J.; Kim, W.; Choi, W. *J. Phys. Chem. C* **2011,** *115,* 9797–9805. doi:10.1021/jp1122823

37. Perera, S. D.; Mariano, R. G.; Vu, K.; Nour, N.; Seitz, O.; Chabal, Y.; Balkus, K. J., Jr. *ACS Catal.* **2012,** *2,* 949–956. doi:10.1021/cs200621c

38. Wang, X.-j.; Yang, W.-y.; Li, F.-t.; Xue, Y.-b.; Liu, R.-h.; Hao, Y.-j. *Ind. Eng. Chem. Res.* **2013,** *52,* 17140–17150. doi:10.1021/ie402820v

39. Luo, B.; Liu, G.; Wang, L. *Nanoscale* **2016,** *8,* 6904–6920. doi:10.1039/C6NR00546B

40. Liu, P.; Jin, Z.; Katsukis, G.; Drahushuk, L. W.; Shimizu, S.; Shih, C.-J.; Wetzel, E. D.; Taggart-Scarff, J. K.; Qing, B.; Van Vliet, K. J.; Li, R.; Wardle, B. L.; Strano, M. S. *Science* **2016,** *353,* 364–367. doi:10.1126/science.aaf4362

41. Harvey, A.; Boland, J. B.; Godwin, I.; Kelly, A. G.; Szydłowska, B. M.; Murtaza, G.; Thomas, A.; Lewis, D. J.; O'Brien, P.; Coleman, J. N. *2D Mater.* **2017,** *4,* 025054. doi:10.1088/2053-1583/aa641a

42. Meyer, J. C.; Geim, A. K.; Katsnelson, M. I.; Novoselov, K. S.; Booth, T. J.; Roth, S. *Nature* **2007,** *446,* 60–63. doi:10.1038/nature05545

43. Wang, S.; Ang, P. K.; Wang, Z.; Tang, A. L. L.; Thong, J. T. L.; Loh, K. P. *Nano Lett.* **2010,** *10,* 92–98. doi:10.1021/nl9028736

44. Huang, X.; Qi, X.; Boey, F.; Zhang, H. *Chem. Soc. Rev.* **2012,** *41,* 666–686. doi:10.1039/C1CS15078B

45. Liu, M.; Yin, X.; Ulin-Avila, E.; Geng, B.; Zentgraf, T.; Ju, L.; Wang, F.; Zhang, X. *Nature* **2011,** *474,* 64–67. doi:10.1038/nature10067

46. Zhang, D.; Gan, L.; Cao, Y.; Wang, Q.; Qi, L.; Guo, X. *Adv. Mater.* **2012,** *24,* 2715–2720. doi:10.1002/adma.201104597

47. Xiang, Q.; Yu, J.; Jaroniec, M. *Chem. Soc. Rev.* **2012,** *41,* 782–796. doi:10.1039/C1CS15172J

48. Wang, J.; Tsuzuki, T.; Tang, B.; Hou, X.; Sun, L.; Wang, X. *ACS Appl. Mater. Interfaces* **2012,** *4,* 3084–3090. doi:10.1021/am300445f

49. Hummers, W. S., Jr.; Offeman, R. E. *J. Am. Chem. Soc.* **1958,** *80,* 1339. doi:10.1021/ja01539a017

50. Wang, G.; Shen, X.; Wang, B.; Yao, J.; Park, J. *Carbon* **2009,** *47,* 1359–1364. doi:10.1016/j.carbon.2009.01.027

51. Ferrari, A. C.; Bonaccorso, F.; Fal'Ko, V.; Novoselov, K. S.; Roche, S.; Bøggild, P.; Borini, S.; Koppens, F. H. L.; Palermo, V.; Pugno, N. *Nanoscale* **2015,** *7,* 4598–4810. doi:10.1039/C4NR01600A

52. Zhang, J.; Yu, J.; Jaroniec, M.; Gong, J. R. *Nano Lett.* **2012,** *12,* 4584–4589. doi:10.1021/nl301831h

53. Zhang, X.-Y.; Li, H.-P.; Cui, X.-L.; Lin, Y. *J. Mater. Chem.* **2010,** *20,* 2801–2806. doi:10.1039/B917240H

54. Xu, Y.; Wu, Q.; Sun, Y.; Bai, H.; Shi, G. *ACS Nano* **2010,** *4,* 7358–7362. doi:10.1021/nn1027104

55. Li, Q.; Li, X.; Wageh, S.; Al-Ghamdi, A. A.; Yu, J. *Adv. Energy Mater.* **2015,** *5,* 1500010. doi:10.1002/aenm.201500010

56. Bai, H.; Li, C.; Shi, G. *Adv. Mater.* **2011,** *23,* 1089–1115. doi:10.1002/adma.201003753

57. Li, W.; Wang, F.; Feng, S.; Wang, J.; Sun, Z.; Li, B.; Li, Y.; Yang, J.; Elzatahry, A. A.; Xia, Y.; Zhao, D. *J. Am. Chem. Soc.* **2013,** *135,* 18300–18303. doi:10.1021/ja4100723

58. Stephanopoulos, N.; Ortony, J. H.; Stupp, S. I. *Acta Mater.* **2013,** *61,* 912–930. doi:10.1016/j.actamat.2012.10.046

59. Kim, H.-i.; Moon, G.-h.; Monllor-Satoca, D.; Park, Y.; Choi, W. *J. Phys. Chem. C* **2011,** *116,* 1535–1543. doi:10.1021/jp209035e

60. Ullah, K.; Lei, Z.; Ye, S.; Ali, A.; Oh, W.-C. *RSC Adv.* **2015,** *5,* 18841–18849. doi:10.1039/C5RA00065C

61. Wang, X.; Blechert, S.; Antonietti, M. *ACS Catal.* **2012,** *2,* 1596–1606. doi:10.1021/cs300240x

62. Wang, X.; Maeda, K.; Chen, X.; Takanabe, K.; Domen, K.; Hou, Y.; Fu, X.; Antonietti, M. *J. Am. Chem. Soc.* **2009,** *131,* 1680–1681. doi:10.1021/ja809307s

63. Wang, Y.; Wang, X.; Antonietti, M. *Angew. Chem., Int. Ed.* **2012,** *51,* 68–89. doi:10.1002/anie.201101182

64. Wang, X.; Maeda, K.; Thomas, A.; Takanabe, K.; Xin, G.; Carlsson, J. M.; Domen, K.; Antonietti, M. *Nat. Mater.* **2009,** *8,* 76–80. doi:10.1038/nmat2317

65. Yang, S.; Gong, Y.; Zhang, J.; Zhan, L.; Ma, L.; Fang, Z.; Vajtai, R.; Wang, X.; Ajayan, P. M. *Adv. Mater.* **2013,** *25,* 2452–2456. doi:10.1002/adma.201204453

66. Christoforidis, K. C.; Melchionna, M.; Montini, T.; Papoulis, D.; Stathatos, E.; Zafeiratos, S.; Kordouli, E.; Fornasiero, P. *RSC Adv.* **2016,** *6,* 86617–86626. doi:10.1039/C6RA15581B

67. Cao, S.; Yu, J. *J. Phys. Chem. Lett.* **2014,** *5,* 2101–2107. doi:10.1021/jz500546b

68. Ong, W.-J.; Tan, L.-L.; Ng, Y. H.; Yong, S.-T.; Chai, S.-P. *Chem. Rev.* **2016,** *116,* 7159–7329. doi:10.1021/acs.chemrev.6b00075

69. Dong, G.; Zhang, Y.; Pan, Q.; Qiu, J. *J. Photochem. Photobiol., C: Photochem. Rev.* **2014,** *20,* 33–50. doi:10.1016/j.jphotochemrev.2014.04.002

70. Li, X.-H.; Antonietti, M. *Chem. Soc. Rev.* **2013,** *42,* 6593–6604. doi:10.1039/C3CS60067J

71. Ma, T. Y.; Ran, J.; Dai, S.; Jaroniec, M.; Qiao, S. Z. *Angew. Chem., Int. Ed.* **2015,** *54,* 4646–4650. doi:10.1002/anie.201411125

72. Zhao, Z.; Sun, Y.; Dong, F. *Nanoscale* **2015,** *7,* 15–37. doi:10.1039/C4NR03008G

73. Chai, B.; Peng, T.; Mao, J.; Li, K.; Zan, L. *Phys. Chem. Chem. Phys.* **2012,** *14,* 16745–16752. doi:10.1039/C2CP42484C

74. Zhu, Y.-P.; Li, M.; Liu, Y.-L.; Ren, T.-Z.; Yuan, Z.-Y. *J. Phys. Chem. C* **2014,** *118,* 10963–10971. doi:10.1021/jp502677h

75. Cao, S.-W.; Yuan, Y.-P.; Fang, J.; Shahjamali, M. M.; Boey, F. Y. C.; Barber, J.; Loo, S. C. J.; Xue, C. *Int. J. Hydrogen Energy* **2013,** *38,* 1258–1266. doi:10.1016/j.ijhydene.2012.10.116

76. Yin, R.; Luo, Q.; Wang, D.; Sun, H.; Li, Y.; Li, X.; An, J. *J. Mater. Sci.* **2014,** *49,* 6067–6073. doi:10.1007/s10853-014-8330-0

77. Tan, L.; Xu, J.; Zhang, X.; Hang, Z.; Jia, Y.; Wang, S. *Appl. Surf. Sci.* **2015,** *356,* 447–453. doi:10.1016/j.apsusc.2015.08.078

78. Cheng, C.; Shi, J.; Hu, Y.; Guo, L. *Nanotechnology* **2017,** *28,* 164002. doi:10.1088/1361-6528/aa651a

79. Hu, S.; Jin, R.; Lu, G.; Liu, D.; Gui, J. *RSC Adv.* **2014,** *4,* 24863–24869. doi:10.1039/C4RA03290J

80. He, Y.; Zhang, L.; Teng, B.; Fan, M. *Environ. Sci. Technol.* **2015,** *49,* 649–656. doi:10.1021/es5046309

81. Wu, S.-Z.; Li, K.; Zhang, W.-D. *Appl. Surf. Sci.* **2015,** *324,* 324–331. doi:10.1016/j.apsusc.2014.10.161

82. Wang, Y.; Wang, Z.; Muhammad, S.; He, J. *CrystEngComm* **2012,** *14,* 5065–5070. doi:10.1039/C2CE25517K

83. Xu, X.; Liu, G.; Randorn, C.; Irvine, J. T. S. *Int. J. Hydrogen Energy* **2011,** *36,* 13501–13507. doi:10.1016/j.ijhydene.2011.08.052

84. Kong, H. J.; Won, D. H.; Kim, J.; Woo, S. I. *Chem. Mater.* **2016,** *28,* 1318–1324. doi:10.1021/acs.chemmater.5b04178

85. Fu, G.; Xu, G.; Chen, S.; Lei, L.; Zhang, M. *Catal. Commun.* **2013,** *40,* 120–124. doi:10.1016/j.catcom.2013.06.013

86. Chang, C.; Zhu, L.; Wang, S.; Chu, X.; Yue, L. *ACS Appl. Mater. Interfaces* **2014,** *6,* 5083–5093. doi:10.1021/am5002597

87. Fu, J.; Tian, Y.; Chang, B.; Xi, F.; Dong, X. *J. Mater. Chem.* **2012,** *22,* 21159–21166. doi:10.1039/C2JM34778D

88. Dong, F.; Wu, L.; Sun, Y.; Fu, M.; Wu, Z.; Lee, S. C. *J. Mater. Chem.* **2011,** *21,* 15171–15174. doi:10.1039/C1JM12844B

89. Zhang, G.; Zhang, J.; Zhang, M.; Wang, X. *J. Mater. Chem.* **2012,** *22,* 8083–8091. doi:10.1039/C2JM00097K

90. Xu, J.; Wu, H.-T.; Wang, X.; Xue, B.; Li, Y.-X.; Cao, Y. *Phys. Chem. Chem. Phys.* **2013,** *15,* 4510–4517. doi:10.1039/C3CP44402C

91. Zhu, B.; Xia, P.; Ho, W.; Yu, J. *Appl. Surf. Sci.* **2015,** *344,* 188–195. doi:10.1016/j.apsusc.2015.03.086

92. Xu, J.; Zhang, L.; Shi, R.; Zhu, Y. *J. Mater. Chem. A* **2013,** *1,* 14766–14772. doi:10.1039/C3TA13188B

93. Pan, C.; Xu, J.; Wang, Y.; Li, D.; Zhu, Y. *Adv. Funct. Mater.* **2012,** *22,* 1518–1524. doi:10.1002/adfm.201102306

94. Lee, E. Z.; Jun, Y.-S.; Hong, W. H.; Thomas, A.; Jin, M. M. *Angew. Chem., Int. Ed.* **2010,** *49,* 9706–9710. doi:10.1002/anie.201004975

95. Zheng, Y.; Liu, J.; Liang, J.; Jaroniec, M.; Qiao, S. Z. *Energy Environ. Sci.* **2012,** *5,* 6717–6731. doi:10.1039/C2EE03479D

96. Zou, Z.; Ye, J.; Sayama, K.; Arakawa, H. *Nature* **2001,** *414,* 625–627. doi:10.1038/414625a

97. Yeh, T.-F.; Cihlář, J.; Chang, C.-Y.; Cheng, C.; Teng, H. *Mater. Today* **2013,** *16,* 78–84. doi:10.1016/j.mattod.2013.03.006

98. Kim, H.-i.; Kim, S.; Kang, J.-K.; Choi, W. *J. Catal.* **2014,** *309,* 49–57. doi:10.1016/j.jcat.2013.08.028

99. Nagaraju, G.; Manjunath, K.; Sarkar, S.; Gunter, E.; Teixeira, S. R.; Dupont, J. *Int. J. Hydrogen Energy* **2015,** *40,* 12209–12216. doi:10.1016/j.ijhydene.2015.07.094

100. Khaselev, O.; Turner, J. A. *Science* **1998,** *280,* 425–427. doi:10.1126/science.280.5362.425

101. Youngblood, W. J.; Lee, S.-H. A.; Kobayashi, Y.; Hernandez-Pagan, E. A.; Hoertz, P. G.; Moore, T. A.; Moore, A. L.; Gust, D.; Mallouk, T. E. *J. Am. Chem. Soc.* **2009,** *131,* 926–927. doi:10.1021/ja809108y

102. Xie, G.; Zhang, K.; Guo, B.; Liu, Q.; Fang, L.; Gong, J. R. *Adv. Mater.* **2013,** *25,* 3820–3839. doi:10.1002/adma.201301207

103. Marschall, R. *Adv. Funct. Mater.* **2014,** *24,* 2421–2440. doi:10.1002/adfm.201303214

104. Maeda, K.; Teramura, K.; Lu, D.; Takata, T.; Saito, N.; Inoue, Y.; Domen, K. *Nature* **2006,** *440,* 295. doi:10.1038/440295a

105. Carp, O.; Huisman, C. L.; Reller, A. *Prog. Solid State Chem.* **2004,** *32,* 33–177.

106. Banerjee, S.; Pillai, S. C.; Falaras, P.; O'shea, K. E.; Byrne, J. A.; Dionysiou, D. D. *J. Phys. Chem. Lett.* **2014,** *5,* 2543–2554. doi:10.1021/jz501030x

107. Yeh, T.-F.; Syu, J.-M.; Cheng, C.; Chang, T.-H.; Teng, H. *Adv. Funct. Mater.* **2010,** *20,* 2255–2262. doi:10.1002/adfm.201000274

108. Lahaye, R. J. W. E.; Jeong, H. K.; Park, C. Y.; Lee, Y. H. *Phys. Rev. B* **2009,** *79,* 125435. doi:10.1103/PhysRevB.79.125435

109. Shishkin, M.; Kresse, G. *Phys. Rev. B* **2006,** *74,* 035101. doi:10.1103/PhysRevB.74.035101

110. Shishkin, M.; Kresse, G. *Phys. Rev. B* **2007,** *75,* 235102. doi:10.1103/PhysRevB.75.235102

111. Eda, G.; Mattevi, C.; Yamaguchi, H.; Kim, H.; Chhowalla, M. *J. Phys. Chem. C* **2009,** *113,* 15768–15771. doi:10.1021/jp9051402

112. Yeh, T.-F.; Chan, F.-F.; Hsieh, C.-T.; Teng, H. *J. Phys. Chem. C* **2011,** *115,* 22587–22597. doi:10.1021/jp204856c

113. Yeh, T.-F.; Chen, S.-J.; Yeh, C.-S.; Teng, H. *J. Phys. Chem. C* **2013,** *117,* 6516–6524. doi:10.1021/jp312613r

114. Zong, X.; Yan, H.; Wu, G.; Ma, G.; Wen, F.; Wang, L.; Li, C. *J. Am. Chem. Soc.* **2008,** *130,* 7176–7177. doi:10.1021/ja8007825

115. Yang, J.; Wang, D.; Han, H.; Li, C. *Acc. Chem. Res.* **2013,** *46,* 1900–1909. doi:10.1021/ar300227e

116. Chang, K.; Mei, Z.; Wang, T.; Kang, Q.; Ouyang, S.; Ye, J. *ACS Nano* **2014,** *8,* 7078–7087. doi:10.1021/nn5019945

117. Wang, X.; Zhi, L.; Müllen, K. *Nano Lett.* **2008,** *8,* 323–327. doi:10.1021/nl072838r

118. Ji, S.; Min, B. K.; Kim, S. K.; Myung, S.; Kang, M.; Shin, H.-S.; Song, W.; Heo, J.; Lim, J.; An, K.-S.; Lee, I.-Y.; Lee, S. S. *Appl. Surf. Sci.* **2017,** *419,* 252–258. doi:10.1016/j.apsusc.2017.05.028

119. Khoa, N. T.; Kim, S. W.; Yoo, D.-H.; Cho, S.; Kim, E. J.; Hahn, S. H. *ACS Appl. Mater. Interfaces* **2015,** *7,* 3524–3531. doi:10.1021/acsami.5b00152

120. Song, S. M.; Park, J. K.; Sul, O. J.; Cho, B. J. *Nano Lett.* **2012,** *12,* 3887–3892. doi:10.1021/nl300266p

121. Yang, F.; Lublow, M.; Orthmann, S.; Merschjann, C.; Tyborski, T.; Rusu, M.; Kanis, M.; Thomas, A.; Arrigo, R.; Haevecker, M. *arXiv* **2012,** arXiv:1202.3266.

122. Liu, P.; Sun, Q.; Zhu, F.; Liu, K.; Jiang, K.; Liu, L.; Li, Q.; Fan, S. *Nano Lett.* **2008,** *8,* 647–651. doi:10.1021/nl0730817

123. Peng, T.; Li, K.; Zeng, P.; Zhang, Q.; Zhang, X. *J. Phys. Chem. C* **2012,** *116,* 22720–22726. doi:10.1021/jp306947d

124. Xiang, Q.; Yu, J.; Jaroniec, M. *Nanoscale* **2011,** *3,* 3670–3678. doi:10.1039/C1NR10610D

125. Lv, X.-J.; Zhou, S.-X.; Zhang, C.; Chang, H.-X.; Chen, Y.; Fu, W.-F. *J. Mater. Chem.* **2012,** *22,* 18542–18549. doi:10.1039/C2JM33325B

126. Xiang, Q.; Yu, J.; Jaroniec, M. *J. Am. Chem. Soc.* **2012,** *134,* 6575–6578. doi:10.1021/ja302846n

127. Zhang, P.; Steelant, W.; Kumar, M.; Scholfield, M. *J. Am. Chem. Soc.* **2007,** *129,* 4526. doi:10.1021/ja0700707

128. Yang, M.-Q.; Xu, Y.-J. *J. Phys. Chem. C* **2013,** *117,* 21724–21734. doi:10.1021/jp408400c

129. Du, A.; Ng, Y. H.; Bell, N. J.; Zhu, Z.; Amal, R.; Smith, S. C. *J. Phys. Chem. Lett.* **2011,** *2,* 894–899. doi:10.1021/jz2002698

130. Zhang, Y.; Zhang, N.; Tang, Z.-R.; Xu, Y.-J. *ACS Nano* **2012,** *6,* 9777–9789. doi:10.1021/nn304154s

131. Zeng, P.; Zhang, Q.; Zhang, X.; Peng, T. *J. Alloys Compd.* **2012,** *516,* 85–90. doi:10.1016/j.jallcom.2011.11.140

132. Shen, J.; Shi, M.; Yan, B.; Ma, H.; Li, N.; Ye, M. *Nano Res.* **2011,** *4,* 795. doi:10.1007/s12274-011-0136-7

133. Li, Q.; Guo, B.; Yu, J.; Ran, J.; Zhang, B.; Yan, H.; Gong, J. R. *J. Am. Chem. Soc.* **2011,** *133,* 10878–10884. doi:10.1021/ja2025454

134. Tran, P. D.; Batabyal, S. K.; Pramana, S. S.; Barber, J.; Wong, L. H.; Loo, S. C. J. *Nanoscale* **2012,** *4,* 3875–3878. doi:10.1039/C2NR30881A

135. Min, S.; Lu, G. *J. Phys. Chem. C* **2012,** *116,* 25415–25424. doi:10.1021/jp3093786

136. Khan, Z.; Chetia, T. R.; Vardhaman, A. K.; Barpuzary, D.; Sastri, C. V.; Qureshi, M. *RSC Adv.* **2012,** *2,* 12122–12128. doi:10.1039/C2RA21596A

137. Pei, F.; Liu, Y.; Xu, S.; Lü, J.; Wang, C.; Cao, S. *Int. J. Hydrogen Energy* **2013,** *38,* 2670–2677. doi:10.1016/j.ijhydene.2012.12.045

138. Liu, M.; Li, F.; Sun, Z.; Ma, L.; Xu, L.; Wang, Y. *Chem. Commun.* **2014,** *50,* 11004–11007. doi:10.1039/C4CC04653F

139. Wang, Y.; Yu, J.; Xiao, W.; Li, Q. *J. Mater. Chem. A* **2014,** *2,* 3847–3855. doi:10.1039/C3TA14908K

140. Zhu, B.; Lin, B.; Zhou, Y.; Sun, P.; Yao, Q.; Chen, Y.; Gao, B. *J. Mater. Chem. A* **2014,** *2,* 3819–3827. doi:10.1039/C3TA14819J

141. Singh, G.; Shrestha, K.; Nepal, A.; Klabunde, K. J.; Sorensen, C. M. *Nanotechnology* **2014,** *25,* 265701. doi:10.1088/0957-4484/25/26/265701

142. Li, L.; Yu, L.; Lin, Z.; Yang, G. *ACS Appl. Mater. Interfaces* **2016,** *8,* 8536–8545. doi:10.1021/acsami.6b00966

143. Xu, J.; Wang, L.; Cao, X. *Chem. Eng. J.* **2016,** *283,* 816–825. doi:10.1016/j.cej.2015.08.018

144. Wang, P.; Zhan, S.; Xia, Y.; Ma, S.; Zhou, Q.; Li, Y. *Appl. Catal., B: Environ.* **2017,** *207,* 335–346. doi:10.1016/j.apcatb.2017.02.031

145. Raziq, F.; Qu, Y.; Zhang, X.; Humayun, M.; Wu, J.; Zada, A.; Yu, H.; Sun, X.; Jing, L. *J. Phys. Chem. C* **2016,** *120,* 98–107. doi:10.1021/acs.jpcc.5b10313

146. Hu, B.; Cai, F.; Chen, T.; Fan, M.; Song, C.; Yan, X.; Shi, W. *ACS Appl. Mater. Interfaces* **2015,** *7,* 18247–18256. doi:10.1021/acsami.5b05715

147. Jiang, D.; Li, J.; Xing, C.; Zhang, Z.; Meng, S.; Chen, M. *ACS Appl. Mater. Interfaces* **2015,** *7,* 19234–19242. doi:10.1021/acsami.5b05118

148. Peña, M. A.; Fierro, J. L. G. *Chem. Rev.* **2001,** *101,* 1981–2018. doi:10.1021/cr980129f

149. Tan, H.; Zhao, Z.; Zhu, W.-b.; Coker, E. N.; Li, B.; Zheng, M.; Yu, W.; Fan, H.; Sun, Z. *ACS Appl. Mater. Interfaces* **2014,** *6,* 19184–19190. doi:10.1021/am5051907

150. Liu, Y.; Xie, L.; Li, Y.; Yang, R.; Qu, J.; Li, Y.; Li, X. *J. Power Sources* **2008,** *183,* 701–707. doi:10.1016/j.jpowsour.2008.05.057

151. Chai, S. Y.; Kim, Y. J.; Jung, M. H.; Chakraborty, A. K.; Jung, D.; Lee, W. I. *J. Catal.* **2009,** *262,* 144–149. doi:10.1016/j.jcat.2008.12.020

152. Zhang, X.; Ai, Z.; Jia, F.; Zhang, L. *J. Phys. Chem. C* **2008,** *112,* 747–753. doi:10.1021/jp077471t

153. Jiang, D.; Chen, L.; Zhu, J.; Chen, M.; Shi, W.; Xie, J. *Dalton Trans.* **2013,** *42,* 15726–15734. doi:10.1039/C3DT52008K

154. Sun, Y.; Zhang, W.; Xiong, T.; Zhao, Z.; Dong, F.; Wang, R.; Ho, W.-K. *J. Colloid Interface Sci.* **2014,** *418,* 317–323. doi:10.1016/j.jcis.2013.12.037

155. Subramanian, V.; Wolf, E. E.; Kamat, P. V. *J. Am. Chem. Soc.* **2004,** *126,* 4943–4950. doi:10.1021/ja0315199

156. Clavero, C. *Nat. Photonics* **2014,** *8,* 95–103. doi:10.1038/nphoton.2013.238

157. Hayakawa, K.; Yoshimura, T.; Esumi, K. *Langmuir* **2003,** *19,* 5517–5521. doi:10.1021/la034339l

158. Jain, P. K.; Huang, X.; El-Sayed, I. H.; El-Sayed, M. A. *Acc. Chem. Res.* **2008,** *41,* 1578–1586. doi:10.1021/ar7002804

159. Conway, B. E. *J. Electrochem. Soc.* **1991,** *138,* 1539–1548. doi:10.1149/1.2085829

160. Samanta, S.; Martha, S.; Parida, K. *ChemCatChem* **2014,** *6,* 1453–1462. doi:10.1002/cctc.201300949

161. Bai, X.; Zong, R.; Li, C.; Liu, D.; Liu, Y.; Zhu, Y. *Appl. Catal., B: Environ.* **2014,** *147,* 82–91. doi:10.1016/j.apcatb.2013.08.007

162. Zhao, Y.; Zhang, J.; Qu, L. *ChemNanoMat* **2015,** *1,* 298–318. doi:10.1002/cnma.201500060

163. Xiang, Q.; Yu, J.; Jaroniec, M. *J. Phys. Chem. C* **2011,** *115,* 7355–7363. doi:10.1021/jp200953k

164. Dong, F.; Zhao, Z.; Xiong, T.; Ni, Z.; Zhang, W.; Sun, Y.; Ho, W.-K. *ACS Appl. Mater. Interfaces* **2013,** *5,* 11392–11401. doi:10.1021/am403653a

165. Kang, H. W.; Lim, S. N.; Song, D.; Park, S. B. *Int. J. Hydrogen Energy* **2012,** *37,* 11602–11610. doi:10.1016/j.ijhydene.2012.05.020

166. Hong, J.; Wang, Y.; Wang, Y.; Zhang, W.; Xu, R. *ChemSusChem* **2013,** *6,* 2263–2268. doi:10.1002/cssc.201300647

167. Hou, Y.; Laursen, A. B.; Zhang, J.; Zhang, G.; Zhu, Y.; Wang, X.; Dahl, S.; Chorkendorff, I. *Angew. Chem., Int. Ed.* **2013,** *52,* 3621–3625. doi:10.1002/anie.201210294

168. Zhang, J.; Wang, Y.; Jin, J.; Zhang, J.; Lin, Z.; Huang, F.; Yu, J. *ACS Appl. Mater. Interfaces* **2013,** *5,* 10317–10324. doi:10.1021/am403327g

169. Chen, J.; Shen, S.; Guo, P.; Wang, M.; Wu, P.; Wang, X.; Guo, L. *Appl. Catal., B: Environ.* **2014,** *152–153,* 335–341. doi:10.1016/j.apcatb.2014.01.047

170. Zang, Y.; Li, L.; Li, X.; Lin, R.; Li, G. *Chem. Eng. J.* **2014,** *246,* 277–286. doi:10.1016/j.cej.2014.02.068

171. Han, C.; Wang, Y.; Lei, Y.; Wang, B.; Wu, N.; Shi, Q.; Li, Q. *Nano Res.* **2015,** *8,* 1199–1209. doi:10.1007/s12274-014-0600-2

172. Chen, W.; Liu, T.-Y.; Huang, T.; Liu, X.-H.; Duan, G.-R.; Yang, X.-J.; Chen, S.-M. *RSC Adv.* **2015,** *5,* 101214–101220. doi:10.1039/C5RA18302B

173. Zheng, D.; Zhang, G.; Wang, X. *Appl. Catal., B: Environ.* **2015,** *179,* 479–488. doi:10.1016/j.apcatb.2015.05.060

174. Zheng, D.; Pang, C.; Wang, X. *Chem. Commun.* **2015,** *51,* 17467–17470. doi:10.1039/C5CC07867A

175. Chen, J.; Shen, S.; Wu, P.; Guo, L. *Green Chem.* **2015,** *17,* 509–517. doi:10.1039/C4GC01683A

176. Chen, J.; Zhao, D.; Diao, Z.; Wang, M.; Guo, L.; Shen, S. *ACS Appl. Mater. Interfaces* **2015,** *7,* 18843–18848. doi:10.1021/acsami.5b05714

177. Jiang, Z.; Zhu, C.; Wan, W.; Qian, K.; Xie, J. *J. Mater. Chem. A* **2016,** *4,* 1806–1818. doi:10.1039/C5TA09919F

178. Jiang, Y.; Guo, S.; Hao, R.; Luan, Y.; Huang, Y.; Wu, F.; Tian, C.; Jiang, B. *CrystEngComm* **2016,** *18,* 6875–6880. doi:10.1039/C6CE01442A

179. Yue, X.; Yi, S.; Wang, R.; Zhang, Z.; Qiu, S. *Sci. Rep.* **2016,** *6,* No. 22268. doi:10.1038/srep22268

180. Jiang, Z.; Qian, K.; Zhu, C.; Sun, H.; Wan, W.; Xie, J.; Li, H.; Wong, P. K.; Yuan, S. *Appl. Catal., B: Environ.* **2017,** *210,* 194–204. doi:10.1016/j.apcatb.2017.03.069

181. Thaweesak, S.; Lyu, M.; Peerakiatkhajohn, P.; Butburee, T.; Luo, B.; Chen, H.; Wang, L. *Appl. Catal., B: Environ.* **2017,** *202,* 184–190. doi:10.1016/j.apcatb.2016.09.022

182. Hoffmann, M. R.; Martin, S. T.; Choi, W.; Bahnemann, D. W. *Chem. Rev.* **1995,** *95,* 69–96. doi:10.1021/cr00033a004

183. Chong, M. N.; Jin, B.; Chow, C. W. K.; Saint, C. *Water Res.* **2010,** *44,* 2997–3027. doi:10.1016/j.watres.2010.02.039

184. Chabot, V.; Higgins, D.; Yu, A.; Xiao, X.; Chen, Z.; Zhang, J. *Energy Environ. Sci.* **2014,** *7,* 1564–1596. doi:10.1039/C3EE43385D

185. Li, J.; Liu, X.; Pan, L.; Qin, W.; Chen, T.; Sun, Z. *RSC Adv.* **2014,** *4,* 9647–9651. doi:10.1039/C3RA46956E

186. Ding, Y.; Zhou, Y.; Nie, W.; Chen, P. *Appl. Surf. Sci.* **2015,** *357,* 1606–1612. doi:10.1016/j.apsusc.2015.10.030

187. Ye, A.; Fan, W.; Zhang, Q.; Deng, W.; Wang, Y. *Catal. Sci. Technol.* **2012,** *2,* 969–978. doi:10.1039/C2CY20027A

188. Bai, X.; Wang, L.; Zhu, Y. *ACS Catal.* **2012,** *2,* 2769–2778. doi:10.1021/cs3005852

189. Li, B.; Cao, H. *J. Mater. Chem.* **2011,** *21,* 3346–3349. doi:10.1039/C0JM03253K

190. Zhang, J.; Xiong, Z.; Zhao, X. S. *J. Mater. Chem.* **2011,** *21,* 3634–3640. doi:10.1039/C0JM03827J

191. Kumar, S.; Sharma, V.; Bhattacharyya, K.; Krishnan, V. *New J. Chem.* **2016,** *40,* 5185–5197. doi:10.1039/C5NJ03595C

192. Kumar, S.; Sharma, R.; Sharma, V.; Harith, G.; Sivakumar, V.; Krishnan, V. *Beilstein J. Nanotechnol.* **2016,** *7,* 1684–1697. doi:10.3762/bjnano.7.161

193. Chen, C.; Cai, W.; Long, M.; Zhou, B.; Wu, Y.; Wu, D.; Feng, Y. *ACS Nano* **2010,** *4,* 6425–6432. doi:10.1021/nn102130m

194. Kamegawa, T.; Yamahana, D.; Yamashita, H. *J. Phys. Chem. C* **2010,** *114,* 15049–15053. doi:10.1021/jp105526d

195. Lv, T.; Pan, L.; Liu, X.; Lu, T.; Zhu, G.; Sun, Z. *J. Alloys Compd.* **2011,** *509,* 10086–10091. doi:10.1016/j.jallcom.2011.08.045

196. Zhu, M.; Chen, P.; Liu, M. *ACS Nano* **2011,** *5,* 4529–4536. doi:10.1021/nn200088x

197. Fu, Y.; Wang, X. *Ind. Eng. Chem. Res.* **2011,** *50,* 7210–7218. doi:10.1021/ie200162a

198. Zhou, K.; Zhu, Y.; Yang, X.; Jiang, X.; Li, C. *New J. Chem.* **2011,** *35,* 353–359. doi:10.1039/C0NJ00623H

199. Zhang, X.; Quan, X.; Chen, S.; Yu, H. *Appl. Catal., B: Environ.* **2011,** *105,* 237–242. doi:10.1016/j.apcatb.2011.04.024

200. Gao, E.; Wang, W.; Shang, M.; Xu, J. *Phys. Chem. Chem. Phys.* **2011,** *13,* 2887–2893. doi:10.1039/C0CP01749C

201. Wang, D.; Li, X.; Chen, J.; Tao, X. *Chem. Eng. J.* **2012,** *198–199,* 547–554. doi:10.1016/j.cej.2012.04.062

202. Seema, H.; Kemp, K. C.; Chandra, V.; Kim, K. S. *Nanotechnology* **2012,** *23,* 355705. doi:10.1088/0957-4484/23/35/355705

203. Zhou, X.; Shi, T.; Zhou, H. *Appl. Surf. Sci.* **2012,** *258,* 6204–6211. doi:10.1016/j.apsusc.2012.02.131

204. Anandan, S.; Narasinga Rao, T.; Sathish, M.; Rangappa, D.; Honma, I.; Miyauchi, M. *ACS Appl. Mater. Interfaces* **2012,** *5,* 207–212. doi:10.1021/am302557z

205. Low, W.; Boonamnuayvitaya, V. *J. Environ. Manage.* **2013,** *127,* 142–149. doi:10.1016/j.jenvman.2013.04.029

206. Chen, P.; Su, Y.; Liu, H.; Wang, Y. *ACS Appl. Mater. Interfaces* **2013,** *5,* 12073–12082. doi:10.1021/am403905x

207. Liu, X.; Cong, R.; Cao, L.; Liu, S.; Cui, H. *New J. Chem.* **2014,** *38,* 2362–2367. doi:10.1039/C3NJ01003A

208. Xian, T.; Yang, H.; Huo, Y. S. *Phys. Scr.* **2014,** *89,* 115801. doi:10.1088/0031-8949/89/11/115801

209. Raghavan, N.; Thangavel, S.; Venugopal, G. *Mater. Sci. Semicond. Process.* **2015,** *30,* 321–329. doi:10.1016/j.mssp.2014.09.019

210. Bajorowicz, B.; Reszczyńska, J.; Lisowski, W.; Klimczuk, T.; Winiarski, M.; Słoma, M.; Zaleska-Medynska, A. *RSC Adv.* **2015,** *5,* 91315–91325. doi:10.1039/C5RA18124K

211. Wan, J.; Wei, M.; Hu, Z.; Peng, Z.; Wang, B.; Feng, D.; Shen, Y. *Int. J. Hydrogen Energy* **2016,** *41,* 14692–14703. doi:10.1016/j.ijhydene.2016.07.053

212. Qiu, B.; Deng, Y.; Li, Q.; Shen, B.; Xing, M.; Zhang, J. *J. Phys. Chem. C* **2016,** *120,* 12125–12131. doi:10.1021/acs.jpcc.6b03800

213. Meng, X.; Zhang, Z. *J. Catal.* **2016,** *344,* 616–630. doi:10.1016/j.jcat.2016.10.006

214. Khadgi, N.; Li, Y.; Upreti, A. R.; Zhang, C.; Zhang, W.; Wang, Y.; Wang, D. *Photochem. Photobiol.* **2016,** *92,* 238–246. doi:10.1111/php.12565

215. Meng, X.; Zhang, Z. *Appl. Catal., B: Environ.* **2017,** *209,* 383–393. doi:10.1016/j.apcatb.2017.01.033

216. Li, K.; Zeng, Z.; Yan, L.; Luo, S.; Luo, X.; Huo, M.; Guo, Y. *Appl. Catal., B: Environ.* **2015,** *165,* 428–437. doi:10.1016/j.apcatb.2014.10.039

217. Tian, N.; Huang, H.; Liu, C.; Dong, F.; Zhang, T.; Du, X.; Yu, S.; Zhang, Y. *J. Mater. Chem. A* **2015,** *3,* 17120–17129. doi:10.1039/C5TA03669K

218. Ahn, Y.-H. *Process Biochem. (Oxford, U. K.)* **2006,** *41,* 1709–1721. doi:10.1016/j.procbio.2006.03.033

219. Katsumata, H.; Sakai, T.; Suzuki, T.; Kaneco, S. *Ind. Eng. Chem. Res.* **2014,** *53,* 8018–8025. doi:10.1021/ie5012036

220. Li, Y.; Zhang, H.; Liu, P.; Wang, D.; Li, Y.; Zhao, H. *Small* **2013,** *9,* 3336–3344. doi:10.1002/smll.201203135

221. Chen, Y.; Huang, W.; He, D.; Situ, Y.; Huang, H. *ACS Appl. Mater. Interfaces* **2014,** *6,* 14405–14414. doi:10.1021/am503674e

222. Tong, Z.; Yang, D.; Shi, J.; Nan, Y.; Sun, Y.; Jiang, Z. *ACS Appl. Mater. Interfaces* **2015,** *7,* 25693–25701. doi:10.1021/acsami.5b09503

223. Cheng, N.; Tian, J.; Liu, Q.; Ge, C.; Qusti, A. H.; Asiri, A. M.; Al-Youbi, A. O.; Sun, X. *ACS Appl. Mater. Interfaces* **2013,** *5,* 6815–6819. doi:10.1021/am401802r

224. Tian, Y.; Chang, B.; Lu, J.; Fu, J.; Xi, F.; Dong, X. *ACS Appl. Mater. Interfaces* **2013,** *5,* 7079–7085. doi:10.1021/am4013819

225. Xu, M.; Han, L.; Dong, S. *ACS Appl. Mater. Interfaces* **2013,** *5,* 12533–12540. doi:10.1021/am4038307

226. Yang, Y.; Guo, Y.; Liu, F.; Yuan, X.; Guo, Y.; Zhang, S.; Guo, W.; Huo, M. *Appl. Catal., B: Environ.* **2013,** *142–143,* 828–837. doi:10.1016/j.apcatb.2013.06.026

227. Kumar, S.; Baruah, A.; Tonda, S.; Kumar, B.; Shanker, V.; Sreedhar, B. *Nanoscale* **2014,** *6,* 4830–4842. doi:10.1039/C3NR05271K

228. Chen, D.; Wang, K.; Ren, T.; Ding, H.; Zhu, Y. *Dalton Trans.* **2014,** *43,* 13105–13114. doi:10.1039/C4DT01347F

229. Chen, S.; Hu, Y.; Meng, S.; Fu, X. *Appl. Catal., B: Environ.* **2014,** *150,* 564–573. doi:10.1016/j.apcatb.2013.12.053

230. Aslam, I.; Cao, C.; Tanveer, M.; Khan, W. S.; Tahir, M.; Abid, M.; Idrees, F.; Butt, F. K.; Ali, Z.; Mahmood, N. *New J. Chem.* **2014,** *38,* 5462–5469. doi:10.1039/C4NJ01370K

231. Kumar, S.; Tonda, S.; Baruah, A.; Kumar, B.; Shanker, V. *Dalton Trans.* **2014,** *43,* 16105–16114. doi:10.1039/C4DT01076K

232. Lu, M.; Pei, Z.; Weng, S.; Feng, W.; Fang, Z.; Zheng, Z.; Huang, M.; Liu, P. *Phys. Chem. Chem. Phys.* **2014,** *16,* 21280–21288. doi:10.1039/C4CP02846E

233. Chai, B.; Liao, X.; Song, F.; Zhou, H. *Dalton Trans.* **2014,** *43,* 982–989. doi:10.1039/C3DT52454J

234. Bai, X.; Wang, L.; Wang, Y.; Yao, W.; Zhu, Y. *Appl. Catal., B: Environ.* **2014,** *152–153,* 262–270. doi:10.1016/j.apcatb.2014.01.046

235. Gu, L.; Wang, J.; Zou, Z.; Han, X. *J. Hazard. Mater.* **2014,** *268,* 216–223. doi:10.1016/j.jhazmat.2014.01.021

236. Sun, M.; Yan, Q.; Yan, T.; Li, M.; Wei, D.; Wang, Z.; Wei, Q.; Du, B. *RSC Adv.* **2014,** *4,* 31019–31027. doi:10.1039/C4RA03843F

237. Guo, Y.; Yao, P.; Zhu, D.; Gu, C. *J. Mater. Chem. A* **2015,** *3,* 13189–13192. doi:10.1039/C5TA02262B

238. Pawar, R. C.; Kang, S.; Ahn, S. H.; Lee, C. S. *RSC Adv.* **2015,** *5,* 24281–24292. doi:10.1039/C4RA15560B

239. Li, Y.; Wang, J.; Yang, Y.; Zhang, Y.; He, D.; An, Q.; Cao, G. *J. Hazard. Mater.* **2015,** *292,* 79–89. doi:10.1016/j.jhazmat.2015.03.006

240. Lu, D.; Zhang, G.; Wan, Z. *Appl. Surf. Sci.* **2015,** *358,* 223–230. doi:10.1016/j.apsusc.2015.08.240

241. Li, Y.; Fang, L.; Jin, R.; Yang, Y.; Fang, X.; Xing, Y.; Song, S. *Nanoscale* **2015,** *7,* 758–764. doi:10.1039/C4NR06565D

242. Feng, Y.; Shen, J.; Cai, Q.; Yang, H.; Shen, Q. *New J. Chem.* **2015,** *39,* 1132–1138. doi:10.1039/C4NJ01433B

243. Chen, W.; Liu, T.-Y.; Huang, T.; Liu, X.-H.; Zhu, J.-W.; Duan, G.-R.; Yang, X.-J. *Appl. Surf. Sci.* **2015,** *355,* 379–387. doi:10.1016/j.apsusc.2015.07.111

244. She, X.; Xu, H.; Wang, H.; Xia, J.; Song, Y.; Yan, J.; Xu, Y.; Zhang, Q.; Du, D.; Li, H. *Dalton Trans.* **2015,** *44,* 7021–7031. doi:10.1039/C4DT03793F

245. Liu, X.; Jin, A.; Jia, Y.; Jiang, J.; Hu, N.; Chen, X. *RSC Adv.* **2015,** *5,* 92033–92041. doi:10.1039/C5RA18466E

246. Ye, M.-Y.; Zhao, Z.-H.; Hu, Z.-F.; Liu, L.-Q.; Ji, H.-M.; Shen, Z.-R.; Ma, T.-Y. *Angew. Chem., Int. Ed.* **2017,** *56,* 8407–8411. doi:10.1002/anie.201611127

247. Pant, B.; Park, M.; Lee, J. H.; Kim, H.-Y.; Park, S.-J. *J. Colloid Interface Sci.* **2017,** *496,* 343–352. doi:10.1016/j.jcis.2017.02.012

248. Raza, W.; Bahnemann, D.; Muneer, M. *J. Photochem. Photobiol., A: Chem.* **2017,** *342,* 102–115. doi:10.1016/j.jphotochem.2017.03.036

249. Yao, J.; Chen, H.; Jiang, F.; Jiao, Z.; Jin, M. *J. Colloid Interface Sci.* **2017,** *490,* 154–162. doi:10.1016/j.jcis.2016.11.051

# Oxidative stabilization of polyacrylonitrile nanofibers and carbon nanofibers containing graphene oxide (GO): a spectroscopic and electrochemical study

İlknur Gergin[1], Ezgi Ismar[2] and A. Sezai Sarac[*1,2,3]

## Abstract

In this study, a precursor for carbon nanofibers (CNF) was fabricated via electrospinning and carbonized through a thermal process. Before carbonization, oxidative stabilization should be applied, and the oxidation mechanism also plays an important role during carbonization. Thus, the understanding of the oxidation mechanism is an essential part of the production of CNF. The oxidation process of polyacrylonitrile was studied and nanofiber webs containing graphene oxide (GO) are obtained to improve the electrochemical properties of CNF. Structural and morphological characterizations of the webs are carried out by using attenuated total reflectance Fourier transform infrared spectroscopy and Raman spectroscopy, scanning electron microscopy, atomic force microscopy and transmission electron microscopy. Mechanical tests are performed with a dynamic mechanical analyzer, and thermal studies are conducted by using thermogravimetric analysis. Electrochemical impedance spectroscopy, and cyclic voltammetry are used to investigate capacitive behavior of the products. The proposed equivalent circuit model was consistent with charge-transfer processes taking place at interior pores filled with electrolyte.

## Introduction

Carbon nanofibers are of great interest because of their chemical similarity to fullerenes and carbon nanotubes. Carbon nanofibers (CNF) have promising electrochemical and mechanical properties and a potential for a variety of applications; such as supercapacitor applications, battery applications, and catalyst support materials. Polyacrylonitrile (PAN) is one of the well-known precursor for obtaining carbon nanofibers that have a diameter ranging between nanometers and micrometers and exhibit a high surface area and a high electrical conductivity.

Also, nanofibers can be used with polymeric structures to generate composite materials to improve the electrochemical properties of polymeric structures [1-3]. Nanofiber-reinforced polymeric structures present improved mechanical properties because of the interaction between nanofibers and the matrix material [4]. CNF can be used as reinforcing material inside the polymer composites thanks to their enhanced mechanical and physical properties [5-7]. The manufacturing of CNF/polymer composites is challenging and the manufacturing processes need to be improved to obtain high-performance composite structures [8].

Oxidative stabilization is a crucial heat-treatment process to produce carbon fibers from PAN fibers. PAN chains start to cross-link during this process and the newly composed polymeric structure can endure the rigors of high-temperature processing [9-11]. Oxidative stabilization is crucial to prevent melting or fusion of the fibers. Also, it minimizes volatilization of elemental carbon in the following carbonization step and maximizes the final carbon yield. Chemistry and mechanisms of complex oxidative stabilization reactions for PAN were reported [12]. Oxidative stabilization reactions mainly consist of dehydrogenations and cyclizations, i.e., cyclization of nitrile groups (C≡N) and crosslinking of chain molecules in the form of –C=N–C=N–. Moreover, this stabilization process depends on pyrolysis temperature, heating rate, tension of the fiber, total stabilization time and dwell time, air flow rate and pre-stabilization treatment [13]. Carbonization is the next step in the process. The carbonization processes can be divided into low-temperature and high-temperature carbonization, and graphitization above 2000 °C [14-16]. Carbonization should be conducted under nitrogen environment to prevent burning [17-19]. During the carbonization process, the elimination of other elements ($N_2$, $O_2$, $H_2$) and structural impurities is accelerated and the carbon concentration inside the structure is simultaneously increased.

The most common co-monomers of acrylonitrile in the acrylonitrile copoymers are: vinyl acetate, itaconic acid, methyl metacrylate and acrylic acid [18-20]. Co-monomers are mainly used is to improve the processability of acrylonitrile and to decrease the cyclization temperature [21,22]. For instance, the glass-transition temperature ($T_g$) of PAN homopolymer is reduced by the addition of a co-monomer to form P(AN-*co*-AA), enhancing cyclization reactions and the formation of thermally stable aromatic ladder polymer chains [18]. Acidic co-monomers (itaconic acid and acrylic acid) improve the hydrophilicity of the PAN precursor but also catalyze the cyclization of nitrile groups during the stabilization process by forming a ladder structure. In our previous studies, copolymers of AN have been synthesized by free radical polymerization,

and electrospun nanofibers were obtained with different AN co-polymers as carbon nanofiber precursors [13,18].

Graphene has several desirable features, such as high surface area, high aspect ratio and other properties comparable to those of carbon nanotubes. Thus, graphene attracts attention in science as a new class of material for polymer-based composites [23]. Graphene oxide has been synthesized from graphite with strong acids and oxidants [24,25]. The oxidation level can be adjusted by modifying reaction conditions and systems, and the type of precursor. Moreover, oxygen functional groups increase wettability and capacitance, but not all of the surface oxygen groups have the same effect. For enhancing the capacitance of a supercapacitor, an active electrode material with oxygen functional groups is necessary [24]. Furthermore, the PAN cyclization temperature can be decreased in the presence of graphene oxide. The functional groups of graphene oxide initiate the PAN cyclization at lower temperature via ionic mechanisms. In addition, the performance of an electrochemical capacitor prepared from carbon nanotubes/carbon nanofiber (CNT/CNF) composites is influenced by the oxidation level. Increasing the O/C ratio improves the capacitance of CNT/CNF composites. According to literature, a flexible and free standing composite paper comprising carbon nanofibers and graphene shows a higher specific capacitance than pure carbon nanofibers. Thus, the CNF/graphene combination can be a good candidate for a high-performance flexible capacitor applications [26].

In this paper, graphene oxide was used as an additive to increase the capacitance of oxidized PAN-based nanofibers. Further, GO addition was studied to improve electrochemical properties of CNF webs.

# Experimental
## Materials
Polyacrylonitrile (PAN, $M_w$ 150,000 g/mol) was purchased from Sigma-Aldrich and was used as received. Dimethylformamide (DMF; Sigma-Aldrich), sulfuric acid ($H_2SO_4$, 98%; Sigma-Aldrich), acetonitrile (ACN; Sigma) were chosen as solvents and were used without any further purification. Graphene oxide (GO, purity 99%) was purchased from Grafen Chemical Industries and used as received. The properties of the few-layered GO are: GO consists of a few layers (1–10 layers) and the average thickness of the layer is smaller than 4 nm. The specific surface area of GO is larger than 550 $m^2$/g. GO consists of 68.44 atom % C, 30.92 atom % O and 0.63 atom % S.

For electrospinning, PAN dissolved in DMF and spinning solution was prepared. The solution was fed into a 2 mL syringe and under high voltage (around 15 kV) DMF evaporated and

nanofiber formation was achieved on the collector. Those nanofibers stacked and formed a web. Different collectors were used to fabricate PAN-based nanofiber webs via electrospinning. Before the electrospinning process, GO was also added to the PAN/DMF solution to obtain PAN/GO nanofibers. After electrospinning of the PAN/GO nanofibers, the PAN/GO samples underwent the same heat treatment (oxidation and carbonization) as the PAN nanofibers. Rotating and fixed collectors were used to vary the samples and investigate physical and chemical changes.

Electrospinning solutions were prepared at different PAN/DMF ratios. Electrospinning parameters (e.g., viscosity, voltage, feeding ratio) effect the nanofiber diameter and homogeneity. Lower viscosity helps to produce finer nanofibers, and an increased polymer weight percentage results in higher viscosities. Thus it is one of the significant parameters for electrospinning [27].

In this study, graphene oxide was used as an additive to increase the capacitance of oxidized PAN-based nanofibers. Thus, the nanofibers were produced via electrospinning using a mixture of PAN (10% w/v) and a given amount of GO (at different weight-to-volume percentages) in DMF. The solutions were poured into a 2 mL syringe and delivered at a constant flow rate of 1.0 mL/h (New era, NE-300) to a needle with a blunt tip connected to a high-voltage power supply (Gamma high voltage research) producing a voltage of 15 kV. Aligned nanofibers were deposited on the rotating drum collector at 21.50 Hz rotating frequency at a distance of 15 cm. After producing the nanofibers, oxidative stabilization was performed at 250 °C for 3 h in air atmosphere and carbonization was performed at 900 °C for 1 h under nitrogen atmosphere.

## Characterization

Attenuated total reflectance Fourier transform infrared spectroscopy (ATR-FTIR) and Raman spectroscopy were used to record the characteristic peaks of the oxidized and carbonized nanofibers. Mechanical properties of nanofiber webs were characterized by using a dynamic mechanical analyzer (DMA) (TA Q800 Dynamic Mechanical Analyser).

Thermal behavior of nanofiber webs was examined with thermogravimetric analysis (TGA, Q 50 from TA instruments). The structure of the nanofiber webs was characterized by attenuated total reflectance Fourier transform infrared spectroscopy (ATR-FTIR) (Perkin Elmer, Spectrum One, with a Universal ATR attachment with a diamond and ZnSe crystal). The microstructure of the carbonized nanofiber webs was investigated by Raman spectroscopy (DXR Raman spectrometer, Thermo Scientific, at 532 nm). The sample morphologies were charac-

terized by scanning electron microscopy (Gemini Leo Supra 35 VP) and samples were coated with thin gold film using a sputter coater to prevent the accumulation of charge on their surface.

Electrochemical performances of nanofibers were analyzed by using cyclic voltammetry (CV) and electrochemical impedance spectroscopy (EIS). Electrochemical measurements were performed by using potentiostat 2263 Electrochemical Analyser (Princeton Applied Research, Tennessee, USA). EIS data were simulated with the electrical equivalent circuit by ZSimpWin V.3.10 analysis program (Princeton Applied Research, Tennessee, USA). The surface topography of the fibers was observed by atomic force microscopy (AFM) with Nanosurf EasyScan2$^{TM}$ software. AFM analyses were performed with a non-contact mode by using NCLR-10 model Al-coating silicon tips with 7 μm thickness, 225 μm length, 38 μm width, 190 kHz resonance frequency and 48 N/m force constant. Surface morphology of the nanofibers was observed with scanning electron microscopy (SEM) at Namık Kemal University and transmission electron microscopy (TEM). Fiber diameters were measured within electron micrographs from a population between forty and fifty nanofibers taken from each sample and then the average values were calculated by ImageJ software.

# Results and Discussion
## Oxidative stabilization of PAN nanofibers

Oxidative stabilization is a complex process and should be applied to the webs before carbonization. The mechanism plays an important role in the carbonization. Therefore, a detailed understanding of the mechanism of oxidation has an important part in the success of the production of CNF.

Nanofiber webs are produced with different collectors to achieve fiber alignment. The results for webs of aligned and non-aligned nanofibers are compared. A rotating collector that produces aligned nanofiber webs reduces the nanofiber diameter as shown in SEM images in Figure 1. Non-aligned PAN nanofibers diameter are in the range of 371.6 ± 36 nm; whereas the aligned PAN nanofibers diameter are decreased to 330.8 ± 27 nm. The stress–strain curve obtained by DMA shows that fiber alignment increases the mechanical properties of the web. A directional orientation of the fibers definitely and expectedly has the effect of increasing modulus and reducing the strain to break [18,28,29]. Aligned nanofibers has a greater modulus than non-aligned ones [18,28,30-32]. Also, our previous work [33] exhaustively explains the effects of rotating collector and fixed collector. Rotational movement helps to orient the nanofibers and obtain thinner fibers compared to the fixed collector. Webs of aligned nanofibers present superior mechanical properties in terms of modulus. Figure 2 shows stress–strain plots of aligned and non-aligned PAN nanofibers.
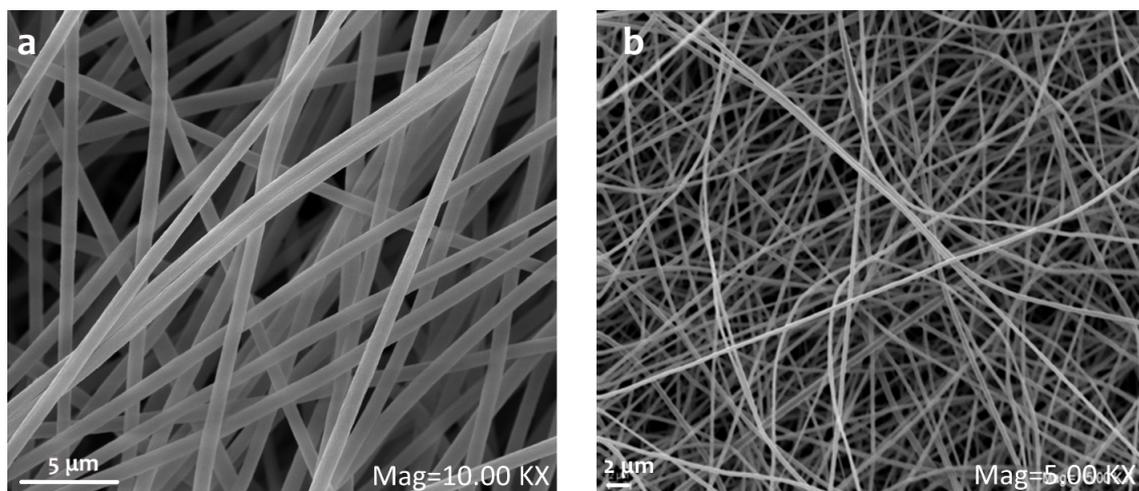
**Figure 1:** a) Web of aligned PAN nanofibers produced with rotating collector and b) web of PAN nanofibers produced with fixed collector.

According to the plots, the elastic modulus of a PAN-nanofiber web increases with fiber orientation from 63 MPa to 159 MPa. Thus, rotating collectors were chosen to obtain nanofibers with better mechanical and morphological properties.
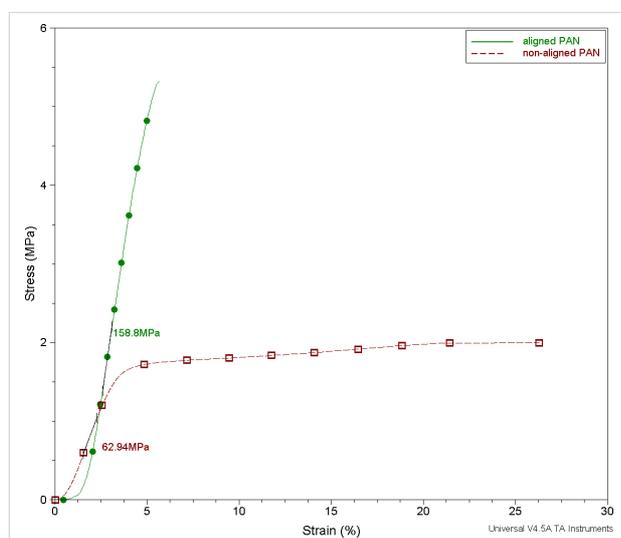


**Figure 2:** Stress–strain plots of webs of aligned and non-aligned PAN nanofibers.

## ATR-FTIR spectroscopy results

The oxidation process including conversions of C≡N bonds to C=N and also dehydrogenation leading to aromatic and supramolecular structures was studied [34]. Structural changes during the oxidation process can be tentatively expressed as in Figure 3, and the oxidation route was explained through cyclization and dehydrogenation reactions. Peaks around 2243 cm$^{-1}$ represent the absorption of C≡N triple bond [17,22,35]. Those

around 1590 cm$^{-1}$ can be assigned to a combined effect of C=N, C=C, N–H groups [12,15,17,35,36], and the broad peak at around 3000 cm$^{-1}$ is connected to C–H bonds [37,38]. ATR-FTIR results are given in Figure 4. The oxidation temperature is too low to eliminate all C≡N triple bonds. This means that cyclization reactions cannot be completed. A schematic description is given in Figure 3. However, the intensity of the C≡N triple bonds is decreased after oxidation [12,36,39]. A weight loss is not observed during the cyclization process, contrary to dehydrogenation [37]. During the dehydrogenation a new peak appears at around 800 cm$^{-1}$ because of the formation of =C−H bonds [38,40,41]. In the presence of oxygen =C−H groups were created during the aromatization by the removal of H atoms in the form of H$_2$O [38]. Also, an increased temperature increases the intensity of the =C−H peak.

The oxidation ratio can be calculated from the absorbance ratio obtained from ATR-FTIR results [12,39,40]. The inset in Figure 4 represents the oxidation ratio as a function of the oxidation temperature by evaluating the ratio between the mixed signals of C=N, C=C, N–H groups and the signal of C≡N triple bonds. At oxidation temperatures of 250 °C and 270 °C, the oxidation ratios are quite close contrary to that of the oxidation at 235 °C. During the oxidation process, C≡N triple bonds are damaged and C=N double bonds are created. Thus the ratios of these peaks from ATR-FTIR can help to calculate the oxidation ratio. GO-containing samples are marked in the inset Figure 4. At 250 °C, the addition of GO to the PAN nanofiber web causes a deviation in the oxidation ratio values compared to pure PAN. GO acts via ionic mechanism in the oxidation step and improves the conversion of C≡N bonds to C=N, C=C and N–H [35,42,43].
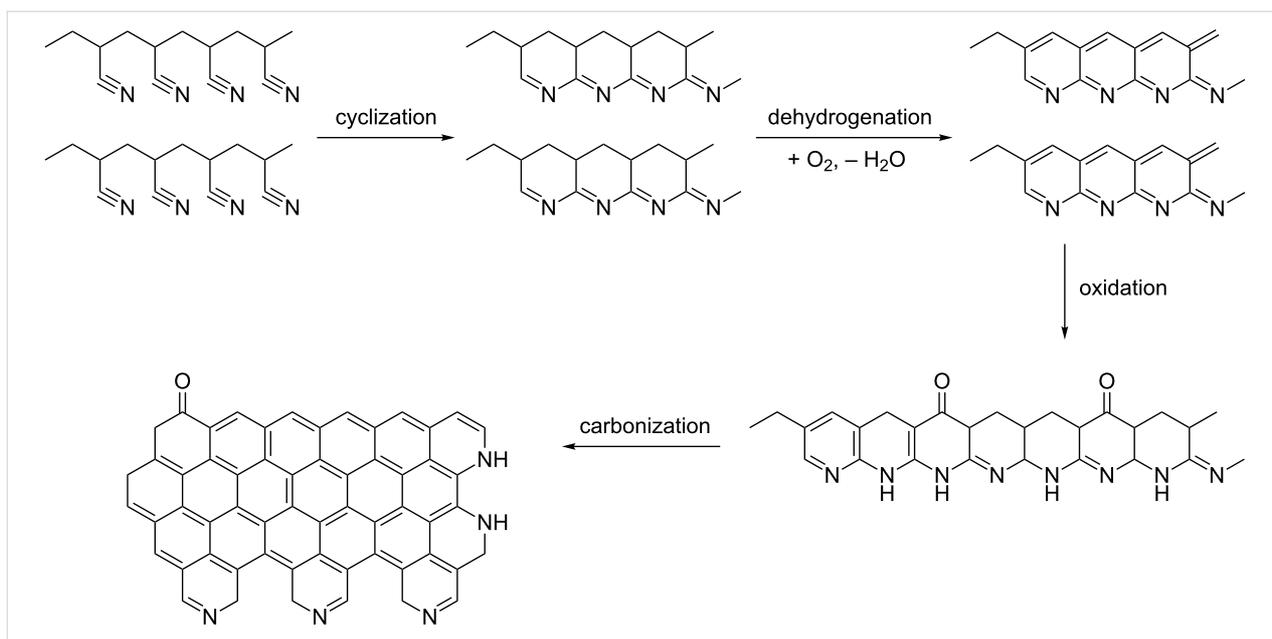
**Figure 3:** Schematic description of carbonization process starting from polyacrylonitrile.
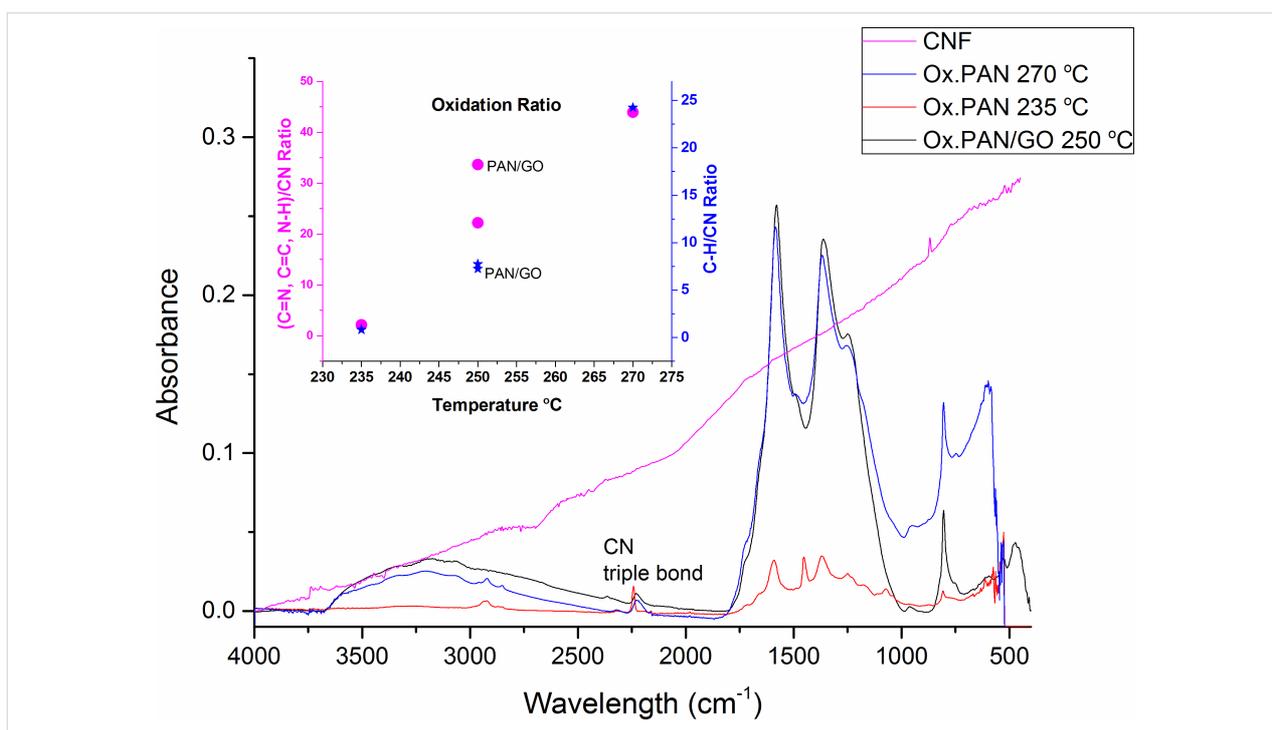


**Figure 4:** ATR-FTIR results of oxidized webs with GO and of the carbon nanofiber web. The inset represents the oxidation ratio of the webs as a function of the temperature according to absorbance ratios of (C=N, C=C, N–H)/C≡N and the newly occurred =C−H/C≡N ratio. (C=N, C=C, N–H) represents the mixture of the corresponding absorbances.

During the stabilization process, the cyclization of the nitrile groups and cross-linking of the chain molecules is followed by dehydrogenation [38]. This reaction promotes the creation of a ladder structure from the linear molecule [36,38,44]. Ladder-

structure polymers are thermally more stable than linear polymers, because the structure prevents them from melting at higher temperatures [38,45]. Weight loss starts at around 100 °C with the removal of moisture and continues with in-

creasing duration and temperature. However, it is not much significant for the oxidation process [12,18,46]. Weight loss as a function of temperature and time was recorded with TGA. There is a region in which there is no weight loss, and this region can be explained by cyclization reactions [37]. Both TGA curves (in $N_2$ and in $O_2$ atmosphere) exhibit the same trend. However, the region with no weight loss is shifted in $N_2$ atmosphere because of $N_2$ suppresses the reactions compared to $O_2$, according to TGA measurements, the PAN polymer stays stable up to ca. 300 °C. This stable phase can be explained by cyclization reactions [37]. Above this temperature, weight loss begins to increase because of the dehydrogenation reactions [37,38]. In $O_2$ atmosphere, weight loss starts above 100 °C, after a stable cyclization phase, dehydrogenation in $O_2$ atmosphere is observed between 100 and 140 °C. In $N_2$ atmosphere this temperature shifts to 300–400 °C. The reaction propagation is faster under $O_2$ atmosphere compared to $N_2$.

The same conditions as in the oxidation procedure were applied during TGA. A 5 °C/min ramp was applied till the samples reached the desired oxidation temperature (235, 250, 270 and 300 °C). After the samples reached the oxidation temperature TGA was carried out for further 300 minutes. It can be seen from the TGA curves that the 300 °C/300 min oxidation process shows the highest weight loss. For the TGA measurement of nanofiber webs in oxygen environment the curves are similar to those of the PAN polymer. However, the temperature ranges are shifted because of the presence of oxygen. In the presence of reactive atmospheres, such as air or oxygen, the oxidation process is faster at lower temperatures [47]. At temperatures above 100 °C weight loss was recorded. A sudden reduction of weight was recorded during dehydrogenation reactions in which hydrogen and oxygen formed $H_2O$, which was released from the structure [37,38]. Figure 5 shows that at for the oxidation temperature of 300 °C a weight loss of around 14.5% is observed after 300 min. During the 300 min of oxidation, the weight loss varies between 4.9% and 14.5%, for increased temperatures (235, 250 and 270 °C). For 300 °C the weight loss is recorded as 14.5%. The energy applied to the sample depends on temperature and duration. Together they promote bond breakage, thus the weight loss of the samples increases with temperature. Also, using a co-polymer instead of a homopolymer can strengthen the fiber structure and lead to a higher heat stability [13,18]. A dramatic weight loss (around 45%) is recorded during the low-temperature carbonization process with increasing elimination of other elements (N,H,O) [38,48].
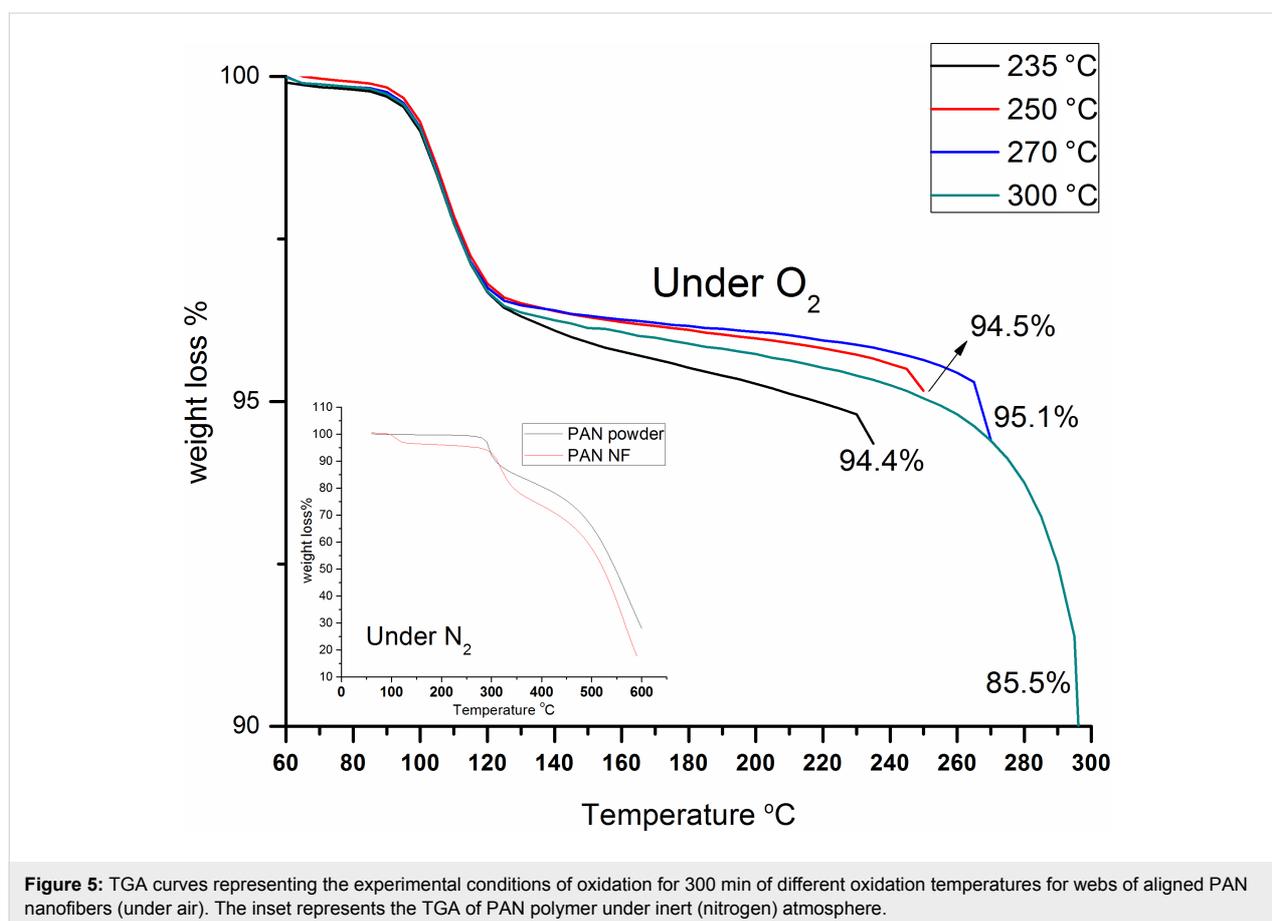


**Figure 5:** TGA curves representing the experimental conditions of oxidation for 300 min of different oxidation temperatures for webs of aligned PAN nanofibers (under air). The inset represents the TGA of PAN polymer under inert (nitrogen) atmosphere.

# Electrochemical impedance measurements of oxidized PAN nanofibers

Electrochemical properties of oxidized PAN nanofibers were analyzed by using electrochemical impedance spectroscopy (EIS). EIS measurements were performed in 0.5 M $H_2SO_4$ electrolyte in the frequency range of 100 mHz to 100 kHz at open circuit potential with an AC perturbation of 10 mV. A standard three-electrode cell was used to study the electrochemical performances of PAN nanofibers which were stabilized at 250 °C for 1 h in air. Oxidized PAN nanofiber mats were used as free standing working electrodes, a platinum wire was used as counter electrode, and a silver wire was used as pseudo-reference electrode. EIS data were simulated with electrical equivalent circuit by using the ZSimpWin V.3.10 analysis program.

Experimental and calculated measurements were fitted by equivalent circuit modelling. EIS plots with measured and calculated data are shown in Figure 6. An excellent agreement between experimental results and simulation was found with $\chi^2 \approx 5 \cdot 10^{-4}$ ($\chi^2$ is function defined as the sum of the squares of the residuals). $R_s$ is the ohmic resistance of the solution, $R_{ct}$ represents the charge-transfer resistance between nanofiber electrodes and electrolyte interface and $Q_{dl}$ (constant phase element (CPE)) is the double-layer CPE, a frequency-dependent element.

The Nyquist plot in Figure 6a consists of a semicircle related to the electron-transfer process. The charge-transfer resistance ($R_{ct}$) can be calculated from measuring the diameter of the semicircle. According to the Bode phase plot in Figure 6b, the phase angle of the sample was 10° around 80 Hz. In the Bode magnitude plot, the absolute values of impedance are plotted as a function of the frequency. The impedance values between low-frequency region and high-frequency region do not change drastically compared to the GO-containing PAN nanofibers (see below in Figure 14). Addition of GO to PAN nanofibers changes the homogeneity of the electrode. Thus, the penetration of electrolyte ions penetration varies with frequency.

The values of $R_s$, $R_{ct}$ and $Q_{dl}$ were determined as 552 Ω, 340 Ω and $2 \cdot 10^{-2}$ μS·s$^n$ according to the Randles circuit model for non-ideal electrodes described as $R_s(Q_{dl}R_{ct})$ in short hand. The CPE ($Q_{dl}$) can also be attributed to the double-layer capacitance ($C_{dl}$) in the non-homogeneous systems [49]. Double-layer capacitance occurs at the electrode/electrolyte interface of materials with especially high surface area. The electrical charge is stored based on the separation of charged species in an electrolytic double layer across the interface of electrode/solution. This capacitance value is proportional to the surface area of the electrode and inversely proportional to the thickness of the double layer [50].

The impedance of the non-ideal electrode is defined by

$$Z_{CPE} = T_{CPE} \left( j\omega \right)^{-n},\qquad(1)$$

where $j$ is the imaginary unit $\sqrt{-1}$, $\omega$ is the angular frequency, and $T_{CPE}$ and $n$ are frequency-independent experimental constants; $T_{CPE}$ relates to the size, thickness, and materials properties, while $n$ relates to the degree of energy dissipation and measures the arc depression, which is frequency-independent. Moreover, $n$ is a parameter describing the deviation from an ideal capacitor and arises from the slope of the log $Z$ versus log $f$ plot. The values for $n$ vary from 0 to 1, and $n = 1$ describes an ideal capacitor, while $n = 0$ describes the behavior of a resistor. The $n$ value of oxidized PAN was equal to 0.83.



**Figure 6:** a) Nyquist plots of webs of oxidized PAN nanofibers. Inset: Randles circuit model. b) Bode magnitude and Bode phase plots of PAN nanofiber webs.
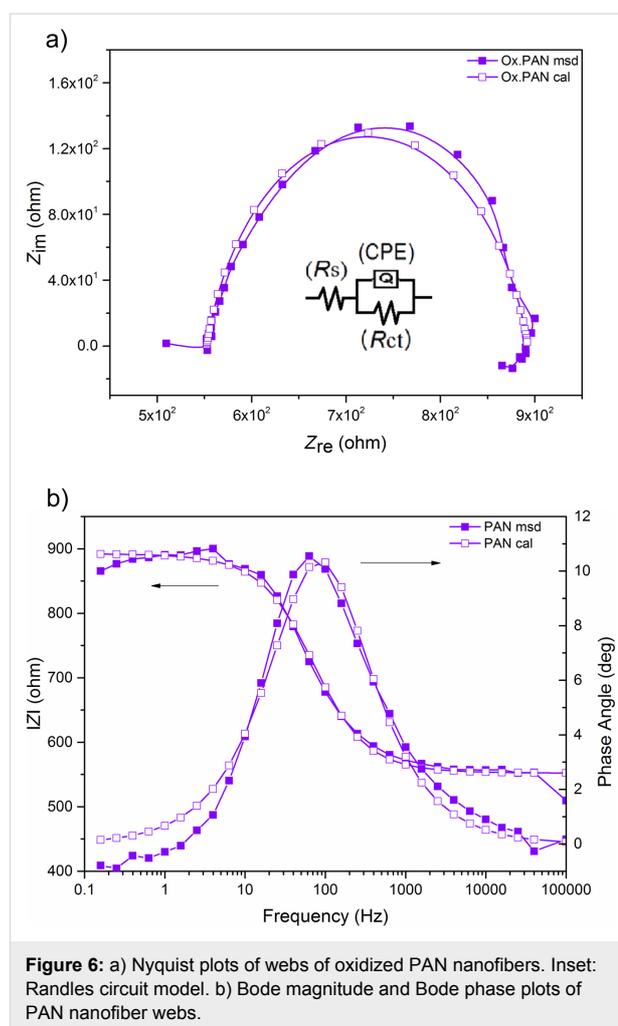
# Oxidative stabilization of PAN/GO nanofibers and CNF

The Raman spectroscopic measurements show characteristic peaks of carbon materials, namely D band and G band at around

1360 cm$^{-1}$ and 1580–1600 cm$^{-1}$, respectively [51,52] (Figure 7). Oxidation and carbonization contributed to the conversion of PAN fibers into a graphitic form via fraction of disordered sp$^2$-hybridized C–C bonds [53]. The ratio of the D and G bands provides an information about the crystallinity of the carbonaceous material [52,54]. The G band (1590 cm$^{-1}$) represents ordered graphitic crystallites [52], while the D band around 1350 cm$^{-1}$ is related to disordered turbostratic structures [55]. The measured intensity ratio between D band and G band ($R = I_D/I_G$) indicates structurally ordered graphite crystallites [30,54]. The $R$ value of CNF is around 0.9. A lower $R$ value means a more crystalline material with higher conductivity [56]. Position and intensity of D and G band demonstrate the electronic structure and electron–phonon interactions of the material [51].
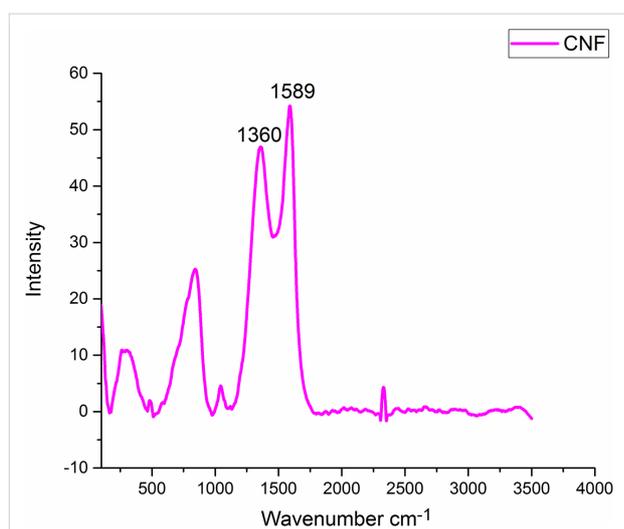


**Figure 7:** Raman spectrum of carbon nanofiber webs.

## ATR-FTIR spectroscopy of oxidized PAN/GO nanofibers

The ATR-FTIR results show a broad OH stretching peak of GO around 3300 cm$^{-1}$ [57] and the C–H vibrations of the CH, CH$_2$ and CH$_3$ structures of oxidized polyacrylonitrile around 2920 cm$^{-1}$ [38,40]. Through the carbonization process most of the bonds are damaged and eliminated. The ladder structure of carbon atoms becomes more dominant and it is not always possible to follow further structural changes of carbonaceous materials with FTIR. Also, ATR-FTIR results of carbonized nanofibers (Figure 4) are not clear not only because of the changing bond structure of PAN but also because of the black color of the carbon nanofiber webs. A photo of GO-containing PAN-based electrospun, oxidized and carbonized nanofibers are shown in Figure 8. The colors of the nanofibers change from white to brown after oxidation and then from brown to black after carbonization.
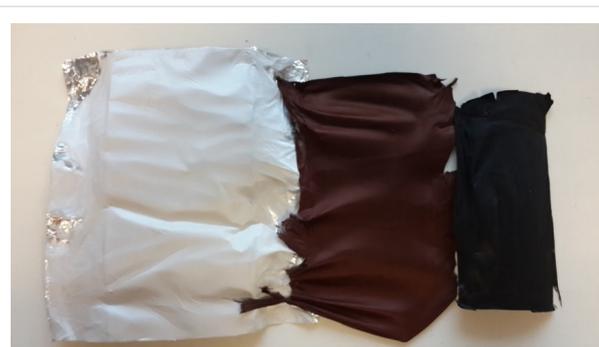


**Figure 8:** GO-containing PAN-based electrospun, oxidized and carbonized nanofibers.

## Morphologic studies

The surface of the nanofibers is not smooth and has pores, which can be related to graphene oxide content. This can be seen very clearly from the AFM, SEM and TEM images in Figure 9, Figure 10 and Figure 11. AFM was performed to observe the topography of nanofibers. Oxidized PAN nanofibers formed with GO nanosheets can be seen in AFM image (Figure 9). The nanofibers have rough surfaces with flaky shapes attributed to GO. The morphology of GO is also shown in Figure 10a. Layers of GO can be seen in the SEM image. Also, some layer edges of GO and the interspaces of the layers can be observed in the SEM image. GO-containing electrospun nanofibers are seen in Figure 10b,c. GO nanosheets that are formed with PAN nanofibers are observed on the structure in Figure 10b. A rough surface with a kind of joints is presented in the image. Distance between two nodes in the structure is around 50 nm calculated by ImageJ Software.
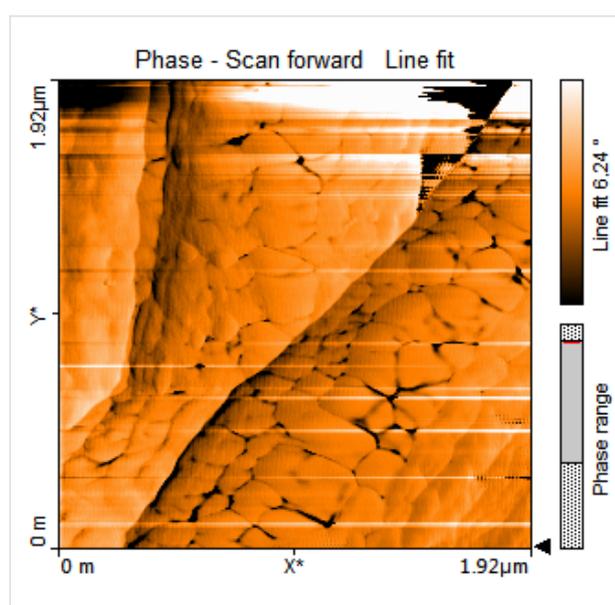


**Figure 9:** AFM image of GO-containing oxidized PAN nanofiber webs.
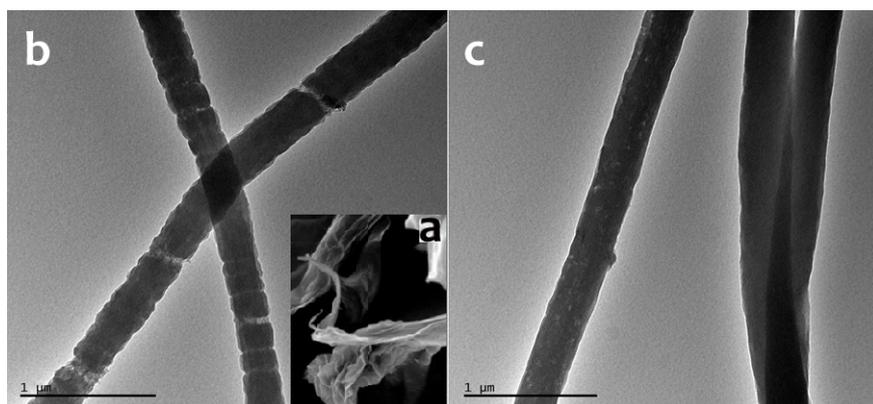
**Figure 10:** a) SEM image of GO; b) TEM images of GO-containing PAN nanofibers; c) carbon nanofibers.
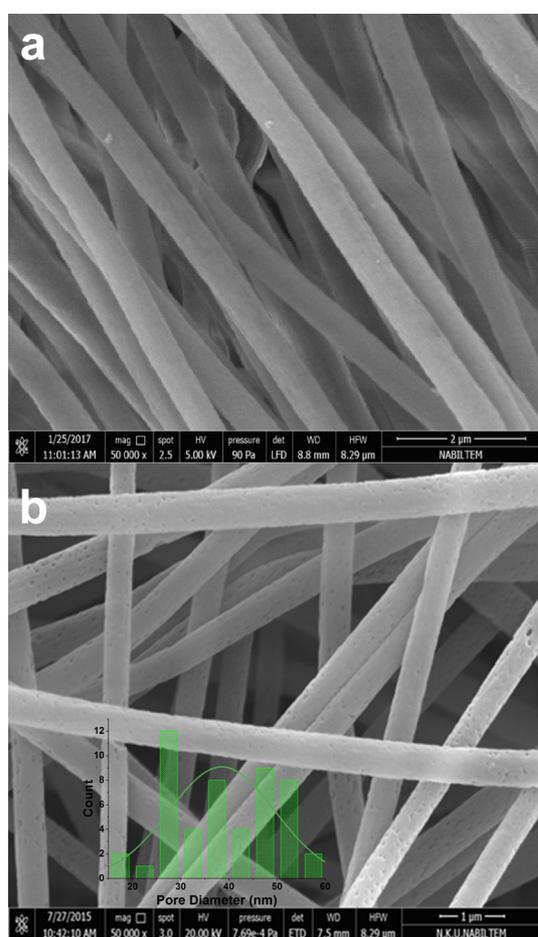


**Figure 11:** SEM images of (a) oxidized PAN nanofiber webs and (b) GO-containing oxidized PAN nanofiber webs with pore distribution chart.

The morphology of PAN nanofibers with smooth surfaces is presented in Figure 1 and Figure 11a for comparison with GO-containing PAN nanofibers. When GO is included into PAN nanofibers rough surface can be seen. Furthermore, the porous structure of carbon nanofibers with GO is shown in Figure 10b,c. Figure 11b represents the porous surface of oxidized PAN/GO nanofibers and a pore distribution chart was added on the SEM image. It can be seen from Figure 11 that addition of GO makes the nanofiber surface porous and these pores are well distributed on the fibers. The morphological property of the porous carbon electrodes such as the surface and pore size distributions are the factor that influences the double-layer capacitance. Therefore, the pore size distribution of porous carbons also affect the performance of carbon-based electrochemical capacitors [58].

According to SEM images (Figure 11b) pore size on the nanofibers were measured as $38.5 \pm 11$ nm. All morphologic characterizations prove the porous structure of GO containing nanofibers.

In supercapacitors that use nanoporous electrodes to store large amounts of charge, ions penetrate into the pores of the electrode. Raymundo-Piñero et al. considered that an adequate pore size is more important than a high surface area and reported optimum pore sizes as 0.7 nm and 0.8 nm in aqueous and organic media, respectively [59]. Graphene oxide shows a high specific capacitance because of layered graphene sheets [24].

## Electrochemical impedance studies of PAN and GO-containing PAN-based nanofibers

A standard three-electrode cell was used to study electrochemical performances of nanofibers by using cyclic voltammetry (CV) and electrochemical impedance spectroscopy (EIS). Carbonized nanofibers were used as free standing electrodes whereas oxidized nanofibers were deposited on fluorine-doped tin oxide (FTO) glass to use as working electrodes. EIS analysis were investigated in 0.1 M $NaClO_4$/ACN electrolyte in a fre-
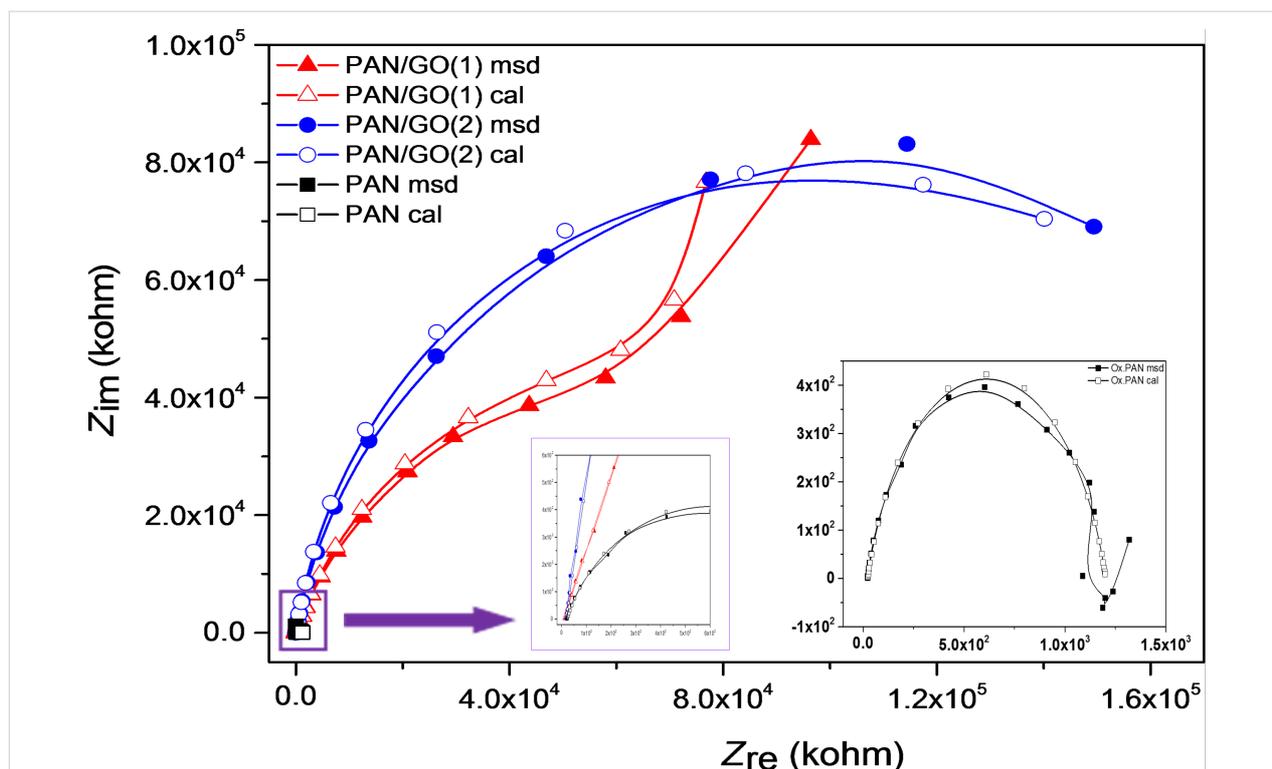
**Figure 12:** Nyquist plots of oxidized PAN and GO-containing oxidized PAN nanofiber webs (inset: Nyquist plots of oxidized nanofiber webs at high frequencies and Ox.PAN nanofiber webs up to 100 kHz).

quency range of 10 mHz to 100 kHz at open circuit potential with an AC perturbation of 10 mV. The samples of oxidized nanofibers are designated as Ox.PAN, Ox.PAN/GO(1) and Ox.PAN/GO(2) indicating concentration of 0, 1.25 and 2.5% graphene oxide relative to PAN, respectively.

Nyquist plots in Figure 12 represent a semicircle in the high to medium frequency range. The inclined line corresponding to diffusion processes at low frequencies region appears only in PAN/GO(1). The charge-transfer resistances ($R_{ct}$) were evaluated by using equivalent circuit modelling. $R_{ct}$ is attributed to the pore size of the electrodes. The values of $R_{ct}$ of Ox.PAN, Ox.PAN/GO(1) and Ox.PAN/GO(2) were equal to 1180 k$\Omega$, 119700 k$\Omega$ and 182800 k$\Omega$, respectively, $R_{ct}$ increases with GO content.

According to the Bode phase plots, the sample of Ox.PAN/GO(1) and Ox.PAN/GO(2) show similar properties while Ox.PAN behaves differently (Figure 13). After adding GO to the nanofibers the phase angle increases linearly and exhibits larger plateau regions. This indicates the capacitive behavior.

The Bode magnitude plots exhibit two different shapes for high and low frequencies (Figure 14). At high frequencies, the impedance values of Ox.PAN and Ox.PAN/GO nanofibers do
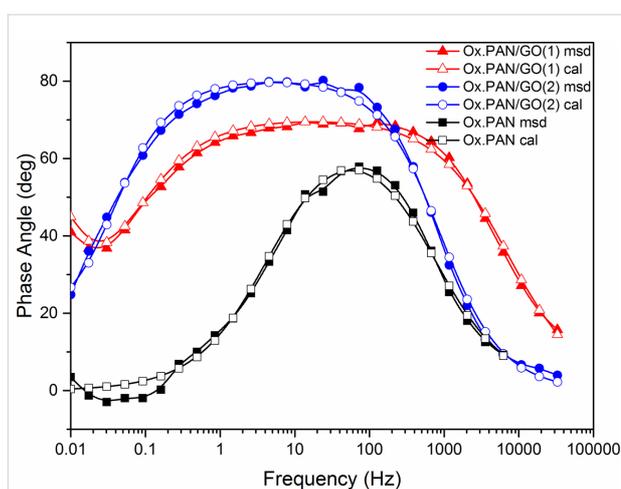


**Figure 13:** Bode phase plots of oxidized PAN nanofiber webs and GO-containing oxidized PAN nanofiber webs.

not change significantly and this is attributed to the disability of the electrolyte ions to penetrate into the electrode. The solution resistance ($R_s$) of the electrochemical system changes very slightly, which can be seen in Table 1. On the other hand, the impedance of Ox.PAN/GO nanofibers is very high due to the penetration of ions into the electrode surfaces at low frequencies [24].

**Table 1:** Fitting values for the equivalent circuit elements by simulation of the impedance spectra of oxidized nanofibers.

| sample | $R_s$ (kΩ) | $Q_{el}$ (CPE) (µS·s$^n$) | $n$ | $C_{dl}$ (µF) | $R_{ct}$ (kΩ) | $\chi^2$ ($10^{-3}$) |
|---|---|---|---|---|---|---|
| Ox.PAN[a] | 21.80 | 0.060 | 0.79 | — | 1180 | 5.54 |
| Ox.PAN/GO(1) | 9.55 | 0.024 | 0.78 | 0.190 | 119700 | 4.72 |
| Ox.PAN/GO(2) | 17.05 | 0.025 | 0.90 | 0.600 | 182800 | 3.99 |

[a]An $R_s(Q_{el}R_{ct})$ equivalent circuit model has shown a better correlation with this sample.
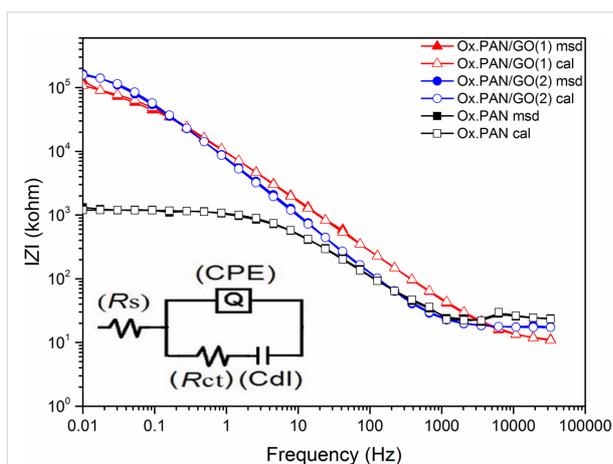


**Figure 14:** Bode magnitude plots of oxidized PAN nanofiber webs and GO-containing oxidized PAN nanofiber webs (inset shows the electrochemical equivalent circuit).

The parameters of the simulated equivalent circuit models obtained from the Nyquist and Bode phase plots are given in Table 1. Fitting with equivalent circuit modelling exhibited a good correlation between the calculated and experimental values with $\chi^2$ values around $10^{-3}$. The result shows two different models. $R_s(Q_{el}R_{ct})$ circuit modeling was compatible with Ox.PAN, while a $R_s(Q_{el}(R_{ct}C_{dl}))$ circuit modelling was chosen for Ox.PAN/GO(1) and Ox.PAN/GO(2).

$R_s$ corresponds to the solution resistance, $R_{ct}$ corresponds to the charge-transfer resistance of electrode surface and solution interface, and $Q_{el}$ corresponds to the combined capacitance of nanofibers and FTO glass electrode. $R_{ct}$ and $C_{dl}$ change linearly with the amount of GO and the values of $n$ of Ox.PAN and Ox.PAN/GO(1) are is very similar (Table 1). After increasing the GO content in the nanofibers, the value of $n$ increases and exhibits nearly ideal capacitive behavior for Ox.PAN/GO(2). The $C_{dl}$ value of Ox.PAN/GO(2) is 3.16 times higher than that of Ox.PAN/GO(1). A CPE is generally used in heterogeneous systems associated with non-ideal capacitive behavior resulting from electrode roughness, inhomogeneous conductivity, or even diffusion [60]. CPE is also related to the composition of the nanofibers. The proposed model is consistent with charge-

transfer processes taking place at interior pores filled with electrolyte.

Heat treatment was applied to Ox.PAN and Ox.PAN/GO nanofibers to produce carbon nanofibers (CNF) and GO-containing carbon nanofibers (CNF/GO). CNF and CNF/GO, which include very small amount of graphene oxide (1.25% relative to PAN) were used as free standing working electrodes during CV. Figure 15 shows the CV of CNF and CNF/GO electrodes at a scan rate of 50 mV·s$^{-1}$ between −0.5 V and 1.2 V in 0.1 M NaClO$_4$/ACN electrolyte. It can be seen that CNF/GO electrode exhibits a larger CV area than the CNF electrode, indicating a higher specific capacitance compared to CNF. Adding GO increases the O/C ratio, which could result in an enhanced capacitive behavior of the carbon nanofibers.
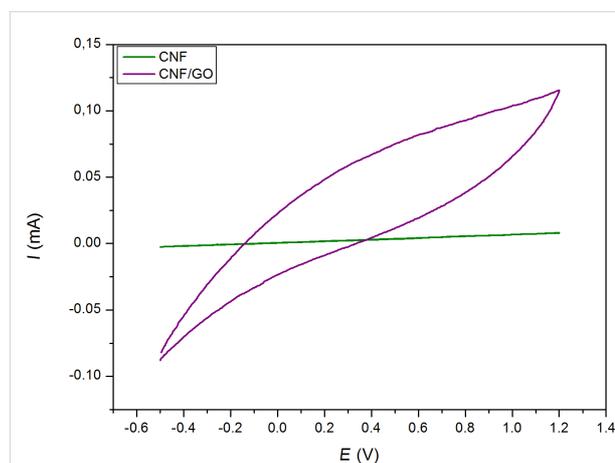


**Figure 15:** Cyclic voltammograms of carbon nanofibers and GO-containing carbon nanofiber webs at scan rate of 50 mV·s$^{-1}$ (PAN-based nanofibers with and without GO, first oxidized then carbonized).

## Conclusion

In this paper, CNF webs and GO-containing CNF webs were successfully fabricated. Nanofiber webs were fabricated via electrospinning. Nanofiber alignment was achieved with a rotating collector, which also had the definite and expected effect of increasing modulus and reducing the strain to break of the webs. Different oxidation temperatures were studied and

250 °C was selected as optimum temperature for this study. Increased the oxidation temperature increases the oxidation level of the sample. However, thermal oxidation between 200 and 300 °C was not enough to eliminate all C≡N triple bonds. GO-containing oxidized nanofibers have a rough surface. Nanopores of around $38.5 \pm 11$ nm pore size on the nanofiber surface can help to store large amounts of charge. GO addition into PAN makes a significant change on the EIS results, i.e., the capacitive behavior increases with the increase in the $C_{dl}$ value of GO-containing oxidized nanofibers. The $C_{dl}$ value of Ox.PAN/GO(2) is the highest as being 0.600 µF. Individual layered sheets of GO with high surface area are supposedly exposed to the electrolyte, which can result in the increase of the double layer capacitance. GO functional groups enhance the capacitance performance of CNF webs. As a result, CNF/GO can be a potential candidate for capacitive applications.

## Acknowledgements

## References

1. Wu, Q.; Xu, Y.; Yao, Z.; Liu, A.; Shi, G. *ACS Nano* **2010,** *4,* 1963–1970. doi:10.1021/nn1000035
2. Vieira, R.; Pham-Huu, C.; Keller, N.; Ledoux, M. J. *Chem. Commun.* **2002,** 954–955. doi:10.1039/b202032g
3. Tamura, T.; Kawakami, H. *Nano Lett.* **2010,** *10,* 1324–1328. doi:10.1021/nl1007079
4. Li, D.; Xia, Y. *Adv. Mater.* **2004,** *16,* 1151–1170. doi:10.1002/adma.200400719
5. Green, K. J.; Dean, D. R.; Vaidya, U. K.; Nyairo, E. *Composites, Part A* **2009,** *40,* 1470–1475. doi:10.1016/j.compositesa.2009.05.010
6. Sadeghian, R.; Gangireddy, S.; Minaie, B.; Hsiao, K.-T. *Composites, Part A* **2006,** *37,* 1787–1795. doi:10.1016/j.compositesa.2005.09.010
7. Tibbetts, G. G.; Lake, M. L.; Strong, K. L.; Rice, B. P. *Compos. Sci. Technol.* **2007,** *67,* 1709–1718. doi:10.1016/j.compscitech.2006.06.015
8. Rodriguez, A. J.; Guzman, M. E.; Lim, C.-S.; Minaie, B. *Carbon* **2011,** *49,* 937–948. doi:10.1016/j.carbon.2010.10.057
9. Ko, T.-H. *J. Appl. Polym. Sci.* **1991,** *42,* 1949–1957. doi:10.1002/app.1991.070420719
10. Shokuhfar, A.; Sedghi, A.; Farsani, R. E. *Mater. Sci. Technol.* **2006,** *22,* 1235–1239. doi:10.1179/174328406X129887
11. Yusof, N.; Ismail, A. F. *J. Anal. Appl. Pyrolysis* **2012,** *93,* 1–13. doi:10.1016/j.jaap.2011.10.001
12. Dalton, S.; Heatley, F.; Budd, P. M. *Polymer* **1999,** *40,* 5531–5543. doi:10.1016/S0032-3861(98)00778-2
13. Faraji, S.; Yardim, M. F.; Can, D. S.; Sarac, A. S. *J. Appl. Polym. Sci.* **2017,** *134,* 44381. doi:10.1002/app.44381
14. Rahaman, M. S. A.; Ismail, A. F.; Mustafa, A. *Polym. Degrad. Stab.* **2007,** *92,* 1421–1432. doi:10.1016/j.polymdegradstab.2007.03.023
15. Arshad, S. N.; Naraghi, M.; Chasiotis, I. *Carbon* **2011,** *49,* 1710–1719. doi:10.1016/j.carbon.2010.12.056
16. de Almeida Coelho, N. M.; Furtado, J. L. B.; Pham-Huu, C.; Vieira, R. *Mater. Res. (Sao Carlos, Braz.)* **2008,** *11,* 353–357. doi:10.1590/S1516-14392008000300020
17. Lee, S.; Kim, J.; Ku, B.-C.; Kim, J.; Joh, H.-I. *Adv. Chem. Eng. Sci.* **2012,** *2,* 275–282. doi:10.4236/aces.2012.22032
18. Ismar, E.; Sarac, A. S. *Polym. Adv. Technol.* **2016,** *27,* 1383–1388. doi:10.1002/pat.3807
19. Morgan, P. *Carbon Fibers and Their Composites;* Taylor & Francis, 2005. doi:10.1201/9781420028744
20. Masson, J. *Acrylic Fiber Technology and Applications;* CRC Press, 1995.
21. Devasia, R.; Nair, C. P. R.; Sivadasan, P.; Katherine, B. K.; Ninan, K. N. *J. Appl. Polym. Sci.* **2003,** *88,* 915–920. doi:10.1002/app.11706
22. Kakida, H.; Tashiro, K.; Kobayashi, M. *Polym. J.* **1996,** *28,* 30–34. doi:10.1295/polymj.28.30
23. Lee, S.; Kim, Y.-J.; Kim, D.-H.; Ku, B.-C.; Joh, H.-I. *J. Phys. Chem. Solids* **2012,** *73,* 741–743. doi:10.1016/j.jpcs.2012.01.015
24. Karthika, P.; Rajalakshmi, N.; Dhathathreyan, K. S. *Soft Nanosci. Lett.* **2012,** *2,* 59–66. doi:10.4236/snl.2012.24011
25. Zhu, Y.; Murali, S.; Cai, W.; Li, X.; Suk, J. W.; Potts, J. R.; Ruoff, R. S. *Adv. Mater.* **2010,** *22,* 3906–3924. doi:10.1002/adma.201001068
26. Tai, Z.; Yan, X.; Lang, J.; Xue, Q. *J. Power Sources* **2012,** *199,* 373–378. doi:10.1016/j.jpowsour.2011.10.009
27. Sarac, A. S. *Nanofibers of Conjugated Polymers;* Pan Stanford, 2016.
28. Fennessey, S. F.; Farris, R. J. *Polymer* **2004,** *45,* 4217–4225. doi:10.1016/j.polymer.2004.04.001
29. Naraghi, M.; Arshad, S. N.; Chasiotis, I. *Polymer* **2011,** *52,* 1612–1618. doi:10.1016/j.polymer.2011.02.013
30. Zhou, Z.; Lai, C.; Zhang, L.; Qian, Y.; Hou, H.; Reneker, D. H.; Fong, H. *Polymer* **2009,** *50,* 2999–3006. doi:10.1016/j.polymer.2009.04.058
31. El-Hadi, A. M.; Mohan, S. D.; Davis, F. J.; Mitchell, G. R. *J. Polym. Res.* **2014,** *21,* 605. doi:10.1007/s10965-014-0605-2
32. Fennessey, S. F. Continuous carbon nanofibers prepared from electrospun polyacrylonitrile precursor fibers. Ph.D. Thesis, University of Massachusetts, Amherst, MA, USA, 2006.
33. Ismar, E.; Sarac, A. S. *Polym. Bull.* **2017,** *74,* 1493–1517. doi:10.1007/s00289-017-2043-x
34. Ma, S.; Liu, J.; Liu, Q.; Liang, J.; Zhao, Y.; Fong, H. *Mater. Des.* **2016,** *95,* 387–397. doi:10.1016/j.matdes.2016.01.134
35. Ouyang, Q.; Cheng, L.; Wang, H.; Li, K. *Polym. Degrad. Stab.* **2008,** *93,* 1415–1421. doi:10.1016/j.polymdegradstab.2008.05.021
36. Liu, J.; Zhou, P.; Zhang, L.; Ma, Z.; Liang, J.; Fong, H. *Carbon* **2009,** *47,* 1087–1095. doi:10.1016/j.carbon.2008.12.033
37. Xue, T. J.; McKinney, M. A.; Wilkie, C. A. *Polym. Degrad. Stab.* **1997,** *58,* 193–202. doi:10.1016/S0141-3910(97)00048-7
38. Farsani, R. E.; Raissi, S.; Shokuhfar, A.; Sedghi, A. *Int. J. Mech. Aerosp. Ind. Mechatronic Manuf. Eng.* **2009,** *3,* 161–164.
39. Ogawa, H.; Saito, K. *Carbon* **1995,** *33,* 783–788. doi:10.1016/0008-6223(95)00007-Z
40. Mittal, J.; Bahl, O. P.; Mathur, R. B.; Sandle, N. K. *Carbon* **1994,** *32,* 1133–1136. doi:10.1016/0008-6223(94)90222-4
41. Clarke, A. J.; Bailey, J. E. *Nature* **1973,** *243,* 146–150. doi:10.1038/243146a0
42. Fu, Z.; Gui, Y.; Cao, C.; Liu, B.; Zhou, C.; Zhang, H. *J. Mater. Sci.* **2014,** *49,* 2864–2874. doi:10.1007/s10853-013-7992-3
43. Park, O.-K.; Lee, S.; Joh, H.-I.; Kim, J. K.; Kang, P.-H.; Lee, J. H.; Ku, B.-C. *Polymer* **2012,** *53,* 2168–2174. doi:10.1016/j.polymer.2012.03.031

44. Bashir, Z. *Carbon* **1991,** *29,* 1081–1090.
doi:10.1016/0008-6223(91)90024-D

45. Salamone, J. C. *Concise Polymeric Materials Encyclopedia;* CRC
Press, 1998.

46. Chang-qing, L. I.; Yang, X.; Hong-jiang, Z.; Xin, C.; Zhou-wen, H. E.;
Liang-hua, X. U. *Trans. Mater. Heat Treat.* **2015,** *5,* 35–38.

47. Chand, S. *J. Mater. Sci.* **2000,** *35,* 1303–1313.
doi:10.1023/A:1004780301489

48. Mittal, J.; Konno, H.; Inagaki, M.; Bahl, O. P. *Carbon* **1998,** *36,*
1327–1330. doi:10.1016/S0008-6223(98)00113-4

49. Sagirli, F. Z. E.; Kayali, E. S.; Sarac, A. S. *J. Electrochem. Soc.* **2016,**
*163,* H205–H212. doi:10.1149/2.0681603jes

50. Qu, D.; Shi, H. *J. Power Sources* **1998,** *74,* 99–107.
doi:10.1016/S0378-7753(98)00038-X

51. Ferrari, A. C. *Solid State Commun.* **2007,** *143,* 47–57.
doi:10.1016/j.ssc.2007.03.052

52. Kim, C.; Park, S.-H.; Cho, J.-I.; Lee, D.-Y.; Park, T.-J.; Lee, W.-J.;
Yang, K.-S. *J. Raman Spectrosc.* **2004,** *35,* 928–933.
doi:10.1002/jrs.1233

53. Wang, Y.; Serrano, S.; Santiago-Aviles, J. J. *J. Mater. Sci. Lett.* **2002,**
*21,* 1055–1057. doi:10.1023/A:1016081212346

54. Jawhari, T.; Roid, A.; Casado, J. *Carbon* **1995,** *33,* 1561–1565.
doi:10.1016/0008-6223(95)00117-V

55. Rodriguez, N. M. *J. Mater. Res.* **1993,** *8,* 3233–3250.
doi:10.1557/JMR.1993.3233

56. Sharma, C. S.; Katepalli, H.; Sharma, A.; Madou, M. *Carbon* **2011,** *49,*
1727–1732. doi:10.1016/j.carbon.2010.12.058

57. Gong, Y.; Li, D.; Fu, Q.; Pan, C. *Prog. Nat. Sci.: Mater. Int.* **2015,** *25,*
379–385. doi:10.1016/j.pnsc.2015.10.004

58. Manaf, N. S. A.; Bistamam, M. S. A.; Azam, M. A.
*ECS J. Solid State Sci. Technol.* **2013,** *2,* M3101–M3119.
doi:10.1149/2.014310jss

59. Raymundo-Piñero, E.; Kierzek, K.; Machnikowski, J.; Béguin, F.
*Carbon* **2006,** *44,* 2498–2507. doi:10.1016/j.carbon.2006.05.022

60. Rubinson, J. F.; Kayinamura, Y. P. *Chem. Soc. Rev.* **2009,** *38,*
3339–3347. doi:10.1039/B904083H

# Carbon nano-onions as fluorescent on/off modulated nanoprobes for diagnostics

Stefania Lettieri[1], Marta d'Amora[2], Adalberto Camisasca[1,3], Alberto Diaspro[2,4,5] and Silvia Giordani[*1,6]

## Full Research Paper

Address:
[1]Nano Carbon Materials, Istituto Italiano di Tecnologia (IIT), via Livorno 60, 10144, Turin, Italy, [2]Nanoscopy, Istituto Italiano di Tecnologia (IIT), via Morego 30, 16163, Genoa, Italy, [3]Department of Chemistry, University of Genoa, Via Dodecaneso 31, Genoa, 16145, Italy, [4]NIC@IIT, Istituto Italiano di Tecnologia (IIT), Via Morego 30, Genoa, 16163, Italy, [5]Department of Physics, University of Genoa, Via Dodecaneso 33, Genoa, 16145, Italy and [6]Department of Chemistry, University of Turin, via Giuria 7, 10125, Turin, Italy

Email:
Silvia Giordani[*] - silvia.giordani@iit.it

* Corresponding author

Keywords:
carbon nanomaterials; fluorescence; imaging; nanomedicine; nano-onion

## Abstract

Multishell fullerenes, known as carbon nano-onions (CNOs), have emerged as a platform for bioimaging because of their cell-penetration properties and minimal systemic toxicity. Here, we describe the covalent functionalization of CNOs with a π-extended distyryl-substituted boron dipyrromethene (BODIPY) dye with on/off modulated fluorescence emission activated by an acidic environment. The switching properties are linked to the photoinduced electron transfer (PET) characteristics of the dimethylamino functionalities attached to the BODIPY core. The on/off emission of the fluorescent CNOs is fast and reversible both in solution and in vitro, making this nanomaterial suitable as pH-dependent probes for diagnostic applications.

## Introduction

Nanomaterial-based probes (nano-probes) that are able to interact with disease markers or capable of sensing physiological changes in cells are widely used in diagnostic applications. In particular, fluorescent nano-probes are a relatively inexpensive platform compared to other biosensors and are capable of generating an optical output in response to a specific stimulus, making this technique operationally simple. Such stimuli can be a disease biomarker or changes in the cell chemical environment. In particular, intracellular pH plays a significant role in the physiological cellular activity indicating their health. Thus, a change in H$^+$ can indicate physiological changes in the cells and tissues. Some of these events include cell proliferation and

apoptosis [1], ion transport [2] and other cellular process and diseases such as cancer [3-5], Parkinson's, and Alzheimer's disease [6]. Despite the large number of nanotechnology platforms available to date for sensing applications [7], multishell fullerenes, known as carbon nano-onions (CNOs) [8,9], prepared by thermal annealing of detonation nanodiamonds (d-NDs) [10], are an attractive class of carbon nanomaterials (CNMs) for imaging, diagnostic and therapeutic applications, due to their unique properties. They exhibit low density and a high surface area to volume ratio [11,12] and have a spherical shape [13]. Moreover, they can be chemically functionalized, either covalently through chemical reaction [14] (e.g. oxidation [15,16]) or through adsorption of organic molecules by π–π stacking [17]. Our recent reports have shown that CNOs exhibit weak inflammatory potential and low cytotoxicity [16], and they are readily internalized by cancer cells and localize in the lysosomes [18,19]. Moreover, our in vivo studies performed on zebrafish (*Danio Rerio*) during the development stage demonstrated their biocompatibility [20]. We have previously shown that the pH-dependent switching ability of a dye is preserved when attached to CNOs [21] and on single-wall carbon nanotubes, [22] both in solution and in vitro. Thus, CNOs are suitable nanomaterials for biosensing applications. We exploited the photoinduced electron transfer (PET) and internal charge transfer (ICT) donor characteristics of the dimethylamino functionalities attached to a π-extended distyryl-substituted boron dipyrromethene (BODIPY) dye [23,24] to obtain a pH-sensitive nano-probe. Hence, CNOs grafted with BODIPY **3** molecules (fluo-CNOs) led to the development of a nanosensor which can be "turned on" in an acidic environment. Remarkably, the fluo-CNOs maintained the switching properties upon cell internalization, as they were "switched-on" in response to acidic pH. In vitro experiments on HeLa cells showed excellent cellular uptake and low toxicity of these fluorescent probes. Our

findings pave the way for the development of fluorescent on/off modulated diagnostic nanomaterials.

## Results and Discussion
### Synthetic procedures

The synthetic procedures are shown in Scheme 1 and Scheme 2. Compounds **1** and **2** were synthetized following a previously reported procedure [25,26]. The condensation with dimethylaminobenzaldehyde led to the NIR-BODIPY derivative **3**. The surface functionalization of 5 nm pristine CNOs (p-CNOs), synthetized by thermal annealing of d-NDs, was obtained by an oxidation process using a 3 M solution of nitric acid under reflux condition. The oxidation was performed directly on the $sp^2$ carbon present on the p-CNOs surface, leading to the introduction of carboxylic acid groups. The highly functionalized oxidized CNOs (oxi-CNOs) were then grafted with BODIPY **3** molecules through an ester bond using 1-ethyl-3-(3-dimethylaminopropyl)carbodiimide (EDC) as the coupling agent at room temperature for 20 h (Scheme 2) to obtain fluo-CNOs.

### BODIPY

Compound **1** was synthetized from 3,5-dimethylphenol following a published procedure [25]. 3,5-dimethylphenol (46.5 g, 0.38 mol) and KOH (39 g, 0.70 mol) were dissolved in water (150 mL). $CHCl_3$ (60 mL, 0.34 mol) was added drop wise with a dropping funnel and the reaction mixture was left to react for 24 h in total. The next day the brown reaction mixture was transferred in a separation funnel and the chloroform layer was separated from the aqueous one. The aqueous layer was then poured into a $H_2SO_4$ solution and a white precipitate formed. The precipitate was filtered and washed with fresh chloroform until the total removal of impurities was reached (4.5 g, 8%). $^1$H NMR (400 MHz, DMSO-$d_6$) δ 2.49 (s, 6H), 6.52 (s, 2H),
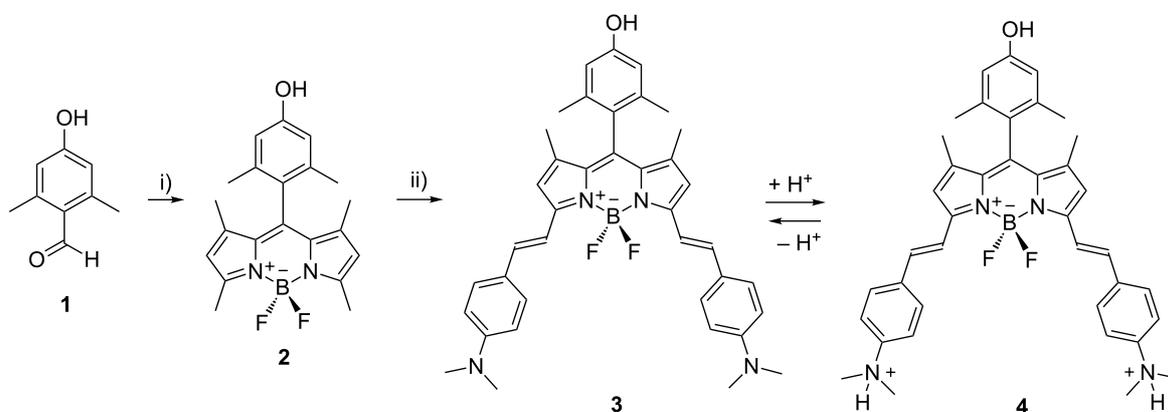


**Scheme 1:** Synthesis of BODIPY derivatives **2** and **3**. i) 2,4-dimethylpyrrole, TFA, DCM, DIPEA, $BF_3OEt_2$; ii) 4-(*N,N*-dimethylamino)benzaldehyde, toluene, piperidine, glacial acetic acid, $Mg(ClO_4)_2$, Dean–Stark condenser.

**Scheme 2:** Procedure for the preparation of carboxy-functionalized oxi-CNO and fluorescently labelled fluo-CNO. i) Nitric acid, reflux, 48 h; ii) EDC, NHS, DMAP, **3**, dry DMF, $N_2$, RT, 20 h.
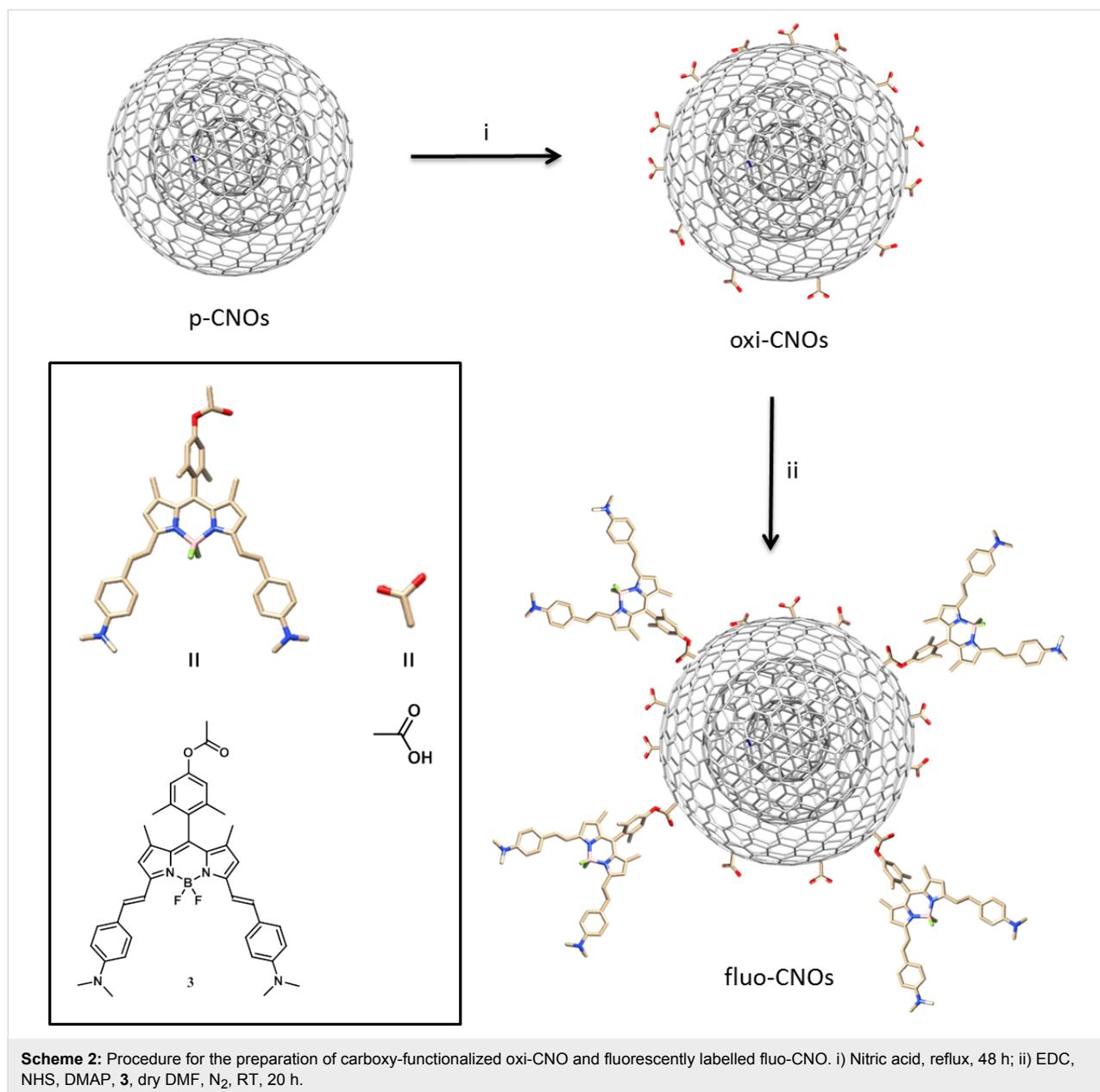
10.28 (s, 1H), 10.32 (s, 1H). See Supporting Information File 1, Figure S1.

Compound **2** was synthetized according to a previously reported procedure [26]. 706 mg of 4-hydroxy-2,6-dimethylbenzaldehyde was dissolved in a degassed solution of EtOH (20 mL) and dichloromethane (DCM) (280 mL). 0.974 mL (9.4 mmol) of 2,4-dimethylpyrrole was added and the condensation was initiated with few drops of trifluoroacetic acid (TFA). The reaction mixture was stirred at RT for 16 h in the dark. Tetrachloro-1,4-benzoquinone (1144 mg/7.85 mmol) was added, followed by stirring for 30 min. The solvents were then removed under vacuum and the dark residue was redissolved in 150 mL of

DCM. *N,N*-diisopropylethylamine (DIPEA) (4.9 mL) was added, and after 30 min, boron trifluoride diethyl etherate ($BF_3OEt_2$) (5.2 mL) was added. The mixture was stirred for 3 h. The crude was eluted on a silica plug using DCM before purification by column chromatography ($SiO_2$, DCM/hexane 50:50, increasing amount of DCM) to obtain a red powder (850 mg, 49%). ^{1}H NMR (400 MHz, chloroform-*d*) δ 1.43 (s, 6H), 2.08 (s, 6H), 2.56 (s, 6H), 4.78 (s, 1H), 5.97 (s, 2H), 6.63 (s, 2H). See Supporting Information File 1, Figure S2.

BODIPY **3** was synthesized by dissolving 220 mg of **2** (0.6 mmol) and 4-(*N,N*-dimethylamino)benzaldehyde (1.34 g, 0.009 mol) in 50 mL of dry toluene and deoxygenated by

purging with di-nitrogen ($N_2$). Piperidine (2.4 mL), glacial acetic acid (2.9 mL) and a catalytic amount of $Mg(ClO_4)_2$ were added and the reaction mixture was refluxed at 150 °C for 27 h with a Dean–Stark condenser. The crude was eluted on a silica plug using acetone before purification by chromatography ($SiO_2$, EtOAc/hexane 2:8, increasing amount of EtOAc). The pure fractions were distilled, and the pure compound was precipitated from DCM in hexane to obtain a black powder (145 mg, 40%). $^1$H NMR (400 MHz, chloroform-*d*) δ 1.50 (s, 6H), 2.14 (s, 6H), 3.06 (s, 12H), 4.78 (s, 1H), 6.61 (s, 2H), 6.66 (s, 2H), 6.75 (d, *J* = 8.4 Hz, 4H), 7.21 (d, *J* = 16.1 Hz, 2H), 7.56 (d, *J* = 8.5 Hz, 5H), 7.61 (s, 3H). See Supporting Information File 1, Figure S3. $^{13}$C NMR (101 MHz, DMSO-$d_6$) δ 158.04, 152.38, 151.44, 140.38, 137.26, 136.80, 135.86, 132.44, 129.11, 124.84, 124.50, 117.67, 115.33, 113.93, 112.67, 19.84, 13.65. See Supporting Information File 1, Figure S4. HRMS-ESI *m/z*: $[M+H]^+$ calcd for $C_{39}H_{41}N_4OBF_2$, 630.3341; found, 630.3363.

## p-CNOs

The synthesis of small, pristine carbon nano-onions (p-CNOs) was performed by thermal annealing of detonation nanodiamonds (d-NDs) of 5 nm average particle diameter in a tube furnace under a positive pressure of helium at 1650 °C.

## oxi-CNOs

A dispersion of p-CNOs (50 mg) was prepared by ultrasonication (20 min at 37 kHz) in 30 mL of a 3 M solution of nitric acid ($HNO_3$). The solution was stirred under reflux conditions for 48 h. The oxi-CNOs were separated from the reaction mixture by centrifugation (15 min at 1800 rpm) and filtered off on a nylon filter membrane (pore size 0.2 µm) and washed with $dH_2O$, DMF, methanol and acetone. After drying overnight at RT, 51.2 mg of oxi-CNOs were obtained as a black powder.

## fluo-CNOs

A dispersion of oxi-CNOs (10 mg) was prepared by ultrasonication (30 min at 37 kHz) in 10 mL of anhydrous DMF. To the mixture 9.2 mg (0.08 mmol) of NHS, 12 mg (0.01 mmol) of DMAP and 14 µL of EDC were added consecutively. The reaction mixture was briefly sonicated and after the addition of 4 mg (0.0044 mmol) of BODIPY **3**, and the mixture was stirred at room temperature for 20 h under di-nitrogen atmosphere. The fluo-CNOs were filtered off thought a nylon membrane (pore size 0.2 µm) and washed with fresh DMF, THF and MeOH to remove the unreacted dye and the remaining reagents. 9.7 mg of fluo-CNOs were recovered as a black powder.

## PET and ICT effect

The on/off modulation of the fluo-CNOs emission is linked to the protonated/non-protonated form of the dimethylamino group attached to the BODIPY core. Upon protonation of the dimethylamino functional groups attached to the BODIPY core (BODIPY **4**, Scheme 1), which are capable of introducing photoinduced electron transfer (PET) [27] properties to the fluorophore, the dye molecule exhibited a bright red fluorescence
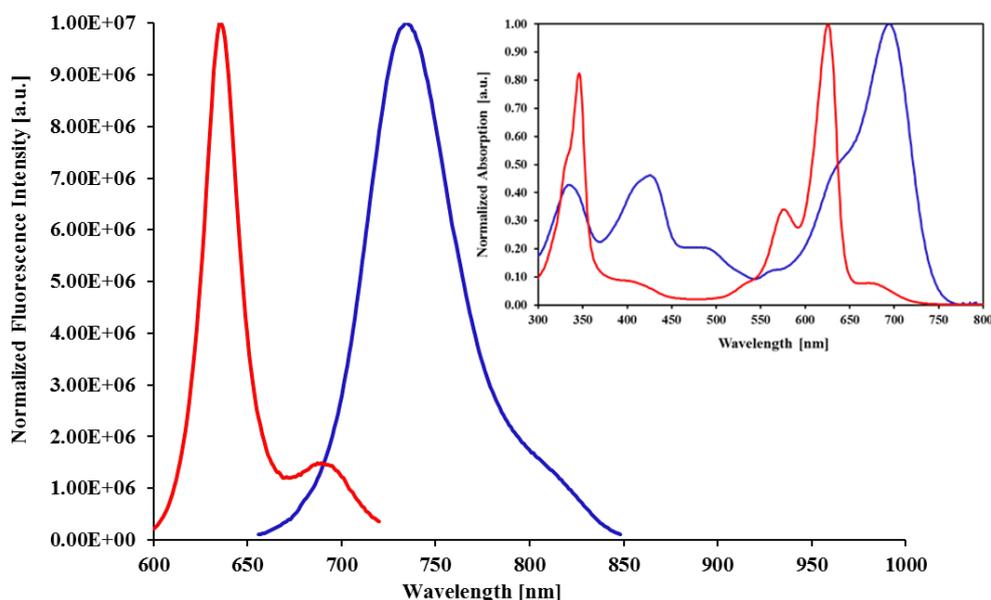


**Figure 1:** Emission spectra of BODIPY **3** (blue line: Excitation at 680 nm; emission at 737 nm) and BODIPY **4** (red line: Excitation at 600 nm; emission at 637 nm). Inset: absorption spectra of BODIPY **3** (blue line) and BODIPY **4** (red line) (solvent: chloroform). BODIPY **4** was protonated upon addition of $H^+$ in the solution.

with maximum emission centered at 637 nm in chloroform (Figure 1).

These PET groups were activated in neutral or basic environment (BODIPY **3**, Scheme 1), where the non-protonated form of BODIPY is present, and a low intensity maximum emission was observed at 737 nm in chloroform. They were instead deactivated upon protonation (BODIPY **4**) resulting in the enhancement of the fluorescence with emission maximum centered at 637 nm (see Figure 1, Table 1).

**Table 1:** Photophysical data for BODIPY **3** and **4**, absorption maximum ($\lambda_{abs}$), and emission maximum ($\lambda_{em}$).

| Sample | Solvent | $\lambda_{exc}$ (nm) | $\lambda_{em}$ (nm) | $\lambda_{abs}$ (nm) |
|---|---|---|---|---|
| BODIPY **3** | DMSO | 680 | 768 | 712 |
| BODIPY **3** | CHCl$_3$ | 680 | 737 | 696 |
| BODIPY **4** | CHCl$_3$ | 600 | 637 | 624 |

We observed that the on/off process is fast and reversible making this dye suitable for pH-dependent probes. Interestingly, this BODIPY sample also exhibited an internal charge transfer (ICT) characteristic resulting in a hypsochromic shift of the dye emission upon nitrogen protonation at acidic pH (Figure 1). At an excitation wavelength of 680 nm in chloroform, BODIPY **3** showed a maximum emission in the NIR window at 737 nm. Instead, when the dye was protonated (BODIPY **4**), a maximum emission at 637 nm was recorded when excited at 600 nm (Figure 1, Table 1). The ICT effect causes a variation of the intramolecular electron redistribution of the molecule. Accordingly, the amino groups of the dye attract electrons due to their electron-withdrawing characteristic, which led to an emission of BODIPY **3** at longer wavelengths (Table 1). This effect is reversed when the amino groups are protonated (BODIPY **4**). Despite the desired NIR window emission spectrum of BODIPY **3**, its quantum yield ($\Phi_F$) in DMSO is very low ($\Phi_F = 0.05$), due to the active PET groups (amino groups), which causes a pH-dependent quenching of the fluorescent dyes. Overall, the non-protonated form of the dye (BODIPY **3**) is the switched-off form while the protonated form (BODIPY **4**) is the switched-on form. The successful functionalization of CNOs with BODIPY **3** was confirmed by photoemission studies. Upon photoexcitation at 680 nm, fluo-CNOs-1a (Figure 2) exhibited a maximum emission ($\lambda_{em}$) at 768 nm, while fluo-CNOs-1b had a $\lambda_{em}$ of 633 upon photoexcitation of 600 nm in DMSO. Hence, the ICT characteristics of the dye are preserved on the CNOs.

## Characterization of CNOs

Oxi- and fluo-CNOs were characterized by thermogravimetric analysis (TGA) and Raman spectroscopy to prove the success-

ful surface functionalization of the CNOs. The high degree of surface functionalization of the oxi-CNOs and the successful attachment of the dye molecules on the oxi-CNOs was observed by TGA analysis. The TGA spectrum of the oxi-CNOs performed in air (Figure 3, blue) showed a decrease in decomposition temperature from 686 °C to 668 °C, with a weight loss of 7.70% compared to the p-CNOs. From the TGA weight loss at 450 °C, a total of 122 carboxylic groups per CNO were estimated. The functionalization of oxi-CNOs with the dye molecules causes a further weight loss of the fluo-CNOs of 3.2% compared to the oxi-CNOs, with a decomposition temperature of 639 °C. We estimate that around four dye molecules per CNO were present. A high-resolution TEM image of the p-CNOs is given in Supporting Information File 1, Figure S5.

The Raman spectra of p-, oxi- and fluo-CNOs showed the D-band (1320 cm$^{-1}$) and the G-band (1580 cm$^{-1}$) typical for CNOs [28]. The D-band at 1320 cm$^{-1}$ refers to the defects present on the outer graphitic layer and is due to the presence of sp$^3$-hybridized carbons. The G-band at around 1580 cm$^{-1}$ corresponds to the E$_{2g}$ mode of sp$^2$-hybridized carbon frameworks. As shown in Figure 4, the D/G ratio increased in the oxi-CNOs compared to the p-CNOs due to the presence of defects on the CNO outer layer created by the oxidation process, confirming the introduction of carboxylic groups. Fluo-CNOs did not show any significant change in the ratio between the D and G bands, as the sample was excited with a built-in 632 nm laser which can alter the measurements due to background signal.

Dynamic light scattering (DLS) was carried out to determine the hydrodynamic radius of the dispersed CNOs (Table 2, Figure 5). DLS experiments were performed on CNOs samples dispersed in 0.01 M PBS to partially mimic the biological environment. The oxi-CNOs were found to have an effective hydrodynamic diameter of 274 ± 16 nm, while the fluo-CNOs have an average diameter of 357 ± 32 nm. The zeta potential changed from −45 ± 5 mV for the oxi-CNOs to −35.9 ± 1 mV for the fluo-CNOs, confirming the functionalization of the oxi-CNOs with the dye molecules (Table 2).

## Cytotoxicity studies

The possible adverse effects of fluo-CNOs on HeLa cells were tested by using a colorimetric assay (WST1). Cells were exposed to different concentrations of fluo-CNOs (1, 2, 5, 10 and 20 µg mL$^{-1}$) for different time periods (12, 24, 48 and 72 h). Cells treated with only cell culture medium were used as a control. The cell viability percentage was above 80%, showing that CNOs exhibited moderate toxicity to the cells at the tested concentrations (Figure 6). The observed high viability of the HeLa cells treated with CNOs demonstrated their suitability for application as intracellular sensors.
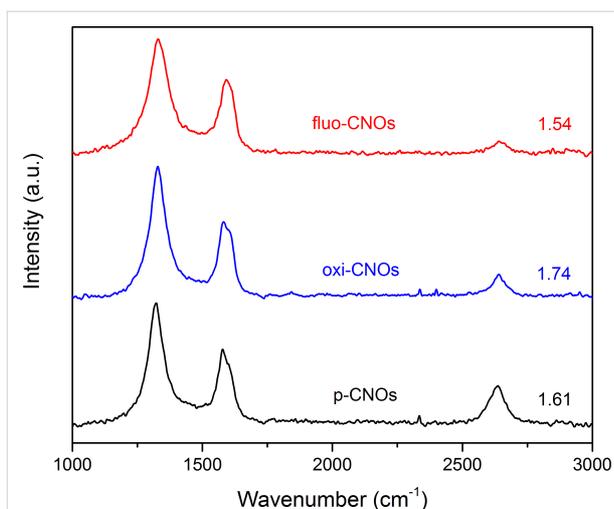
**Figure 2:** A) Protonated (fluo-CNOs-1a) and non-protonated (fluo-CNOs-1b) forms of fluo-CNOs. B) Emission spectra of fluo-CNOs-1a (blue line: Excitation at 680 nm; emission at 768 nm) and fluo-CNOs-1b (red line: Excitation at 600 nm; emission at 633 nm) in DMSO.



**Figure 3:** Thermogravimetric analysis (TGA) spectra of the functionalized CNOs. TGA (solid lines) and the corresponding weight loss derivatives (dotted lines) of p-CNOs (black), oxi-CNOs (blue) and fluo-CNOs (red). All experiments were run in air at a temperature rate of 10 °C min$^{-1}$.

**Figure 4:** Raman spectra of the functionalized CNOs. The Raman spectra are normalized to the G-band at 1580 cm$^{-1}$ and the ratios of the D-band to the G-band intensities are indicated.

**Table 2:** Effective hydrodynamic diameter (0.01 M PBS) obtained from dynamic light scattering (DLS) measurements and zeta potential (phosphate buffer) of oxi-CNOs and fluo-CNOs at a concentration of 5 µg mL$^{-1}$ in PBS.

| Sample | Effective hydrodynamic diameter (nm) | Zeta potential (mV) |
|---|---|---|
| oxi-CNOs | 274 ± 16 | −45 ± 5 mV |
| fluo-CNOs | 357 ± 32 | −35.9 ± 1 mV |
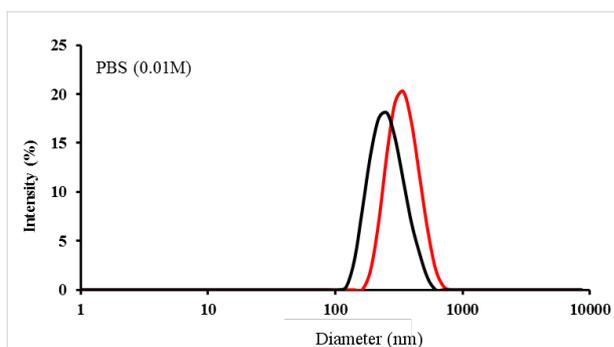


**Figure 5:** Effective hydrodynamic diameter of oxi-CNOs (black line) and fluo-CNOs (red line) in PBS at a concentration of 5 µg mL$^{-1}$.

## Confocal imaging

Confocal imaging was performed on human cervical carcinoma (HeLa) cells treated with fluo-CNOs, in order to confirm the preservation of the PET and ICT characteristics of the dye attached to CNOs after cell internalization, hence the possible use of fluo-CNOs as pH-activated fluorescent probes. HeLa cells were incubated with fluo-CNOs (20 µg mL$^{-1}$) and observed by confocal microscopy at different pH values in PBS to demon-
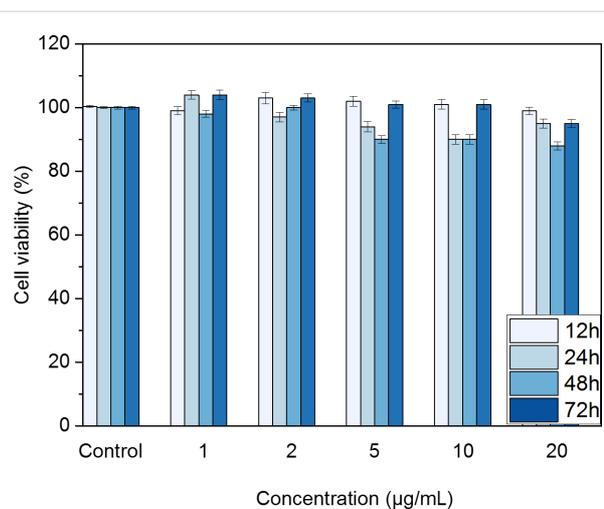


**Figure 6:** Cellular viability of HeLa cells treated with different concentrations (1, 2, 5, 10 and 20 µg mL$^{-1}$) of fluo-CNOs for 12, 24, 28 and 72 h in DMEM (pH 7.4), revealed by the WST 1 assay. Cell viability (%) was evaluated for the CNO-treated samples against a non-treated control. As a positive control, the cells were incubated with 5% DMSO (showing a viability decrease of ca. 45%). Data are expressed as mean ± standard error as calculated from three separate experiments.

strate the activation of the fluorescent emission in acidic environment. After the fixation, the nuclei were stained with a blue fluorescent dye (Hoechst 33232). Bright-field transmission images after fluo-CNO treatment confirmed that the HeLa cells were viable throughout all the experiments. From the fluorescence microscopy images (Figure 7), it was observed that cells treated with fluo-CNOs and maintained at a physiological pH (7.4) for 1 h exhibited no detectable red fluorescence signal (Figure 7A).

Successively, when the cells were incubated with acidic PBS (at pH 4.5), a strong red fluorescence signal was clearly observed in the intracellular region (Figure 7B). The overlay of fluorescence and bright-field images showed that fluo-CNOs were successfully internalized by cells and were distributed throughout the cytoplasm. Remarkably the cellular uptake of the fluo-CNOs was clearly observed soon after the incubation, as shown by the presence of CNOs inside the cell after 2 h (Figure 8A).

After 12 and 48 h of incubation (Figure 8B,C), a progressive accumulation of fluo-CNOs was observed during the cell proliferation. Additionally, the efficient uptake was supported by a three dimensional reconstruction of cells treated with CNOs (Figure 9).

Finally, we demonstrated that the on/off fluorescent emission properties of the fluo-CNOs was reversible, as the intracellular fluorescence completely disappeared after treatment in a basic buffer (at pH 8.5) for 1 h (data not shown). Our results report
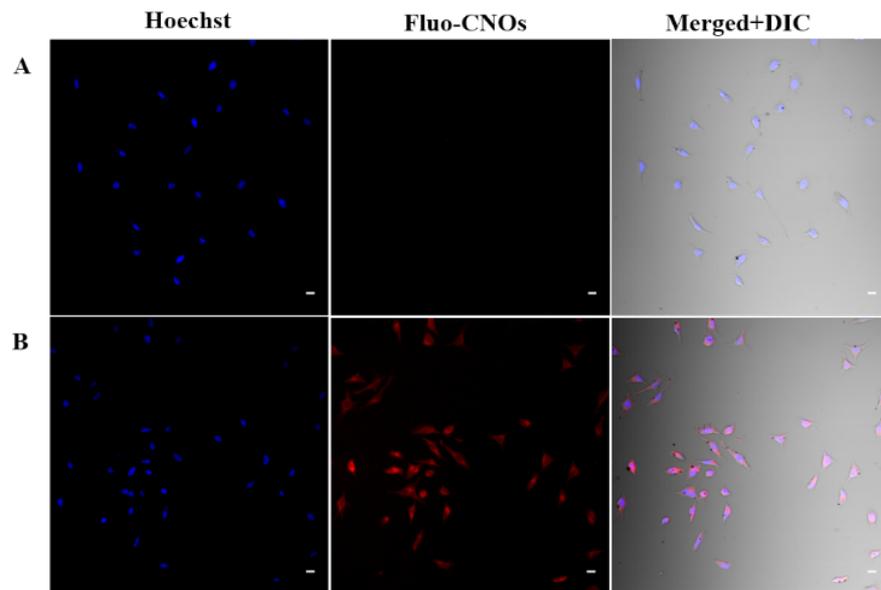
**Figure 7:** Confocal fluorescence images of HeLa cells treated with 20 µg mL$^{-1}$ of fluo-CNOs. (A) PBS for 1 h, pH 7.4; (B) acid buffer for 1 h, pH 4.5; Scale bars = 20 µm.
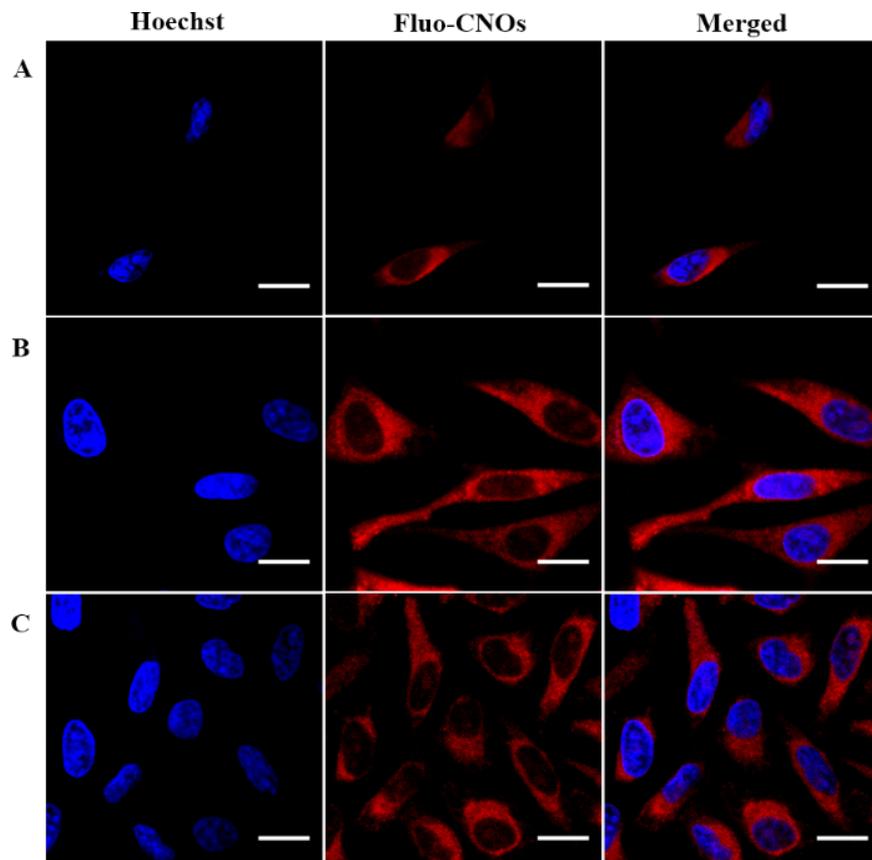


**Figure 8:** Cellular uptake and localization of fluo-CNOs in HeLa cells in acidic conditions (PBS, pH 4.5) observed by confocal fluorescence microscopy after incubation for 2 h (A), 12 h (B) and 48 h (C), respectively. Scale bars = 20 µm.
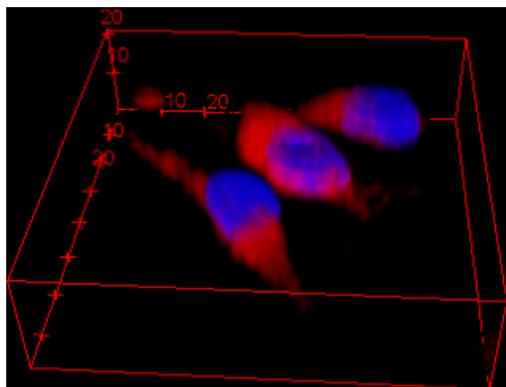
**Figure 9:** Three-dimensional reconstruction by confocal microscopy of cells incubated for 12 h with 20 μg mL$^{-1}$ of fluo-CNOs in DMEM, and then for 1 h in acidic PBS (pH 4.5) and stained with Hoechst 33342.

that CNOs exhibit no fluorescence in neutral and basic environment (pH ≥ 7.0) and bright red fluorescence in acidic condition (pH ≤ 5.0). We proved that fluo-CNOs possess unique pH-switchable properties at acidic (pH 4.5), neutral (pH 7.4) and basic (pH 8.5) pH and can be potentially used as an intracellular pH-sensing nanoprobe.

## Conclusion

In summary, pH-sensitive BODIPY–CNO conjugates have been synthesized and characterized. The fluorescent carbon nano-onions (fluo-CNOs) were readily internalized by HeLa cells after 2 h of exposure and showed no major toxicity. The ability to switch the red fluorescence using pH control was demonstrated both in solution and in vitro, upon modification of the environmental pH, which resulted in an intracellular pH change. HeLa cells treated with fluo-CNOs exhibited no fluorescence at neutral and basic environment (≥7.0) and a bright red fluorescence in acidic condition (≤5.0). The on/off process was fast and reversible, making this nanomaterial suitable as a pH-sensitive probe for diagnostic applications.

## Experimental
### Materials
All solvents and reagents were purchased from Sigma-Aldrich in high purity grade. All reactions and measurements were carried out under ambient conditions, unless otherwise stated.

### Instrumentation
#### Thermogravimetric analysis (TGA)
TGA was conducted on a TA Q500 analyzer, using a platinum pan as sample holder. After equilibrating the sample at 30 °C for 5 min and then at 100 °C for additional 20 min, the measurement was performed in air using a heating rate of 10 °C/min. The sample weight was monitored until 900 °C.

### Raman spectroscopy
Raman spectra were measured on a Horiba Jobin Yvon HR 800 UV LabRam Raman microscope. For the Raman measurements, the samples were deposited directly on a silicon wafer and excited with a built-in 632 nm laser.

### Absorption and fluorescence spectroscopy
Absorption spectra were recorded on an Agilent Cary 8454 UV–vis diode array spectrophotometer. Fluorescence spectra were taken on a Horiba Jobin Yvon Fluoromax-4 spectrofluorometer in 1.00 × 1.00 cm quartz glass cells. The CNO samples were dispersed in DMSO to a final concentration of 1 mg mL$^{-1}$. The dispersion of CNOs was sonicated for 15 min at 37 kHz and further diluted in DMSO to achieve final concentrations of 20, 10 and 5 μg mL$^{-1}$.

### Dynamic light scattering and zeta potential measurements
DLS measurements were performed on the Malvern Nano-ZS instrument operating in backscattering (173°) mode and analyzed with the Zetasizer software, with automatic selection of the optimal detector position and number of independent measurements. The CNO samples were dispersed to a final concentration of 1 mg mL$^{-1}$ in PBS 0.01 M (PBS pH 7.4, composition 0.14 M NaCl, 0.0027 M KCl, 0.010 M PO$_4$$^{3-}$) The samples were sonicated for 10 min at 37 kHz and then diluted in 0.01 M PBS to achieve a final concentration of 5 μg mL$^{-1}$. The CNO samples were sonicated for an additional 20 min and the particle size was measured. Zeta potential measurements were performed on the same apparatus using the disposable zeta potential cuvettes.

### NMR spectroscopy
NMR spectroscopy was performed on a Bruker Avance III 400 MHz system (400.13 MHz for $^1$H and 100.62 MHz for $^{13}$C) in CDCl$_3$ or DMSO-$d_6$.

### High-resolution mass spectrometry (HRMS)
The accurate mass measurements (HRMS) were performed on a Waters SYNAPT G2 high-resolution mass spectrometry instrument equipped with an electrospray ionization interface and coupled to a Waters ACQUITY UPLC. Electrospray ionization in positive mode was applied in the mass scan range 50–1200 Da. The analysis was performed on a Waters ACQUITY UPLC BEH C18 column 100 × 2.1 mm ID (particle size 1.7 μm) with an in-line filter. The mobile phase was 0.1% formic acid in H$_2$O and 0.1% formic acid in acetonitrile.

### Fluorescence quantum yield
Fluorescence quantum yields were determined by the comparative method published by Williams et al. [29]. The

integrated fluorescence intensities of a known dye and the tested compound were compared and the fluorescence quantum yields were calculated using the following equation: $\Phi_x = \Phi_{st}\left(Grad_x / Grad_{st}\right)(\eta_x^2/\eta_{st}^2)\Phi_x$, where st and x denote the standard and test respectively, while $\Phi$ is the fluorescence quantum yield. Grad is the gradient obtained from the plot of integrated fluorescence intensity vs absorbance of the dye at the excitation wavelength. $\eta$ represents the refractive index of the used solvents.

## Cell culture

HeLa cells (obtained from a human cervix carcinoma) were cultured in Dulbecco's modified Eagle's medium (DMEM) (Life Technologies) supplemented with 10% fetal bovine serum (FBS) (Life Technologies), 100 IU/mL penicillin and 100 µg mL$^{-1}$ (Life Technologies) in humidified atmosphere at 37 °C with 5% $CO_2$. HeLa cells were passaged at 80% confluency and split 1:10 in fresh media and discontinued after passage 15.

## Confocal imaging

Hela cells were plated on chambered coverglass (Thermo Scientific Nunc Lab-Tek II) and cultured overnight in the maintenance medium in humidified atmosphere at 37 °C with 5% $CO_2$. Cells were incubated with 20 µg mL$^{-1}$ of fluo-CNOs for 2, 5, 12, 24 and 48 h. As a control, the cells were left untreated (data not shown). After incubation, the cells were rinsed three times with phosphate buffered saline (PBS) (0.1 M, pH 7.4), fixed in a combination of paraformaldehyde (3%) and PBS and incubated with a solution of Hoechst 33342 (5 µg mL$^{-1}$) (Sigma) for 20 min. Finally, the cells were rinsed three times and filled with PBS. Confocal fluorescence imaging was then carried out with a Nikon A1R laser scanning microscope and a plan apo 20× DIC M and a plan apo VC 60× oil DIC N2 objective. In order to switch the fluorescence on and off, the cells were incubated respectively with an acidic PBS solution (pH 4.5) and a basic PBS solution (pH 8.5) for 1 h before imaging.

## Viability assay

For the cytotoxicity assays, the cells were seeded at $5 \times 10^4$ cells in in 96-well plates and incubated overnight at 37 °C in a 5% $CO_2$ humidified environment. Fluo-CNOs were suspended in DMEM culture medium at final concentrations of 1, 2, 5, 10 and 20 µg mL$^{-1}$, followed by sonication for 10 min at 37 kHz. The cells were exposed to the different concentrations of fluo-CNO for 12, 24, 48 and 72 h. As a positive control for cytotoxicity, the cells were incubated with 5% DMSO. Cell viability was determined using the cell proliferation reagent WST-1 (Roche Applied Sciences). After aspiration of the culture medium, a mixture of DMEM and WST1 reagent (1/10 volume) was added to each well. After 2 h of incubation at 37 °C with

5% $CO_2$, the absorbance at 450 nm was measured in a standard plate reader (VICTOR3 V Multilabel Readers, PerkinElmer) (690 nm reference wavelength). The viability of cells in each well was determined as a relative percentage to the control well. Data were reported as a mean of three replicates and the error bars were the results of the standard deviations of these replicates.

## Supporting Information

### Supporting Information File 1
Additional Experimental Data.
[http://www.beilstein-journals.org/bjnano/content/supplementary/2190-4286-8-188-S1.pdf]

## References

1. Gottlieb, R. A.; Giesing, H. A.; Zhu, J. Y.; Engler, R. L.; Babior, B. M. *Proc. Natl. Acad. Sci. U. S. A.* **1995,** *92,* 5965–5968. doi:10.1073/pnas.92.13.5965
2. Varadi, A.; Rutter, G. A. *Endocrinology* **2004,** *145,* 4540–4549. doi:10.1210/en.2004-0241
3. Tannock, I. F.; Rotin, D. *Cancer Res.* **1989,** *49,* 4373–4384.
4. Damaghi, M.; Wojtkowiak, J. W.; Gillies, R. J. *Front. Physiol.* **2013,** *4,* 370. doi:10.3389/fphys.2013.00370
5. Kozin, S. V.; Shkarin, P.; Gerweck, L. E. *Cancer Res.* **2001,** *61,* 4740–4743.
6. Fang, B.; Wang, D.; Huang, M.; Yu, G.; Li, H. *Int. J. Neurosci.* **2010,** *120,* 591–595. doi:10.3109/00207454.2010.505353
7. Wen, J.; Xu, Y.; Li, H.; Lu, A.; Sun, S. *Chem. Commun.* **2015,** *51,* 11346–11358. doi:10.1039/C5CC02887F
8. Ugarte, D. *Nature* **1992,** *359,* 707–709. doi:10.1038/359707a0
9. Ugarte, D. *Carbon* **1995,** *33,* 989–993. doi:10.1016/0008-6223(95)00027-B
10. Kuznetsov, V. L.; Chuvilin, A. L.; Butenko, Y. V.; Mal'kov, I. Yu.; Titov, V. M. *Chem. Phys. Lett.* **1994,** *222,* 343–348. doi:10.1016/0009-2614(94)87072-1
11. Delgado, J. L.; Herranz, M. Á.; Martín, N. *J. Mater. Chem.* **2008,** *18,* 1417. doi:10.1039/b717218d
12. Molina-Ontoria, A.; Chaur, M. N.; Plonska-Brzezinska, M. E.; Echegoyen, L. *Chem. Commun.* **2013,** *49,* 2406–2408. doi:10.1039/c3cc39077b
13. Li, Y.; Kröger, M.; Liu, W. K. *Nanoscale* **2015,** *7,* 16631–16646. doi:10.1039/C5NR02970H
14. Bartelmess, J.; Giordani, S. *Beilstein J. Nanotechnol.* **2014,** *5,* 1980–1998. doi:10.3762/bjnano.5.207

15. Flavin, K.; Kopf, I.; Del Canto, E.; Navio, C.; Bittencourt, C.; Giordani, S. *J. Mater. Chem.* **2011,** *21,* 17881–17887. doi:10.1039/c1jm12217g

16. Yang, M.; Flavin, K.; Kopf, I.; Radics, G.; Hearnden, C. H. A.; McManus, G. J.; Moran, B.; Villalta-Cerdas, A.; Echegoyen, L. A.; Giordani, S.; Lavelle, E. C. *Small* **2013,** *9,* 4194–4206. doi:10.1002/smll.201300481

17. Bartelmess, J.; Frasconi, M.; Balakrishnan, P. B.; Signorelli, A.; Echegoyen, L.; Pellegrino, T.; Giordani, S. *RSC Adv.* **2015,** *5,* 50253–50258. doi:10.1039/C5RA07683H

18. Bartelmess, J.; De Luca, E.; Signorelli, A.; Baldrighi, M.; Becce, M.; Brescia, R.; Nardone, V.; Parisini, E.; Echegoyen, L.; Pompa, P. P. *Nanoscale* **2014,** *6,* 13761–13769. doi:10.1039/C4NR04533E

19. Frasconi, M.; Marotta, R.; Markey, L.; Flavin, K.; Spampinato, V.; Ceccone, G.; Echegoyen, L.; Scanlan, E. M.; Giordani, S. *Chem. – Eur. J.* **2015,** *21,* 19071–19080. doi:10.1002/chem.201503166

20. d'Amora, M.; Rodio, M.; Bartelmess, J.; Sancataldo, G.; Brescia, R.; Zanacchi, F. C.; Diaspro, A.; Giordani, S. *Sci. Rep.* **2016,** *6,* No. 33923. doi:10.1038/srep33923

21. Giordani, S.; Bartelmess, J.; Frasconi, M.; Biondi, I.; Cheung, S.; Grossi, M.; Wu, D.; Echegoyen, L.; O'Shea, D. F. *J. Mater. Chem. B* **2014,** *2,* 7459–7463. doi:10.1039/C4TB01087F

22. Flavin, K.; Kopf, I.; Murtagh, J.; Grossi, M.; O'Shea, D. F.; Giordani, S. *Supramol. Chem.* **2012,** *24,* 23–28. doi:10.1080/10610278.2011.622381

23. Çetindere, S.; Çoşut, B.; Yeşilot, S.; Durmuş, M.; Kiliç, A. *Dyes Pigm.* **2014,** *101,* 234–239. doi:10.1016/j.dyepig.2013.10.015

24. Deniz, E.; Isbasar, G. C.; Bozdemir, Ö. A.; Yildirim, L. T.; Siemiarczuk, A.; Akkaya, E. U. *Org. Lett.* **2008,** *10,* 3401–3403. doi:10.1021/ol801062h

25. Yamada, K.; Toyota, T.; Takakura, K.; Ishimaru, M.; Sugawara, T. *New J. Chem.* **2001,** *25,* 667–669. doi:10.1039/b100757m

26. Bartelmess, J.; Baldrighi, M.; Nardone, V.; Parisini, E.; Buck, D.; Echegoyen, L.; Giordani, S. *Chem. – Eur. J.* **2015,** *21,* 9727–9732. doi:10.1002/chem.201500877

27. Aigner, D.; Freunberger, S. A.; Wilkening, M.; Saf, R.; Borisov, S. M.; Klimant, I. *Anal. Chem.* **2014,** *86,* 9293–9300. doi:10.1021/ac502513g

28. Roy, D.; Chhowalla, M.; Wang, H.; Sano, N.; Alexandrou, I.; Clyne, T. W.; Amaratunga, G. A. J. *Chem. Phys. Lett.* **2003,** *373,* 52–56. doi:10.1016/S0009-2614(03)00523-2

29. Williams, A. T. R.; Winfield, S. A.; Miller, J. N. *Analyst* **1983,** *108,* 1067–1071. doi:10.1039/an9830801067

# Enhancement of mechanical and electrical properties of continuous-fiber-reinforced epoxy composites with stacked graphene

Naum Naveh[*1,2], Olga Shepelev[2] and Samuel Kenig[1,2]

## Abstract

Impregnation of expandable graphite (EG) after thermal treatment with an epoxy resin containing surface-active agents (SAAs) enhanced the intercalation of epoxy monomer between EG layers and led to further exfoliation of the graphite, resulting in stacks of few graphene layers, so-called "stacked" graphene (SG). This process enabled electrical conductivity of cured epoxy/SG composites at lower percolation thresholds, and improved thermo-mechanical properties were measured with either Kevlar, carbon or glass-fiber-reinforced composites. Several compositions with SAA-modified SG led to higher dynamic moduli especially at high temperatures, reflecting the better wetting ability of the modified nanoparticles. The hydrophilic/hydrophobic nature of the SAA dictates the surface energy balance. More hydrophilic SAAs promoted localization of the SG at the Kevlar/epoxy interface, and morphology seems to be driven by thermodynamics, rather than the kinetic effect of viscosity. This effect was less obvious with carbon or glass fibers, due to the lower surface energy of the carbon fibers or some incompatibility with the glass-fiber sizing. Proper choice of the surfactant and fine-tuning of the crosslink density at the interphase may provide further enhancements in thermo-mechanical behavior.

## Introduction

Carbon nanotubes (CNTs) have been suggested as an efficient conductive filler because of the outstanding electrical properties and the high aspect ratio. CNT-modified carbon epoxy composites have been studied, where the CNTs are either dispersed in the matrix and/or grafted on the carbon fibers [1,2].

However, the cost of CNTs limits intensive industrial applications. Other treatments have been attempted, among these, oxidation of the carbon fibers, plasma treatment, radiation, modification with rubber, silica, carbon or other nanoparticles, showing interesting enhancements in interlaminar shear strength

(ILSS), fracture toughness, fatigue life and related properties [2-6].

Graphite nanoplatelets (GNPs) or stacked graphene (SG) have been developed as a low-cost conductive alternative [7]. GNPs can be produced by intercalation of the graphitic layers with an appropriate agent followed by exfoliation of the graphite flakes. Exfoliation is obtained by rapid heating resulting in conversion of the intercalant to a gas phase forcing the adjacent graphene layers to separate. Consequently, formation of worm-like accordion structured materials takes place with partially separated graphite sheets, i.e., expanded graphite (EG), characterized by a high expansion ratio of 100–400 cm$^3$/g. For instance, the increase to about 200 cm$^3$/g caused a thickness increase of about 80–100 times by a thermal shock at 600 °C [8]. Sonication in an acetone bath allowed for further exfoliation and separation of the loosely connected graphite nanosheets.

Further size reduction of these large (several micrometers long) structures produces fine particles consisting of a few layers of graphene loosely joined together, i.e., SG or GNP, also called few layered graphene (FLG). The exfoliation volume is governed by the structure of the starting expandable graphite, exfoliation temperature and heat rate [9]. The largest increase in volume to 300 cm$^3$/g at 900 °C was obtained by exfoliating graphite treated by a mixture of H$_2$SO$_4$/HNO$_3$/KMnO$_4$ at a ratio of 1:9:3:0.44 over an immersing time of 150 min in formic acid [10]. Intercalation with 98% HNO$_3$ followed by hydrolysis resulted in the the formation of graphite nitrate with negligible damage to the sp$^2$ graphite lattice. An interlayer distance of 0.336 nm was measured. Nevertheless, numerous multi-pores ranging from 2 to 10 nm were also detected. The acid and hydroxy groups on the multi-pore walls promote the interaction of EG with organic compounds, more specifically, with monomers before curing and with polymer segments after curing, thus contributing to the mechanical properties and percolation threshold reduction of conductive polymer/graphite nanocomposites [11,12].

Graphite intercalation compounds (GIC) may provide a plausible high-yield source for polymer nanocomposites [8]. However, most of the methods described in the literature either require expensive chemicals and/or are characterized by low yields of the final material, and therefore are hardly applicable for mass production.

Low percolation thresholds have been demonstrated in polymer compositions with nanosized fillers. The high aspect ratio and large surface area of graphene, along with the high electrical conductivity, promote percolation thresholds much lower than with metallic powders, carbon fibers or carbon black [13].

Epoxy resins are used as a matrix in high-performance composite materials for aerospace structures, coatings and adhesives for a variety of applications. Epoxy systems combined with reinforcing fibers provide composites with high strength and stiffness, ease of molding complex shapes and environmental resistance at low densities. The properties of epoxy systems can be varied as a function of the molecular weight or the functionality of the hardener constituent, by variations in processing conditions or by changing the ratio between hardener and monomer. Incorporation of functional silanes can improve the dispersibility of fillers in an epoxy system and increase the mechanical properties of the cured resin. The combination of SG and epoxy fiber composites was hardly studied. Nevertheless, it may offer special properties by reinforcing the epoxy matrix and providing higher electrical conductivities depending on the localization of the SG. Consequently, the present investigation deals with epoxy-based conductive compositions containing treated stacked graphene and continuous fabric reinforcement based on carbon fibers, Aramid and glass fibers.

# Experimental
## Materials
Diglycidyl ether of bisphenol A (DGEBA) (DER 331, Dow Chemical Company) with epoxy equivalent weight (EEW) 182–192; triethylenetetramine (TETA) hardener, amine equivalent weight 24 (LEUNA-Harze GmbH); graphite intercalated compound (GIC) of 30–50 mesh, 3.1% sulfur (3772, Anthracite Industries, Inc. a subsidiary of Asbury Carbons); surface-active agents (SAAs) for SG treatment used in this study: polyether polyol ($M_W$ = 4000, hydroxyl number: 28 mg KOH/g, (Grade 4200 from Bayer)), octylphenol ethoxylate (Triton X-100, HLB = 13.5, and Triton X-15, HLB = 4.9), as well as 3-methacryloxypropyltrimethoxysilane (MEMO) and (3-glycidyloxypropyl)trimethoxysilane (GLYMO) (Sigma-Aldrich); fabrics used: 3k carbon fiber of plain weave, 200 g/m$^2$ (Primetex ZB type 43199 from Hexcel), Kevlar of plain weave, 450 g/m$^2$ (Type 745) and fiberglass fabric of plain weave, 300 g/m$^2$.

## Preparation of expanded graphite (EG)
The commercial sulfuric acid intercalated expandable graphite (GIC 3772) was subjected to thermal shock at 600–620 °C in a preheated muffle furnace in air, with further heating of the expanded material for 15–20 min to perform homogeneous exfoliation of the graphite sheets into stacked graphene (SG) consisting of layered graphene structures.

## Preparation of epoxy compositions
The properties of epoxy-based compositions with various concentrations of EG incorporated by different techniques were investigated. The principle method comprised the following steps: impregnation at elevated temperatures of EG in epoxy resin

premixed with SAAs, further size reduction of EG worm-like particles using intensive mixing, and degassing of the paste-like epoxy/SG compositions in vacuum to remove the entrapped air. Two nonionic surfactants (Triton X100 and X-15) with different hydrophilic/lyophilic balance (HLB) were used in order to evaluate the thermodynamic effect on the localization of the SG. Hardener TETA was added to the mixture before specimens casting.

The basic formulation (by weight) was as follows: epoxy: 100 parts; SAA: 1 pph; expanded graphite (EG): 2.5 pph (or 2.1 wt %); hardener TETA: 14.1 pph.

## Fabrication of composite materials

Composite laminates were prepared using carbon fiber (CF) fabric, Kevlar fabric alone or a combination of CF/Kevlar combinations, and fiberglass (FG) fabrics. CF was used as received, and Kevlar was cleaned by dipping in isopropyl alcohol (IPA) with further drying.

FG was used as received or modified by silanes and surfactants. FG specimens (150 × 150 mm) were dipped in solutions of MEMO and GLYMO silanes in IPA/water. The silane/IPA/water ratio was 2:90:10. Acetic acid (2 g) was added to adjust the pH value of the solution to 5.0. Wet specimens were rinsed with IPA, dried at room temperature and finally cured at 120 °C for 30 min.

Specimens of FG fabrics were heat-treated at 600 °C for 2 h to burn out the sizing material and dried at 150 °C just before dipping into a variety of treatment solutions. Solutions of (3-aminopropyl)triethoxysilane (AMEO), Triton X-15 and TETA in IPA were used as modifiers of the FG surface.

Laminates were fabricated by the hand lay-up technique using brush and roller to apply the matrix composition on the fabric plies. The samples were designed to provide a thickness of 2.5–3.0 mm. The fiber volume fraction was controlled by applying pressure to the laminates to a predetermined thickness. The samples were cured under pressure for two days at ambient temperature, and after that post-cured at 80 °C for 4 h and at 120 °C for 2 h.

## Characterization

The thermo-mechanical properties of the compositions were measured at 1 Hz according to ASTM D 4065 using a DMA-Dynamic Mechanical Analysis (Q800 TA Instruments). Flexural testing followed ASTM D790 (3 point bending) at 1.3 mm/min. Electrical resistivity, both surface and volume, was determined with an electrometer (Keithley 6517D). Typically, the characterization comprised five specimens with stan-dard deviations of 5–8%. Morphology of the composite materials was characterized with high-resolution scanning electron microscopy (Zeiss). Specimens were cut from samples frozen in liquid nitrogen.

# Results and Discussion
## Composite materials based on Kevlar

The electrical, mechanical and thermo-mechanical properties of composite materials prepared with Kevlar fabrics are exhibited in Table S1 (Supporting Information File 1). Laminated composites based on Kevlar fabrics with epoxy/SG matrix demonstrated good electrical properties, despite the insulating nature of the fabric. Enhanced rigidity in three-point bending and increased DMA storage moduli were achieved for compositions where EG was impregnated with epoxy resin modified with the surfactants Triton X-100, Triton X-15 or MEMO. These results are in good correlation with the changes in morphology of the composite materials determined by SEM. It can be seen in Figure 1 that the morphology of the composite materials changes depending on the composition of the matrix. Combination of epoxy resin with Triton X-100 and MEMO provides improved wetting of the Kevlar fabric with the matrix compound. Kevlar filaments are covered with adhered particles of SAA/SG, while laminates prepared with the same neat epoxy or unmodified epoxy/SG exhibit bare surfaces of the fabric. Triton X-100 and MEMO have lower viscosities than Triton X-15 and Polyol 4200, this supports their contribution to better wetting.

For compositions in which epoxy resin was modified by hydrophobic Triton X-15 or GLYMO the fiber coverage is less pronounced. Some uncovered sections of Kevlar filaments can be observed in Figure 1e,f. This is in spite of the very low viscosity of GLYMO. The hydrophilic/hydrophobic nature of the SAA dictates the surface energy balance, such that more hydrophilicity (thus, higher surface energies) drives the treated nanoparticles to the fiber/matrix interface, due to the higher surface energy of the Kevlar fibers. The morphology is thermodynamically driven, and the proper choice of the surfactant controls the localization of SG at the interface. However, a higher concentration of SG on the fibers does not translate into better mechanical properties. Composites with Polyol 4200 or Triton X-15 show the highest flexural strengths in spite of the larger viscosities and the, supposedly, unfavorable surface energy. We may speculate on the weak contribution of Triton X-100 and MEMO to strength, compared to Triton X-15 and Polyol 4200. The effect of better wetting is second to the more significant weakening effect of the interphase by the low molecular weight of the SAAs. Thus, to enhance the properties of the interface wetting is not sufficient. It might also be the case that more hydrophobic SAAs interact more strongly with SG, allowing for a better local dispersion. Further work is required to unveil the
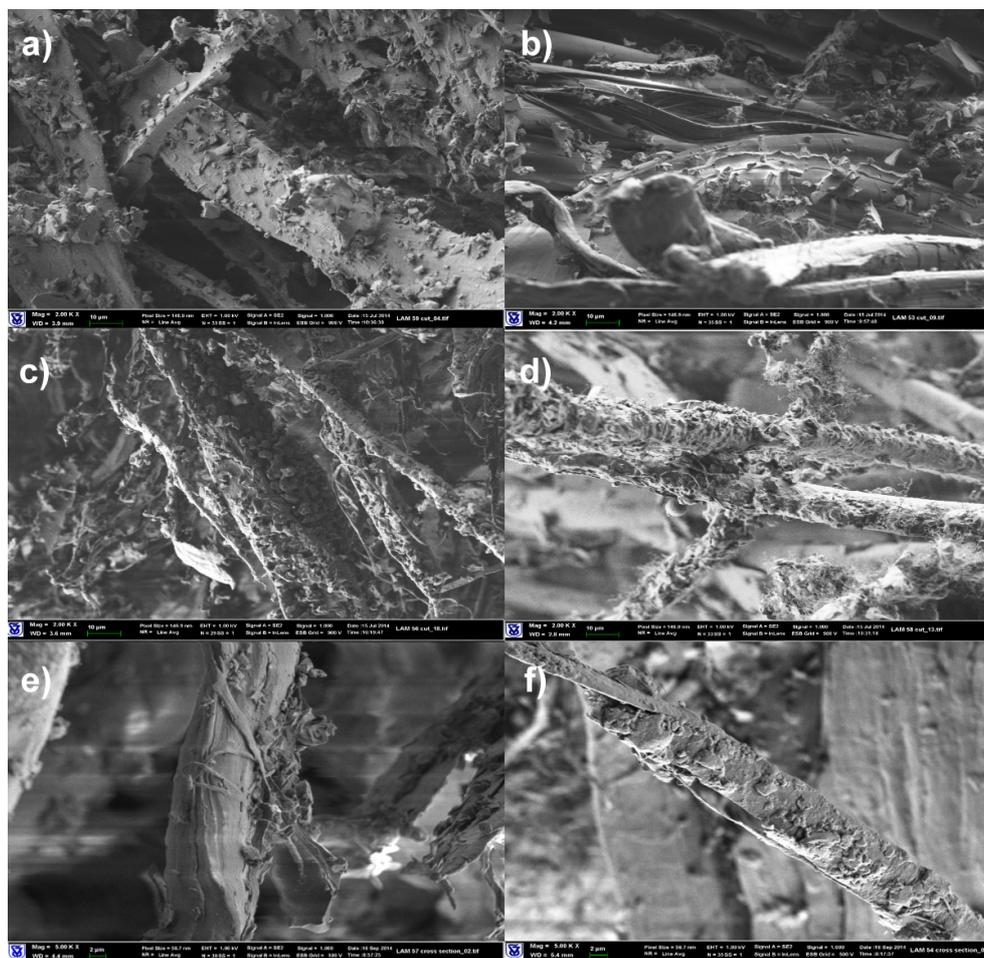
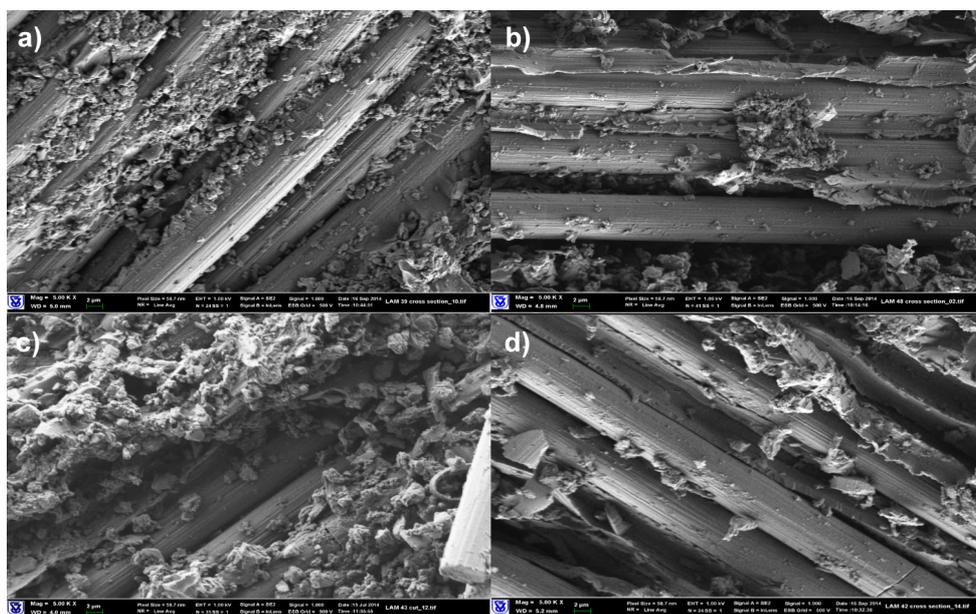**Figure 1:** SEM images of composite materials based on Kevlar fabric (magnification: 2000×). (a) Neat Epoxy matrix, (b) epoxy/SG (2.5 pph) matrix, (c) epoxy/Triton X-100 (1 pph)/SG (2.5 pph) matrix, (d) epoxy/MEMO (1 pph)/SG (2.5 pph) matrix, (e) epoxy/Triton X-15 (1 pph)/SG (2.5 pph) matrix, (f) epoxy/GLYMO (1 pph)/SG (2.5 pph) matrix.

contributions of both thermodynamic and dynamic effects, but, in general, one can state that stronger interfaces are reflected in the higher flexural strength of the composites.

## Composite materials based on carbon fabrics

SEM images of composite materials based on carbon fabrics in Figure 2 did not reveal distinctive differences in morphology. Due to the lower surface energy of the carbon fibers, compared to Kevlar, the driving force for localization of the nanoparticles at the fiber/matrix interface is weaker, and less coverage of the fabric is obtained. The effect of SAAs on the flexural strength is either negligible or minor but negative, and SG agglomeration seen in Figure 2 is supporting these findings.

All laminated composites manifested increased DMA storage moduli. Composites with modified epoxy/SG matrices demonstrated a significant increase of storage moduli at elevated tem-

peratures, and higher Young's moduli (Table S2, Supporting Information File 1). The distributed SG within the epoxy matrix contributes to increase in modulus, a 10% increase is seen in the range of 25–100 °C, and a significant 60% increase is exhibited at 120 °C with either SG treated with Triton X-100 or MEMO. Further exfoliation of SG by SAAs leads to higher moduli, and in the case of Polyol 4200 the modulus is almost doubled compared to the neat matrix. Again, the higher viscosity of Polyol 4200 is not detrimental to its role in enhancing the properties, and the good interaction with SG is due to a low surface energy.

The surface resistivity of the composite materials with epoxy/ SG matrix systems dropped by 7–8 orders of magnitude, but the volume resistivity remained at the level of carbon fabrics/neat epoxy composite. Resistivities of the carbon/epoxy composite without SG are already lower than the lowest resistivities
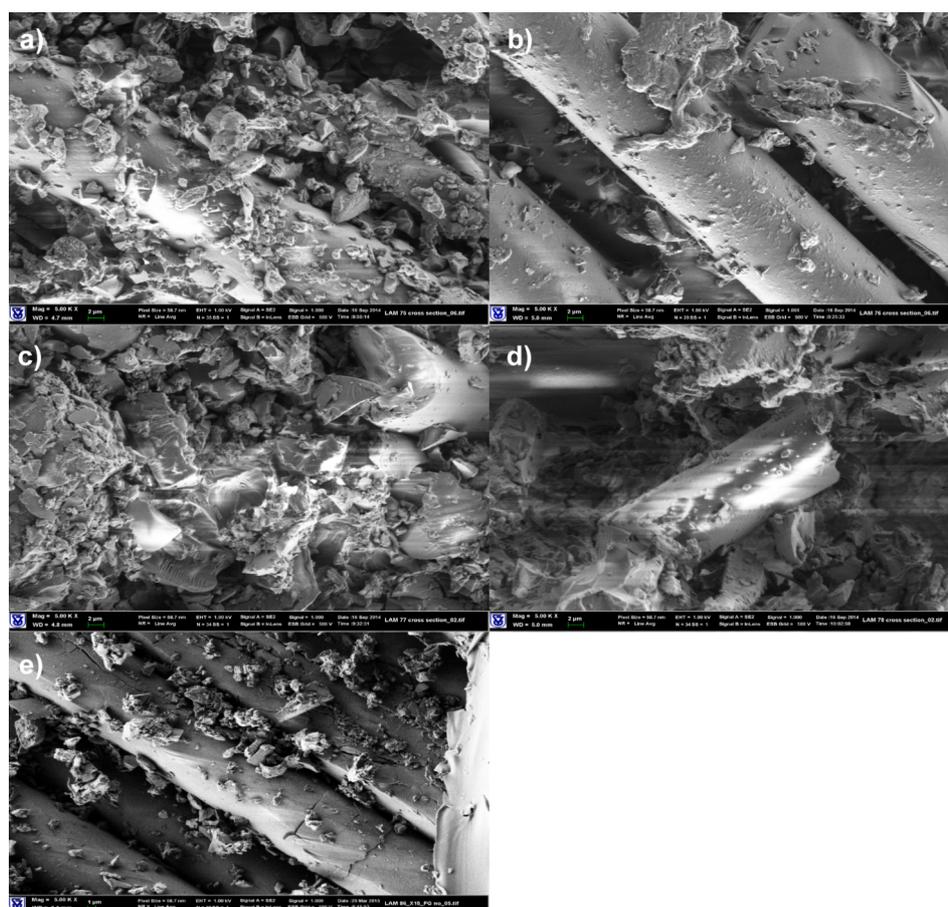
**Figure 2:** SEM images of composite materials based on carbon fabrics (magnification 5000×). (a) Neat epoxy matrix, (b) epoxy/MEMO (1 pph)/SG (2.5 pph) matrix, (c) epoxy/Triton X-100 (1 pph)/SG (2.5 pph) matrix, (d) epoxy/Triton X-15 (1 pph)/2.5 pph SG matrix.

achieved with Kevlar/epoxy/SG. Thus, the volume resistivity is not expected to decrease, yet the surface resistivities are reduced by the effect of SG in the matrix and reach lower values than their Kevlar/epoxy/SG counterparts, probably due to dispersion of some carbon fiber fraction in the resin during impregnation of the plies.

## Composite materials prepared with carbon fabric/Kevlar combinations

Composite laminates were prepared from combinations of Kevlar and carbon fabric. Asymmetric layering provides the possibility to create composite materials with regulated surface resistivity for the different external laminates of the composite structure. Laminated composites were prepared in two different configurations:

1. asymmetric structure: $(0/90 \text{ CF})_3/(0/90 \text{ Kev})_3$,
2. symmetric structure: $(0/90 \text{ CF})_2/(0/90 \text{ Kev})_1/(0/90 \text{ CF})_1/(0/90 \text{ Kev})_1/(0/90 \text{ CF})_2$.

The properties of the composite materials are presented in Table S3 and Table S4 (Supporting Information File 1). Laminated composites fabricated with the first configuration manifested increased DMA storage moduli, especially for the composition with epoxy/Triton X-15 which consistently showed higher moduli at all temperatures up to 120 °C (Table S3, Supporting Information File 1). Increased Young's moduli were determined for all materials in a three-point-bend loading, while stress at yield was mostly unaffected. The $T_g$ evaluated from the

tan δ values of the DMA showed some scatter but remained at roughly the same level as the unmodified resin system.

The properties of laminated composite materials prepared with the second configuration are demonstrated in Table S4 (Supporting Information File 1). The introduction of SG leads to enhanced moduli, however, the various surface treatments do not further contribute to the moduli beyond these values. Interestingly, at the highest temperature of 120 °C, the relatively high values of DMA storage moduli are comparable with those of composites prepared with 10 ply CF/neat epoxy matrix. The enhancement in DMA storage moduli of composites with epoxy/SAA/SG binding matrices in comparison with the neat epoxy matrix seems to reflect the better wetting ability of the nanomodified matrix, which is expected to improve as temperature rises and is likely to explain the high moduli at 120 °C.

Surface resistivities of the asymmetric laminate in Table S3 demonstrate the ability to control one-sided conductivity or gradient conductivities of up to three orders of magnitude in a composite structure. Surface resistivities for both symmetric and asymmetric laminates are expectedly similar to the all-carbon laminates.

Table S4 indicates that, again, Kevlar plies interleaved between carbon plies do not prevent volume conductivity, especially with Triton X-15 and MEMO surfactants where resistivity is only one order of magnitude higher than the all-carbon laminates.

## Composite materials based on fiberglass fabrics

SEM images of FG/epoxy-laminated composites indicated no marked differences in the morphology of composite materials with the investigated SG modified matrices. The epoxy based compositions do not provide sufficient wetting and coverage of fiberglass filaments, even when surfactants were added (Figure 3).

The properties of laminated composite materials based on FG fabrics are summarized in Table S5 (Supporting Information File 1). As can be seen, significant improvements in electrical properties were achieved due to a percolation network being formed by the conductive matrix between the insulating fiberglass filaments. Surface and volume resistivities dropped down by 7–9 orders of magnitude. However, The thermo-mechanical properties of the composite materials indicated some deterioration. The DMA storage moduli slightly decreased, especially at elevated temperatures. Young's moduli determined by 3-point bending remained at the level of the neat epoxy composites. A

significant decrease in stress at yield values was observed. The reason for the latter deterioration could be attributed to the increased rigidity of the laminates expressed as lower strain at yield, or the incompatibility between the FG sizing and the various SAAs leading to agglomeration in the matrix phase, as shown in Figure 3.

Experiments aimed at modification of the FG surface, using silanes with either acrylic or epoxy functionalities, in order to provide better wetting of filaments, were carried out, as explained in detail in the Experimental section. Examination of morphology and mechanical properties of laminated materials did not reveal any substantial changes in the performance of the laminates (Figure 4 and Table S5, Supporting Information File 1). It can be concluded that these types of silanes do not contribute to the improvement of FG/epoxy-based matrix compatibility.

Further FG treatments were carried out with (3-aminopropyl)triethoxysilane (AMEO), triethylenetetramine (TETA), and



**Figure 3:** SEM images of composite materials based on FG fabrics (magnification: 5000×). (a) Neat Epoxy matrix, (b) epoxy/SG (2.5 pph) matrix, (c) epoxy/Triton X-100 (1 pph)/SG (2.5 pph) matrix, (d) epoxy/MEMO (1 pph)/SG (2.5 pph) matrix, (e) epoxy/Triton X-15 (1 pph)/SG (2.5 pph) matrix.
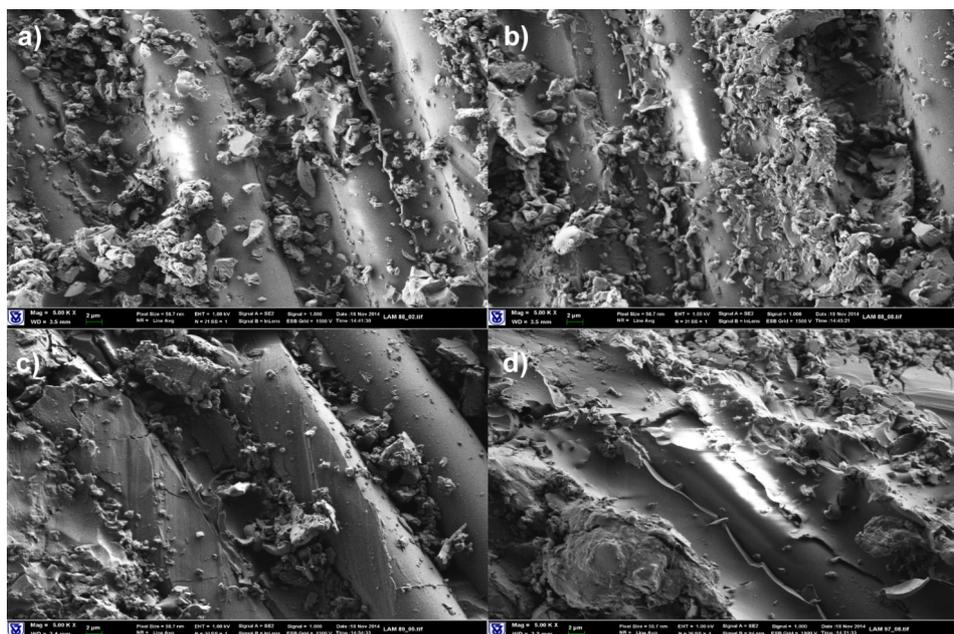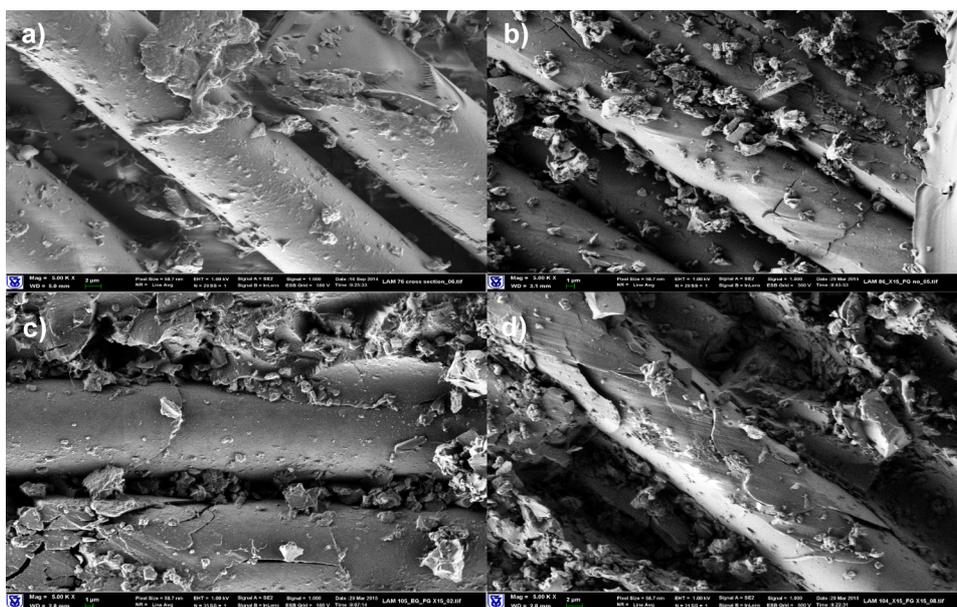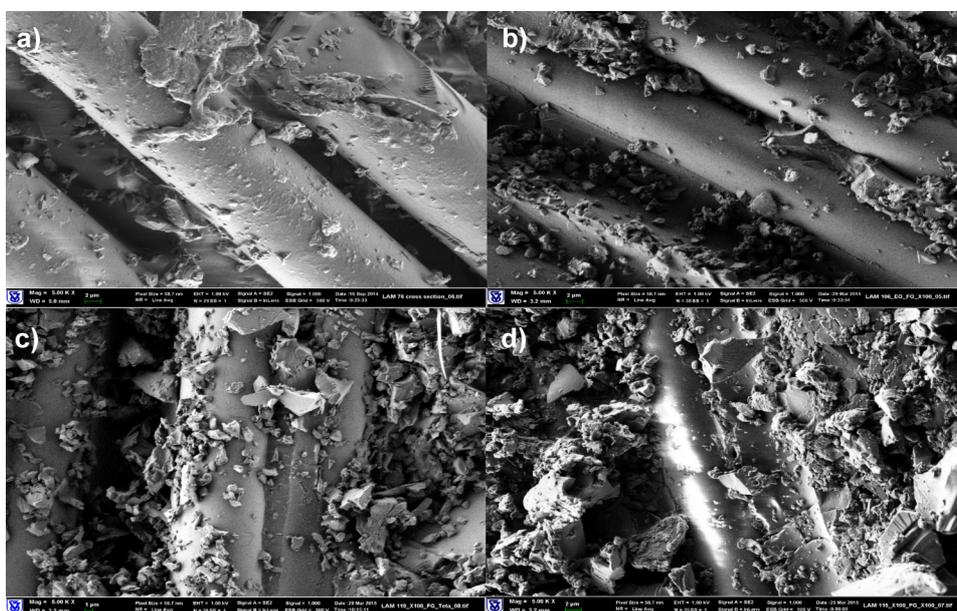
**Figure 4:** SEM images of composite materials based on FG fabrics, FG treated with MEMO or GLYMO (magnification: 5000×). (a) Epoxy/MEMO silane/SG (2.5 pph) matrix, FG treated with MEMO; (b) epoxy/MEMO SG (2.5 pph) matrix, FG treated with MEMO; (c) epoxy/SG (2.5 pph) matrix, FG treated with GLYMO; (d) epoxy/Triton X-100 (1 pph)/SG (2.5 ph) matrix, FG treated with GLYMO.

the non-ionic SAAs Triton X-100 and Triton X-15 dissolved in IPA at various concentrations. Results of electrical and thermo-mechanical tests are shown in Table S6 (Supporting Information File 1). As can be seen, modification of FG with AMEO led to deterioration of the properties of the laminated composite. After the addition of epoxy-functionalized silane GLYMO as a surfactant to the matrix composition the values of DMA storage moduli, Young's modulus and stress at yield were restored.

Interesting results were observed with the non-ionic hydrophobic SAA Triton X-15. Addition of this SAA to the epoxy/SG matrix blend, as well as the modification of FG with 1% solution of Triton X-15 led to improved mechanical properties. The SAA concentration must be balanced an excess of this SAA during FG modification (2% solution) had a negative effect on the stress at yield.

Improved thermo-mechanical properties of laminated FG composites were observed also with moderate concentrations of Triton X-100 applied for FG modification and incorporated into the matrix composition. Here, an excess of SAA in the FG fabric also results in a decrease of the stress at yield value. Increase in DMA storage moduli and stress at yield was noticed when FG was treated with TETA hardener. Further crosslinking at the interphase may take place when testing at high temperatures, explaining the higher modulus at 100 °C. Fine

tuning of the epoxy composition at the interphase may turn out to be an interesting way to improve its properties, and there is some potential in this practice to improve properties.

SEM images of composite materials based on modified FG are shown in Figures 5–7. Morphology of the composite materials in Figure 5 explains the observed improvement in mechanical properties of epoxy/Triton X-15/SG laminated materials. The nanoparticle platelets cover the surface of FG fibers modified with Triton X-15. With Triton X-100 modification of FG, Figure 6, the coverage is less obvious since bare and decorated sections of FG filaments can be found. These results suggest a rather hydrophobic sizing has been applied to the FG, and this is reasonable since this sizing is recommended for epoxy compositions. The SEM image of laminates prepared with TETA modification of FG fibers in Figure 6 demonstrates a great number of small matrix fragments bonded to the surface of FG fiber. As can be seen, in composites based on GLYMO-modified epoxy matrix and AMEO-modified FG, more epoxy matrix fragments are bonded to the surface of FG filaments (Figure 7). The morphology of laminated FG composite materials depends on the chemical structure of FG surface layers and is finally reflected in the mechanical properties of the composites.

The unknown composition of the sizing material used for the FG filaments could be the reason for FG/matrix composition incompatibility. Hence, experiments were carried out to remove

**Figure 5:** SEM images of composite materials based on FG fabrics, FG treated with 2% Triton X-15 (magnification: 5000×). (a) Epoxy/SG (2.5 pph) matrix; (b) epoxy/Triton X-15 (1 pph)/SG (2.5 pph) matrix; (c) epoxy/SG (2.5 pph) matrix, FG treated with 2% Triton X-15; (d) epoxy/Triton X-15 (1 pph)/SG (2.5 pph) matrix, FG treated with 2% Triton X-15.



**Figure 6:** SEM images of composite materials based on FG fabrics, FG treated with Triton X-100 or TETA (magnification: 5000×). (a) Epoxy/SG (2.5 pph) matrix; (b) epoxy/SG (2.5 pph) matrix, FG treated with 2% Triton X-100; (c) epoxy/Triton X-100 (1 pph)/SG (2.5 pph) matrix, FG treated with 2% TETA; (d) epoxy/Triton X-100 (1 pph)/SG (2.5 pph) matrix, FG treated with 1% Triton X-100.

the original treatment in order to reveal an influence of selected FG impregnating material on the properties of laminated composites. Subsequently, composites based on heat-treated FG fabrics that were further modified with SAAs (procedure is described in the Experimental section) demonstrated higher DMA storage moduli, especially at elevated temperatures as shown in Table S7 (Supporting Information File 1). FG modified with Triton X-15, AMEO and TETA, and the epoxy/SG matrix modified with Triton X-15 and GLYMO manifested improved performance after removal of the commercial sizing.
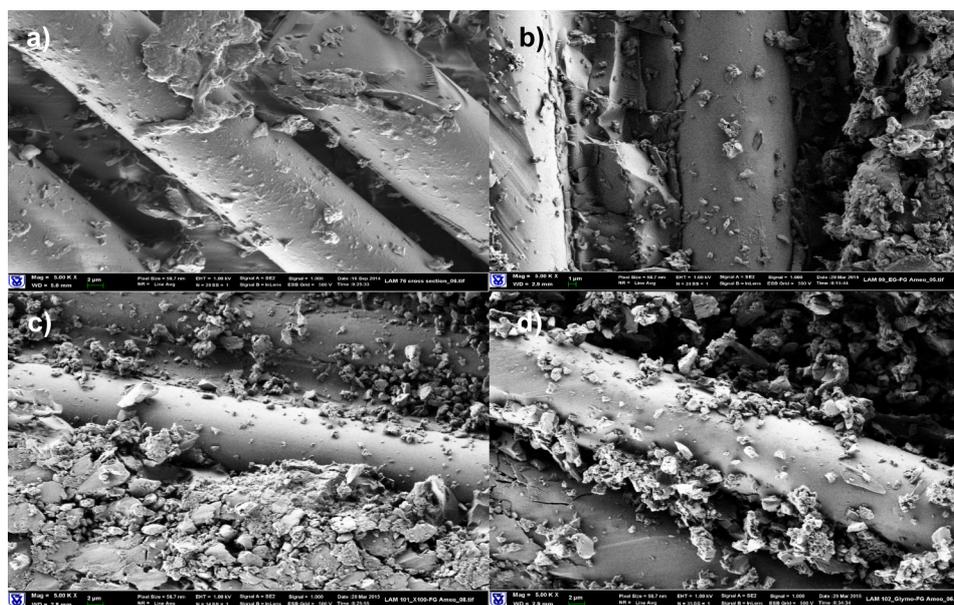
**Figure 7:** SEM images of FG fabric based composite materials, FG treated with 2% AMEO (magnification: 5000×). (a) Epoxy/SG (2.5 pph) matrix; (b) epoxy/SG (2.5 pph) matrix, FG treated with 2% AMEO; (c) epoxy/Triton X-100 (1 pph)/SG (2.5 pph) matrix, FG treated with 2% AMEO; (d) epoxy/GLYMO (1 pph)/SG (2.5 pph) matrix, FG treated with 2% AMEO.

## Conclusion

The exfoliation of commercially available expandable graphite (EG) is enhanced by impregnation in an epoxy/surfactant mixture, allowing on to downsize the nanoplatelets to "stacked" graphene (SG) or few graphene layers (FGL) platelets. The effect of such exfoliation on continuous-fiber-reinforced epoxy composites was studied in terms of electrical conductivity and thermo-mechanical properties at low loadings. Modification of epoxy resin by SAAs prior to EG impregnation enhanced intercalation of epoxy monomer between EG layers and further exfoliation. Morphology and compositions are reflected by the mechanical properties of composite laminates. Electrically conductive laminated composites, based on Kevlar or glass fibers, can be obtained by introducing treated stacked graphene at low concentrations.

The morphology of composite materials based on Kevlar fabrics varies depending on the composition of the matrix. Laminates prepared with neat epoxy or unmodified epoxy/SG exhibited bare surfaces of Kevlar fibers. Modification of epoxy resin with Triton X-100 and methacrylate-functionalized silane (MEMO) resulted in improved wetting of the Kevlar filaments with the nanocomposite matrix. Enhanced rigidity in three-point bending and increased DMA storage moduli were achieved for composites where EG was impregnated with epoxy resin modified by Triton X-100, Triton X-15 and MEMO. All Kevlar-based laminates demonstrated improved electrical properties, indicating the possibility to obtain electrically conductive composite mate-

rials on the basis of electrically insulating fibers using binder matrices with low content of inexpensive SG. Both surface and volume resistivity dropped by 7–8 orders of magnitude.

Laminated composites based on carbon fabric showed increased DMA storage moduli, improved thermal stability and increased Young's moduli. SEM images of SAA-modified epoxy/SG/carbon fabric composites revealed no distinctive effect of the epoxy composition on the morphology of laminates, yet the compounds demonstrated significant improvement in thermal stability at elevated temperatures, especially with a polyol surfactant. A reduction of electrical surface resistivity was registered, while volume resistivity remained at the level determined for the neat epoxy composite.

Composite materials consisting of Kevlar/carbon fabric combinations with epoxy/SAA/SG manifested increase in DMA storage moduli and enhanced Young's moduli. Asymmetric layering of the Kevlar/carbon layers provided the possibility to form hybrid composite materials with regulated surface resistivity for the different external plies of the laminate.

For fiberglass-based composites with various nanocomposite matrices no marked differences in the morphology were noticed. Epoxy-based compositions, even modified with SAA, do not provide sufficient wetting and coating of fiberglass filaments. DMA storage moduli and Young's moduli remained at the level of the neat epoxy matrix, or were even reduced

slightly. Treatment of fiberglass fabrics using moderate concentrations (1–2%) of non-ionic SAA (Triton X-15 and Triton X-100), or TETA hardener in IPA allowed for improvement of mechanical and thermo-mechanical properties of FG composites. Electrical properties manifested significant improvement as surface and volume resistivities dropped by 7–9 orders magnitude.

Thermomechanical properties of FG-reinforced laminated composite materials can be improved by removal of the commercial sizing and modification of the fiberglass surface using moderate concentrations (about 1%) of either AMEO, non-ionic Triton X-15 or even TETA hardener. We suggest to develop strategies to fine-tune the crosslink density at the interphase. A graded crosslink density transition from the fiber to the matrix may prove beneficial.

## Supporting Information

Supporting Information contains all tables with the measured thermo-mechanical and electrical properties of all samples.

### Supporting Information File 1
Thermo-mechanical and electrical properties.
[http://www.beilstein-journals.org/bjnano/content/supplementary/2190-4286-8-191-S1.pdf]

## Acknowledgements

## References
1. Zhang, J. Different surface treatments of carbon fibers and their influence on the interfacial properties of carbon fiber/epoxy composites. Ph.D. Thesis, Ecole Central Paris, France, 2012.
2. Tiwari, S.; Bijwe, J. *Procedia Technol.* **2014,** *14,* 505–512. doi:10.1016/j.protcy.2014.08.064
3. Tien Phong, N.; Gabr, M. H.; Anh, L. H.; Duc, V. M.; Betti, A.; Okubo, K.; Chuong, B.; Fujii, T. *J. Mater. Sci.* **2013,** *48,* 6039–6047. doi:10.1007/s10853-013-7400-z
4. Liu, L.; Li, L.; Gao, Y.; Tang, L.; Zhang, Z. *Compos. Sci. Technol.* **2013,** *77,* 101–109. doi:10.1016/j.compscitech.2012.12.015
5. Sprenger, S. *J. Compos. Mater.* **2015,** *49,* 53–63. doi:10.1177/0021998313514260
6. Njuguna, J.; Pielichowski, K.; Alcock, J. R. *Adv. Eng. Mater.* **2007,** *9,* 10. doi:10.1002/adem.200700118
7. Drzal, L. T.; Fukushima, H. Expanded graphite and products produced therefrom. U.S. Patent US020060231792A1, Oct 19, 2006.
8. Ramanathan, T.; Abdala, A. A.; Stankovich, S.; Dikin, D. A.; Herrera-Alonso, M.; Piner, R. D.; Adamson, D. H.; Schniepp, H. C.; Chen, X.; Ruoff, R. S.; Nguyen, S. T.; Aksay, I. A.; Prud'Homme, R. K.; Brinson, L. C. *Nat. Nanotechnol.* **2008,** *3,* 327–331. doi:10.1038/nnano.2008.96
9. Lee, S.; Cho, D.; Drzal, L. T. *J. Mater. Sci.* **2005,** *40,* 231–234. doi:10.1007/s10853-005-5715-0
10. Shengtao, Z.; Anyan, G.; Huanfang, G.; Xiangqian, C. *Int. J. Ind. Chem.* **2011,** *2,* 123–130.
11. Afanasov, I. M.; Shornikova, O. N.; Kirilenko, D. A.; Vlasov, I. I.; Zhang, L.; Verbeeck, J.; Avdeev, V. V.; Van Tendeloo, G. *Carbon* **2010,** *48,* 1862–1865. doi:10.1016/j.carbon.2010.01.055
12. Afanasov, I. M.; Morozov, V. A.; Kepman, A. V.; Ionov, S. G.; Seleznev, A. N.; Van Tendeloo, G.; Avdeev, V. V. *Carbon* **2009,** *47,* 263–270. doi:10.1016/j.carbon.2008.10.004
13. Kim, H.; Abdala, A. A.; Macosko, C. W. *Macromolecules* **2010,** *43,* 6515–6530. doi:10.1021/ma100572e

## License and Terms

# Freestanding graphene/MnO$_2$ cathodes for Li-ion batteries

Şeyma Özcan[*], Aslıhan Güler, Tugrul Cetinkaya[*§], Mehmet O. Guler and Hatem Akbulut

## Abstract

Different polymorphs of MnO$_2$ (α-, β-, and γ-) were produced by microwave hydrothermal synthesis, and graphene oxide (GO) nanosheets were prepared by oxidation of graphite using a modified Hummers' method. Freestanding graphene/MnO$_2$ cathodes were manufactured through a vacuum filtration process. The structure of the graphene/MnO$_2$ nanocomposites was characterized using X-ray diffraction (XRD) and Raman spectroscopy. The surface and cross-sectional morphologies of freestanding cathodes were investigated by scanning electron microcopy (SEM). The charge–discharge profile of the cathodes was tested between 1.5 V and 4.5 V at a constant current of 0.1 mA cm$^{-2}$ using CR2016 coin cells. The initial specific capacity of graphene/α-, β-, and γ-MnO$_2$ freestanding cathodes was found to be 321 mAhg$^{-1}$, 198 mAhg$^{-1}$, and 251 mAhg$^{-1}$, respectively. Finally, the graphene/α-MnO$_2$ cathode displayed the best cycling performance due to the low charge transfer resistance and higher electrochemical reaction behavior. Graphene/α-MnO$_2$ freestanding cathodes exhibited a specific capacity of 229 mAhg$^{-1}$ after 200 cycles with 72% capacity retention.

## Introduction

Nowadays low cost, clean and sustainable energy storage requirements with high performance are of great need because of rapid improvement of mobile and stationary electronic applications. Lithium-ion batteries have been one of the key energy storage devices to meet these energy demands since the last century [1]. However, increased capacity and energy density of Li-ion batteries is desired in order to store more, efficient energy. Although researchers have made significant progress in the development of high capacity anode electrodes, such as

SnO$_2$ [2], Sn-Ni [3], and Si [4], the performance of cathodes has been bottlenecked by the energy density and capacity of Li-ion batteries. In commercial Li-ion batteries, LiCoO$_2$, which has a specific capacity of 140 mAh/g, is used as the cathode material although it has many disadvantages such as high cost, toxicity and limited sources. Therefore, researchers have been developing different cathode materials such as LiMn$_2$O$_4$ and LiFePO$_4$, which have a capacity of merely 150 mAh/g and 170 mAh/g, respectively [5,6].

Manganese dioxide ($MnO_2$) is one of the most promising metal oxide as a replacement for the Li-ion electrode material owing to its high theoretical capacity (308 mAh/g), environmental friendliness and low cost [7]. It has gained a great deal of attention because of its wide application in areaa such as catalysts for Li–air batteries [8], molecular sieves [9] and electrodes in rechargeable batteries [10-12]. However, its drastic volume change, aggregation problems, and poor electronic conductance (resulting in low cyclability) has extremely limited its potential applications [10,13]. Therefore, nanostructured $MnO_2$ has been fabricated and used with carbon materials to achieve excellent conductivity with a large specific surface area [14]. On one hand, reducing the dimensions of the electrode particles from the micrometer to the nanometer regime can enhance the ion exchange rate in Li-ion batteries [15], while on the other hand, supporting the cathode with carbon materials such as carbon nanotubes, acetylene black and graphene, helps to improve the conductivity of the electrode. Among these carbon materials graphene has become one the most attractive carbon support materials with its extraordinary properties.

Graphene is a two-dimensional (2D) atomic-scale honeycomb lattice made of carbon atoms. Its unique properties such as high electrical and thermal conductivity, high chemical stability, large specific surface area and high mechanical strength have made graphene one of the most promising materials for energy storage devices [16]. In recent reports, $MnO_2$/graphene composite electrodes have been used in order to enhance the electrical conductivity and prevent volume change during charge–discharge cycles [17].

$MnO_2$ has many crystallographic polymorphs including α-, β-, δ-, γ-, ε-, and λ-$MnO_2$. The electrochemical characteristics of $MnO_2$, such as electrocatalytic activity, specific capacity and oxygen reduction reaction, vary according to its crystalline structure and morphology [18]. However, there are few reports explaining their electrochemical reaction response relating to their different manganese oxide crystalline structures.

In this work, different polymorphs of $MnO_2$ (α-, β-, and γ-) were produced by a microwave hydrothermal method. Freestanding graphene/$MnO_2$ cathodes were manufactured through a vacuum filtration process without using any additional additives such as a binder. The effect of the different polymorphs, α-, β-, and γ-$MnO_2$, on the structural and electrochemical properties of the manufactured, freestanding graphene/$MnO_2$ cathodes was investigated. To the best of our knowledge, this study is the first to investigate the electrochemical performance of freestanding graphene/$MnO_2$ cathodes for Li-ion batteries. The freestanding graphene/$MnO_2$ cathodes exhibit a high specific capacity and excellent electrochemical cycling performance.

# Experimental
## Preparation of $MnO_2$ phases
The α-, β-, and γ-$MnO_2$ phases were synthesized by a microwave-assisted hydrothermal method. α-$MnO_2$ nanowires and β-$MnO_2$ nanorods were prepared according to our previous report [8]. To prepare γ-$MnO_2$, 1.83 mg of $(NH_4)_2S_2O_8$, 1.35 mg of $MnSO_4$ and 3 mmol were dissolved in 80 mL of distilled water. Then, the resulting solution was transferred into a Teflon (PTFE)-lined autoclave, sealed and placed in a microwave oven (Milestone ROTOSYNTH). The hydrothermal reaction was carried out for 60 min at 90 °C. Then the autoclave was cooled down to room temperature and the as-prepared black precipitate was filtered and washed several times with distilled water. γ-$MnO_2$ was obtained after drying at 80 °C in a vacuum oven for 12 h.

## Preparation of freestanding graphene/$MnO_2$ electrodes
Graphite oxide (GO) was synthesized according to a modified Hummers' method [19] by using pretreated graphite flakes as the starting material, as explained in a previous study [17]. The freestanding graphene/$MnO_2$ cathodes were prepared via a vacuum filtration technique. Firstly, 30 mg of GO was dissolved in 50 mL distilled water by ultrasonication for 1 h to obtain GO. Then 30 mg of as-synthesized $MnO_2$ was added to the solution and ultrasonicated for another 1 h. The GO/$MnO_2$ solution was filtered on a PVDF membrane by a vacuum filtration technique. In order to reduce the GO to graphene, the as-synthesized GO/$MnO_2$ was subjected to a hydrazine solution after filtration of GO. 5.6 mL of a hydrazine solution was slowly poured onto GO/$MnO_2$ and filtered. Then the obtained solid was peeled-off from the PVDF membrane and the freestanding graphene/$MnO_2$ was obtained (approximate thickness is 15 μm). This process was carried out for all $MnO_2$ phases.

The microstructural morphology of the freestanding graphene/ α-, β-, and γ-$MnO_2$ composite cathodes was characterized using scanning electron microscopy (SEM). The structural and phase investigation of the freestanding cathodes was tested using X-ray diffraction (XRD) and Raman spectroscopy.

## Electrochemical characterization of graphene/$MnO_2$ cathodes
A CR2016 coin cell was used to investigate the electrochemical performance of the produced freestanding composite cathodes, assembled in an Ar-filled glove box. In this coin cell, the produced cathodes were used as a working electrode, and lithium foil was used as an anode. 1 M lithium hexafluorophosphate ($LiPF_6$) was dissolved in ethylene carbonate (EC) and dimethyl carbonate (DMC) (EC/DMC, 1:1 v/v), which was used as the electrolyte. In order to separate the electrodes, a microporous

polypropylene membrane was used. Electrochemical tests of the cathodes were implemented between 1.5 and 4.5 V at a constant current density of 0.1 mA cm$^{-2}$. The specific capacity of the freestanding graphene/MnO$_2$ cathodes was calculated depending on the active mass of the graphene/MnO$_2$ composite (about 20 mg) on Al foil. The resistance of the electrodes was evaluated via electrochemical impedance spectroscopy (EIS) using a Nyquist curve in the frequency range 1000 kHz–0.1 Hz with an AC amplitude of 10 mV with fresh electrode applied before the electrochemical cycling test.

## Results and Discussion

The surface morphologies of α-, β-, and γ-polymorphs of MnO$_2$ and as-prepared graphene/MnO$_2$ samples were investigated by SEM analysis. Figure 1a shows that the α-MnO$_2$ nanostructure composed of uniform nanowires have 1–2 µm length and 40–60 nm average diameter. β-MnO$_2$ (Figure 1b) shows that the as-prepared β-MnO$_2$ sample has a nanorod structure with 0.5–1 µm length and 20–40 nm average diameter. The γ-MnO$_2$ (Figure 1c) exhibits an urchin-like structure with 0.5–1 µm average diameter with very thin nanoneedles. The structure of graphene/MnO$_2$ nanocomposites was also investigated. It can be seen from Figure 1d,e that α-MnO$_2$ nanowires and β-MnO$_2$ nanorods were homogeneously distributed on the surface and between the layers of graphene. Moreover, it also indicates that the urchin-like γ-MnO$_2$ microspheres were wrapped by transparent graphene layers. In order to illustrate the dispersion of MnO$_2$ polymorphs (i.e. not only the surface of graphene sheets, but also interlayers of graphene), cross-sectional characterization of graphene/MnO$_2$ composite layers was implemented
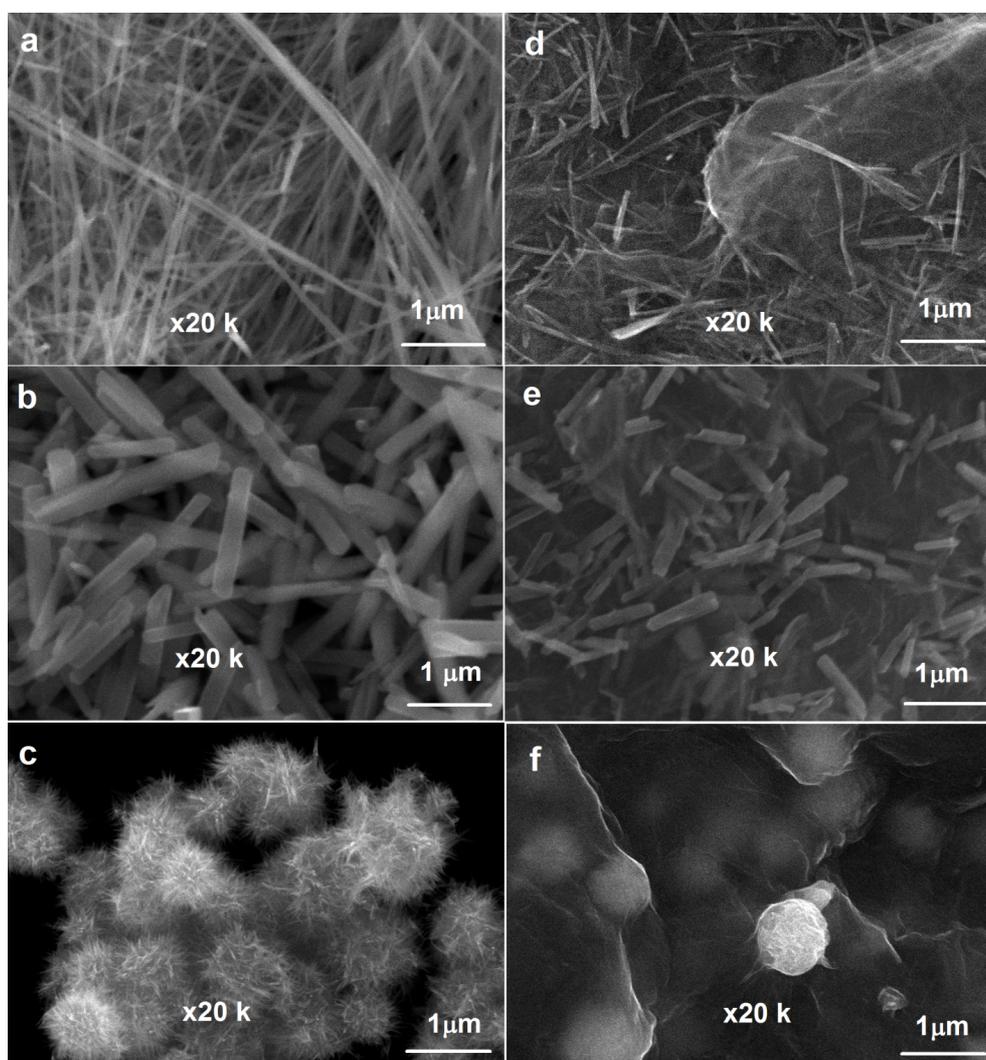


**Figure 1:** Surface morphology of (a) α-MnO$_2$, (b) β-MnO$_2$, (c) γ-MnO$_2$, (d) graphene/α-MnO$_2$, (e) graphene/β-MnO$_2$, and (f) graphene/γ-MnO$_2$ freestanding cathodes.
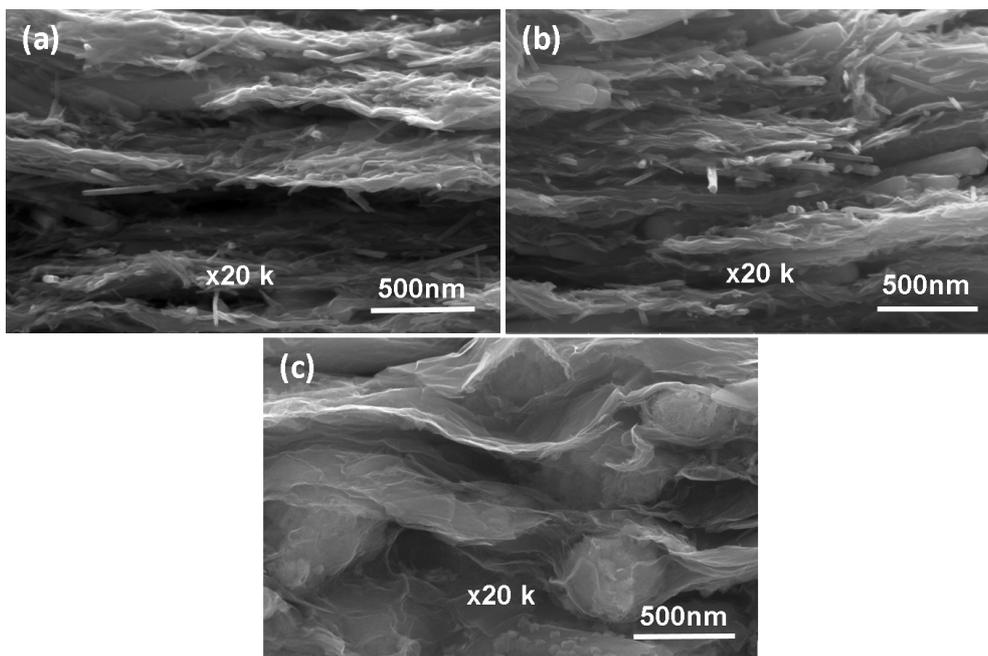
**Figure 2:** Cross-sectional SEM images of (a) graphene/α-MnO₂, (b) graphene/β-MnO₂, and (c) graphene/γ-MnO2 freestanding cathodes.

using SEM. As it can be seen from Figure 2, $\alpha$-MnO$_2$, $\beta$-MnO$_2$ and $\gamma$-MnO$_2$ structures were homogenously distributed and fixed between graphene layers.

Figure 3a shows the XRD patterns of $\alpha$-, $\beta$-, and $\gamma$-MnO$_2$. The typical reflection peaks of $\alpha$-MnO$_2$ are observed at 2$\theta$ values of 12.7°, 18.0°, 28.6°, 36.7°, 38.6°, 41.9°, 49.7°, 56.4° 60.2°, 65.4°, 69.6°, and 72.9° corresponding to (110), (200), (310), (400), (211), (420), (301), (600), (521), (002), (541), and (312) planes of $\alpha$-MnO$_2$ crystals [20,21]. For $\beta$-MnO$_2$, reflection peaks were observed at 2$\theta$ values of 28.7º, 37.4º, 41.0º, 42.9º, 46.1º, 56.7º, 59.4º, 65.0º, 66.8º, 67.3º, 72.3º, 79.7º and 86.6º corresponding to (110), (101), (200), (111), (210), (211), (220),

(002), (310), (301), (202) and (321) planes of $\beta$-MnO$_2$ [22]. Lastly, for $\gamma$-MnO$_2$, reflection peaks were observed at 2$\theta$ values of 22.0°, 34.8°, 37.0°, 38.5°, 42.2°, 57.0°, 65.4° and 68.6°, corresponding to (101), (130), (210), (400), (211), (402), (020), (421) planes of $\gamma$-MnO$_2$ [23]. Figure 3b shows XRD patterns of graphene oxide, graphene/$\alpha$-MnO$_2$, graphene/$\beta$-MnO$_2$ and graphene/$\gamma$-MnO$_2$ composite structures. The graphene peak observed at a 2$\theta$ value of 25.8º indicates the (002) plane of carbon. However, there are still some remaining graphene oxide phases observed at 2$\theta$ values of 10.9º in graphene/$\alpha$-MnO$_2$ and graphene/$\beta$-MnO$_2$, while almost all graphene oxide is transformed to graphene in the graphene/$\gamma$-MnO$_2$ structure [24-26].
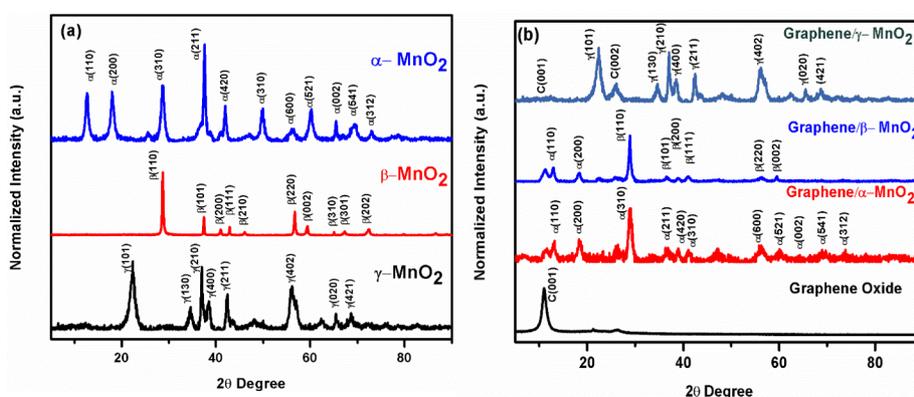


**Figure 3:** XRD patterns of (a) α-MnO₂, β-MnO₂, γ-MnO₂, (b) graphene/α-MnO₂, graphene/β-MnO₂, and graphene/γ-MnO₂ freestanding cathodes.

Further phase characterization of graphene/α-MnO$_2$, graphene/β-MnO$_2$ and graphene/γ-MnO$_2$ composites was performed via Raman spectroscopy using a 785 nm laser and the results are shown in Figure 4. Although the Raman spectrum of MnO$_2$ is generally used to characterize MnO$_2$ structures, MnO$_2$ structures may show different characteristic peaks due to different laser wavelengths and energy. Generally, in the Raman spectra of MnO$_2$, the peaks between 500 and 700 cm$^{-1}$ are attributed to the stretching mode of MnO$_6$ octahedra [27] and the weak peaks between 200 and 400 cm$^{-1}$ originate from the formation of Mn$_2$O$_3$ or Mn$_3$O$_4$ and correspond to the bending mode of O–Mn–O [28]. In the graphene/α-MnO$_2$ composite, α-MnO$_2$ shows three weak peaks at 289 cm$^{-1}$, 319 cm$^{-1}$ and 376 cm$^{-1}$ and one strong peak observed at 661 cm$^{-1}$. In graphene/β-MnO$_2$ composites, three weak peaks at 230, 330 and 385 cm$^{-1}$ and two strong peaks at 562 and 648 cm$^{-1}$ are observed. Graphene/β-MnO$_2$ exhibited two weak peaks at 314 and 367 cm$^{-1}$ and one strong peak at 658 cm$^{-1}$. The observed peaks

at around 1320 and 1590 cm$^{-1}$ are related to the D- and G-bands of graphene [29] in the graphene/MnO$_2$ composite structures.

In order to investigate the effect of different crystal structures of MnO$_2$ in the graphene/MnO$_2$ composites on the resistance of the cell, electrochemical impedance spectroscopy (EIS) measurements were performed and results are shown in Figure 5. The width of the Nyquist curves indicates the charge transfer resistance ($R_{ct}$) of the graphene/α-MnO$_2$, graphene/β-MnO$_2$ and graphene/γ-MnO$_2$ cathodes [30]. As seen from Figure 5, the graphene/β-MnO$_2$ composite cathode has the largest width, showing $R_{ct}$ = 102 Ω. Graphene/α-MnO$_2$ with a $R_{ct}$ = 42 Ω has a smaller width than that of graphene/γ-MnO$_2$ with $R_{ct}$ = 90 Ω. These $R_{ct}$ values indicate that the graphene/α-MnO$_2$ composite cathode has better electronic contact and conductivity among the produced freestanding graphene/MnO$_2$ cathodes [31].
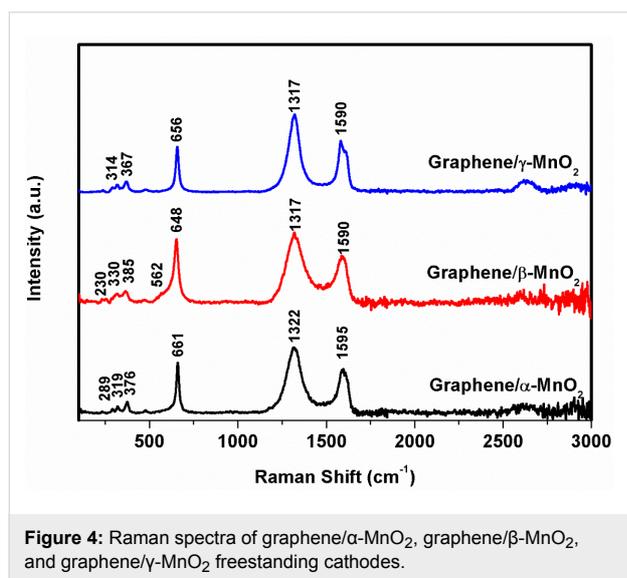


**Figure 4:** Raman spectra of graphene/α-MnO$_2$, graphene/β-MnO$_2$, and graphene/γ-MnO$_2$ freestanding cathodes.
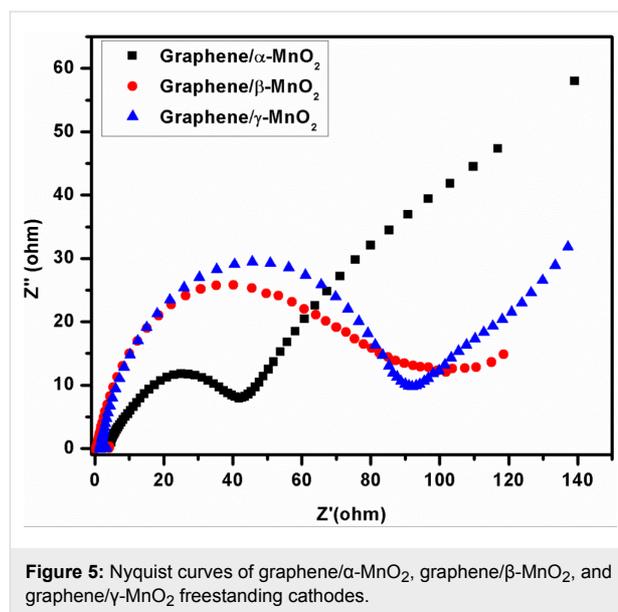


**Figure 5:** Nyquist curves of graphene/α-MnO$_2$, graphene/β-MnO$_2$, and graphene/γ-MnO$_2$ freestanding cathodes.
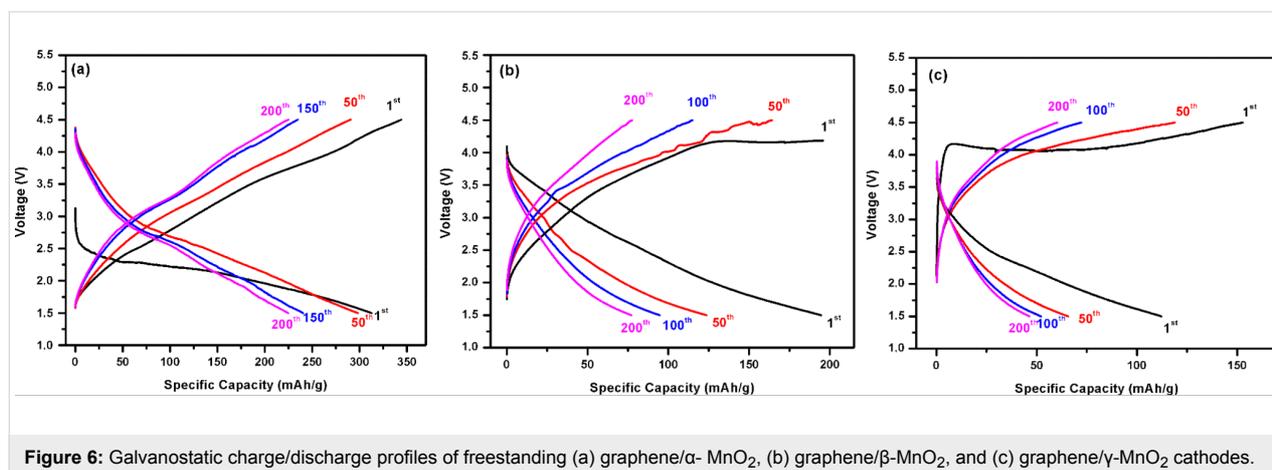


**Figure 6:** Galvanostatic charge/discharge profiles of freestanding (a) graphene/α- MnO$_2$, (b) graphene/β-MnO$_2$, and (c) graphene/γ-MnO$_2$ cathodes.

The electrochemical performance of the as-synthesized cathodes was first evaluated by galvanostatic charge/discharge cycling at a constant current density of 254 mA g$^{-1}$ in a voltage range from 1.5 to 4.5 V. In Figure 6, the typical charge/discharge profiles of freestanding graphene/α-MnO$_2$, graphene/β-MnO$_2$ and graphene/γ-MnO$_2$ cathodes are given for the 1st, 50th, 100th and 200th cycles. As shown in Figure 6a, the graphene-supported α-MnO$_2$ cathode exhibited a specific capacity of 321 mAhg$^{-1}$ upon first discharge with an open-circuit potential of about 3.2 V and an average voltage of approximately 2.25 V. It can also be seen that the capacity of the graphene/α-MnO$_2$ cathode was sustained with a small amount of capacity loss. This could be attributed to the wire-like structure of α-MnO$_2$ allowing ions to pass from the cathode. When the graphene-supported β-MnO$_2$ cathode was investigated (Figure 6b), it can be seen that the capacity was found to be much lower than for graphene/α-MnO$_2$. While the first discharge capacity of graphene/β-MnO$_2$ cathode was 198 mAhg$^{-1}$, the graphene/γ-MnO$_2$ cathode displayed a specific discharge capacity of 251 mAhg$^{-1}$ (Figure 6c). The specific capacity of both graphene-reinforced β-MnO$_2$ and γ-MnO$_2$ electrodes decreased dramatically with increasing number of cycles. This could be attributed to the poor electrical conductivity and the textural modification during Li$^+$ intercalation and de-intercalation processes. Cheng et. al. [32] prepared α-MnO$_2$ cathodes and demonstrated a discharge capacity of 204.4 mAhg$^{-1}$ for the first discharge with a constant current of 50 mAg$^{-1}$. In our work, the as-prepared α-MnO$_2$/graphene cathode was reached a specific capacity of 318 mAhg$^{-1}$. This is probably due to graphene reinforcement, which increases the conductivity and electrochemical reaction of α-MnO$_2$ with Li ions, as is reported in previous studies [10,13].

Figure 7 reveals the cycling stability of graphene/α-MnO$_2$, graphene/β-MnO$_2$, and graphene/γ-MnO$_2$ cathodes. A remarkable result is obtained from the graphene/α-MnO$_2$ cathode which has an initial capacity of 321 mAhg$^{-1}$. It can be seen that there is no sudden loss of capacity and between cycles 2 and 44 it exhibits almost a stable capacity of 305 mAhg$^{-1}$. The total capacity loss is 27% during 200 cycles. Graphene/β-MnO$_2$ and graphene/γ-MnO$_2$ cathodes were also cycled until the 200th cycle but they exhibited very poor capacity retention when compared with the graphene/α-MnO$_2$ cathode. Although both of these cathodes display a high capacity during the first cycle, the capacity value decreases dramatically during the second cycle. While the total capacity loss for the graphene/β-MnO$_2$ cathode was 61%, the graphene/γ-MnO$_2$ cathode showed a 55% capacity loss after 200 cycles. Tu et al. [33] also reported nanorods-shaped MnO$_2$-graphene cathodes and a γ-MnO$_2$ cathode, and they observed huge capacity reduction due to the formation of Li$_2$MnO$_3$.
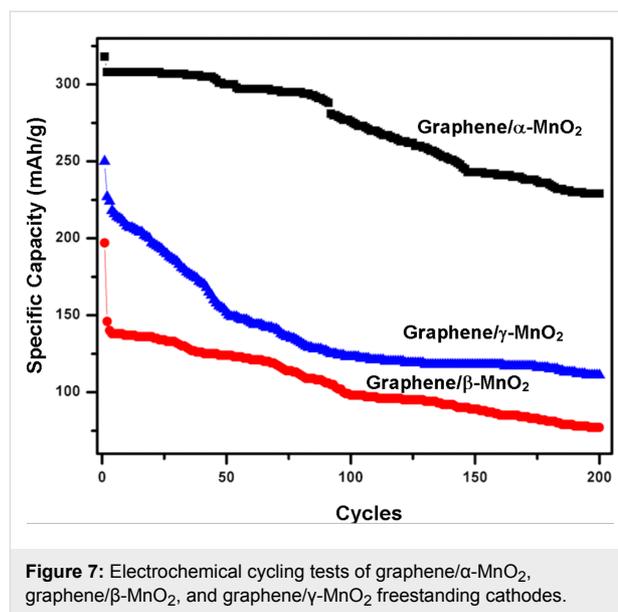


**Figure 7:** Electrochemical cycling tests of graphene/α-MnO$_2$, graphene/β-MnO$_2$, and graphene/γ-MnO$_2$ freestanding cathodes.

## Conclusion

A facile and rapid microwave-assisted hydrothermal method was demonstrated to synthesize α-, β-, and γ-MnO$_2$ phases. Freestanding graphene/MnO$_2$ was successfully prepared with no further additives. The prepared nanocomposite samples were operated as positive electrodes for Li-ion batteries. The SEM images showed that α-MnO$_2$ nanowires and β-MnO$_2$ nanorods were homogenously dispersed not only at the surface, but also in the interlayer space of grapheme layers. Moreover, urchin-like γ-MnO$_2$ microspheres were found wrapped by graphene nanosheets. The electrochemical cycling results demonstrated that the graphene/α-MnO$_2$ cathode showed the best electrochemical performance among all prepared samples with an achieved initial capacity of 321 mAhg$^{-1}$ and maintained its remarkable performance after many cycles. This study proved that α-MnO$_2$ nanowires with graphene reinforcement could be promising cathodes for Li-ion batteries due to the high capacity and long cycle life.

## Acknowledgements

## References

1. Ma, Z.; Zhao, T. *Electrochim. Acta* **2016,** *201,* 165–171. doi:10.1016/j.electacta.2016.03.200
2. Alaf, M.; Gultekin, D.; Akbulut, H. *Acta Phys. Pol., A* **2013,** *123,* 323–325. doi:10.12693/APhysPolA.123.323

3. Uysal, M.; Gul, H.; Alp, A.; Akbulut, H. *Int. J. Hydrogen Energy* **2014,** *39,* 21391–21398. doi:10.1016/j.ijhydene.2014.01.099

4. Tokur, M.; Algul, H.; Ozcan, S.; Cetinkaya, T.; Uysal, M.; Akbulut, H. *Electrochim. Acta* **2016,** *216,* 312–319. doi:10.1016/j.electacta.2016.09.048

5. Cetinkaya, T.; Tocoglu, U.; Uysal, M.; Guler, M. O.; Akbulut, H. *Microelectron. Eng.* **2014,** *126,* 54–59. doi:10.1016/j.mee.2014.05.028

6. Liu, D.; Cao, G. *Energy Environ. Sci.* **2010,** *3,* 1218–1237. doi:10.1039/b922656g

7. Zhao, G.; Zhang, D.; Zhang, L.; Sun, K. *Electrochim. Acta* **2016,** *202,* 8–13. doi:10.1016/j.electacta.2016.03.203

8. Ozcan, S.; Tokur, M.; Cetinkaya, T.; Guler, A.; Uysal, M.; Guler, M. O.; Akbulut, H. *Solid State Ionics* **2016,** *286,* 34–39. doi:10.1016/j.ssi.2015.12.016

9. Mallakpour, S.; Madan, M. *Carbohydr. Polym.* **2016,** *147,* 53–59. doi:10.1016/j.carbpol.2016.03.076

10. Cetinkaya, T.; Tokur, M.; Ozcan, S.; Uysal, M.; Akbulut, H. *Int. J. Hydrogen Energy* **2016,** *41,* 6945–6953. doi:10.1016/j.ijhydene.2015.12.092

11. Li, X.; Zhang, Y.; Zhong, Q.; Li, T.; Li, H.; Huang, J. *Appl. Surf. Sci.* **2014,** *313,* 877–882. doi:10.1016/j.apsusc.2014.06.096

12. Mao, W.; Ai, G.; Dai, Y.; Fu, Y.; Ma, Y.; Shi, S.; Soe, R.; Zhang, X.; Qu, D.; Tang, Z.; Battaglia, V. S. *J. Power Sources* **2016,** *310,* 54–60. doi:10.1016/j.jpowsour.2016.02.002

13. Li, J.; Zhao, Y.; Wang, N.; Ding, Y.; Guan, L. *J. Mater. Chem.* **2012,** *22,* 13002–13004. doi:10.1039/c2jm31583a

14. Cai, Z.; Xu, L.; Yan, M.; Han, C.; He, L.; Hercule, K. M.; Niu, C.; Yuan, Z.; Xu, W.; Qu, L.; Zhao, K.; Mai, L. *Nano Lett.* **2015,** *15,* 738–744. doi:10.1021/nl504427d

15. Ren, Y.; Armstrong, A. R.; Jiao, F.; Bruce, P. G. *J. Am. Chem. Soc.* **2010,** *132,* 996–1004. doi:10.1021/ja905488x

16. Özcan, S.; Cetinkaya, T.; Tokur, M.; Algül, H.; Guler, M. O.; Akbulut, H. *Int. J. Hydrogen Energy* **2016,** *41,* 9796–9802. doi:10.1016/j.ijhydene.2016.02.044

17. Wang, L.-y.; Wang, Y.; Zhang, H.-x.; Wang, X.-m. *New Carbon Mater.* **2015,** *30,* 48–53. doi:10.1016/S1872-5805(15)60175-5

18. Sun, M.; Lan, B.; Yun, L.; Ye, F.; Song, W.; He, J.; Diao, G.; Zheng, Y. *Mater. Lett.* **2012,** *86,* 18–20. doi:10.1016/j.matlet.2012.07.011

19. Hummers, W. S., Jr.; Offeman, R. E. *J. Am. Chem. Soc.* **1958,** *80,* 1339. doi:10.1021/ja01539a017

20. Thapa, A. K.; Ishihara, T. *J. Power Sources* **2011,** *196,* 7016–7020. doi:10.1016/j.jpowsour.2010.09.112

21. Thapa, A. K.; Pandit, B.; Thapa, R.; Luitel, T.; Paudel, H. S.; Sumanasekera, G.; Sunkara, M. K.; Gunawardhana, N.; Ishihara, T.; Yoshio, M. *Electrochim. Acta* **2014,** *116,* 188–193. doi:10.1016/j.electacta.2013.11.032

22. Singh, I. B.; Park, S. *Indian J. Chem.* **2015,** *54,* 46–51.

23. Kim, J. M.; Huh, Y. S.; Han, Y.-K.; Cho, M. S.; Kim, H. J. *Electrochem. Commun.* **2012,** *14,* 32–35. doi:10.1016/j.elecom.2011.10.023

24. Moon, I. K.; Lee, J.; Ruoff, R. S.; Lee, H. *Nat. Commun.* **2010,** *1,* No. 73. doi:10.1038/ncomms1067

25. Park, S.; An, J.; Potts, J. R.; Velamakanni, A.; Murali, S.; Ruof, R. S. *Carbon* **2011,** *49,* 3019–3023. doi:10.1016/j.carbon.2011.02.071

26. Shin, H.-J.; Kim, K. K.; Benayad, A.; Yoon, S.-M.; Park, H. K.; Jung, I.-S.; Jin, M. H.; Jeong, H.-K.; Kim, J. M.; Choi, J.-Y.; Lee, Y. H. *Adv. Funct. Mater.* **2009,** *19,* 1987–1992. doi:10.1002/adfm.200900167

27. Liang, S.; Teng, F.; Bulgan, G.; Zong, R.; Zhu, Y. *J. Phys. Chem. C* **2008,** *112,* 5307–5315. doi:10.1021/jp0774995

28. Luo, J.; Zhu, H. T.; Fan, H. M.; Liang, J. K.; Shi, H. L.; Rao, G. H.; Li, J. B.; Du, Z. M.; Shen, Z. X. *J. Phys. Chem. C* **2008,** *112,* 12594–12598. doi:10.1021/jp8052967

29. Krishnamoorthy, K.; Kim, G.-S.; Kim, S. J. *Ultrason. Sonochem.* **2013,** *20,* 644–649. doi:10.1016/j.ultsonch.2012.09.007

30. Zeng, Z. Y.; Tu, J. P.; Huang, X. H.; Wang, X. L.; Xiang, J. Y. *Thin Solid Films* **2009,** *517,* 4767–4771. doi:10.1016/j.tsf.2009.03.007

31. Ilango, P. R.; Prasanna, K.; Subburaj, T.; Jo, Y. N.; Lee, C. W. *Acta Mater.* **2015,** *100,* 11–18. doi:10.1016/j.actamat.2015.08.021

32. Cheng, F.; Zhao, J.; Song, W.; Li, C.; Ma, H.; Chen, J.; Shen, P. *Inorg. Chem.* **2006,** *5,* 2038–2044. doi:10.1021/ic051715b

33. Tu, F.; Wu, T.; Liu, S.; Jin, G.; Pan, C. *Electrochim. Acta* **2013,** *106,* 406–410. doi:10.1016/j.electacta.2013.05.108

## License and Terms

# Advances and challenges in the field of plasma polymer nanoparticles

Andrei Choukourov[*1], Pavel Pleskunov[1], Daniil Nikitin[1], Valerii Titov[2], Artem Shelemin[1], Mykhailo Vaidulych[1], Anna Kuzminova[1], Pavel Solař[1], Jan Hanuš[1], Jaroslav Kousal[1], Ondřej Kylián[1], Danka Slavínská[1] and Hynek Biederman[1]

## Abstract

This contribution reviews plasma polymer nanoparticles produced by gas aggregation cluster sources either via plasma polymerization of volatile monomers or via radio frequency (RF) magnetron sputtering of conventional polymers. The formation of hydrocarbon, fluorocarbon, silicon- and nitrogen-containing plasma polymer nanoparticles as well as core@shell nanoparticles based on plasma polymers is discussed with a focus on the development of novel nanostructured surfaces.

## Review

### Historical background

"A macromolecule is a molecule of high relative molecular mass, the structure of which essentially comprises the multiple repetition of units derived, actually or conceptually, from molecules of low relative molecular mass." "A polymer is a substance composed of macromolecules." These are the definitions the IUPAC gives to macromolecules and polymers, respectively [1]. The ubiquity of polymers in everyday life is due to the huge diversity of chemical composition and architecture they may possess, both factors leading to an extremely broad spec-

trum of polymer properties. Nevertheless, the word "plasma" was added to the title of this article to reflect the fact that this manuscript will not deal with conventional polymers per se, regardless of the attractiveness and utility of these may be, but will rather focus on materials that are created as a result of a low-temperature non-equilibrium plasma operating in organic vapours. The term "plasma polymer" was introduced in the 1960s to convey the interrelation between the use of a gas discharge and the formation of solid deposits from low molar mass

organic precursors [2-4], although the history of plasma polymers is much longer. Organic deposits created as by-products of electrical discharges have been known presumably since the end of the18th century (see [5] and references therein). The significant scientific interest in plasma polymers was motivated by the attractive possibility to introduce various organic monomers into the plasma, including those which do not polymerize by conventional chemical routes. A new kind of polymer with advanced properties was anticipated. It was however soon realized that these materials have little in common with conventional polymers due mainly to the fact that they typically have random, highly cross-linked and highly branched structures in which regularly repeating monomeric units can hardly be expected. The lack of predictable structure hampered the extensive use of plasma polymers in real world applications, although a multitude of potential utilizations have been suggested.

In the mid-twentieth century, such deposits were studied as possible candidates for the production of thin dielectric films for microelectronics [6]. The choice of hydrocarbon, halocarbon and organosilicon precursors in these studies logically stemmed from the requirement of the compatibility with technological processes used in the semiconductor industry. The formation of disperse polymeric particulates in the gas volume was also observed at about that time [7-10]. The phenomenon was earlier considered as unwanted and as something to be avoided; later, it laid a foundation for the field of dusty plasmas in which the research was focused on particle–plasma interactions [11]. A legacy from the semiconductor processing phase explains the fact that close attention was paid to silane-based plasmas [9,11-22] followed by hydrocarbon [16,17,23-27] and fluorocarbon plasmas [27-36].

## Gas aggregation sources

In recent years, scientific interest spread to the investigation of the properties of plasma polymer particles themselves, regardless of the effects their presence produces on the plasma. It was recognized that polymeric nanoparticles (NPs) can be highly desired in various fields including photonics [37] and biomedical applications where they can be used as biomolecule and drug carriers [38-40]. Gas aggregation cluster sources (GAS) were considered feasible for the synthesis of plasma polymer NPs with a tuneable size distribution, retention of functional groups and cross-link density. The concept of GAS was originally developed for the production of metal NPs by vacuum thermal evaporation with subsequent condensation of atomic metal vapours on a cool buffer gas and later thermal evaporation was replaced by magnetron sputtering [41]. At least one work investigated the formation of polymeric NPs by thermal evaporation of poly(*N*-vinyl-2-pyrrolidone) in a GAS [42].

At present, a typical GAS consists of a tubular vacuum chamber equipped with a DC or RF electrode (or magnetron) which is used to ignite a plasma and which serves as a source of material to be "vaporized" (Figure 1). In the case of the production of plasma polymer NPs, carbonaceous precursors are introduced into the GAS in the form of volatile vapours of organic monomers or as a result of evaporation or sputtering of a solid polymer target attached to the electrode. The latter process was shown to lead to a release of volatile fragments of macromolecules which can be further used as precursors for plasma polymerization [43-52]. Depending on the experimental conditions, plasma polymerization can be forced to proceed in a gas phase which results in the formation of NPs of different chemical and physical properties and with different size distribution. The GAS configuration offers an advantage of creating a co-axial gas flow to transport the NPs away from the discharge zone through an orifice into another vacuum chamber where they can be collected on solid supports.
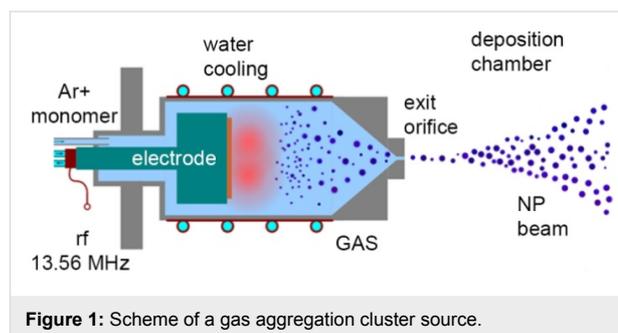


**Figure 1:** Scheme of a gas aggregation cluster source.

Figure 2a–d shows scanning electron microscopy (SEM) examples of NPs created as a result of plasma polymerization of *n*-hexane and hexamethyldisiloxane (HMDSO) [53] or as a result of RF magnetron sputtering of nylon [54] and poly(tetrafluoroethylene) (PTFE) [55]. One can readily judge the diversity of shape and morphology of the NPs with diameters ranging from tens to hundreds of nanometers. Here and further in this Review, for simplicity, we shall use the designation "NPs" to describe all particles in this size range having in mind that objects of hundreds of nanometers are more accurately described as submicrometer-sized particles.

## Charge of plasma polymer nanoparticles

It has been recognized that NPs grow via a three-step process involving nucleation, coagulation and growth by accretion. The nucleation stage is often considered to be governed by negative ions [19,56-59], leading to the formation of nanometer-sized nuclei. These embryonic clusters may be neutral or bear either negative or positive charge [60,61] which results in their effective coagulation into larger NPs with a typical diameter of 10–20 nm. Negative charge begins to dominate for NPs of this
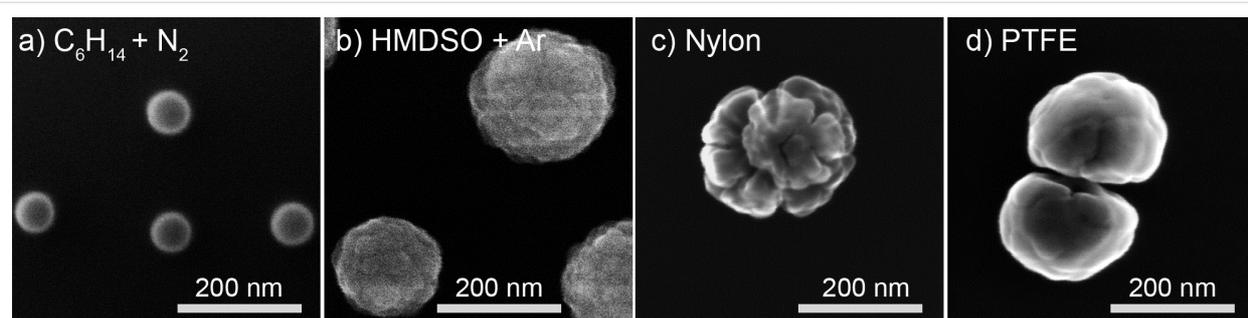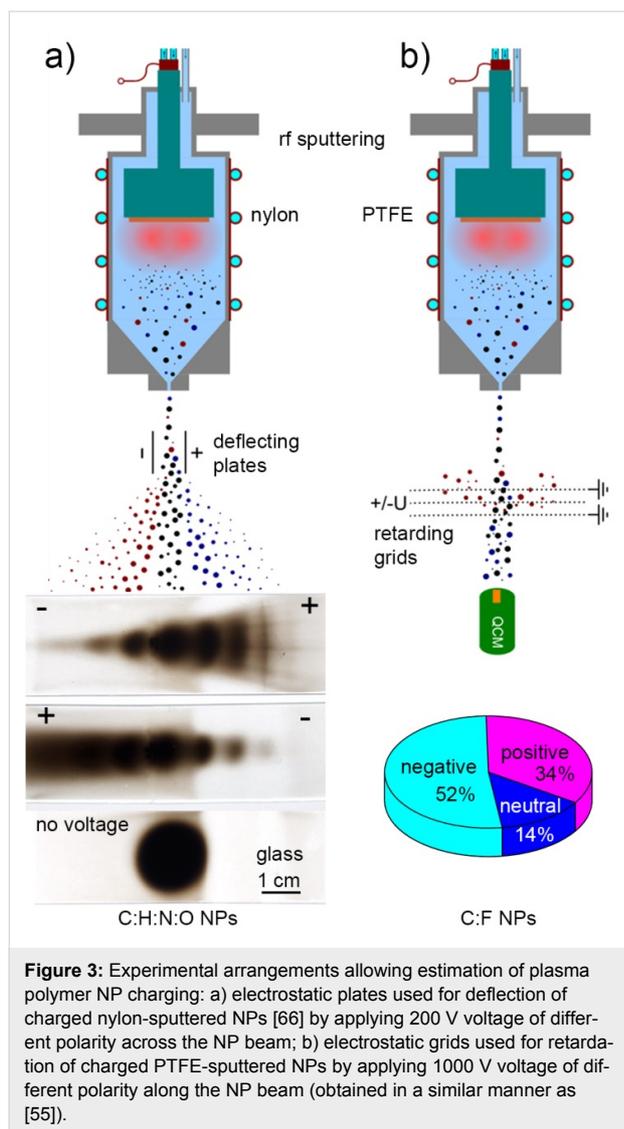
**Figure 2:** SEM images of different types of plasma polymer nanoparticles produced: a) by plasma polymerization of *n*-hexane in its mixture with N₂; b) by plasma polymerization of HMDSO in its mixture with Ar (obtained in a similar manner as [53]); c) by RF magnetron sputtering of nylon in the Ar/N₂ mixture (republished from [54] with permission IOP Publishing Ltd.); d) by RF magnetron sputtering of PTFE in Ar (obtained in a similar manner as [55]). The references shown here and in the following figures cite the authors' previous works where similar (but not necessarily identical) data were presented; the unreferenced data represent the authors' new material which has not been published yet, but which is necessary for a comparative analysis in this review.

and larger size because of the high mobility of electrons with respect to positive ions. The coagulation is therefore suppressed by Coulomb repulsion, and further NP growth proceeds by accretion via the accumulation of polymer-forming neutral species (radicals) and positive ions from the gas phase.

The resultant plasma polymer NPs have a spherical symmetry but can exhibit different morphology. Although it is very difficult to generalize about the shape of the NPs prepared in different experiments, it seems that larger plasma polymer particles typically reveal a more complex structure (Figure 2), the exact understanding of which is still lacking. The phenomenon can be associated with the changes in the heat balance of NPs during their growth in plasma. It has been shown both theoretically and experimentally that smaller NPs may reach the temperature that significantly exceeds that of a neutral gas, whereas larger NPs are heated much less [58,62,63]. Thus, the continuous growth of NPs in plasma may be accompanied by radially directed changes in the material properties (cross-link density and branching) induced by temperature changes and resulting in the accumulation of mechanical stress. If the critical value of stress is achieved, the surface of a NP relaxes with the formation of the surface instabilities, similar to a popcorn effect observed in conventional polymer particles [64]. As it was mentioned, the involvement of low-temperature plasma represents a unique feature that distinguishes this approach from other non-plasma-based methods: NPs acquire an electrical charge when nucleating, growing and passing through the zone of the glow discharge. Clouds of charged NPs may exhibit collective behaviour coupled with plasma instabilities, a phenomenon of high scientific interest in the field of dusty plasmas [52]. In the framework of GAS, the gas flow conditions are deliberately chosen to overcome trapping of NPs by electromagnetic fields and to extrude beams of NPs into the separate deposition chamber. Haberland [65] was one of the first to realize that NPs

(metallic in his case) ionized in the magnetron plasma can be advantageous in terms of size separation in accord with their mass-to-charge ratio. It can be shown that plasma polymer NPs also leave GAS partially charged and can be manipulated by an electrostatic field. Electrostatic plates can be installed at a close distance from the exit orifice of the GAS to deflect the charged NPs. Figure 3a shows the scheme of such arrangement used for the production of NPs by RF magnetron sputtering of nylon [66]. Here, photos of glass substrates taken after the depositions with or without the electrostatic field applied are shown. The nylon-sputtered NPs produce a circular deposit opposing the exit orifice when no voltage is applied to the deflection plates. In contrast, the deposit becomes spread towards the edges when 200 V voltage of different polarity is applied to the deflection plates. Remarkably, the presence of both negatively and positively charged NPs can be observed as the deposit is smeared in both directions from the central point. From the opacity of the deposit, it can be qualitatively estimated that neutral NPs are in minority and that negatively charged NPs constitute the majority of all the charged NPs.

For a quantitative evaluation, a system of electrostatic retarding grids can be utilized as shown in Figure 3b. Quartz crystal microbalance (QCM) can measure the total mass flux of the NPs (neutral, positively and negatively charged) without any voltage applied to the grids. A highly positive or negative potential applied to the central grid repels the NPs of the opposite charge and allows the rest to pass through. One can obtain the ratio between the neutral, the positively and the negatively charged NPs by measuring their mass fluxes with opposing voltages on the central grid. The calculations performed for the PTFE-sputtered NPs [55] support the qualitative data obtained for nylon sputtering and prove that the majority of the NPs bear the electric charge and that negatively charged NPs are the most abundant.

**Figure 3:** Experimental arrangements allowing estimation of plasma polymer NP charging: a) electrostatic plates used for deflection of charged nylon-sputtered NPs [66] by applying 200 V voltage of different polarity across the NP beam; b) electrostatic grids used for retardation of charged PTFE-sputtered NPs by applying 1000 V voltage of different polarity along the NP beam (obtained in a similar manner as [55]).



**Figure 4:** C 1s XPS of the NPs prepared a) by plasma polymerization of *n*-hexane in its mixture with Ar (total pressure 88 Pa, discharge power 40 W, $C_6H_{14}$ flow 1.2 sccm, Ar flow 12.2 sccm); b) by RF magnetron sputtering of nylon in the $Ar/N_2$ 3:1 mixture (obtained in a similar manner as [54]); c) by RF magnetron sputtering of PTFE in Ar (reprinted from [67], with permission from Elsevier).

## Control of chemical composition of plasma polymer nanoparticles

Chemical composition can also vary drastically depending on the precursor/target used as can be seen in Figure 4 where high-resolution C 1s XPS peaks are shown for a number of chosen NPs. Starting from C/H plasma polymers (Figure 2a), the chemistry of the resulting NPs may range from nitrogen-containing (Figure 2b) to fluorocarbon (Figure 2c) plasma polymers, to cite just a few, in which multitudes of chemical bonding environments can be present.

The choice of the working gas strongly influences the plasma chemistry and may be used as a tool for tuning the chemical composition of resultant NPs. For example, adding nitrogen to a hydrocarbon plasma may trigger the formation of nitrogen-containing NPs [68,69]. Figure 5a,b shows the NPs produced by plasma polymerization from the mixtures of *n*-hexane with Ar
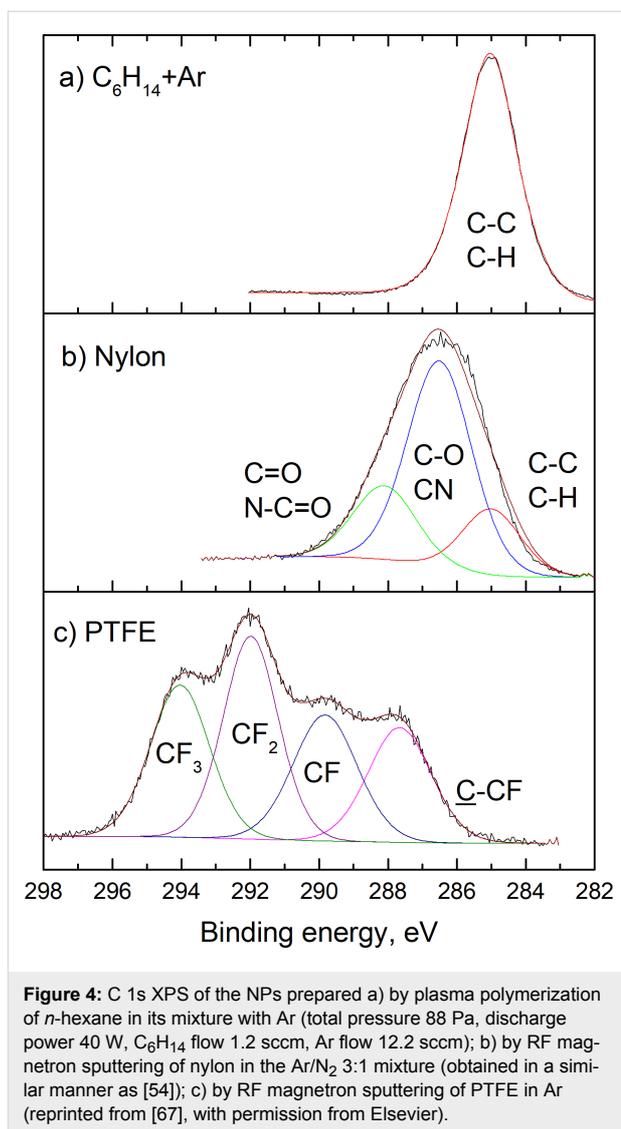
and with nitrogen, and for comparison Figure 5c shows the NPs produced by RF magnetron sputtering of nylon in the $Ar/N_2$ mixture [54].

The chemical composition of these NPs is shown in Figure 6a in terms of FTIR spectra and in Figure 6b in terms of the XPS elemental nitrogen content as a function of the concentration of $N_2$ in the working gas. Apart from narrowing the size distribution, adding nitrogen results in an increase of the nitrogen content in the NPs. Incorporation of nitrogen-bearing species into thin films of plasma polymers has been considered to be of paramount importance, especially in terms of retention of primary amines which are attractive in biomedical applications as linkers for binding biomolecules. Yet, it has been recently argued that primary amines find it difficult to survive the influence of the plasma and that amino groups overwhelmingly reported for plasma polymers are actually other nitrogen-contain-
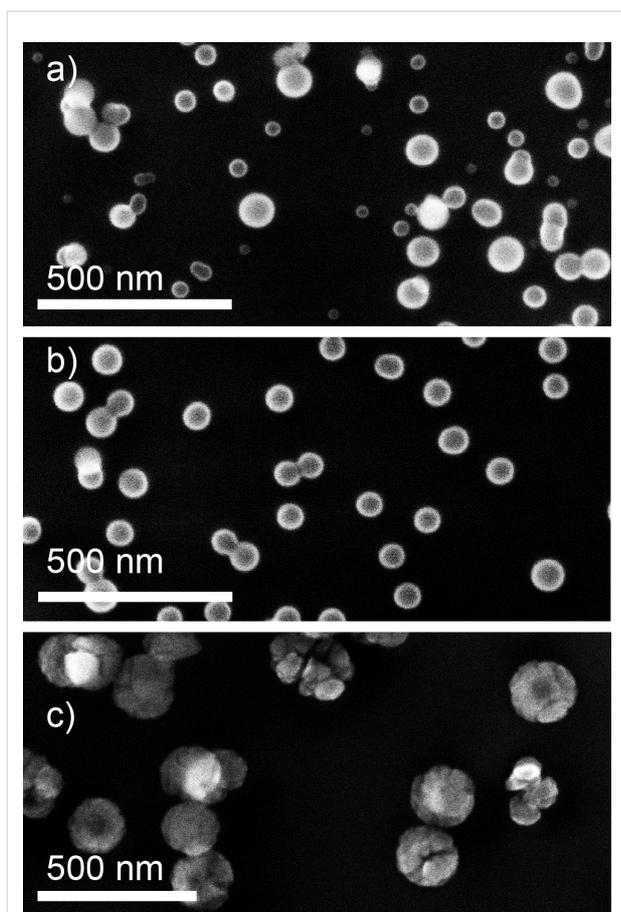
**Figure 5:** SEM images of nitrogen-containing NPs prepared a) by plasma polymerization of *n*-hexane in its mixture with Ar (total pressure 88 Pa, discharge power 40 W, $C_6H_{14}$ flow 1.2 sccm, Ar flow 12.2 sccm); b) by plasma polymerization of *n*-hexane in its mixture with $N_2$ (total pressure 88 Pa, discharge power 40 W, $C_6H_{14}$ flow 1.2 sccm, $N_2$ flow 12.2 sccm); c) by RF magnetron sputtering of nylon in the Ar/$N_2$ 3:1 mixture (obtained in a similar manner as [54]).



**Figure 6:** Chemical composition of nitrogen-containing NPs shown in Figure 5: a) FTIR spectra; b) the nitrogen content calculated from the XPS spectra as a function of the $N_2$ concentration in the working gas.

ing functionalities [70]. The data obtained for the NPs confirm that plasma polymerization of *n*-hexane in $N_2$ does not lead to the substantial retention of amines as can be seen from the absence of the characteristic IR band at >3000 cm$^{-1}$. Carbonyl-, amide- and, to a lesser extent, imine-based functionalities constitute an ensemble of nitrogen-bearing species. In contrast, RF magnetron sputtering of nylon in the Ar/$N_2$ mixture results in a much better retention of nitrogen which is, at least to some extent, bound in amine functionalities. Nevertheless, a reliable and quantitative control over the amount of amines in both NPs and thin films of plasma polymers still represents a formidable challenge.

Another example of a strong dependence of the chemical composition of NPs on the composition of the gas mixture can be found for plasma polymerization of HMDSO. It has been known for a long time in the thin film deposition community that adding oxygen to HMDSO switches plasma chemistry to preferential oxidation of carbonaceous species. A pumping system effectively evacuates gaseous carbon oxides whereas siloxane moieties tend to adsorb on surfaces and form silicon oxide coatings. The amount of added oxygen determines the chemical composition of the coatings. The same paradigm can be adapted for the synthesis of NPs in the configuration of GAS [53]. Plasma polymerization can be performed at elevated pressure in a mixture of HMDSO and Ar with the constant ratio of both components. The process results in the formation of

210 ± 40 nm diameter spherical particles with a more structured surface (Figure 7a). Adding $O_2$ to the working mixture results in morphological changes and produces NPs with fewer irregularities on the surface (Figure 7b,c). Remarkably, the NP diameter does not change significantly and reaches 180 ± 40 nm for the most oxygen-rich gas mixture.
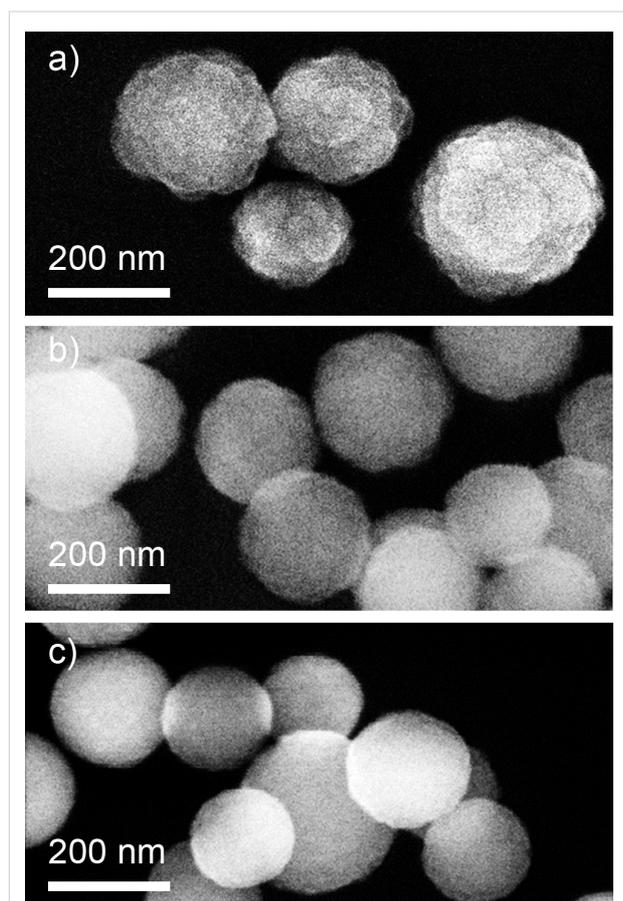


**Figure 7:** SEM images of NPs prepared by plasma polymerization of HMDSO mixed with Ar: a) without adding oxygen; b) with addition of oxygen at $O_2$/HMDSO 1:1 ; c) with addition of oxygen at $O_2$/HMDSO 5:1 (obtained in a similar manner as [53]). Total pressure is 55 Pa, discharge power is 30 W, HMDSO flow is 0.2 sccm, Ar flow is 2 sccm.

The stability of the size distribution becomes even more remarkable when compared to the chemical changes induced by the addition of oxygen. FTIR and XPS (Figure 8a,b) analyses demonstrate the organosilicon character of the NPs produced without $O_2$ and its gradual transfer to the inorganic state with the addition of $O_2$. The gas phase composition can be optimized to produce nearly stoichiometric $SiO_2$ NPs (Figure 7c), which are rare examples of organic plasma-derived material with well-established chemical composition. As it was discussed above, plasma polymers are typically cross-linked macromolecular networks having the chemical composition of more diverse character than that of the precursors. Mono-func-

tional plasma polymers are still beyond reach and even preferential retention of a specific functional group with a good control over the surface chemistry represents a significant challenge for the scientific community today.

## Control of size distribution of plasma polymer nanoparticles

The discharge power and the gas flow in the GAS are additional parameters to control the NP properties. In close analogy with the Yasuda parameter (see [71] and the following debate), both determine the specific energy supplied to a precursor molecule and, as a result, the intensity of precursor fragmentation. A typical pressure of tens of Pa ensures a viscous and laminar gas flow regime, and hence the gas flow rate determines also the time that NPs spend in the GAS (the residence time). Figure 9a,b summarizes the data available in the literature. Here, the mean NP diameter is given as a function of the residence time and discharge power for nylon- [54] and PTFE-sputtered [67] NPs as well as for plasma polymerization of HMDSO in Ar [53].

For nylon and HMDSO, an increase is observed of the NP diameter with the residence time (under constant power) which simply reflects the kinetics of the NP growth when they travel along the GAS. The opposite trend of decreasing NP diameter with the discharge power is readily explained by stronger fragmentation of precursor molecules. The fragmentation results in a larger amount of free radicals that serve as nucleation centres and, under constant supply of the precursor (constant gas flow rate), these produce larger amounts of smaller NPs. Nevertheless, the data for the NPs produced by magnetron sputtering of PTFE [67] by no means obey the above trend. These NPs are also in contradiction with other fluorocarbon NPs produced by plasma polymerization of heptadecafluorodecyl acrylate [35] showing the same trend as the nylon-sputtered and the HMDSO NPs. For PTFE-sputtered NPs, neither the residence time nor the discharge power has influence on the NP diameter which stays constant over the entire range of both parameters. The formation of the NPs in close proximity to the PTFE target and their subsequent transport through the GAS volume saturated with low sticking probability $CF_2$ bi-radicals were suggested as possible explanations of the phenomenon. It can be concluded that, although the opposing influence of the residence time and the discharge power on the NP diameter is fulfilled in many cases, a global generalization should be made with caution and each particular combination of precursor and GAS parameters should be thoroughly investigated. For example, other experiments with PTFE-sputtered NPs revealed that their diameter can be controlled over a wide range by changing the intensity of the magnetic field above the magnetron target [55]. Figure 10a,b shows SEM images of the NPs prepared under identical condi-
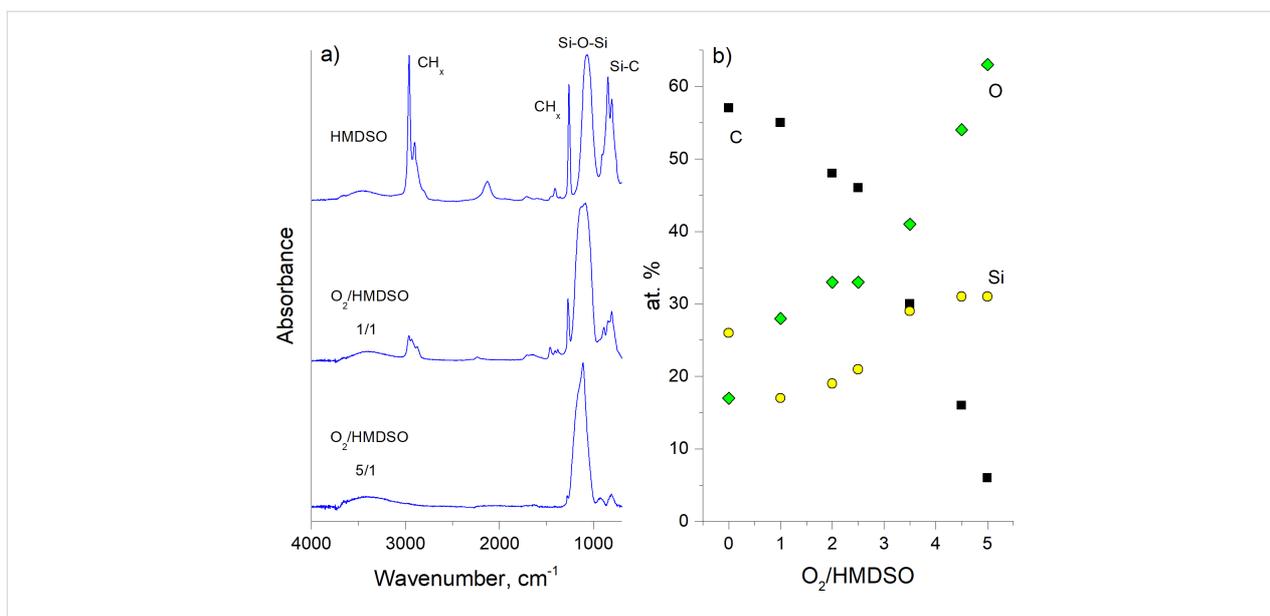
**Figure 8:** Chemical composition of the NPs shown in Figure 7: a) FTIR spectra b) the elemental content calculated from the XPS spectra as a function of the O$_2$ concentration in the working gas (republished from [53] with permission of IOP Publishing Ltd.).
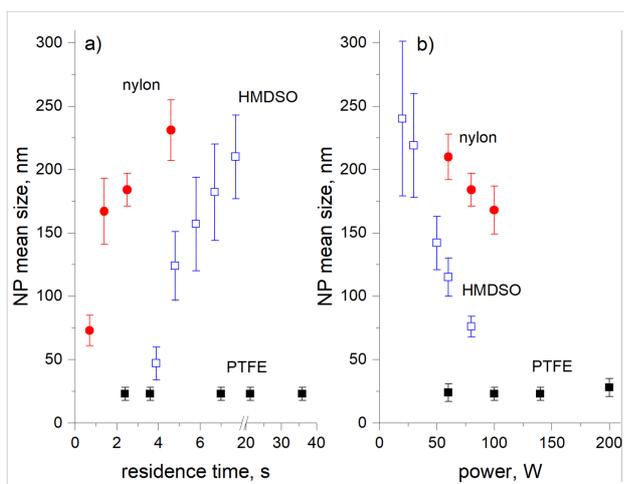


**Figure 9:** Mean diameter of nylon-sputtered, PTFE-sputtered and HMDSO plasma polymer NPs as a function of a) the residence time and b) the power of the discharge. The data are calculated from the results presented in [53,54,67].

exact reason for this interesting phenomenon is still not clear and requires further investigation.
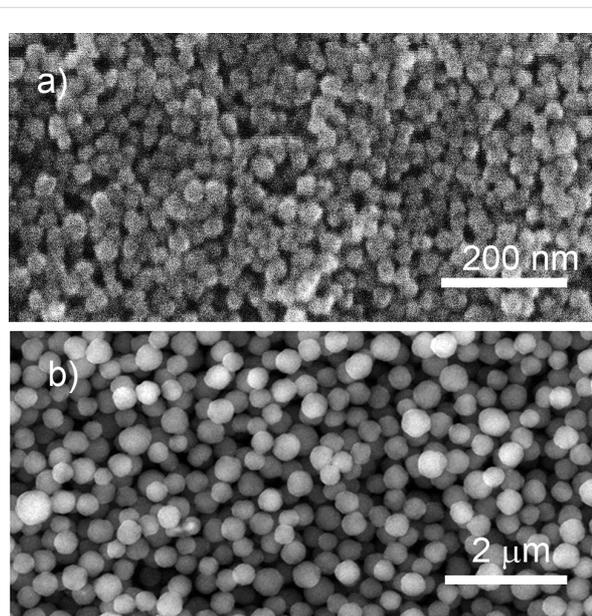


**Figure 10:** SEM images of the PTFE-sputtered NPs deposited with different intensity of the magnetic field: a) 100 G, b) 250 G; Ar pressure is 100 Pa, flow rate is 9.2 sccm, residence time is 9 s, discharge power is 140 W, deposition time is 20 min; obtained in a similar manner as in [55].

tions in the GAS but with different permanent magnet circuits installed in the magnetron, giving either a 100 G or 250 G field above the position of the erosion track on the PTFE target. An increase of the intensity of the magnetic field leads to a decrease of the magnetron self-bias from 620 V to 350 V due to more effective trapping of electrons within the magnetic channel. This in turn results in the formation of particles which are an order of magnitude larger (250 nm) as compared to the ones fabricated with the weaker magnetic field (30 nm). Apparently, the differences in intensity of ion bombardment should be manifested in the change of the plasma chemistry, although the

Apart from being of scientific interest, tuning the NP size by replacement of magnetic circuits can hardly be viewed as practical and technological reasons. More feasible is to control the

power/flow parameters or to modify the construction of the GAS itself. A GAS can be constructed to allow the length of the aggregation chamber to be changed, and Figure 11a,b shows the results of plasma polymerization of HMDSO in Ar with two values of the aggregation length [53]. Logically, a shorter aggregation zone reduces the NP residence time and prevents them from growing larger. Figure 11c shows the dual-scale surface obtained as a result of the combined deposition when a layer of 220 nm NPs was prepared with the longer aggregation zone and it was subsequently over coated by another layer of 40 nm NPs prepared with the shorter aggregation zone. Manipulation of the discharge power can also be effective for the creation of dual- and even multi-scale structures. For example, NPs of three different sizes can be prepared in a single run by a stepwise increase of power, in this case resulting in the deposition of 200, 110 and 70 nm NPs. Figure 11d shows the outcome of such a triple deposition method and the histogram in Figure 11e confirms the formation of the triple-scale surface. Thus, plasma polymer NPs produced by GAS prove to be very

versatile for the design of hierarchical structures, which can be very efficient for fine tuning of optical properties, surface wettability, interaction with cells, and in other applications.

## Core@shell nanoparticles

The versatility of GAS may be further extended if two different processes are combined in one experimental run. One can take advantage of magnetron sputtering of metals and plasma polymerization of organic precursors to create heterogeneous NPs in which metallic inclusions are enveloped by layers of plasma polymer (core@shell NPs). For example, the process can be performed in the GAS by RF magnetron sputtering of metal in argon with the addition of an organic precursor (Figure 12a) or metal NPs can be pre-formed in the GAS by DC magnetron sputtering and the beam of the NPs can be allowed to pass through an auxiliary glow discharge in organic vapours (Figure 12b).
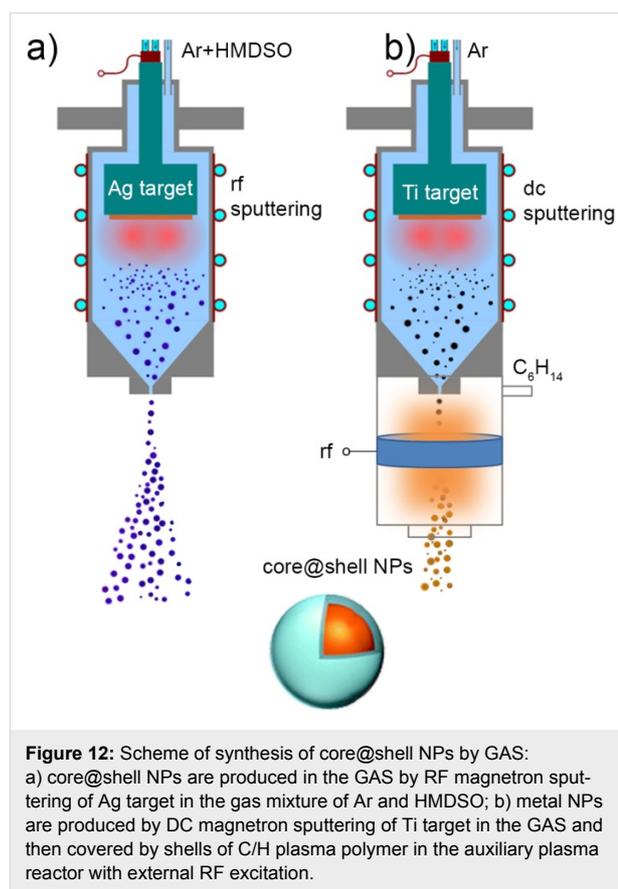


**Figure 11:** SEM images of NPs prepared by plasma polymerization of HMDSO in Ar: a) 220 nm NPs produced with 10 cm aggregation length; b) 40 nm NPs produced with 4 cm aggregation length; c) dual-scale structure produced by sequential deposition of a) and b); d) triple-scale structure produced by power-dependent sequential deposition of 200, 110 band 70 nm diameter NPs; e) size distribution histogram corresponding to d) (republished from [53] with permission of IOP Publishing Ltd.).



**Figure 12:** Scheme of synthesis of core@shell NPs by GAS: a) core@shell NPs are produced in the GAS by RF magnetron sputtering of Ag target in the gas mixture of Ar and HMDSO; b) metal NPs are produced by DC magnetron sputtering of Ti target in the GAS and then covered by shells of C/H plasma polymer in the auxiliary plasma reactor with external RF excitation.

In the first case, the conditions should be optimized to provide the supply of atomic metal supersaturated vapours into the gas phase where they start to condense by homogeneous nucleation. Simultaneously, fragmentation of organic molecules in the plasma proceeds with the formation of free radicals that subsequently recombine to create the plasma polymer phase.

Remarkably, the two processes do not interfere, probably due to strong cohesive forces between metal atoms and weak metal–polymer interaction. As a result, phase-separated core@shell NPs are created, an example of which is shown in Figure 13a. Here, silver NPs enveloped by shells of HMDSO plasma polymer are shown. The structure of the NPs, in which multiple metal inclusions of about 5 nm diameter are concentrated within a single plasma polymer shell producing 36 nm diameter multicore@shell NPs, is appealing. The multicore-in-



**Figure 13:** TEM images of core@shell NPs: a) Ag@HMDSO NPs prepared in configuration of Figure 12a (total pressure 190 Pa, discharge power 50 W, HMDSO flow 0.45 sccm, Ar flow 105 sccm); b) Ti@C/H NPs prepared in configuration of Figure 12b (Ar pressure/flow in the GAS is 40 Pa/4.0 sccm, DC 0.4 A, total pressure in the auxiliary plasma zone is 1 Pa (0.65 Pa of Ar and 0.35 Pa of $C_6H_{14}$), RF power is 10 W).

one-shell structure can be explained by the initial formation of single core@shell NPs which subsequently coalesce into one bigger NP joining multiple metal inclusions in a single shell.

The second strategy relies on spatial separation of the formation of metal NPs and their embedding into polymer or plasma polymer shells, similar to what has been realized in [72,73]. This strategy allows the decoupling of the processes of magnetron sputtering and plasma polymerization and may prove advantageous, especially if more reactive metals are considered. For example, titanium is known to form strong TiC bonds when sputtered in organic plasma [74]. Carbidization of titanium atoms may hinder metal–polymer phase separation and it may even change the properties of titanium inclusions themselves. Instead, Ti NPs can be created in the GAS by magnetron sputtering in Ar and then their beams can be transported by the gas flow through an auxiliary glass tube attached to the GAS and equipped with an external ring electrode for RF excitation of plasma. Vapours of *n*-hexane are introduced into the glass tube via a separate inlet port and the conditions of plasma polymerization should be optimized to produce in-flight coating of Ti NPs with hydrocarbon plasma polymer. Figure 13b shows that both single core@shell NPs as well as their agglomerations can be obtained by this procedure. The thickness of the overcoat can be controlled by the flight velocity of the NPs and by the deposition rate of the plasma polymer. Overall, gas-phase fabrication of metal–polymer core@shell NPs may offer new possibilities in preventing metal particles from oxidation, in fine tuning the optical properties and biological interactions, and, in general, in designing novel materials with advanced properties.

## Plasma polymer nanoparticles as building blocks for nanostructured composite surfaces

The configuration of GAS allows the deposition of NPs onto any high-vacuum-compatible supports. Typical operational conditions used in GAS produce NP beams that deposit on substrates with subsonic velocity [75]. If the range of masses of NPs is taken into account, one may conclude that NPs hit the substrate in a soft-landing regime in which the kinetic energy borne by a NP as a single entity is too small to break bonds between the highly numerous species constituting this NP. Hence, NP interaction with the substrate does not induce noticeable changes either in the NPs or in the substrates. Preservation of the NP shape and structure may or may not be of benefit, depending on the target application. A major drawback of the situation is related to the weak van der Waals forces acting between NPs and substrate so that a NP layer can be easily destroyed by a tiny mechanical impact. This drawback can be overcome by depositing a capping layer that should be sufficiently robust to fix the NPs on the surface yet sufficiently thin so as not to introduce morphological changes to the surface,
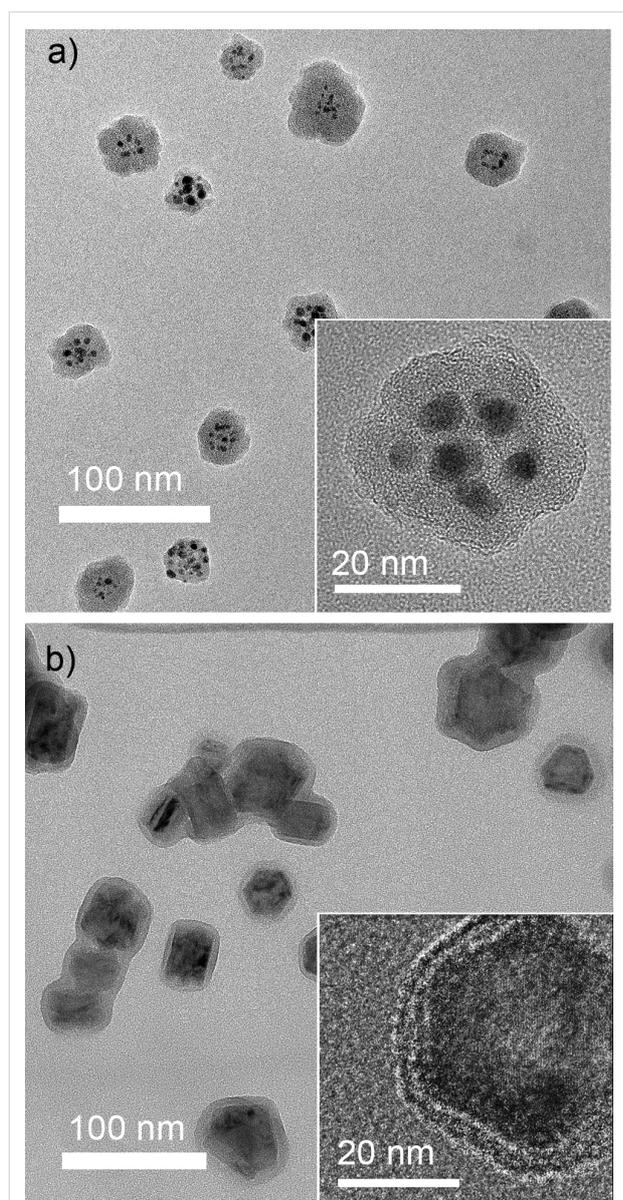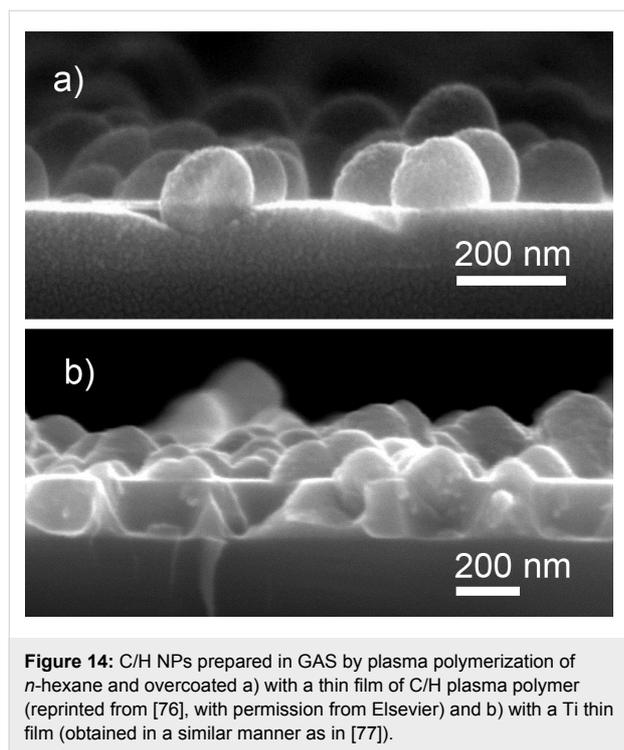
unless otherwise required. The layer can be of the same or similar material as the underlying NPs to preserve the surface chemistry. For example, hydrocarbon NPs produced by plasma polymerization of *n*-hexane in GAS can be fixed on the surface by coating them with a thin film of hydrocarbon plasma polymer (Figure 14a). The capping layer can also be made of a different material as can be seen in Figure 14b where the same NPs are shown over-coated with a magnetron-sputtered Ti film.



**Figure 14:** C/H NPs prepared in GAS by plasma polymerization of *n*-hexane and overcoated a) with a thin film of C/H plasma polymer (reprinted from [76], with permission from Elsevier) and b) with a Ti thin film (obtained in a similar manner as in [77]).

In both of the above cases, the overlayer was deposited to preserve the initial surface morphology. Certain applications however may require control over the structure in a broader range covering both nanometer and micrometer scales. Plasma polymer NPs may be useful for this purpose as well, especially if glancing angle deposition (GLAD) is considered. Evaporative GLAD was developed in the late 20th century for creating metallic films with a highly porous structure [78]. It has been known that time and spatial fluctuations exist in atomic fluxes arriving onto the substrate from the gas phase during evaporation or sputtering. The noise in the atomic flux results in the situation that some spots on the surface may receive a larger amount of particles deposits than the others, and generally, noise is responsible for roughening the growing front. In contrast, surface diffusion tends to redistribute the arriving material over the larger area and leads to smoothening of the surface. The competition between the two phenomena determines the resultant roughness/smoothness of the film. If deposition is performed onto a sufficiently cold substrate, surface diffusion

can be suppressed and roughening will dominate. It has been also recognized that roughening can be significantly enhanced if shadowing instabilities are present on the surface, especially if the depositing flux is collimated and tilted at an oblique (glancing) angle to the surface normal. Nuclei of the adsorbed material create shadow zones in areas opposite to the direction of the incoming flux. Arrays of well isolated zig-zag, spiral or pillar nanostructures made of metals and other inorganics have been successfully fabricated by GLAD. GLAD of polymeric materials has also been demonstrated [74,79,80]. However, the separation between the individual polymer nano-columns is typically worse than in the case of metals, probably due to a relatively large characteristic surface diffusion length of macromolecular species which compromises the shadowing effect. To enhance the shadowing mechanism, blank substrates can be preseeded with NPs produced by GAS (Figure 15a) that will serve as artificially created obstacles to the incoming flux in the second step (Figure 15b).



**Figure 15:** Scheme of GLAD: a) preseeding of substrates with nylon-sputtered NPs produced by GAS; b) GLAD of nylon-sputtered plasma polymer over the preseeded NPs.
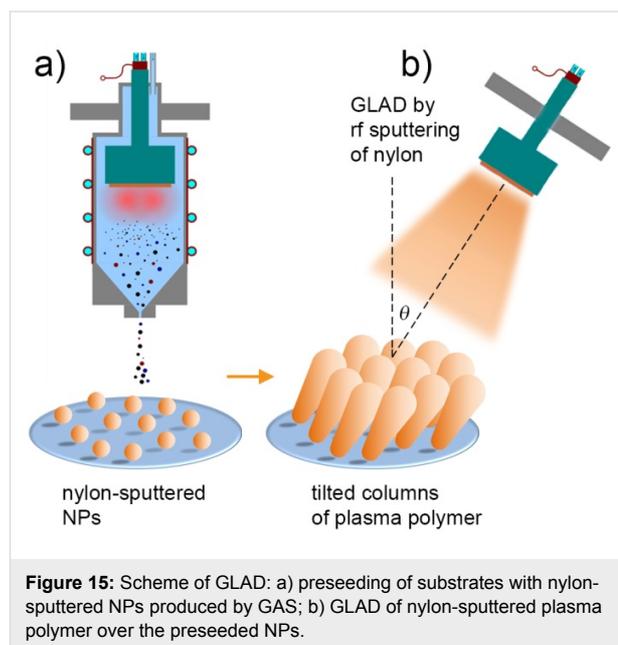
Figure 16a,b shows the top view and cross-sectional images of a plasma polymer film created as a result of RF magnetron sputtering of nylon at normal (0°) and glancing angle (80°) deposition on blank silicon substrates whereas Figure 16c,d shows their counterparts deposited over the preseeded nylon-sputtered NPs. As expected, normal depositions produce compact coatings with the surface replicating the underlying structure (correspondingly, smooth blank Si or roughened NP seeds). Using GLAD, a columnar structure develops with columns inclined towards the direction of the deposition. Obviously, the porosity of the coatings is greatly increased when it is deposited over the preseeded NPs. This approach also offers the possibility to com-

bine different materials, and hence, to independently tune the surface morphology and the chemical composition. Thus, it represents an attractive route for designing nanocomposite coatings with advanced properties.
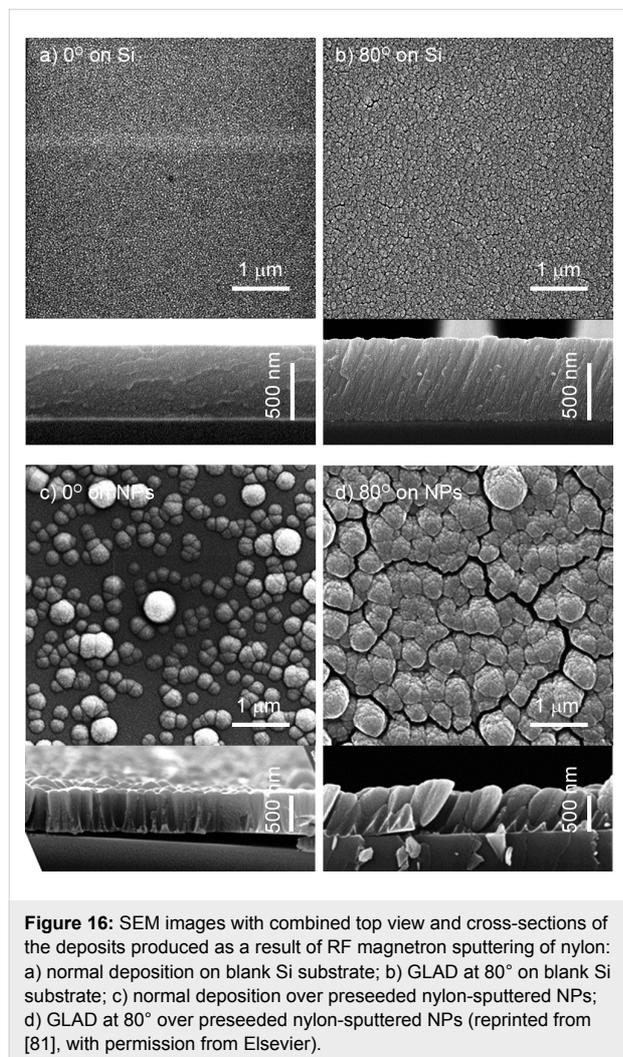


**Figure 16:** SEM images with combined top view and cross-sections of the deposits produced as a result of RF magnetron sputtering of nylon: a) normal deposition on blank Si substrate; b) GLAD at 80° on blank Si substrate; c) normal deposition over preseeded nylon-sputtered NPs; d) GLAD at 80° over preseeded nylon-sputtered NPs (reprinted from [81], with permission from Elsevier).

## Conclusion

Plasma polymer NPs have great potential and may provide a valuable addition to the field of nanoscale-dispersed polymers. The involvement of gas aggregation cluster sources in the production of plasma polymer NPs opens new horizons in precise tuning of their size, shape, chemical composition, surface charge and wettability. There are great potential benefits for the use of plasma polymer NPs in photonics, nanomedicine and other applications, but also significant challenges remain unresolved. Fundamental knowledge on the mechanisms of plasma polymer nanoparticle formation is still far from being complete. Although rich information regarding the nucleation and growth of nanoparticles in organosilicon and hydrocarbon plasmas is available, a deep understanding of these processes for other pre-

cursors is missing. The lack of knowledge is especially striking in the field of the plasma-based fabrication of functionalized polymeric NPs and core@shell NPs, which remains in its budding stage. The retention of specific functional groups, control over their concentration, control over the cross-link density and the concentration of radicals captured within plasma polymer NPs, control over the morphology and shape of NPs, and nanophase separation within core@shell NPs are only a few issues that scientists in this research field face. The solution of these issues requires finding correlations between the properties of the plasma (energy distribution functions, plasma density, floating and plasma potential), the gas phase composition and the gas flow dynamics. Therefore, future research work should join efforts of scientists with different expertise to cope effectively with these complex issues.

## Acknowledgements

## References

1. Jenkins, A. D.; Kratochvíl, P.; Stepto, R. F. T.; Suter, U. W. *Pure Appl. Chem.* **1996,** *68,* 2287–2311. doi:10.1351/pac199668122287
2. Yasuda, V. H., Ed. *Plasma Polymerization;* Academic Press: New York, NY, U.S.A., 1985.
3. Biedermann, H.; Osada, Y. *Plasma Polymerization Processes (Plasma Technology);* Elsevier: Amsterdam, Netherlands, 1992.
4. Biedermann, H., Ed. *Plasma polymer films;* Imperial College Press: London, United Kingdom, 2004. doi:10.1142/p336
5. Friedrich, J. *Plasma Processes Polym.* **2011,** *8,* 783–802. doi:10.1002/ppap.201100038
6. Williams, T.; Hayes, M. W. *Nature* **1967,** *216,* 614–615. doi:10.1038/216614a0
7. Denaro, A. R.; Owens, P. A.; Crawshaw, A. *Eur. Polym. J.* **1968,** *4,* 93–106. doi:10.1016/0014-3057(68)90010-4
8. Neisewender, D. D. *Adv. Chem.* **1969,** *80,* 338–349. doi:10.1021/ba-1969-0080.ch029
9. Thompson, L. F.; Smolinsky, G. *J. Appl. Polym. Sci.* **1972,** *16,* 1179–1190. doi:10.1002/app.1972.070160512
10. Kobayashi, H.; Bell, A. T.; Shen, M. *J. Appl. Polym. Sci.* **1973,** *17,* 885–892. doi:10.1002/app.1973.070170318
11. Vladimirov, S. V.; Ostrikov, K. *Plasmas Polym.* **2003,** *8,* 135–152. doi:10.1023/A:1024050512623
12. Zyn, V. I.; Potapov, V. K.; Tuzov, L. S.; Shterenberg, A. M. *High Energy Chem.* **1986,** *20,* 541–547.
13. Bouchoule, A.; Plain, A.; Boufendi, L.; Blondeau, J. P.; Laure, C. *J. Appl. Phys.* **1991,** *70,* 1991–2000. doi:10.1063/1.349484

14. Bouchoule, A.; Boufendi, L. *Plasma Sources Sci. Technol.* **1993,** *2,* 204–213. doi:10.1088/0963-0252/2/3/011

15. Boufendi, L.; Bouchoule, A. *Plasma Sources Sci. Technol.* **1994,** *3,* 262–267. doi:10.1088/0963-0252/3/3/004

16. Hollenstein, C.; Schwarzenbach, W.; Howling, A. A.; Courteille, C.; Dorier, J.-L.; Sansonnens, L. *J. Vac. Sci. Technol., A* **1996,** *14,* 535. doi:10.1116/1.580140

17. Kersten, H.; Deutsch, H.; Stoffels, E.; Stoffels, W. W.; Kroesen, G. M. W.; Hippler, R. *Contrib. Plasma Phys.* **2001,** *41,* 598–609. doi:10.1002/1521-3986(200111)41:6<598::AID-CTPP598>3.0.CO;2-Z

18. Denysenko, I. B.; Ostrikov, K.; Xu, S.; Yu, M. Y.; Diong, C. H. *J. Appl. Phys.* **2003,** *94,* 6097. doi:10.1063/1.1618356

19. De Bleecker, K.; Bogaerts, A.; Goedheer, W.; Gijbels, R. *IEEE Trans. Plasma Sci.* **2004,** *32,* 691–698. doi:10.1109/TPS.2004.826095

20. Melikhov, K. G.; Shterenberg, A. M.; Zyn, V. I. *J. Phys. D: Appl. Phys.* **2006,** *39,* 944–949. doi:10.1088/0022-3727/39/5/008

21. Cavarroc, M.; Mikikian, M.; Tessier, Y.; Boufendi, L. *Phys. Rev. Lett.* **2008,** *100,* 045001. doi:10.1103/PhysRevLett.100.045001

22. Larriba-Andaluz, C.; Girshick, S. L. *Plasma Chem. Plasma Process.* **2017,** *37,* 43–58. doi:10.1007/s11090-016-9749-7

23. Deschenaux, C.; Affolter, A.; Magni, D.; Hollenstein, C.; Fayet, P. *J. Phys. D: Appl. Phys.* **1999,** *32,* 1876–1886. doi:10.1088/0022-3727/32/15/316

24. Stoykov, S.; Eggs, C.; Kortshagen, U. *J. Phys. D: Appl. Phys.* **2001,** *34,* 2160–2173. doi:10.1088/0022-3727/34/14/312

25. Mao, M.; Benedikt, J.; Consoli, A.; Bogaerts, A. *J. Phys. D: Appl. Phys.* **2008,** *41,* 225201. doi:10.1088/0022-3727/41/22/225201

26. Do, H. T.; Sushkov, V.; Hippler, R. *New J. Phys.* **2009,** *11,* 033020.

27. Andreeva, A. V.; Kutsarev, I.; Shatsky, A. V.; Shterenberg, A. M.; Zyn, V. I. *Plasma Processes Polym.* **2012,** *9,* 772–781. doi:10.1002/ppap.201100204

28. Vinogradov, G. K.; Imanbayev, G. Z.; Polak, L. S.; Slovetsky, D. I. *High Energy Chem.* **1983,** *17,* 372–377.

29. Takahashi, K.; Tachibana, K. *J. Vac. Sci. Technol., A* **2001,** *19,* 2055–2060. doi:10.1116/1.1372901

30. Takahashi, K.; Tachibana, K. *J. Appl. Phys.* **2001,** *89,* 893–899. doi:10.1063/1.1334636

31. Ostrikov, K. N.; Kumar, S.; Sugai, H. *J. Appl. Phys.* **2001,** *89,* 5919–5926. doi:10.1063/1.1368397

32. Ostrikov, K. N.; Kumar, S.; Sugai, H. *Phys. Plasmas* **2001,** *8,* 3490–3497. doi:10.1063/1.1375149

33. Teare, D. O. H.; Spanos, C. G.; Ridley, P.; Kinmond, E. J.; Roucoules, V.; Badyal, J. P. S.; Brewer, S. A.; Coulson, S.; Willis, C. *Chem. Mater.* **2002,** *14,* 4566–4571. doi:10.1021/cm011600f

34. Fu, G. D.; Kang, E. T.; Neoh, K. G. *J. Phys. Chem. B* **2003,** *107,* 13902–13910. doi:10.1021/jp036529a

35. Feng, J. C.; Huang, W.; Fu, G. D.; Kang, E.-T.; Neoh, K.-G. *Plasma Processes Polym.* **2005,** *2,* 127–135. doi:10.1002/ppap.200400030

36. Yang, S. H.; Liu, C.-H.; Hsu, W.-T.; Chen, H. *Surf. Coat. Technol.* **2009,** *203,* 1379–1383. doi:10.1016/j.surfcoat.2008.11.007

37. Paquet, C.; Kumacheva, E. *Mater. Today* **2008,** *11,* 48–56. doi:10.1016/S1369-7021(08)70056-7

38. Yonamine, Y.; Yoshimatsu, K.; Lee, S.-H.; Hoshino, Y.; Okahata, Y.; Shea, K. J. *ACS Appl. Mater. Interfaces* **2013,** *5,* 374–379. doi:10.1021/am302404q

39. Zhang, H.; Wu, F.; Li, Y.; Yang, X.; Huang, J.; Lv, T.; Zhang, Y.; Chen, J.; Chen, H.; Gao, Y.; Liu, G.; Jia, L. *Beilstein J. Nanotechnol.* **2016,** *7,* 1861–1870. doi:10.3762/bjnano.7.178

40. Kuhn, D. A.; Vanhecke, D.; Michen, B.; Blank, F.; Gehr, P.; Petri-Fink, A.; Rothen-Rutishauser, B. *Beilstein J. Nanotechnol.* **2014,** *5,* 1625–1636. doi:10.3762/bjnano.5.174

41. Binns, C. *Surf. Sci. Rep.* **2001,** *44,* 1–49. doi:10.1016/S0167-5729(01)00015-2

42. Wan, J.; Ma, Z.; Han, M.; Hong, J.; Wang, G. *Solid State Commun.* **2002,** *121,* 251–256. doi:10.1016/S0038-1098(01)00502-6

43. Harrop, P. J. *Vacuum* **1969,** *19,* 502. doi:10.1016/S0042-207X(69)91821-1

44. Pratt, I. H.; Lausman, T. C. *Thin Solid Films* **1972,** *10,* 151–154. doi:10.1016/0040-6090(72)90281-7

45. Holland, L.; Biederman, H.; Ojha, S. M. *Thin Solid Films* **1976,** *35,* L19–L21. doi:10.1016/0040-6090(76)90267-4

46. Youngblood, J. P.; McCarthy, T. J. *Thin Solid Films* **2001,** *382,* 95–100. doi:10.1016/S0040-6090(00)01683-7

47. Kholodkov, I.; Biederman, H.; Slavínská, D.; Choukourov, A.; Trchova, M. *Vacuum* **2003,** *70,* 505–509. doi:10.1016/S0042-207X(02)00702-9

48. Pihosh, Y.; Biederman, H.; Slavinska, D.; Kousal, J.; Choukourov, A.; Trchova, M.; Mackova, A.; Boldyreva, A. *Vacuum* **2006,** *81,* 32–37. doi:10.1016/j.vacuum.2006.02.006

49. Choukourov, A.; Hanuš, J.; Kousal, J.; Grinevich, A.; Pihosh, Y.; Slavínská, D.; Biederman, H. *Vacuum* **2006,** *80,* 923–929. doi:10.1016/j.vacuum.2005.12.012

50. Drabik, M.; Kousal, J.; Pihosh, Y.; Choukourov, A.; Biederman, H.; Slavinska, D.; Mackova, A.; Boldyreva, A.; Pesicka, J. *Vacuum* **2007,** *81,* 920–927. doi:10.1016/j.vacuum.2006.10.013

51. Kylián, O.; Hanuš, J.; Choukourov, A.; Kousal, J.; Slavínská, D.; Biederman, H. *J. Phys. D: Appl. Phys.* **2009,** *42,* 142001. doi:10.1088/0022-3727/42/14/142001

52. Mikikian, M.; Labidi, S.; von Wahl, E.; Lagrange, J. F.; Lecas, T.; Massereau-Guilbaud, V.; Géraud-Grenier, I.; Kovacevic, E.; Berndt, J.; Kersten, H.; Gibert, T. *Plasma Phys. Controlled Fusion* **2017,** *59,* 14034. doi:10.1088/0741-3335/59/1/014034

53. Shelemin, A.; Nikitin, D.; Choukourov, A.; Kylián, O.; Kousal, J.; Khalakhan, I.; Melnichuk, I.; Slavínská, D.; Biederman, H. *J. Phys. D: Appl. Phys.* **2016,** *49,* 254001. doi:10.1088/0022-3727/49/25/254001

54. Polonskyi, O.; Kylián, O.; Solař, P.; Artemenko, A.; Kousal, J.; Slavínská, D.; Choukourov, A.; Biederman, H. *J. Phys. D: Appl. Phys.* **2012,** *45,* 495301. doi:10.1088/0022-3727/45/49/495301

55. Serov, A. Preparation and basic properties of nanostructured plasma polymers; Charles University, 2014.

56. Howling, A. A.; Sansonnens, L.; Dorier, J.-L.; Hollenstein, C. *J. Phys. D: Appl. Phys.* **1993,** *26,* 1003–1006. doi:10.1088/0022-3727/26/6/019

57. Berndt, J.; Kovačević, E.; Stefanović, I.; Boufendi, L. *J. Appl. Phys.* **2009,** *106,* 063309. doi:10.1063/1.3224874

58. Kovacevic, E.; Berndt, J.; Strunskus, T.; Boufendi, L. *J. Appl. Phys.* **2012,** *112,* 013303. doi:10.1063/1.4731751

59. van de Wetering, F. M. J. H.; Beckers, J.; Kroesen, G. M. W. *J. Phys. D: Appl. Phys.* **2012,** *45,* 485205. doi:10.1088/0022-3727/45/48/485205

60. Blažek, J.; Kousal, J.; Biederman, H.; Kylián, O.; Hanuš, J.; Slavínská, D. *J. Phys. D: Appl. Phys.* **2015,** *48,* 415202. doi:10.1088/0022-3727/48/41/415202

61. Mamunuru, M.; Le Picard, R.; Sakiyama, Y.; Girshick, S. L.
    *Plasma Chem. Plasma Process.* **2017,** *37,* 701–715.
    doi:10.1007/s11090-017-9798-6

62. Mangolini, L.; Kortshagen, U.
    *Phys. Rev. E: Stat., Nonlinear, Soft Matter Phys.* **2009,** *79,* 026405.
    doi:10.1103/PhysRevE.79.026405

63. Maurer, H. R.; Kersten, H. *J. Phys. D: Appl. Phys.* **2011,** *44,* 174029.
    doi:10.1088/0022-3727/44/17/174029

64. Du, Y.-Z.; Tomohiro, T.; Kodaka, M. *Macromolecules* **2004,** *37,*
    803–812. doi:10.1021/ma030424o

65. Haberland, H.; Karrais, M.; Mall, M.; Thurner, Y.
    *J. Vac. Sci. Technol., A* **1992,** *10,* 3266–3271. doi:10.1116/1.577853

66. Solař, P.; Melnichuk, I.; Artemenko, A.; Polonskyi, O.; Kylián, O.;
    Choukourov, A.; Slavínská, D.; Biederman, H. *Vacuum* **2015,** *111,*
    124–130. doi:10.1016/j.vacuum.2014.09.023

67. Serov, A.; Choukourov, A.; Melnichuk, I.; Shelemin, A.; Kuzminova, A.;
    Kylián, O.; Hanuš, J.; Kousal, J.; Drábik, M.; Slavínská, D.;
    Biederman, H. *Surf. Coat. Technol.* **2014,** *254,* 319–326.
    doi:10.1016/j.surfcoat.2014.06.014

68. Pereira, J.; Massereau-Guilbaud, V.; Géraud-Grenier, I.; Plain, A.
    *Plasma Processes Polym.* **2005,** *2,* 633–640.
    doi:10.1002/ppap.200500014

69. Massereau-Guilbaud, V.; Pereira, J.; Géraud-Grenier, I.; Plain, A.
    *J. Appl. Phys.* **2009,** *105,* 033302. doi:10.1063/1.3072664

70. Klages, C.-P.; Kotula, S. *Plasma Processes Polym.* **2016,** *13,*
    1213–1223. doi:10.1002/ppap.201600210

71. d'Agostino, R.; Favia, P.; Förch, R.; Oehr, C.; Wertheimer, M. R.
    *Plasma Processes Polym.* **2010,** *7,* 363–364.
    doi:10.1002/ppap.201000040

72. Balasubramanian, B.; Kraemer, K. L.; Reding, N. A.; Skomski, R.;
    Ducharme, S.; Sellmyer, D. J. *ACS Nano* **2010,** *4,* 1893–1900.
    doi:10.1021/nn9016422

73. Yasar-Inceoglu, O.; Zhong, L.; Mangolini, L. *J. Phys. D: Appl. Phys.*
    **2015,** *48,* 314009. doi:10.1088/0022-3727/48/31/314009

74. Choukourov, A.; Solar, P.; Polonskyi, O.; Hanus, J.; Drabik, M.;
    Kylian, O.; Pavlova, E.; Slavinska, D.; Biederman, H.
    *Plasma Processes Polym.* **2010,** *7,* 25–32.
    doi:10.1002/ppap.200900064

75. Kousal, J.; Polonskyi, O.; Kylián, O.; Choukourov, A.; Artemenko, A.;
    Pešička, J.; Slavínská, D.; Biederman, H. *Vacuum* **2013,** *96,* 32–38.
    doi:10.1016/j.vacuum.2013.02.015

76. Solař, P.; Polonskyi, O.; Choukourov, A.; Artemenko, A.; Hanuš, J.;
    Biederman, H.; Slavínská, D. *Surf. Coat. Technol.* **2011,** *205*
    (Suppl. 2), S42–S47. doi:10.1016/j.surfcoat.2011.01.059

77. Solař, P.; Kylián, O.; Polonskyi, O.; Artemenko, A.; Arzhakov, D.;
    Drábik, M.; Slavínská, D.; Vandrovcová, M.; Bačáková, L.;
    Biederman, H. *Surf. Coat. Technol.* **2012,** *206,* 4335–4342.
    doi:10.1016/j.surfcoat.2012.02.005

78. Robbie, K.; Friedrich, L. J.; Dew, S. K.; Smy, T.; Brett, M. J.
    *J. Vac. Sci. Technol., A* **1995,** *13,* 1032–1035. doi:10.1116/1.579579

79. Boduroglu, S.; Cetinkaya, M.; Dressick, W. J.; Singh, A.; Demirel, M. C.
    *Langmuir* **2007,** *23,* 11391–11395. doi:10.1021/la7025413

80. Cetinkaya, M.; Boduroglu, S.; Demirel, M. C. *Polymer* **2007,** *48,*
    4130–4134. doi:10.1016/j.polymer.2007.05.015

81. Kylian, O.; Shelemin, A.; Solar, P.; Choukourov, A.; Hanus, J.;
    Vaidulych, M.; Kuzminova, A.; Biederman, H. *Thin Solid Films* **2017,**
    *630,* 86–91. doi:10.1016/j.tsf.2016.08.054

# Preparation and characterization of polycarbonate/ multiwalled carbon nanotube nanocomposites

Claudio Larosa[1], Niranjan Patra[2], Marco Salerno[*3,§], Lara Mikac[4], Remo Merijs Meri[5] and Mile Ivanda[4]

## Full Research Paper

Address:
[1]Department of Civil, Chemical and Environmental Engineering, University of Genoa, via Opera Pia 15, 16145 Genoa, Italy, [2]Department of Mechanical Engineering, University of Wyoming, 82071 Laramie, USA, [3]Materials Characterization Facility, Istituto Italiano di Tecnologia, via Morego 30, 16163 Genoa, Italy, [4]Rudjer Bošković Institute, Center of Excellence for Advanced Materials and Sensing Devices, Bijenička 54, 10000 Zagreb, Croatia, and [5]Department of Polymer Materials, Riga Technical University, Azenes Str. 14/24, Riga LV-1048, Latvia

Email:
Marco Salerno[*] - marco.salerno@iit.it

* Corresponding author
§ Tel. +39 010 71781444, Fax +39 010 720321

## Abstract

A polymer nanocomposite was produced by ultrasonic-assisted dispersion of multiwalled carbon nanotubes (MWCNTs) in a polycarbonate matrix using *p*-xylene and dichloromethane as the solvents. The filler loading was varied from 1 to 3 wt % in order to examine the effect of MWCNTs on the structure and properties of the composites. The nanocomposites were characterized by DSC, DTA, TGA, UV–vis, FTIR and Raman spectroscopy to evaluate the changes induced by the filler in the polymer matrix. UV–vis, FTIR and Raman spectroscopy measurements confirmed the presence of the dispersed phase in the composite films, while TGA and DSC analysis of the nanocomposites revealed enhanced thermal stability and decreased crystallinity, respectively, as compared to the neat polymer. The proposed composites can find application in a number of everyday products where polycarbonate is the base polymer.

## Introduction

Polycarbonate (PC) is a polymer with remarkable mechanical and optical properties, broadly used for water bottles, monitor screens and aircraft interiors but also in business buildings and automotive light covers [1]. Some of these applications involve extended daylight exposure, which, especially due to UV radiation, induce progressive, irreversible changes affecting the life-

time, for example, optical polarization, which is associated with crystallization [2,3]. PC is an amorphous polymer with very low crystalline content, estimated at 1–2 wt %. Not only does UV exposure induce PC ageing, leading to crystallization, but also some solvents as well. They are thought to cause changes in chain conformation, which is associated with the presence of spherulite aggregates that are visible even under low magnification. Conventional thermoplastic processing is used to manufacture distinct PC products, where triazole compounds are commonly used as additives to stabilize PC and to retard the yellowing of PC upon exposure to light [4]. However, triazoles have serious thermal stability issues at the hot embossing temperature of PC. It has been suggested that the addition of MWCNTs can significantly change the mechanical properties of PC, as well as affect the crystallization behavior [5].

In former work, the effect of adding gold nanoparticles on the optical properties of PC was investigated [6]. Herein, we investigated the effect of MWCNT loading on the solvent-induced crystallization behavior of PC, eventually providing a better understanding that is useful for possible future control this phenomenon in PC-based consumer products. Proper filler dispersion is a common issue in obtaining good quality nanocomposites, especially in the case of high aspect ratio fillers such as CNTs. The efficiency in minimizing the amount of entangled bundles of MWCNTs and ensuring proper dispersion of them in the polymer matrices influences nearly all relevant properties of the composites [5,7]. Among the methods used for introduction of MWCNTs into the polymers [8], solution-based approaches ensure several advantages over direct melt mixing with respect to improved dispersion of the nanofillers within the polymer matrix due to lower viscosity of the dispersion media. Thus, we used *p*-xylene and dichloromethane solvent to mix MWCNTs and prevent their agglomeration induced by strong van der Waals forces. Previous work carried out on PC/MWCNT composites with focus on the mechanical properties showed an increase in the storage modulus obtained from indentation measurements at loadings as high as 10 wt % [9]. However, to the best of our knowledge, this is the first time that this composite system is investigated in detail for crystallinity and thermal stability. The research activity and procedures adopted during this work and reported here are in agreement with the predetermined objectives of the COST action Multi Comp CA15107 [10], aiming to improve the dispersion and stability of carbon-based suspensions and polymer composites.

# Experimental
## Materials
Commercial MWCNTs were used (FutureCarbon GmbH, Bayreuth, Germany), having a nominal diameter of $50 \pm 20$ nm and a length of 1–15 µm. PC pellets were used (Makrolon®,

Bayer), having nominal density of 1.19 g cm$^{-3}$, molecular weight of $\approx M_{\mathrm{w}}$ 54000 and polydispersity of 1.77. *p*-Xylene and dichloromethane of analytical grade (99.99% purity) were used (Sigma-Aldrich, Italy) without further purification.

## Nanocomposite film preparation
The pretreatment of PC, dispersion of MWCNTs and preparation of composite films was carried out using the following procedure. Since PC is a hygroscopic material with a tendency to absorb moisture from the environment, it was preheated in a vacuum oven at 120 °C for 4 h before processing. The moisture absorption was estimated at around 1–3% per day. After drying, the MWCNTs were dispersed in a solvent mixture of *p*-xylene and dichloromethane in 1:8 vol/vol at a concentration of 3 g/L and mixed using an ultrasonic bath (Fisher Scientific, FS60, Italy) operating at 40% amplitude for a total time of 30 min with on/off cycles (4 s and 2 s, respectively) in order to prevent heating which could occur during acoustic cavitation. The initial swelling of MWCNT agglomerates by solvent infiltration and interaction was considered as a crucial precondition to obtain a good dispersion of MWCNTs inside the polymer matrix [7]. Similarly, PC was separately dissolved in the same solvent mixture used to disperse MWCNTs at a concentration of 37 g/L. Then, a given amount of MWCNT dispersion was added to the PC solution in such a way as to obtain the predetermined MWCNT loading versus PC and mixed using a vortex mechanical agitator followed by sonication for thorough mixing of the two components without agglomeration. The obtained nanocomposite solutions (at different MWCNT loadings of 0, 1, 2 and 3 wt %) were cast into glass Petri dishes filled up to similar levels in order to maintain similar film thicknesses. The casted materials were allowed to dry at room temperature for 24 hours to obtain transparent nanocomposite films. The film thickness was estimated at $220 \pm 50$ µm, as determined by a screw gauge micrometer.

## Characterization
The dispersion of MWCNTs in PC, as achieved in the cast films, was characterized by UV–vis spectrometry using a Cary 6000i spectrometer by Varian, UK, in double beam configuration with empty reference sample position.

Fourier-transform infrared spectroscopy (FTIR) of PC/MWCNT composites with different loadings was carried out in the range of 600–4000 cm$^{-1}$ on a Bruker Vertex 70 spectrometer, Bruker, Madison, USA. The samples were analyzed in attenuated total internal reflection absorbance mode, with an aperture diameter of 3 mm and a spectral resolution of 4 cm$^{-1}$. For an optimal signal-to-noise ratio, 64 scans were averaged per sample spectrum and apodized. All the spectra were normalized thereafter.

Raman spectra were acquired with an inVia micro-Raman spectrometer by Renishaw, Gloucester, UK using a He–Ne laser excitation source emitting at a wavelength of 632.8 nm with a 20× objective. The data acquisition time was 30 s. The slit provided a spectral resolution of 1 cm$^{-1}$. Instrument calibration was performed using silicon samples.

To investigate the stability, purity and thermal resistance of the materials, thermogravimetric analysis (TGA) was used [11-14] (TGA/DSC-1, Mettler-Toledo, Italy). Simultaneous differential thermal analysis (DTA) was used to characterize the nanocomposites in nitrogen (flow rate 50 mL/min) from RT to 800 °C at a ramp rate of 10 °C/min. The TGA/DTA instrument was calibrated with standard weight indium standards for DTA heat flow.

A differential scanning calorimetry (DSC) instrument (Pyris Diamond by Perkin Elmer, UK) was used to record the thermal profile. DSC measurements were performed with an initial mass of ≈3 mg. All the tests were carried out in a nitrogen atmosphere at a flow rate of 30 mL/min at a heating rate of 10 °C/min. The DSC instrument was calibrated by using In and Zn as a standard.

# Results and Discussion
## Spectroscopic analysis
The typical quality of the nanocomposite films investigated in the present study is demonstrated by the low-resolution optical micrographs presented in Figure 1. The presence of occasional micrometer-scale aggregates upon drying is evident, especially at higher MWCNT loading, yet the presence of submicrometer-scale filler particles throughout the polymer matrix is also observed even at the highest MWCNT loading (see Figure 1d).

UV–vis absorption spectra of the PC/MWCNT composite films are presented in Figure 2. Good dispersion is crucial for optimal optical properties and ensures maximum surface area for filler/polymer matrix interaction. The absorption band observed at around 289 nm could be assigned to the individual MWCNTs due to the one-dimensional van Hove singularities [15,16]. The
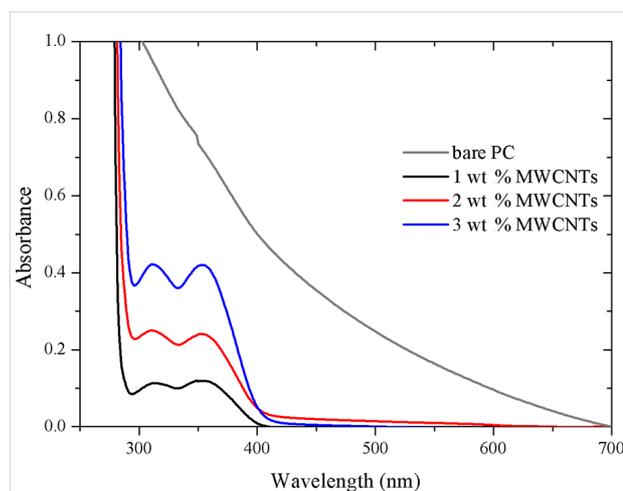


**Figure 2:** UV–vis absorbance of composite samples with different MWCNT loading.
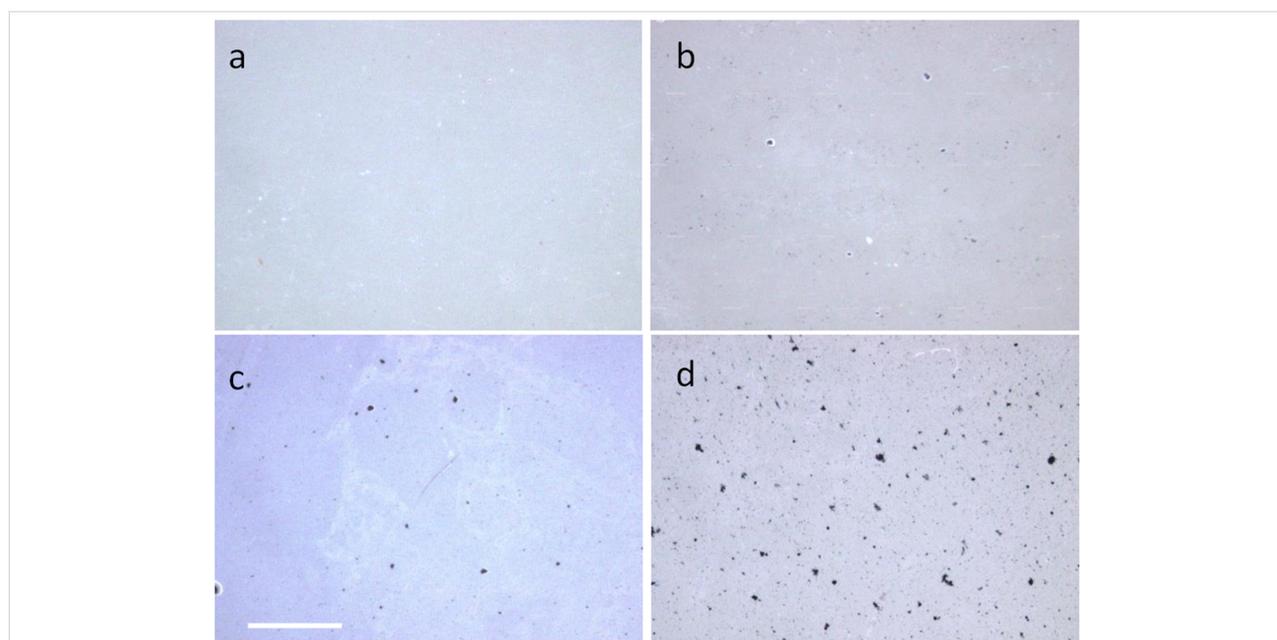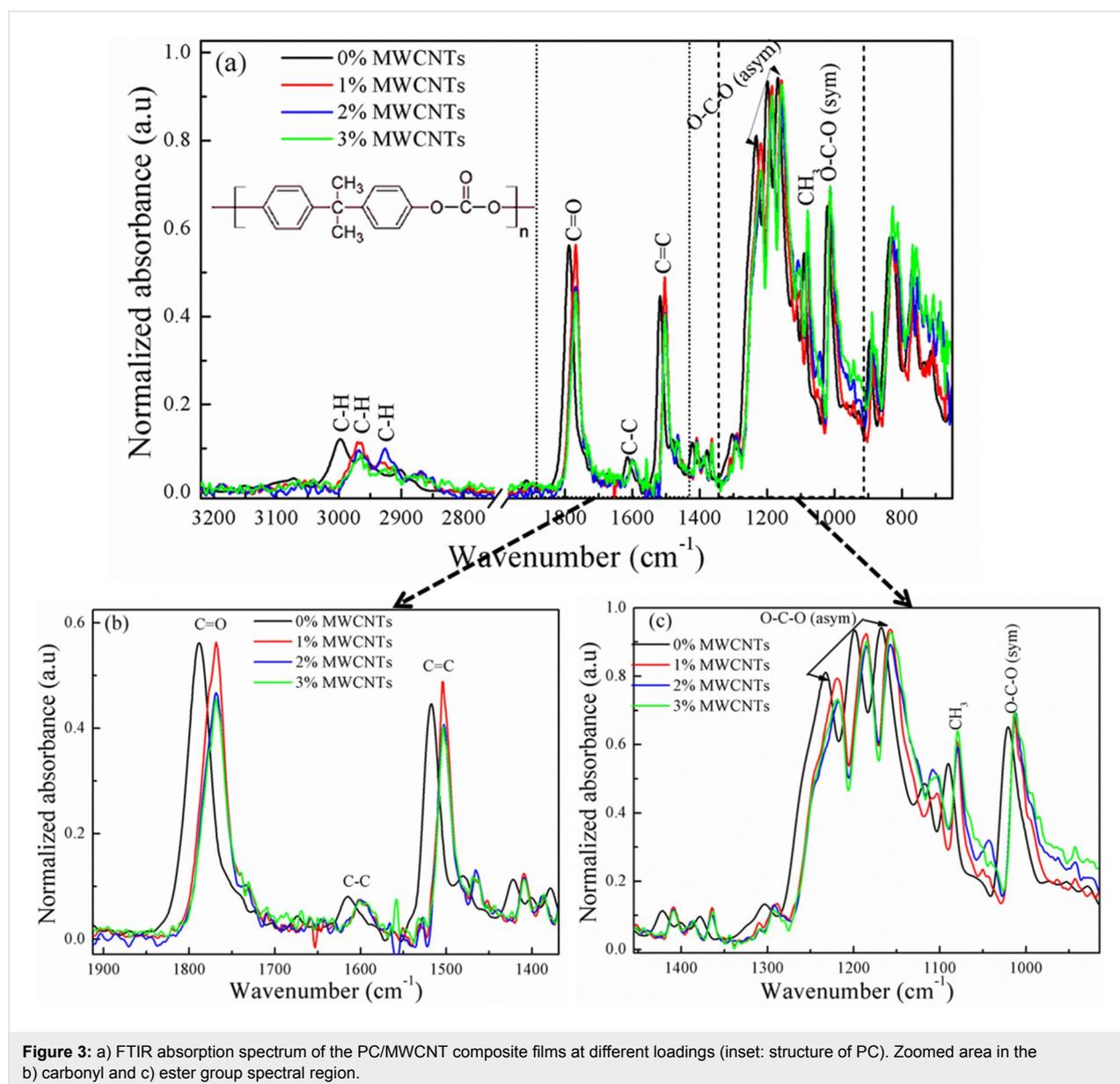


**Figure 1:** Optical stereomicroscope images (30× magnification) of PC composite films at different MWCNT loadings: a) 0, b) 1, c) 2 and d) 3 wt %. Scale bar: 100 µm, same for all images.

absorbance band intensity increases with increasing filler loading with maximum absorbance observed for the composition with 3 wt % loading of MWCNTs. This absorption is characteristic of individually dispersed MWCNTs, whereas strongly bundled MWCNTs do not show an absorption band in 200–1200 nm wavelength region as their photoluminescence is quenched or the carriers are tunneling between the nanotubes [17]. Also the absorption spectrum decreases slowly in the 362–289 nm range due to scattering in the lower wavelength range. These results are an indication that the nanotubes exist as large agglomerates and are strongly entangled before sonication and that the sonication treatment in polar solvent helps to overcome the van der Waals interaction in the nanotubes, eventually leading to better dispersion.

Figure 3 shows the normalized FTIR absorption spectra of principal absorbance bands of the investigated PC/MWCNT nanocomposite films. FTIR spectroscopy demonstrated to be a useful tool to investigate the structural changes in different material systems [18-20].

The characteristic IR bands of C–H from the aromatic rings are observed in the 2927 to 3000 cm$^{-1}$ region, together with the carbonate linker/carbonyl functional group (C=O) deformation at 1790 cm$^{-1}$. The stretching of the C–C bond from the phenyl group (benzene ring) occurs at $\approx$1600 cm$^{-1}$ and the C=C bond vibration at 1504 cm$^{-1}$. The stretching of the ester group (O–C–O) occurs from 1165 to 1232 cm$^{-1}$ [21]. Comparing the spectral band of bare PC with the 1, 2, and 3% MWCNT-loaded



**Figure 3:** a) FTIR absorption spectrum of the PC/MWCNT composite films at different loadings (inset: structure of PC). Zoomed area in the b) carbonyl and c) ester group spectral region.

nanocomposites reveals that the carbonyl band (C=O) in the spectrum of the former is shifted from 1788 to 1768 cm⁻¹. The C=C band at 1518 cm⁻¹ is shifted to 1504 cm⁻¹ and the bands at 1233 and 1200 cm⁻¹ in the region of the asymmetric O–C–O stretching vibration are transferred to a band at 1218 cm⁻¹ with a shoulder at 1258 cm⁻¹. The changes in the observed shift and intensity clearly indicate a change in crystallinity of the nanocomposites after nanotube loading.

The Raman spectra of the different PC/MWCNT composite films are shown in Figure 4. The blue curve represents the spectrum of bare PC, with the full fingerprint of the polymer in the region around 3000 cm⁻¹. The other curves show the spectra of composites with different loading, which are normalized to the G' overtone band of MWCNTs at 2683 cm⁻¹. In these spectra, the characteristic peaks for MWCNTs at 1342 cm⁻¹ (D band) and 1580 cm⁻¹ (G band) are clearly observed [22]. Additionally, one can see that upon increasing the MWCNT loading, the peaks characteristic of PC are depressed. Also, the peak around 1600 cm⁻¹ undergoes doublet formation with overall shifting towards lower wavenumbers, which reveals the interaction between MWCNTs and PC [23].
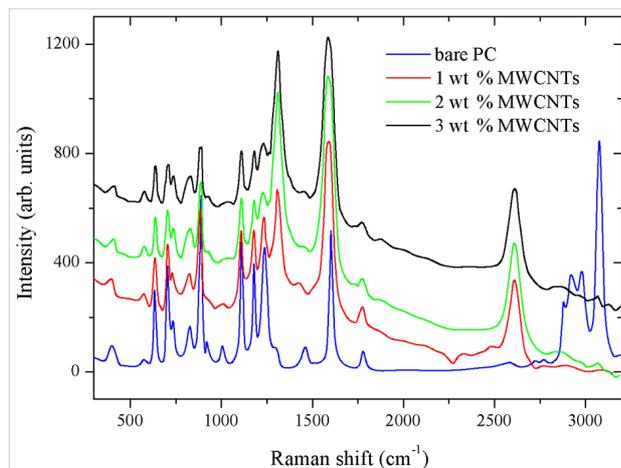


**Figure 4:** Raman spectra of PC/MWCNT composite films at different MWCNT loadings.

## Thermal analysis

Figure 5 shows the TGA/DTG and DTA analysis of the PC/MWCNT sample with 1 wt % loading. The profiles of the other composites (2 and 3 wt %) were qualitatively similar, apart from the shift in final wt % level and have not been included for the sake of clarity. No change in mass is observed in Figure 5 around 100–200 °C, indicating that the nanocomposite is free from any absorbed solvent or moisture. The major mass loss of around 80% occurred from 400 to 525 °C, and is due to the decomposition of the polymer matrix. The residual mass of 20% is comprised of both the MWCNTs and the amorphous carbon,

which obviously comes from the organic matrix. DTA reveals a broad, exothermic peak followed by a small shoulder, which is believed to be due to the interaction and thermal expansion of MWCNTs in the PC matrix. No other thermal changes are observed after 700 °C.
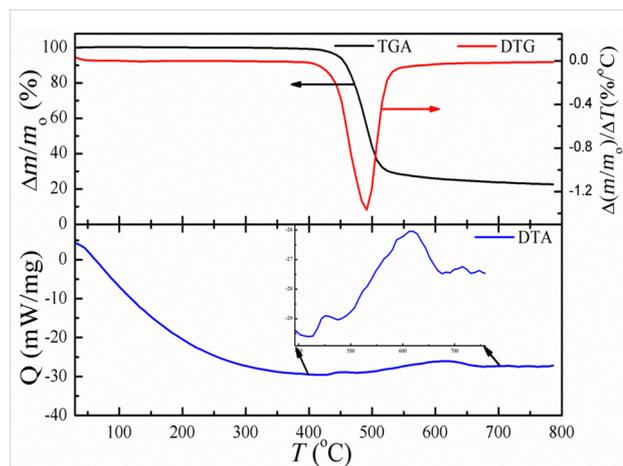


**Figure 5:** TGA/DTG and DTA analysis of the PC/MWCNT films at 1 wt % loading under N₂ flow. The inset in the lower panel shows the zoomed image of the DTA plot in the region of highest mass loss.

Figure 6 shows the DSC analysis of the PC/MWCNT film with 1 wt % loading, in both heating as well as cooling cycles. The DSC curve of the nanocomposite in the heating cycle exhibits a glass transition temperature at ≈143.5 °C. No amorphous polymer can exhibit a melting transition, as melting is a first-order transition occurring only for crystalline polymers. However, an endothermic peak followed by a shoulder with the enthalpy heat of fusion (27 J/g) is observed at 224.4 °C. This might be due to the possible ordered structure or segmental chain mobility of PC macromolecules changed due to the interaction of the MWCNTs. The lack of a cold crystallization peak
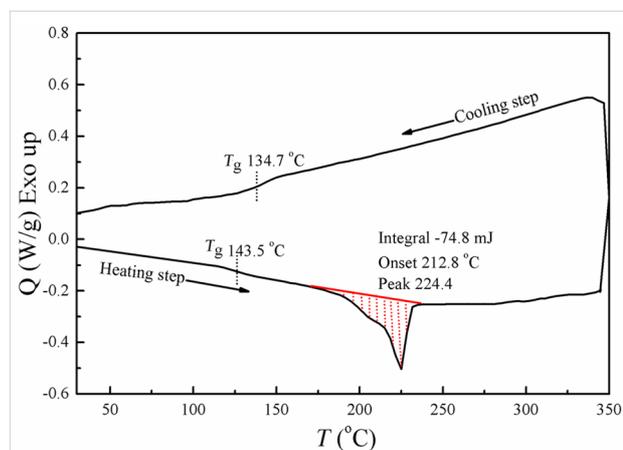


**Figure 6:** DSC profile of the PC/MWCNT film at 1 wt % loading.

appearing in the cooling cycle could be due to the enthalpy relaxation or mesophase transitions. The glass transition observed in the cooling cycle is 9 °C less than the heating cycle.

## Conclusion

PC/MWCNTs composites were prepared as transparent films. The presence of a dispersed, uniform phase in the composite films was confirmed. Vibrational spectroscopy was used to assess the change in behavior of the polymer matrix when adding the selected fillers and to discriminate the crystalline/amorphous balance behavior induced thereof. The fillers decreased the crystallinity as compared to the bare polymer. Thermal analysis allowed interpretation of the effect of filler loading into the PC matrix in terms of thermal stability, which was significantly enhanced with respect to the bare polymer. It can thus be speculated that MWCNT fillers influence the likely solvent-induced crystallization in PC. We think that the demonstrated study is promising and could help the research community in this area. The investigated composites, upon further characterization (e.g., by thermocycling or other artificially accelerated aging protocols), could possibly be a candidate for replacement of bare PC in a variety of applications.

## Acknowledgements

## References

1. Serini, V. Polycarbonates. In *Ullmann's Encyclopedia of Industrial Chemistry,* 28th ed.; Elvers, B., Ed.; Wiley-VCH: Weinheim, 2012; pp 603–611.
2. Seungman, S. Crystallization behavior of Bisphenol-A polycarbonate: effects of time, temperature, and molar mass. Ph.D. Thesis, Virginia Polytechnic Institute and State University, U.S.A., 2000.
3. Reiter, G.; Sommer, J.-U. *Polymer Crystallization: Obervations, Concepts and Interpretations;* Lecture Notes in Physics; Springer: Berlin, Germany, 2008.
4. Miladinova, P. M.; Konstantinova, T. N. *J. Chem. Technol. Metall.* **2015,** *50,* 229–239.
5. Loutfy, R. O.; Withers, J. C.; Abdelkader, M.; Sennett, M. Carbon Nanotube–Polycarbonate Compostles. In *Perspectives of Fullerene Nanotechnology;* Osawa, E., Ed.; Springer: Dordrecht, Netherlands, 2002; pp 317–325.
6. Larosa, C.; Stura, E.; Eggenhöffner, R.; Nicolini, C. *Materials* **2009,** *2,* 1193–1204. doi:10.3390/ma2031193
7. Che, B.; Nguyen, B.; Nguyen, L.-T. T.; Nguyen, H.; Nguyen, V.; Van Le, T.; Nguyen, N. *Chem. Cent. J.* **2015,** *9,* 10–22.
8. Chen, L.; Pang, X.-J.; Yu, Z.-L. *Mater. Sci. Eng., A* **2007,** *457,* 287–291. doi:10.1016/j.msea.2007.01.107
9. Jindal, P.; Yadav, R. N.; Kumar, N. *Iran. Polym. J.* **2017,** *26,* 445–452. doi:10.1007/s13726-017-0533-1
10. MultiComp - COST Action CA15107. http://www.multicomp-ca15107.eu/en/ (accessed Sept 4, 2017).
11. Mishra, N.; Patra, N.; Pandey, S.; Salerno, M.; Sharon, M.; Sharon, M. *J. Therm. Anal. Calorim.* **2014,** *117,* 885–892. doi:10.1007/s10973-014-3793-4
12. Patra, N.; Hladik, J.; Martinová, L. *J. Therm. Anal. Calorim.* **2014,** *117,* 229–234. doi:10.1007/s10973-014-3728-0
13. Patra, N.; Salerno, M.; Cozzoli, P. D.; Athanassiou, A. *J. Colloid Interface Sci.* **2013,** *405,* 103–108. doi:10.1016/j.jcis.2013.04.053
14. Patra, N.; Salerno, M.; Cozzoli, P. D.; Barone, A. C.; Ceseracciu, L.; Pignatelli, F.; Carzino, R.; Marini, L.; Athanassiou, A. *Composites, Part B* **2012,** *43,* 3114–3119. doi:10.1016/j.compositesb.2012.04.028
15. Hamada, N.; Sawada, S.-i.; Oshiyama, A. *Phys. Rev. Lett.* **1992,** *68,* 1579–1581. doi:10.1103/PhysRevLett.68.1579
16. Kataura, H.; Kumazawa, Y.; Maniwa, Y.; Umezu, I.; Suzuki, S.; Ohtsuka, Y.; Achiba, Y. *Synth. Met.* **1999,** *103,* 2555–2558. doi:10.1016/S0379-6779(98)00278-1
17. Lauret, J.-S.; Voisin, C.; Cassabois, G.; Delalande, C.; Roussignol, P.; Jost, O.; Capes, L. *Phys. Rev. Lett.* **2003,** *90,* 57404. doi:10.1103/PhysRevLett.90.057404
18. Thorat, S.; Patra, N.; Ruffilli, R.; Diaspro, A.; Salerno, M. *Dent. Mater. J.* **2012,** *31,* 635–644. doi:10.4012/dmj.2011-251
19. Patra, N.; Barone, A. C.; Salerno, M. *Adv. Polym. Technol.* **2011,** *30,* 12–20. doi:10.1002/adv.20203
20. Patra, N.; Jayaseelan, D. D.; Lee, W. E. *J. Am. Ceram. Soc.* **2015,** *98,* 71–77. doi:10.1111/jace.13321
21. Kuptsov, A. H.; Zhizhin, G. N. *Handbook of Fourier Transform Raman and Infrared Spectra of Polymers,* 1st ed.; Elsevier: Amsterdam, Netherlands, 1998.
22. Bokobza, L.; Zhang, J. *eXPRESS Polym. Lett.* **2012,** *6,* 601–608. doi:10.3144/expresspolymlett.2012.63
23. Babal, A. S.; Gupta, R.; Singh, B. P.; Singh, V. N.; Dhakate, S. R.; Mathur, R. B. *RSC Adv.* **2014,** *4,* 64649–64658. doi:10.1039/C4RA11319E

# Engineering of oriented carbon nanotubes in composite materials

Razieh Beigmoradi[1,2], Abdolreza Samimi[*,1,2,§] and Davod Mohebbi-Kalhori[1,2]

## Abstract

The orientation and arrangement engineering of carbon nanotubes (CNTs) in composite structures is considered a challenging issue. In this regard, two groups of in situ and ex situ techniques have been developed. In the first, the arrangement is achieved during CNT growth, while in the latter, the CNTs are initially grown in random orientation and the arrangement is then achieved during the device integration process. As the ex situ techniques are free from growth restrictions and more flexible in terms of controlling the alignment and sorting of the CNTs, they are considered by some as the preferred technique for engineering of oriented CNTs. This review focuses on recent progress in the improvement of the orientation and alignment of CNTs in composite materials. Moreover, the advantages and disadvantages of the processes are discussed as well as their future outlook.

## Review
### Introduction

Carbon is one of the most abundant elements comprising the world around us. Before 1985 graphite and diamond were the only known structural forms of carbon [1]. In 1991, Iijima discovered a new carbon structure which later became known as the carbon nanotube (CNT) [2]. Depending on the number of walls in the structure, CNTs are categorized as single-walled CNTs (SWCNTs), double-walled CNTs (DWCNTs) or multi-walled CNTs (MWCNTs). A SWCNT is the result of rolling a graphite sheet, and a MWCNT consists of many coaxial single-walled tubes nested inside each other. Considering the excellent mechanical and electrical characteristics of CNTs, interest in using them in industry is increasing every day. Various industrial applications of produced CNT composite materials, especially electronic, military, and new composites, has drawn the attention of researchers to this topic in recent decades [3-5]. Figure 1 and Figure 2 represent the growth rate of papers and patents and the fields of application of CNTs in the past 16 years, based on Scopus data, respectively.
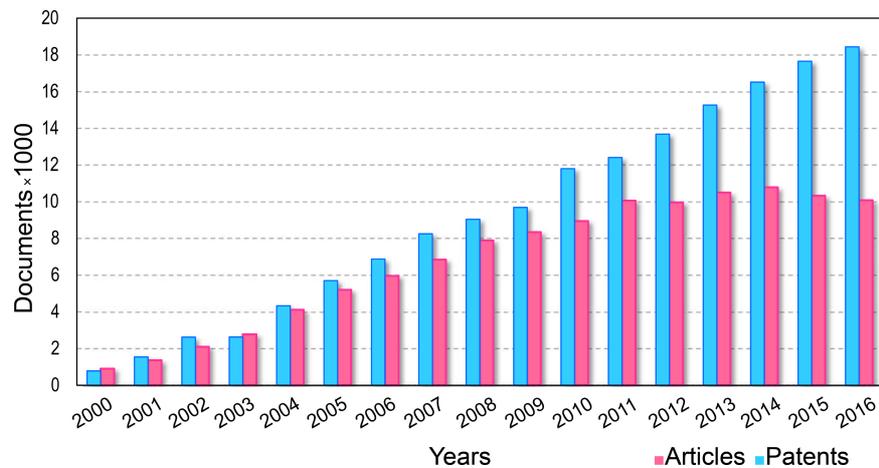
**Figure 1:** Number of papers and patents published in the past 16 years on the topic of CNTs. The numbers were determined based on a Scopus search spanning from 2000 to 2016 using the keywords: carbon nanotubes and CNT.
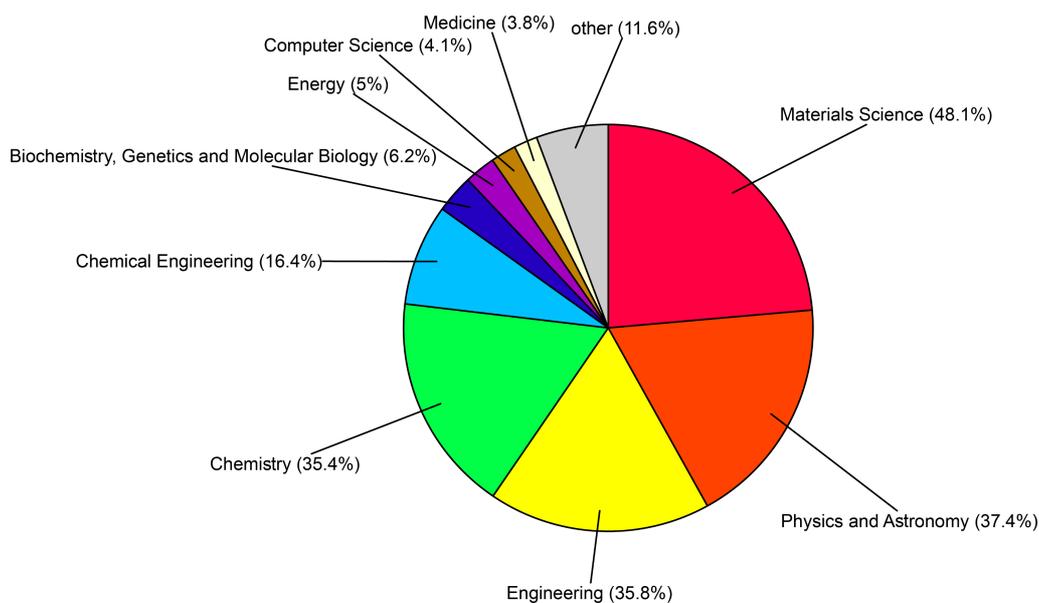


**Figure 2:** Subject areas of papers published in the past 16 years on the topic of CNTs. The numbers were determined based on a Scopus search spanning from 2000 to 2016 using the keyword carbon nanotubes.

As indicated, the areas of research regarding CNTs are vast and extend to several subcategories. In each subcategory issues such as structural uniformity, dispersion and stability, superficial defects, and intermolecular and composite interactions are very important [6-8].

Nowadays, the biggest challenge in using all the capabilities and exceptional properties of CNTs in the production of new materials is essentially the limitation of a lack of uniform structure which could be obtained by controlling their sorting and orientation. Because the properties of CNTs vary according to

size and shape (diameter, length and whether they are open- or close-ended), their arrays and arrangement in composite materials may lead to different properties.

For example, in their recent research, Nam et al. have shown the effect of diameter in a composite material containing aligned CNTs [9]. This study showed that composites fabricated with a smaller average diameter have significantly better mechanical properties. Gulotty et al. have reported that CNTs with a longer and larger diameter more efficiently improve the thermal conductivity of polymer composites [10].

Furthermore, it has been shown that for biological applications the CNT diameter and length are critical parameters in protein corona formation and biocompatibility [11,12].

In another research investigating the effect of aligning CNTs in composite material structures, a remarkable improvement in the electrical properties of CNT composites was observed, as compared to their random placements [13]. In recent research reported by Lee et al., two factors, the CNT length and their arrangement, were introduced as important characteristics affecting electron transport properties in the matrix of composite materials [14].

CNTs are excellent alternatives to metal oxides for metal-free catalysis [15] or in synergy with metal oxides [16,17], especially for sustainable energy applications [18,19]. Because of their electronic properties, CNT composites offer unmatched opportunities for conductive tissue regeneration [20], particularly if alignment, and thus 3D anisotropy, is achieved for the engineering of cardiac [21], muscle [22] and nerve tissues [23]. Finally, CNT properties can be fine-tuned upon chemical functionalization. However, the latter characteristic needs to be well-balanced in order to prevent degradation of the CNT properties [24-26].

The results of these studies and similar reports indicate that methods by which the arrangement of CNTs can be controlled and adjusted are of great importance. In fact, if nanocomposites with an adjusted arrangement and desired distribution of CNTs could be produced, then our expectations about the properties of CNT nanocomposites could be fulfilled [14,27-30].

In terms of processing techniques, the arrangement and alignment of CNTs in a matrix of composite materials are divided in two categories. In the first category alignment is arranged during growth, where the regular placement of catalyst nanoparticles on the substrate leads to growth of CNT masses in regular rows. In the second category, the arrangement occurs after growth. There have been several review articles written about the alignment methods of CNTs [6,31-35]. However, most of these focus on the synthesis of aligned CNTs, and the number of methods reporting the arrangement of CNTs after their production is limited.

In this paper, arrangement techniques utilized after the growth of CNTs, regardless of the orientation of the CNTs, are specifically reviewed. In these techniques, CNTs are added using various methods as an additive to the structure of the desired material to attempt to align the CNTs in the network of composite material. The uniform alignment is obtained to achieve the expected desirable and unique properties for CNTs.

Furthermore, methods for characterization and evaluation of CNTs (regarding their arrangement) are presented and discussed.

## Post-growth sorting of CNTs in a composite material structure

As mentioned above, the methods for arranging CNTs are divided into two main categories: orientation during growth (in situ) and post-growth (ex situ). In post-growth orientation processes, the CNTs are initially produced using conventional methods. Then, by applying a distinct process, they are arranged for a specific purpose. Compared with in situ methods, ex situ methods do not have limitations in the production of CNTs, such as restriction on the substrate type and processing temperature, and also the variety of their final product is much greater. In the following, the post-growth sorting methods are discussed in more detail.

### Carbon nanotube/polymer film stretching

By dipping a polymer substrate into a well-dispersed CNT solution a thin layer of CNTs is set on the polymer, and then the clamped opposite edges of the substrate are uniaxially stretched. A relatively warm air flow (approximately 60–100 °C) is used during the stretching process to keep the polymer soft. Then, a very small but steady twisting action is performed by hand. During the stretching process, the CNT direction is changed under the elastic field from the polymer matrix [33] (Figure 3). The stretching ratio depends on the length ratio of the thin layer before/after stretching. Yao et al. prepared a MWCNT/polyvinylidene fluoride (PVDF) nanocomposite at a relatively high concentration of CNTs and aligned them inside the polymer matrix by stretching. They reported that a high degree of alignment was achieved and the composite dielectric properties changed upon CNT alignment [36].
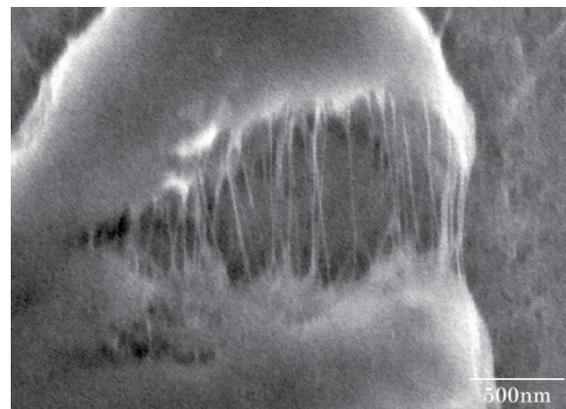


**Figure 3:** SEM image of a CNT/polymer film. The oriented CNTs are indicated in the fractured part of the composite. Reproduced with permission from [33], copyright 2009 Versita Warsaw.

Although this method is relatively simple, and some polymers such as polyethylene can be stretched more than 30 times without failure, its application is limited to the laboratory because of the inhomogeneous stretching ratio at the edge of films need manual operation and a skillful operator [17].

## Fracture stretching

An ultimate case of stretching is known as fracture and occurs when a hard polymer composite comprising CNTs, such as polyurethane (PU) or polystyrene (PS), is stretched too far. Fracture occurs and the oriented CNTs are formed in the fracture gap as shown in Figure 4. Since CNTs have the desired electronic properties and the method is easy to perform, this technique might be suitable for making CNT electronic devices such as field emitters [6,27,28,31,33,37-39].

In recent research, fracture and stretching processes have jointly been used to align CNTs in a controlled manner [40]. In this process, functionalized CNTs were initially well-dispersed in water using ultrasound and then were sprayed on a nylon membrane or the polymeric membrane was directly dipped in a suspended mixture of CNTs. By using vacuum evaporation, the water content of the composite was ultimately evaporated. The latter CNT–polymer composite was then covered with a polysulfone (PSF) layer. The resulting composite was then pressed for 10–20 seconds at a temperature of 100–120 °C and pressure of 106 Pa. Lastly, the composite sheet was carefully peeled off to form two uniform layers of PSF/nylon/CNTs (Figure 5). In fact, compression under heat treatment leads to a strong interaction between the membrane surface and CNTs. Because of the angle of the gap between the two layers and the simultaneous effects of the shear force and mechanical tensile stretch, a slight drag force pulls the CNT in the vertical direction. However, the obtained free CNTs are certainly not vertical relative to the sur-

face of layers. Although the small length of the tubes limits the angle of the gap, it also leads to a very small angle deviation in the direction of the shear force. In principle the tubes were not constrained to be quite vertically oriented, but a microscopic view showed satisfactory alignment. To keep the CNTs aligned, the top layer of the CNT/PSF membrane could be coated by cellulose acetate (CA) solution.

## Frictional orientation

The frictional orientation method is known as the doctor blade (DB) technique or tape casting. This technique is widely used to produce a variety of thin layers and coat substrates with wet films. A blade or a spiral film applicator is generally used to rub the layers. When a polymer layer including CNTs is rubbed in a certain direction while being softened by a heating process, elastic forces tend to orient and align the CNTs. Although this method can be performed automatically, due to damages that may be exerted on the polymer layer, manual alignment is preferred [41].

Based on the fundamental principles of this approach, another method for making thin films of CNTs has been developed using the same tools. Fluid containing CNTs is spread on a solid substrate using a spiral film applicator. The surface tension and viscosity of the fluid are two important factors affecting the final result of deposition on the substrate. In Figure 6a, a schematic of a designed tool for this purpose is shown [42].

## Carbon nanotube/fibrous composites

Over the last century, fibrous structure nanocomposites have been extensively considered due to their desirable physical properties [43]. In this regard, CNT/fibers have obtained a special spotlight because of their possibility to be arranged in a controlled way, the dependency of bulk electrical and mechani-
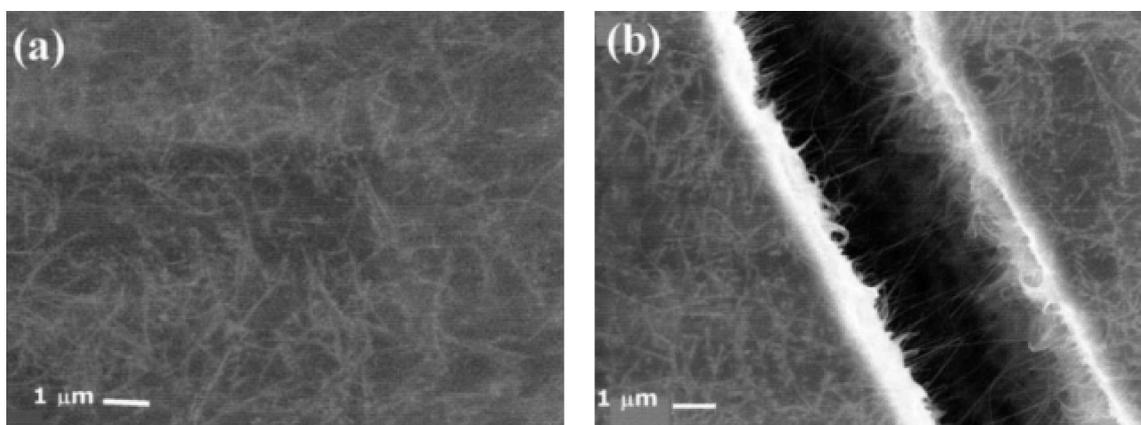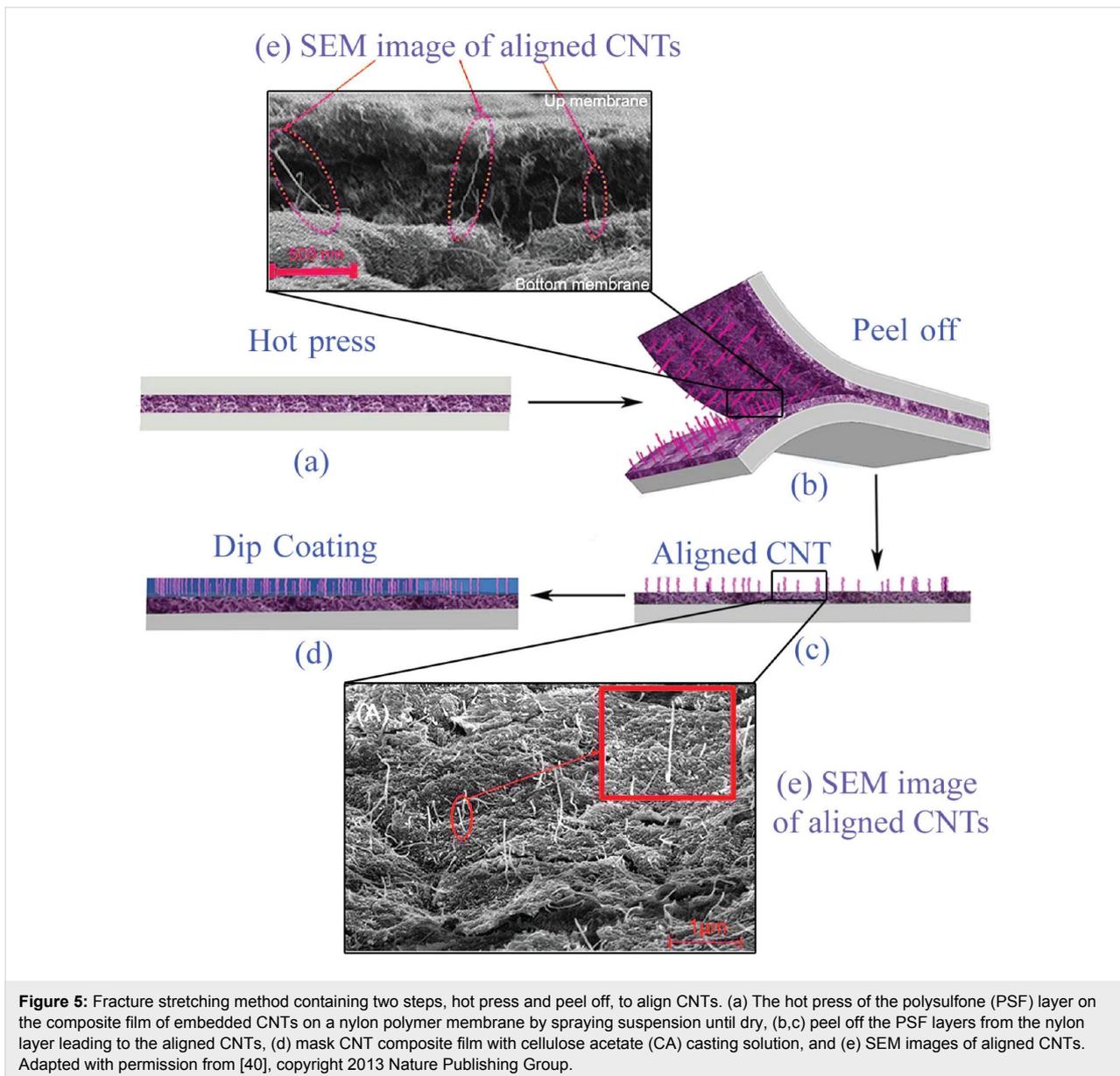


**Figure 4:** SEM images of a polystyrene (PS) composite film containing 25 wt % CNTs. (a) Random networked CNTs on the film surface and (b) oriented CNTs by fracturing, reproduced with permission from [37], copyright 2002 AIP publishing LLC.

**Figure 5:** Fracture stretching method containing two steps, hot press and peel off, to align CNTs. (a) The hot press of the polysulfone (PSF) layer on the composite film of embedded CNTs on a nylon polymer membrane by spraying suspension until dry, (b,c) peel off the PSF layers from the nylon layer leading to the aligned CNTs, (d) mask CNT composite film with cellulose acetate (CA) casting solution, and (e) SEM images of aligned CNTs. Adapted with permission from [40], copyright 2013 Nature Publishing Group.

cal properties of composites on the characteristics of the CNT, and the ensemble and production ability of the fibers in semi-industrial quantities [44]. The two methods commonly used to make CNT/nanofiber are described below.

**Electrospinning:** Electrospinning (ES) can be used to produce fibers from a viscous solution of polymer/CNTs, it is also employed for aligning CNTs in the fibers. In this method, a high voltage DC current (about 25 kV) is used between a charged polymer and a metallic collector to produce continuous filaments. Experiments revealed that the functionalized CNTs are aligned in the direction of the axis of the nanofiber polymers [45-47]. Figure 7 shows a TEM image of an orientated CNT embedded in a polymeric fiber.

As the orientation of the fibers also orients the CNTs in the same direction, in ES, the design of the collector plays the key role in the regular arrangement of the fibers and in enhancing the desired composite properties [49-52]. For example, Park et al. described how better alignment and mechanical and actuating performance of CNT/PVDF ES nanofibers was achieved by changing the drum collector parameters [51]. Their results indicated that the mechanical properties were improved up to 300% in the arranged direction.

A standard setup of an ES device, including power supply, syringe pump, and collector plate, is indicated in the central part of Figure 8. The upper and lower sections of Figure 8 show other types of collectors developed to collect the oriented fibers.
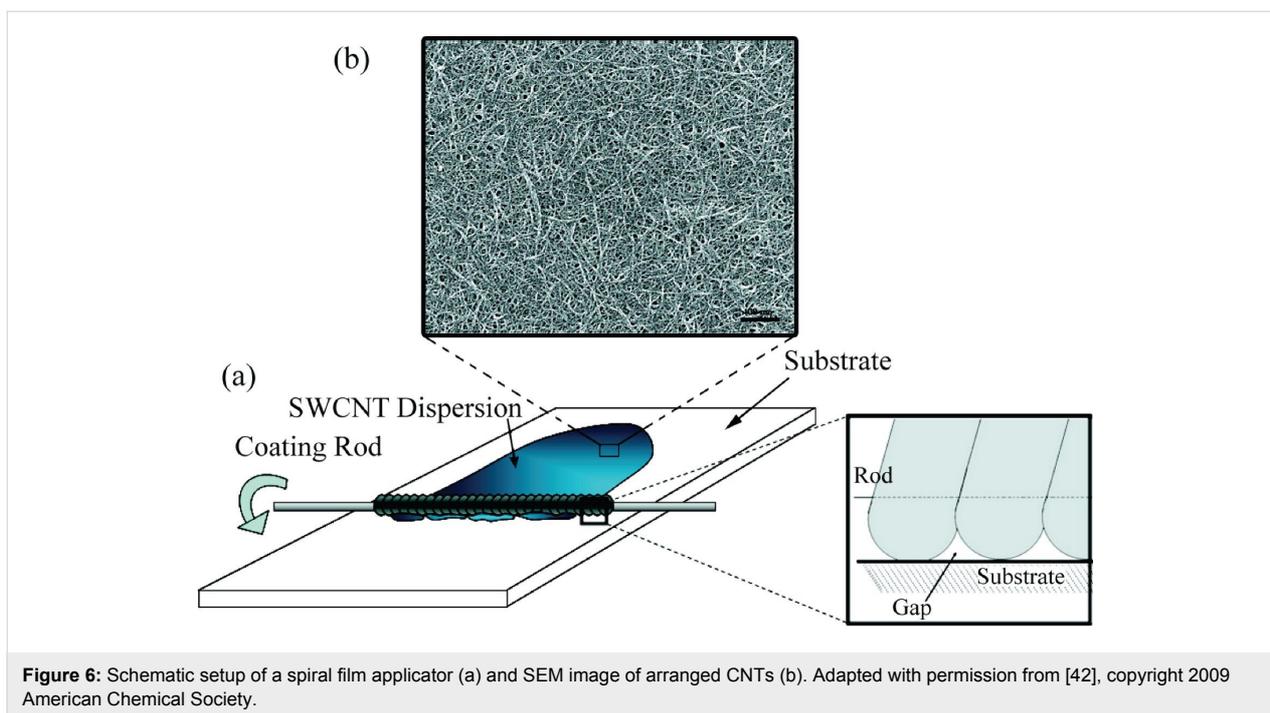
**Figure 6:** Schematic setup of a spiral film applicator (a) and SEM image of arranged CNTs (b). Adapted with permission from [42], copyright 2009 American Chemical Society.
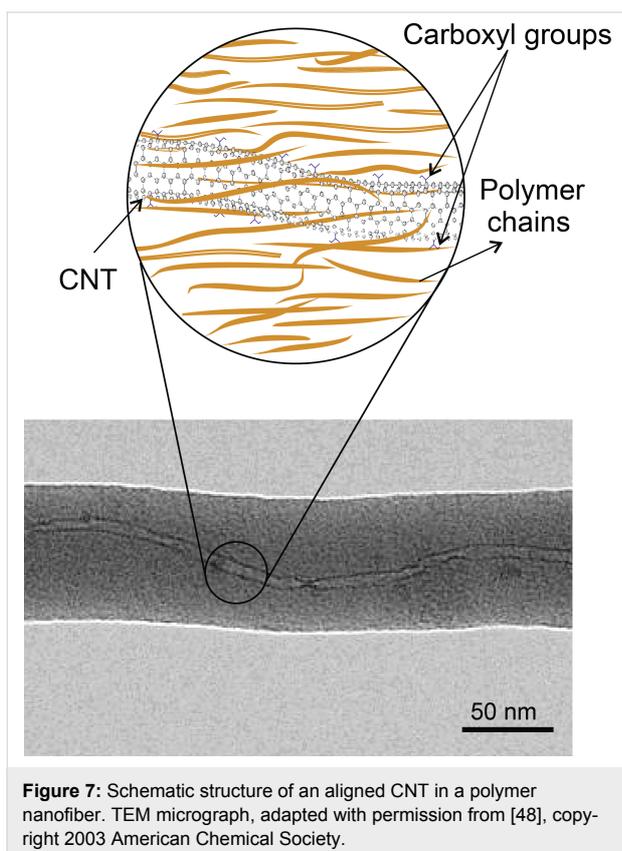


**Figure 7:** Schematic structure of an aligned CNT in a polymer nanofiber. TEM micrograph, adapted with permission from [48], copyright 2003 American Chemical Society.

**Fiber Drawing:** Coagulation spinning is another method recommended for producing concentrated and aligned composite nanomaterials. In this method SWCNTs are initially dispersed in an aqueous solution of poly(vinyl alcohol) (PVA) and are stabilized using surfactants. By applying the wet spinning method, a web of nanocomposite material fibers is produced where the arrangement of CNTs and sorting of nanofibers are done at the same time, as shown in Figure 9 [70].

Recently, direct spinning to a vertical chemical vapor deposition (CVD) synthesis zone has also been studied and is under development to produce CNT fibers and ribbons [44,71]. In a vertical CVD reactor, the CNT fibers are fabricated by drawing an aerogel of CNTs from the gas phase during growth [44]. The drawing orients the CNT bundles and can be combined with other techniques to fabricate diverse composites. The experimental works indicate the ability of the method to produce continuous CNT fibers with a high degree of orientation on a large scale. However, catalytic impurities are still the biggest challenge of this method [72].

## Spray winding and layer-by-layer deposition

Two of the latest controlled methods to produce composite polymer nanomaterial/CNTs are spray winding [73-76] and layer-by-layer deposition (LBL) [77-83].

Spraying [84-86] and electrospraying [87-92] are efficient methods to create a homogeneous layer of polymer liquid on the winding mandrel. Because of the simplicity and adjustability of the process and potential for use of a wide range of materials, spraying can be combined with other methods to fabricate composite materials.
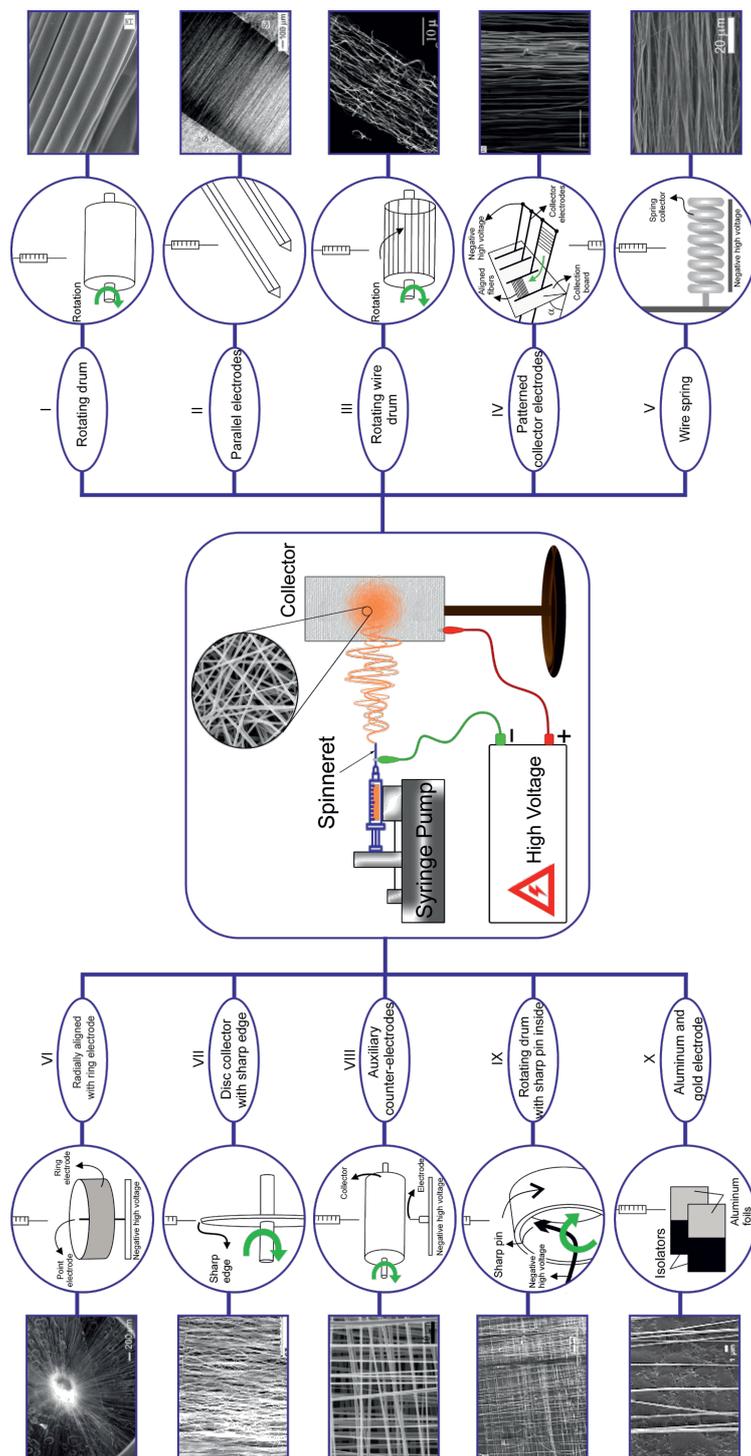
**Figure 8:** An electrospinning workflow illustrates a standard electrospinning setup, including power supply, syringe pump and collector plate and other collectors developed to collect oriented fibers. (I) [50,53-55], (II) [56], (III) [57], (IV) [58], (V) [59], (VI) [60], (VII) [61,62], (VIII) [63], (IX) [64], (X) [65]. SEM images: (I) Reproduced with permission from [55], copyright 2005 American Chemical Society, (II) Reproduced with permission from [56], copyright 2003 American Chemical Society, (III) Reproduced with permission from [57], copyright 2004 American Chemical Society, (IV) Reproduced with permission from [58], copyright 2008 AIP publishing LLC, (V) Adapted with permission from [59], copyright 2015 American Chemical Society, (VI) Adapted with permission from [60], copyright 2010 American Chemical Society, (VII) Reproduced with permission from [62], copyright 2009 American Chemical Society, (VIII) Reproduced with permission from [63], copyright 2008 American Chemical Society, (IX) Reproduced with permission from [64], copyright 2004 AIP publishing LLC, (X) Reproduced with permission from [65], copyright 2006 AIP publishing LLC. It should be noted that the electrospinning method is also appropriate for commercial applications due to its high throughput [66-69].
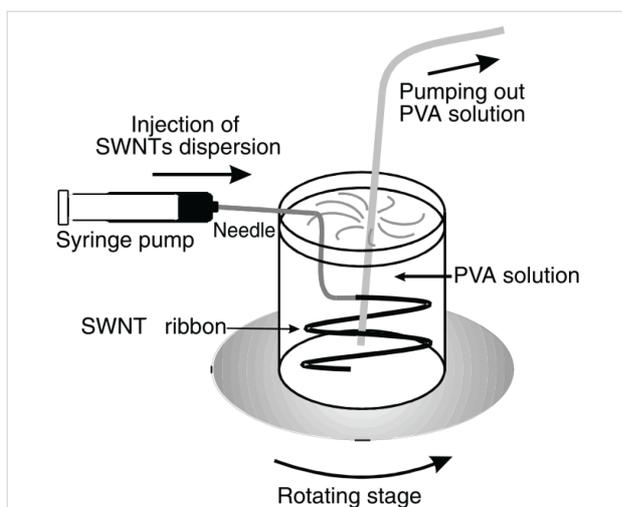
**Figure 9:** Schematic of the experimental setup for the wet spinning technique, reproduced with permission from [70], copyright 2000 The American Association for the Advancement of Science.

In this method, a sheet of CNTs is produced by chemical vapor deposition (CVD) on a $SiO_2$/Si substrate that is coated with a very thin layer of iron as a catalyst. The CNT rows have been grown perpendicular to the substrate so that they form a completely continuous sheet, resulting in a very elastic structure [93]. Then this elastic sheet is placed on a mandrel and small droplets of solution are deposited by spraying a dilute solution of a polymer on the CNT sheet during controlled rotation of the mandrel. As a result, a layer of polymer/CNT composite material is formed as shown in Figure 10. Finally, this composite layer is compressed between two hot plates to remove air bubbles and enhance the bond between the polymer and carbon nanotube. This method is highly regarded because of the simplicity of the manufacturing process, industrial scalability and controllability of CNTs [94]. Although the alignment of CNTs occurs during their growth, in the spray winding method, the main orientation of the CNTs in the matrix of the composite material is carried out in a separate mechanical method. That is why this method is classified as an after growth orientation method rather than during growth alignment.

In the layer-by-layer deposition method, the substrate is alternately and repeatedly dipped into an aqueous solution of functionalized targeted material, and in accordance with the functionalized material, controlled layers are deposited on the substrate. This method can be used to produce very thin and coherent layers, under mild conditions, in a wide range of composite materials (Figure 11).

This method, accompanied by other methods, can also be used in membrane manufacturing. In this regard, the spray-assisted LBL method is employed to produce a thin layer of polyelectrolyte/CNT [82]. A 20% solution of MWCNT/ethanol that has been ultrasonicated for 30 minutes is added to an aqueous poly(sodium 4-styrenesulfonate) (PSS) solution to produce a homogeneous PSS solution. Furthermore, poly(diallyldimethyl-ammonium chloride) (PDDA) aqueous solution is made by adding the polymer to deionized water. Both resulting solutions are strong polyelectrolytes and can be ionized in a wide range of pH. Before producing the film, the polyestersulfone (PES) substrates are soaked in 25 °C water for 24 hours and the water is replaced every three hours. Then the spraying process is carried out with a 0.35 mm nozzle under 20 psi pressure. By repeating this process, a thin film of PSS/MWCNT-PDDA is formed on the PES substrate. In this process, the deposition of PSS/MWCNT on the PES substrate was initiated by hydrogen bonds and hydrophobic interactions and the positively charged PDDA bonds with the PSS/MWCNT layer via electrostatic and van der Waals forces. This scheme is illustrated in Figure 12.

## Inert gas flow

In this method, the CNTs are arranged by flowing a gas along the substrate. The CNT suspension is deposited drop-by-drop on a substrate and an inert gas, with a linear velocity of approximately 10 cm/s, and flows along the substrate simultaneously. The gas flow concurrently spreads the droplets and also orients the CNTs in the direction of the gas flow (Figure 13). This simple method can automatically cover a wide area of the substrate [95].
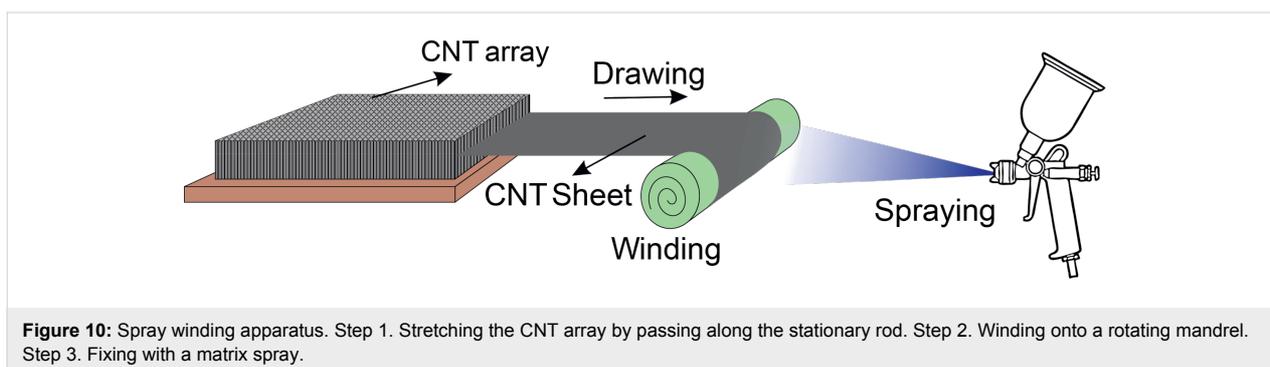


**Figure 10:** Spray winding apparatus. Step 1. Stretching the CNT array by passing along the stationary rod. Step 2. Winding onto a rotating mandrel. Step 3. Fixing with a matrix spray.
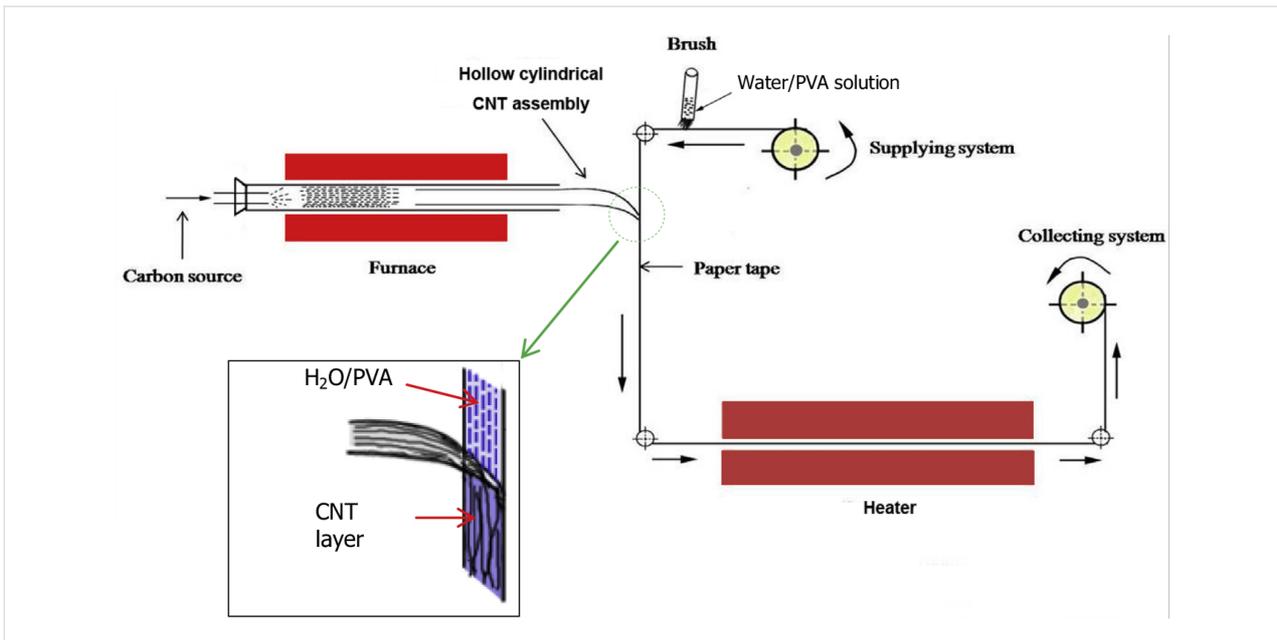
**Figure 11:** Schematic of the layer-by-layer deposition process. Step 1. Wetting a paper tape with water/poly(vinyl alcohol) (PVA). Step 2. Introducing the assembled CNT layer in the reactor. Step 3. Winding up after drying. Reproduced with permission from [78], copyright 2015 Elsevier.
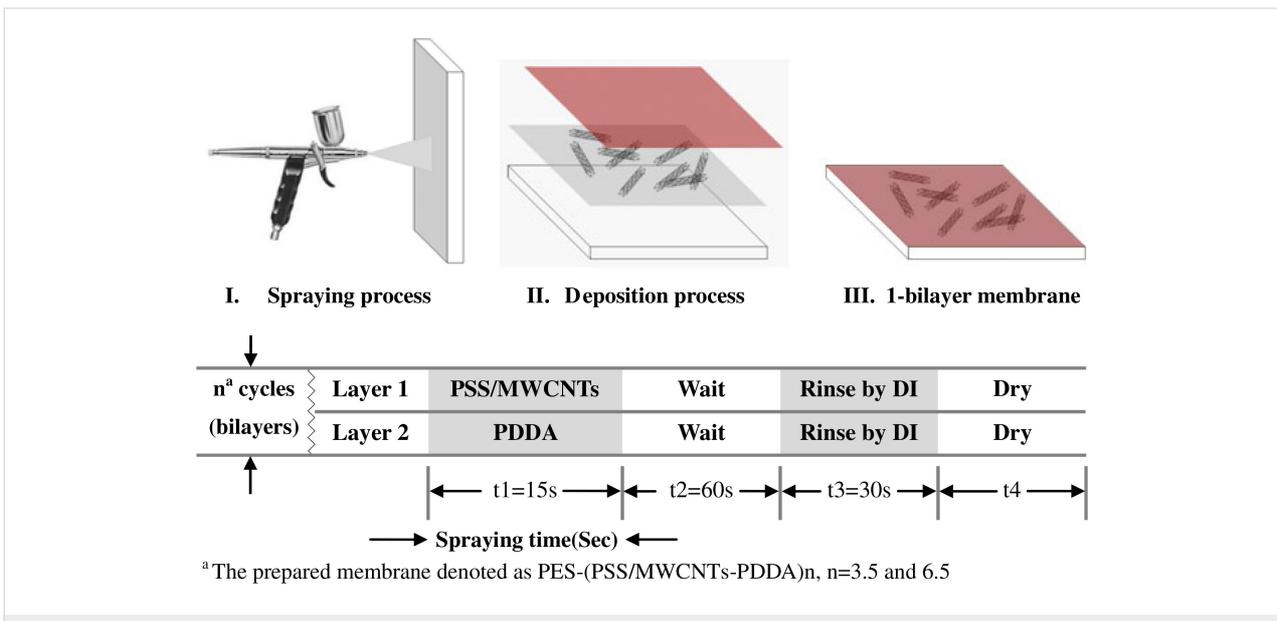


**Figure 12:** Layer-by-layer technique to fabricate an ultrathin CNT composite membrane. Reproduced with permission from [82], copyright 2013 Desalination and Water Treatment.

## Liquid crystal molecules

When a solid is heated to its melting point it loses its molecular order and is converted to a liquid with molecules in random orientation. When heated, some materials such as cholesteryl benzoate first convert to a liquid crystal (LC) phase and then convert to a liquid. Liquid crystals are made of rod-shaped molecules that are aligned parallel to each other and show different properties in different directions (Figure 14). For example, they

become transparent at high frequency and opaque at low frequency.

Because of the unique molecular structure of the liquid crystal (LC) (i.e., that it can be simply oriented in the direction of an applied electric or magnetic field) the alignment and dispersion of the CNTs in a solution of liquid crystals is also achievable (Figure 15). The biggest advantage of this method is that small
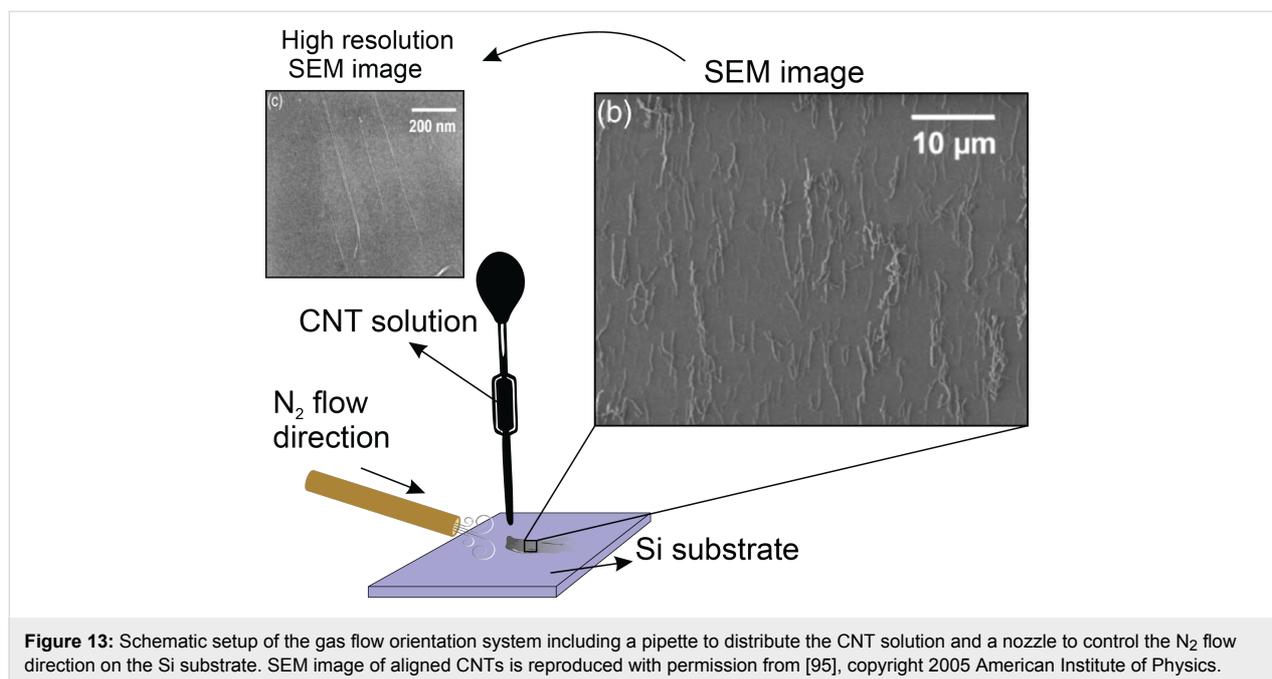
**Figure 13:** Schematic setup of the gas flow orientation system including a pipette to distribute the CNT solution and a nozzle to control the N₂ flow direction on the Si substrate. SEM image of aligned CNTs is reproduced with permission from [95], copyright 2005 American Institute of Physics.
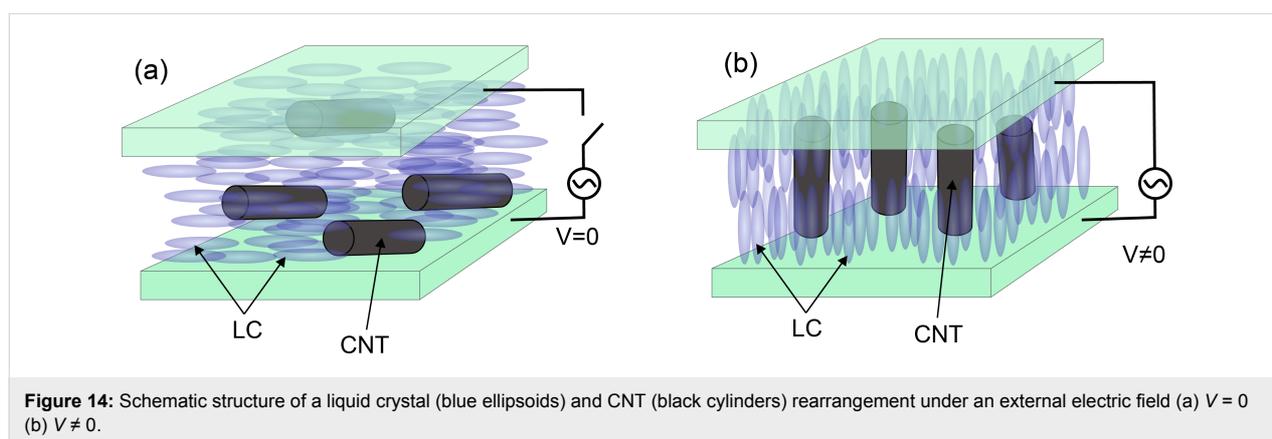


**Figure 14:** Schematic structure of a liquid crystal (blue ellipsoids) and CNT (black cylinders) rearrangement under an external electric field (a) $V = 0$ (b) $V \neq 0$.

fields are required to align CNTs as compared to cases where liquid crystals are not used. However, difficulties in the preparation of LC phases, especially at high concentrations, limit its applications [96-98]. On the other hand, it is known that progress in CNT alignment using this technology depends more on the quality of the CNTs than the ability to control the interactions of the CNT and LC [84].

## Filtration method

Filtering a well-dispersed and dilute solution of CNTs through a porous membrane may lead to the arrangement of the CNTs [99]. A very narrow pore size distribution (a thousand nanometers, approximately) in the membrane structure is needed to achieve a significant arrangement, which makes the process slow and inefficient. Furthermore, large masses of CNTs may quickly block the pores, causing some non-arranged CNTs to be

transferred onto the substrate [100]. Nevertheless, combining the properties of LCs (as mentioned in the previous section) with the filtration method was found to effectively enhance the alignment [101]. Figure 16 shows a filtration apparatus to fabricate the aligned CNT film on the membrane surface.

## Forming thin carbon nanotube layers by the pulling procedure

The method is illustrated schematically in Figure 17. The main step in this method, known as the Langmuir–Blodgett (LB) technique, is to immerse a solid substrate into a well-dispersed CNT solution and slowly and gently pull it out (≤1 cm/min). The result is the formation of a thin homogeneous layer of CNTs oriented in the immersing direction. The three factors controlling the thickness of the layers are the CNT concentration in the solution, the number of dips and the speed by which
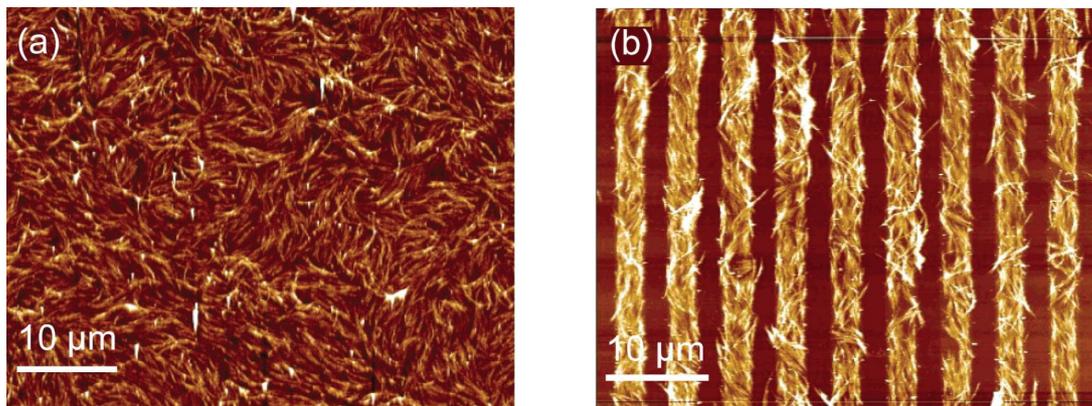
**Figure 15:** AFM images of a CNT-thin-film transistor with (a) randomly and (b) well-oriented CNT arrays, adapted with permission from [98], copyright 2006 American Chemical Society.
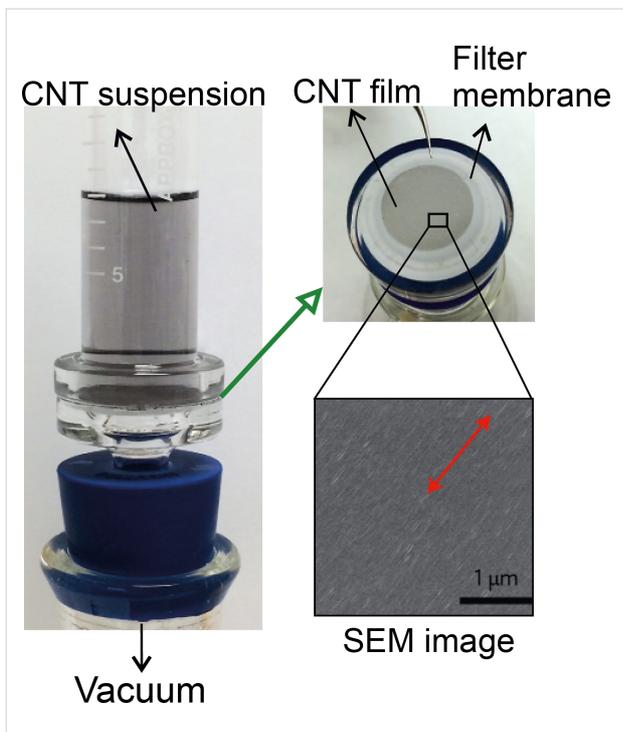


**Figure 16:** The filtration apparatus to fabricate the aligned CNT film on the membrane surface. The SEM image confirms the alignment of the CNTs, adapted with permission from [99], copyright 2016 Nature Publishing Group.

the substrate is pulled from the solution. The alignment of the CNTs, in this method, is achieved as a result of capillary forces. Although the method is slow, because it supports a wide variety of substrates and the whole process is automatic, it is an appropriate method for industrial applications [7,102-104].
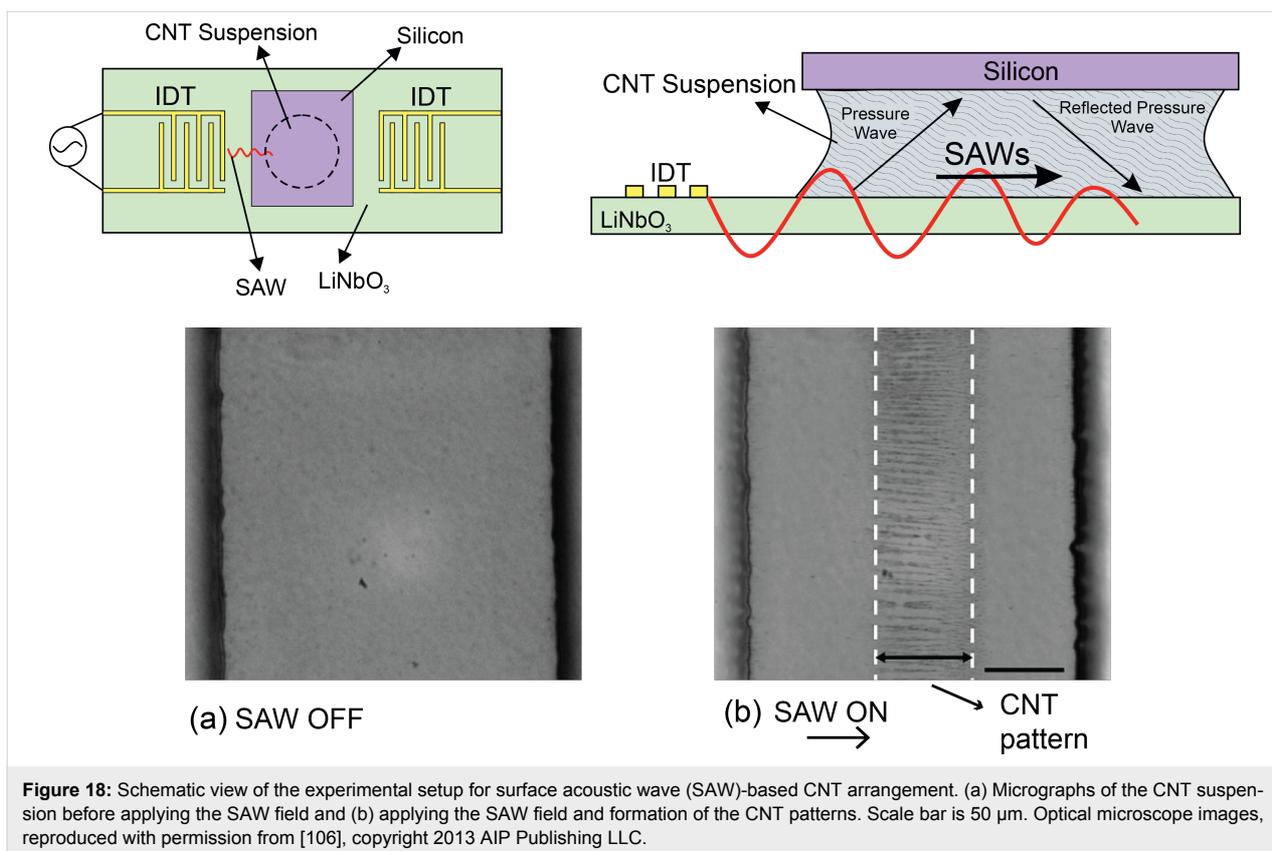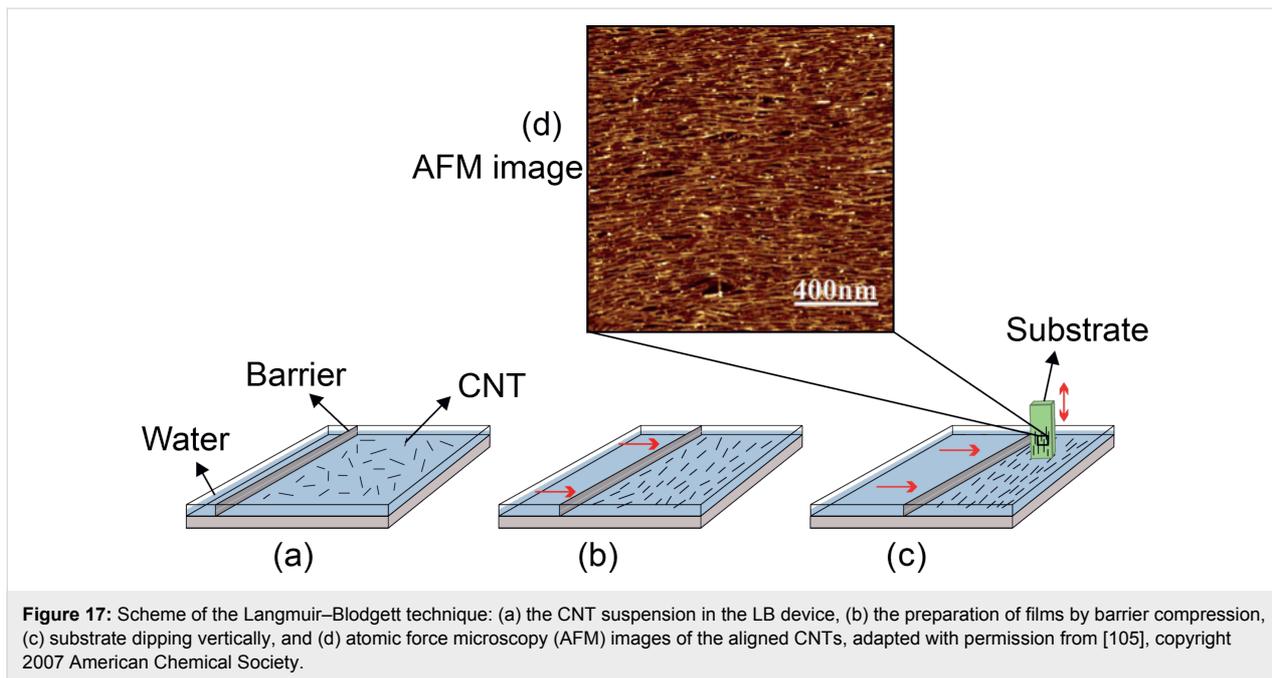
## Acoustic waves

In this method, surface acoustic waves (SAWs) are used to align and orient CNTs. SAWs are produced by applying a suit-able electric field to a piezoelectric material such as $LiNbO_3$. One set of metallic interdigital transducers (IDTs) intercalated on the piezoelectric surface introduces the electric field, generating a SAW displacement amplitude on the order of 10 Å. A solution of CNTs, produced by using a surfactant such as sodium dodecylbenzene sulfonate (SDBS), is dropped on a thin silicon layer that has gap-cell electrodes. An acoustic field is applied to the drops and aligns the CNTs (Figure 18). An electrical circuit is completed by creating a bridge of CNTs between the electrodes. This method is also used to produce electrical contacts with individual CNTs [28,106,107]; and recently, the ability of the technique has been investigated to purify metallic SWCNTs from the mixture species [106].

## Magnetic field

The alignment of CNTs using a magnetic field is a unique technique because of its remote action. One of the most common methods to apply a magnetic field is to cast the suspension of CNTs onto a substrate that is placed in the vicinity of a magnet. While the layer on the substrate is drying, CNTs are aligned in the direction of the magnetic field. In this case, unlike an electric field which moves the CNTs, the magnetic field only reorients them. This method is not limited to CNTs and can be used to align any carbon fiber. Figure 19 indicates the SEM image of the arranged CNTs in ethanol. In this study, the magnetic field magnitude was 10 T [108].

Although magnetic field alignment seems to be ideal, due to the weak magnetic properties of CNTs, it postulates a very strong magnetic field of ≥7 T. This is why samples are usually placed inside a very narrow tube of a magnetic superconductor. Assembling CNTs with magnetic nanoparticles (MNPs) or packing them with LC molecules may reduce the required magnetic field [108-110]. Aleman et al. have recently reported the ferromagnetism of residual catalysts in CVD growth of CNTs.

**Figure 17:** Scheme of the Langmuir–Blodgett technique: (a) the CNT suspension in the LB device, (b) the preparation of films by barrier compression, (c) substrate dipping vertically, and (d) atomic force microscopy (AFM) images of the aligned CNTs, adapted with permission from [105], copyright 2007 American Chemical Society.



**Figure 18:** Schematic view of the experimental setup for surface acoustic wave (SAW)-based CNT arrangement. (a) Micrographs of the CNT suspension before applying the SAW field and (b) applying the SAW field and formation of the CNT patterns. Scale bar is 50 μm. Optical microscope images, reproduced with permission from [106], copyright 2013 AIP Publishing LLC.

This work shows that adjustment of the size and shape of the catalyst nanoparticle can control the CNT ferromagnetism behavior. This phenomenon can be effective in developing the method [111].

The magnetic field strength and sample size are the limiting parameters of this method. Moreover, as previously mentioned, the CNTs are aligned in the direction of the axis of electrospun nanofiber polymers. In new research, well-aligned electrospun
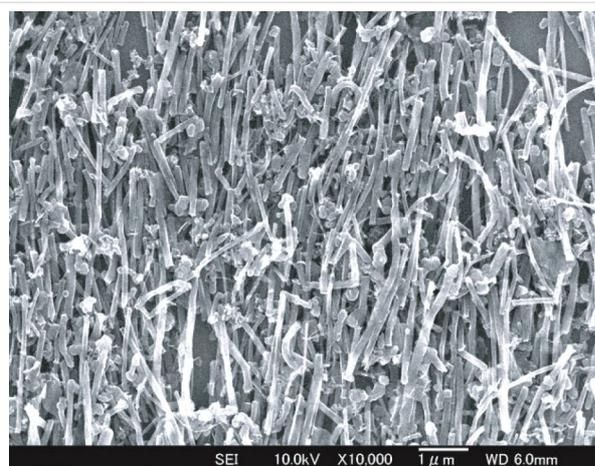
**Figure 19:** SEM image of CNTs arranged in ethanol by a magnetic field, reproduced with permission from [108], copyright 2009 Science and Technology of Advanced Materials.

nanofibers containing MWCNTs were successfully fabricated by a magnetic field [110].

## Electric field

The alignment and orientation of CNTs by an electric field is applied in two ways: as electrophoresis (EP) and dielectrophoresis (DEP). EP is the transport of charged particles through a medium enforced by a uniform electric field. This method has some limitations as the particles must be charged. DEP is also a phenomenon related to electrophoresis but with some important differences. It uses a nonuniform electric field to enforce uncharged particles to move. In this method, small droplets of a CNT suspension are placed on a substrate that has some interdigitated electrodes. After applying an AC electric field, the CNTs are aligned between the electrodes. This product is widely used in electrical CNT equipment. A DC electric field is not suitable because it causes the accumulation of CNTs near one of the electrodes. Another advantage of this method is the possibility of separating metallic CNTs (m-CNTs) and semiconducting CNTs (s-CNTs). Because of different the responses to an electric field, m-CNTs are attracted to the electrodes while s-CNTs are eliminated from the substrate by the flow of fluid.

Although this method is simple, its success depends on many factors including the CNT concentration in the solution, the electric field strength (103 V/cm) and its frequency (kHz–MHz) [112-115]. A system of aligning SWCNTs using an AC electric field is shown in Figure 20.

## Other techniques

Besides the above techniques summarized in Table 1, there are other less widespread methods such as the dip-pen nanolithog-
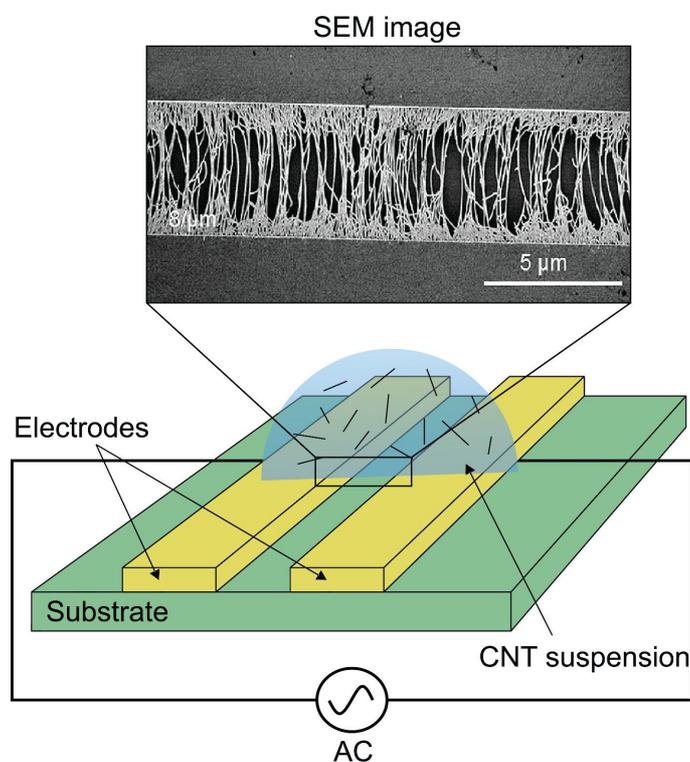


**Figure 20:** Schematic of a general dielectrophoresis (DEP) system to fabricate the oriented CNT patterns by an AC electric field. The SEM image of the aligned CNTs adapted with permission from [115], copyright 2011 American Chemical Society.

**Table 1:** A summary of the discussed techniques for the orientation and arrangement of carbon nanotubes.

| Technique | Effective force[a] | Phase application[b] | Advantage | Restriction | Ref. |
|---|---|---|---|---|---|
| stretching | M | S | high degree of alignment and high production rate | scale-up | [33,38] |
| fracture | M | S | simple setup | not easy to control | [6,27-29,31-34,38,39] |
| doctor blade (DB) | M | S | simple setup, ability to use various substrates | destructive | [41,42] |
| filtration | M | L | simple setup | slow, inefficient | [100] |
| electrospinning (ES) | E | S | simple setup, high degree of alignment, fast | unusable for all polymers, effectiveness depends on quality of CNT dispersion | [45-47] |
| layer-by-layer (LBL) | M/Ch | L/S | flexibility combined with other methods, widespread usage of materials in various shapes | compatibility of materials used as varied layers | [40,78-83, 93,94,103] |
| gas flow | M | L | simple setup | scale-up | [95] |
| Langmuir–Blodgett (LB) | M/Ch | L | flexibility combined with other methods, useful for fabrication of electromagnetic devices on a large scale | effectiveness depends on CNT suspension and minimization of intermolecular interactions | [7,102-104] |
| acoustic waves | M | S | ability to scale up for fabrication of large-area planar structures and composite material, fast | limitations on the type of materials (low viscosity thermosets) | [28,106,107] |
| magnetic field | MG | L/S | real-time manipulation and engineered patterning of CNTs, high degrees of orientation, use in electronic devices | small sample, requires high magnetic field, hindrance in industrial mass production | [108-110] |
| electrophoresis (EP)/ dielectrophoresis (DEP) | E | L/S | real-time manipulation and engineered patterning of CNTs, high degrees of orientation, use in electronic devices | small sample requires high voltage | [112-115] |
| liquid crystal (LC) | M/Ch/E/MG | L | requires small fields for orienting CNTs, use in electronic devices | unusable for various materials, depends on CNT quality | [96,97,120] |

[a]M = Mechanical, Ch = Chemical, E = Electrical, MG = Magnetic; [b]L = Liquid, S = Solid.

raphy technique [116], uniaxial pressure technique [117,118] and the use of femtosecond laser pulses [119], which are not presented here.

## Evaluating the arrangement and alignment of CNTs

After describing the techniques that can be implemented to align CNTs, understanding the methods for evaluating and characterizing them is necessary. These methods are, based on the nature of identification, classified into three main groups: microscopic analysis methods, phase analysis methods and surface analysis methods.

### Microscopic analysis methods

The aim of these methods is to create magnified images of the material. The resolution is determined according to the lowest achievable concentration of rays. For example, a resolution of about 1 μm and of about 1 Å is achievable by using optical and ion microscopes, respectively. In analyzing the alignment of CNTs, the most common microscopic methods are atomic force microscopy (AFM), transmission electron microscopy (TEM), scanning electron microscopy (SEM) and scanning transmission microscopy (STM).

**Electron microscope:** By changing the curvature and number of lenses (concave or convex) in the optical microscope we can enlarge the images; but images at a magnification of higher than 2000 lose resolution due to the long wavelength of light. The resolution is the shortest distance between two points that can be distinguished as separate points.

An electron microscope uses a beam of electrons instead of light. Because the electron wavelength is very short, images can be magnified up to a million times or more in some electron microscopes. However, using electron beams creates certain constraints. The first limitation is that images are in black and white because, unlike light, the electron beam does not carry color information. However, in modern in systems with image

analysis software, a pseudo-color image can be obtained by adding artificial colors to the grayscale image. The second limitation is that, unlike light, electrons cannot easily move in the air; therefore, a very strong vacuum is needed along the path of the electrons and also in the sample chamber. Vacuum is usually created by using a rotary pump and a diffusion pump. The complementary information is available in detail in reference books [121-124].

Three types of electron microscopes are used in analyzing the alignment and arrangement of CNTs. The first type is a scanning electron microscope (SEM), in which electrons are emitted and reflected from the surface of the sample, then they are collected by the detectors and converted to photons of visible light to create a visible image. These images offer useful qualitative information about the placement and alignment of CNTs, the diameter distribution and their relative purity [125].

The second type, TEM, is one of the most useful and important techniques used in research on CNTs. In this method, the size and shape of particles are determined by a resolution of a few tenths of a nanometer, which depends on the type of material and equipment that is used [124]. Nowadays, high-resolution TEM (HR-TEM) is used in analyzing properties of nanostructured materials.

The third type, AFM, is a technique that is used to study the structure and properties of materials at the nanometer scale. Flexibility, having multiple potential signals, and the capability of operating under various conditions have enabled researchers to examine a wide variety of surfaces under different environmental conditions. Furthermore, this technique can work in a vacuum, air, and liquid environments. Unlike other methods of analyzing surface properties, most of the time there is no fundamental limit to the type of surface and environment in this method. With this device, it is possible to analyze conductive or insulating, soft or hard, solid or powder, biological, and organic or inorganic surfaces. This device can measure geometric morphology, adhesion distribution, friction, surface impurities, texture, elasticity, magnetism, chemical bonding forces, distribution of electric charges and electric polarization in different parts of the surface. In practice, this feature is used to study corrosion, cleanness, uniformity, roughness, adhesion, friction, size, etc. AFM, like SEM and TEM, is a suitable technique to characterize the alignment of CNTs, especially horizontal alignment; for instance, when the CNTs grow horizontally on a substrate made of quartz [126].

## Phase analysis methods

In these methods, the crystal structure or the minerals in the material are identified. For example, the type and percentage of

oxides contained in a sample can be identified and measured. The most famous phase analysis method is X-ray diffraction (XRD) spectroscopy. XRD is used to determine most of the properties of a crystal structure such as lattice constants, lattice geometry, recognition of unknown materials, crystalline phases, size of the crystal, single crystal orientation, stress and lattice defects [127-129]. This method is based on the fact that X-rays are electromagnetic waves with a wavelength on the order of 5.0 to 2.5 Å.

2D detectors are very helpful to record XRD patterns. Cao et al. have shown that the degree of CNT alignment can be determined by the peak intensities in XRD patterns. Figure 21 shows four samples with different alignments and their XRD results. It indicates the intensity of the (002) peak is enhanced if the CNTs in the sample are less aligned [130].

Small-angle X-ray scattering (SAXS) is a method for evaluating the particle size distribution or nanohole size distribution in the sample. This sample can be amorphous, crystalline or a macromolecule (e.g., polymer molecule). SAXS provides information about electron density fluctuations that occur in the sample that is calculated by analyzing the intensity of scattered X-rays with a scattering angle of 0.1–5°. The local inhomogeneity in amorphous materials, colloidal particles, and agglomerated particles can be identified by this method.

Also, long-range order and the distance between the particles in a collection of polymer molecules can be determined by using SAXS and structural models. This method is non-destructive and can be used for analyzing samples that are not transparent to visible light.

SAXS can identify particles or holes between 1 to 100 nm. Accurate determination occurs for a particle size of 1 to 10 nm size; however, it can also be used for particles with sizes outside of this range. The average size of the particles or holes can be obtained by the shape. By using SAXS, the surface-to-volume ratio can also be determined. In the case of CNTs, SAXS provide both quality and quantity information on the nanoscale, such as average diameter and orientation, respectively. This is due to the mesoscopic size of the X-rays, which is typically on the order of a few hundred micrometers. This dimension is small relative to the typical millimeter scale of the whole aligned CNT sample and large in relation to individual CNTs on the nanoscale. Thus, a small region of the CNTs can be probed by SAXS beams to get some information about millions of CNTs. The mesoscopic size scale of scattering techniques has been used to reveal information about the alignment of CNTs in CNT fibers [131], the average diameter and orientation of CNTs grown on substrates [132,133], dispersion of
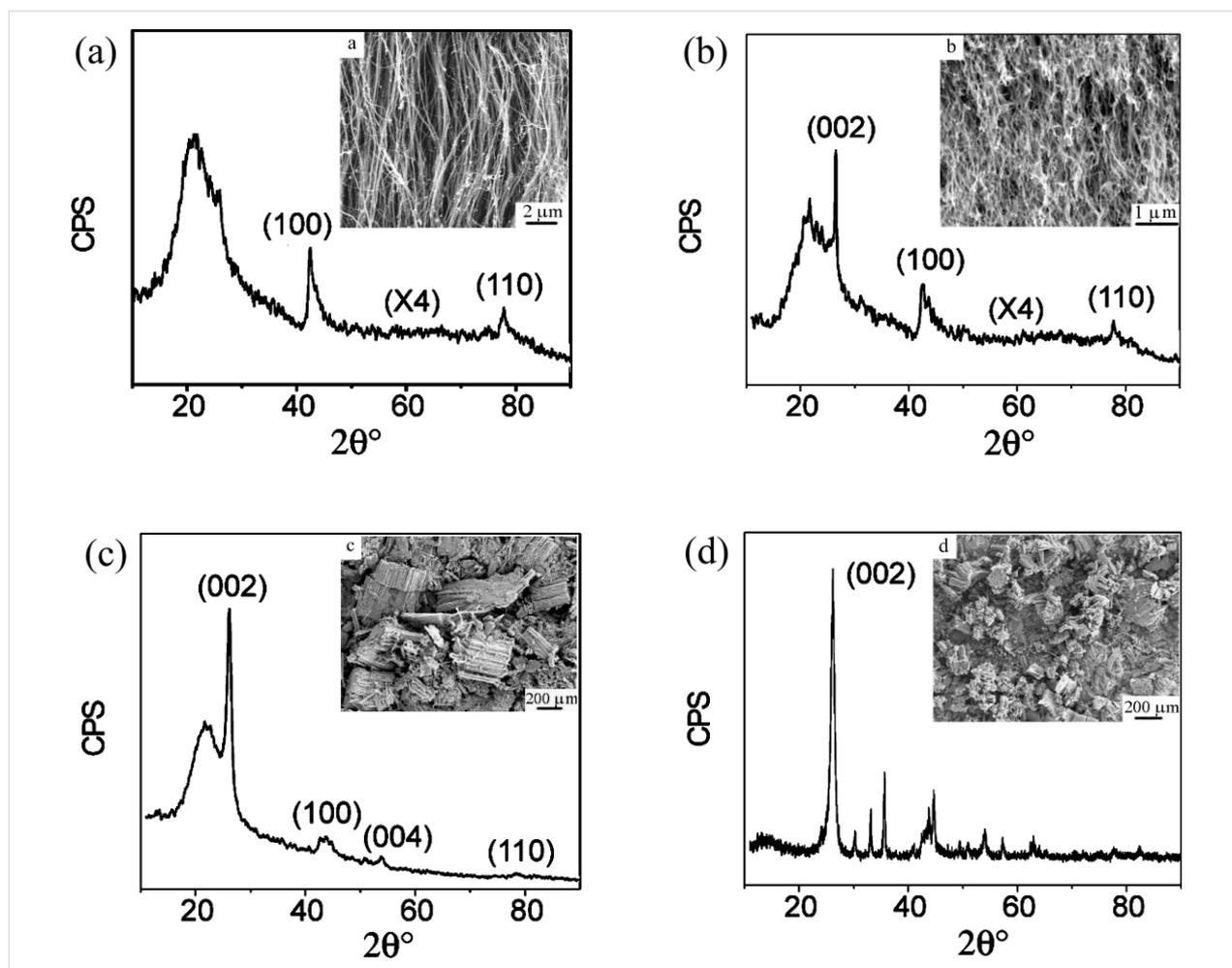
**Figure 21:** XRD results and SEM images of CNTs with various degrees of alignment: (a) as-grown straight CNT arrays with good alignment, (b) as-grown curled CNTs with less alignment, (c) disordered CNT arrays, (d) disordered CNT arrays. The substrate causes the broader peak at 20° and the intensities in (a) and (b) to be increased by times. Reproduced with permission from [130], copyright 2001 Elsevier.

CNTs in liquids [134], and the sorting of CNTs in CNT bundles [135].

## Surface analysis methods

The surface of a solid does not present the same chemical condition as compared to the bulk because of its connection with the surroundings. The surface plays an important role in many applications and processes, especially in alignment and arrangement of CNTs. Also, the chemical composition of the surface is different in the bulk due to the placement of functional groups on the CNT surface. Thus, generalizing the chemical analysis results of a bulk sample from the surface analysis would not be accurate. On the other hand, bonding at the CNT/polymer interface (covalent, van der Waals) also plays a decisive role to enhance the uniformity of the CNT dispersion into the polymer matrix [136]. Therefore, to obtain the desired properties of CNT/polymer composites, such as the thermal, mechanical and electrical properties [8,10,137], the characterization of surface properties including the CNT surface orientation and surface defects are also important [138-140]. The defects can have both positive (increasing the bonding at the interface and between carbon structures [25,137,139,141]) and negative (reduction of the quality of physical properties [10,141]) effects on the application and quality of composites.

For this aim, many techniques have been developed such as Raman spectroscopy, Fourier-transforms infrared spectroscopy (FTIR) and X-ray photoelectron spectroscopy (XPS).

**Raman spectroscopy:** Raman spectroscopy is a powerful tool to identify and quantify samples. This method gives significant information about molecular vibrations. The technique involves the excitation of a sample with a monochromatic light source (i.e., laser) and collecting the scattered light. The Raman spectra of CNTs can be identified with the radial breathing mode (RBM), tangential mode (G-band), disorder-induced mode
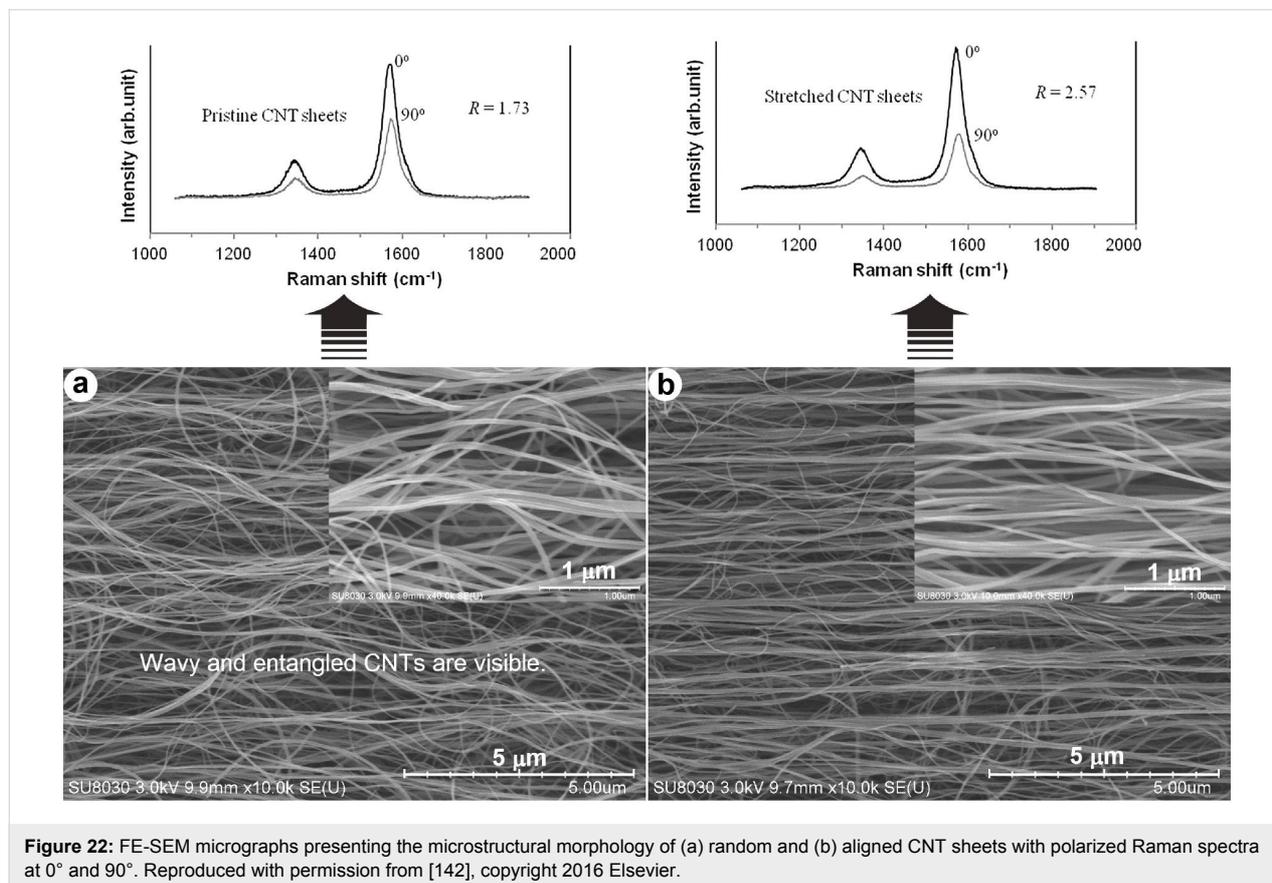
(D-band), and other Raman features, determining the physical properties of the material. The G-band intensity as a function of the angle of polarization for individual CNTs can be related to their arrangement so that the G-band intensity of well-aligned CNT bulk materials should be higher than that of less-aligned CNTs. Figure 22 shows field emission (FE)-SEM micrographs of two CNT samples with random and aligned orientation and their polarized Raman spectra at 0° and 90° (0° related to the polarization direction of the laser light where it is parallel to the CNT alignment direction, and 90° related to the laser light polarization direction where it is perpendicular to the CNT alignment direction). As indicated in the graph, the ratio of the G-mode to the D-mode (*R*) has increased [142].

The composites analyzed by Raman spectroscopy typically have very strong CNT signals that mask the signals of other organic components. In such cases, tunable UV Raman spectroscopy may be used, although this technique is rarely used.

**Fourier-transform infrared spectroscopy:** FTIR is often used to characterize molecular bonding on the CNT surface and to determine the modification of the CNT structure by adding compounds. It is very difficult to get a good FTIR spectrum of CNTs, thus attenuated total reflection (ATR) FTIR can be used

(except with carbon crystal, when germanium is more suitable). The investigation of the intermolecular interaction between the polymer chain and CNT by FTIR can confirm the results of observations [137,143-145]. For example, it has been reported that adhesion of the polymer to the CNT leads to constrained motion of the polymer chains and simplifies the charge transfer process, which consequently improves transport properties [146]. Also, many researchers indicate that the macroscopic optical properties of CNTs depend on the tube orientation with respect to the direction of beam propagation. Thus, FTIR results can be related to the morphology of the CNT mixture such as bundling, length and straightness [125].

**X-ray photoelectron spectroscopy:** The XPS technique does not explore the whole sample volume but rather provides information about the chemical composition of the CNT surface [144,145]. XPS suffers from surface charge artifacts, so correct sample preparation is crucial to achieve a flat and uncontaminated surface. Despite the mentioned limitations of this method and its ineffectiveness in assessing CNT orientation, invaluable surface information can be obtained about superficial functional groups, gases adsorption, structure modification process and defects on the CNT walls. This information is very critical to judge the final composite behavior [139,145,147].



**Figure 22:** FE-SEM micrographs presenting the microstructural morphology of (a) random and (b) aligned CNT sheets with polarized Raman spectra at 0° and 90°. Reproduced with permission from [142], copyright 2016 Elsevier.

## Conclusion

The arrangement and sorting of CNTs is an important factor in engineering and design of nanocomposite materials with desired structures. This article reviews the latest methods that have been proposed to arrange and align CNTs after growth in the structure of the composite materials, emphasizing the type of process. In all methods, CNTs are initially added to the composite and are then subjected to sorting processes using special techniques. The effectiveness of each technique on each of the properties is different, for example, the sorting method may improve the mechanical properties of the composite while its electrical and chemical properties change negligibly. Therefore, selecting an appropriate CNT orientation method in order to modify the material structure depends on the final field of composite application. In addition to the mentioned limitations for each of these methods, one of the big challenges is the need of pretreatment to homogenize the CNTs in terms of their physical characteristics such as diameter, length, number of walls and metallic or semiconducting properties. In fact, the selected pretreatment method can affect all of the CNTs for maximum controllability. In this regard, it seems that focusing on the principles and basic concepts of the CNT orientation mechanism in the composites is essential as well as CNT separation based on geometrical factors.

The effect of parameters such as optimal time to end the process, concentration, interactions of CNTs with polymeric and metallic materials, impact of internal and external CNT walls and the effect of physical properties, such as chirality, length and diameter on alignment needs to be understood. Furthermore, to achieve uniform composite structures, the separation of metallic and semiconducting CNTs is essential before alignment of CNTs. Considering the latest research carried out in this field, it has been indicated that using an electric field combined with mechanical methods would improve the separation of metallic and semiconducting CNTs. However, we are still a long way from achieving an easy, inexpensive, fast and highly applicable process for comprehensive use of CNTs in new composite industries.

## References

1. Bundy, F. P. *Science* **1962,** *137,* 1057–1058.
   doi:10.1126/science.137.3535.1057
2. Iijima, S. *Nature* **1991,** *354,* 56–58. doi:10.1038/354056a0
3. De Volder, M. F. L.; Tawfick, S. H.; Baughman, R. H.; Hart, A. J.
   *Science* **2013,** *339,* 535–539. doi:10.1126/science.1222453
4. Coleman, J. N.; Khan, U.; Blau, W. J.; Gun'ko, Y. K. *Carbon* **2006,** *44,*
   1624–1652. doi:10.1016/j.carbon.2006.02.038
5. Spitalsky, Z.; Tasis, D.; Papagelis, K.; Galiotis, C. *Prog. Polym. Sci.*
   **2010,** *35,* 357–401. doi:10.1016/j.progpolymsci.2009.09.003
6. Xie, X.-L.; Mai, Y.-W.; Zhou, X.-P. *Mater. Sci. Eng., R* **2005,** *49,*
   89–112. doi:10.1016/j.mser.2005.04.002
7. Cesano, F.; Scarano, D. Dispersion of Carbon-Based Materials
   (CNTs, Graphene). *Polymer Matrices, Carbon for Sensing Devices;*
   Springer: Berlin, Germany, 2015; pp 43–75.
8. Khan, F.; Kausar, A.; Siddiq, M. *Polym.-Plast. Technol. Eng.* **2015,** *54,*
   1524–1539. doi:10.1080/03602559.2015.1021486
9. Nam, T. H.; Goto, K.; Yamaguchi, Y.; Premalal, E. V. A.;
   Shimamura, Y.; Inoue, Y.; Naito, K.; Ogihara, S. *Composites, Part A*
   **2015,** *76,* 289–298. doi:10.1016/j.compositesa.2015.06.009
10. Gulotty, R.; Castellino, M.; Jagdale, P.; Tagliaferro, A.; Balandin, A. A.
    *ACS Nano* **2013,** *7,* 5114–5121. doi:10.1021/nn400726g
11. Costa, P. M.; Bourgognon, M.; Wang, J. T.-W.; Al-Jamal, K. T.
    *J. Controlled Release* **2016,** *241,* 200–219.
    doi:10.1016/j.jconrel.2016.09.033
12. Marchesan, S.; Melchionna, M.; Prato, M.
    *Fullerenes, Nanotubes, Carbon Nanostruct.* **2014,** *22,* 190–195.
13. Mecklenburg, M.; Mizushima, D.; Ohtake, N.; Bauhofer, W.;
    Fiedler, B.; Schulte, K. *Carbon* **2015,** *91,* 275–290.
    doi:10.1016/j.carbon.2015.04.085
14. Lee, J.; Stein, I. Y.; Devoe, M. E.; Lewis, D. J.; Lachman, N.;
    Kessler, S. S.; Buschhorn, S. T.; Wardle, B. L. *Appl. Phys. Lett.* **2015,**
    *106,* 053110. doi:10.1063/1.4907608
15. Liu, X.; Dai, L. *Nat. Rev. Mater.* **2016,** *1,* 16064.
    doi:10.1038/natrevmats.2016.64
16. Melchionna, M.; Prato, M.; Fornasiero, P. *Catal. Today* **2016,** *277,*
    202–213. doi:10.1016/j.cattod.2016.04.024
17. Eder, D. *Chem. Rev.* **2010,** *110,* 1348–1385. doi:10.1021/cr800433k
18. Melchionna, M.; Fornasiero, P. *ChemCatChem* **2017,** *9,* 3274–3284.
    doi:10.1002/cctc.201700489
19. Shearer, C. J.; Cherevan, A.; Eder, D. *Adv. Mater.* **2014,** *26,*
    2295–2318. doi:10.1002/adma.201305254
20. Marchesan, S.; Bosi, S.; Alshatwi, A.; Prato, M. *Nano Today* **2016,** *11,*
    398–401. doi:10.1016/j.nantod.2015.11.007
21. Wu, Y.; Wang, L.; Guo, B.; Ma, P. X. *ACS Nano* **2017,** *11,*
    5646–5659. doi:10.1021/acsnano.7b01062
22. Patel, A.; Mukundan, S.; Wang, W.; Karumuri, A.; Sant, V.;
    Mukhopadhyay, S. M.; Sant, S. *Acta Biomater.* **2016,** *32,* 77–88.
    doi:10.1016/j.actbio.2016.01.004
23. Marchesan, S.; Ballerini, L.; Prato, M. *Science* **2017,** *356,* 1010–1011.
    doi:10.1126/science.aan1227
24. Marchesan, S.; Melchionna, M.; Prato, M. *ACS Nano* **2015,** *9,*
    9441–9450. doi:10.1021/acsnano.5b04956
25. Khare, K. S.; Khabaz, F.; Khare, R. *ACS Appl. Mater. Interfaces* **2014,**
    *6,* 6098–6110. doi:10.1021/am405317x
26. Melchionna, M.; Prato, M. *ECS J. Solid State Sci. Technol.* **2013,** *2,*
    M3040–M3045. doi:10.1149/2.008310jss
27. Sun, X.; Chen, T.; Yang, Z.; Peng, H. *Acc. Chem. Res.* **2013,** *46,*
    539–549. doi:10.1021/ar300221r
28. Haslam, M. D.; Raeymaekers, B. *Composites, Part B* **2014,** *60,*
    91–97. doi:10.1016/j.compositesb.2013.12.027
29. Chen, W.; Tao, X. *Appl. Surf. Sci.* **2006,** *252,* 3547–3552.
    doi:10.1016/j.apsusc.2005.05.028
30. Ürk, D.; Demir, E.; Bulut, O.; Çakıroğlu, D.; Cebeci, F. Ç.;
    Öveçoğlu, M. L.; Cebeci, H. *Compos. Struct.* **2016,** *155,* 255–262.
    doi:10.1016/j.compstruct.2016.05.087
31. Ren, Z.; Lan, Y.; Wang, Y. *Aligned carbon nanotubes: physics,
    concepts, fabrication and devices;* Springer Science & Business
    Media: Berlin, Germany, 2012.
32. Ma, Y.; Wang, B.; Wu, Y.; Huang, Y.; Chen, Y. *Carbon* **2011,** *49,*
    4098–4110. doi:10.1016/j.carbon.2011.06.068

33. Iakoubovskii, K. *Cent. Eur. J. Phys.* **2009,** *7,* 645–653. doi:10.2478/s11534-009-0072-2

34. Cooper, C. A.; Ravich, D.; Lips, D.; Mayer, J.; Wagner, H. D. *Compos. Sci. Technol.* **2002,** *62,* 1105–1112. doi:10.1016/S0266-3538(02)00056-8

35. Gangele, A.; Sharma, C. S.; Pandey, A. K. *J. Nanosci. Nanotechnol.* **2017,** *17,* 2256–2273. doi:10.1166/jnn.2017.13818

36. Yao, S.-H.; Yuan, J.-K.; Zhou, T.; Dang, Z.-M.; Bai, J. *J. Phys. Chem. C* **2011,** *115,* 20011–20017. doi:10.1021/jp205444x

37. Poa, C. H.; Silva, S. R. P.; Watts, P. C. P.; Hsu, W. K.; Kroto, H. W.; Walton, D. R. M. *Appl. Phys. Lett.* **2002,** *80,* 3189–3191. doi:10.1063/1.1474608

38. Jin, L.; Bower, C.; Zhou, O. *Appl. Phys. Lett.* **1998,** *73,* 1197–1199. doi:10.1063/1.122125

39. Watts, P. C. P.; Lyth, S. M.; Mendoza, E.; Silva, S. R. P. *Appl. Phys. Lett.* **2006,** *89,* 103113. doi:10.1063/1.2345615

40. Zhao, H.; Zhou, Z.; Dong, H.; Zhang, L.; Chen, H.; Hou, L. *Sci. Rep.* **2013,** *3,* 3480. doi:10.1038/srep03480

41. Lanticse, L. J.; Tanabe, Y.; Matsui, K.; Kaburagi, Y.; Suda, K.; Hoteida, M.; Endo, M.; Yasuda, E. *Carbon* **2006,** *44,* 3078–3086. doi:10.1016/j.carbon.2006.05.008

42. Dan, B.; Irvin, G. C.; Pasquali, M. *ACS Nano* **2009,** *3,* 835–843. doi:10.1021/nn8008307

43. Liu, Y.; Kumar, S. *ACS Appl. Mater. Interfaces* **2014,** *6,* 6069–6087. doi:10.1021/am405136s

44. Yue, H.; Reguero, V.; Senokos, E.; Monreal-Bernal, A.; Mas, B.; Fernández-Blázquez, J. P.; Marcilla, R.; Vilatela, J. J. *Carbon* **2017,** *122,* 47–53. doi:10.1016/j.carbon.2017.06.032

45. Yao, J.; Bastiaansen, C. W. M.; Peijs, T. *Fibers* **2014,** *2,* 158–186. doi:10.3390/fib2020158

46. Kuzmenko, V.; Kalogeropoulos, T.; Thunberg, J.; Johannesson, S.; Hägg, D.; Enoksson, P.; Gatenholm, P. *Mat. Sci. Eng. C* **2016,** *58,* 14–23. doi:10.1016/j.msec.2015.08.012

47. Dai, Y.; Yao, J.; Song, Y.; Wang, S.; Yuan, Y. *Environ. Sci.: Nano* **2016,** *3,* 857–868. doi:10.1039/C6EN00148C

48. Dror, Y.; Salalha, W.; Khalfin, R. L.; Cohen, Y.; Yarin, A. L.; Zussman, E. *Langmuir* **2003,** *19,* 7012–7020. doi:10.1021/la034234i

49. Teo, W. E.; Ramakrishna, S. *Nanotechnology* **2006,** *17,* R89. doi:10.1088/0957-4484/17/14/R01

50. De Prá, M. A. A.; Ribeiro-do-Valle, R. M.; Maraschin, M.; Veleirinho, B. *Mater. Lett.* **2017,** *193,* 154–157. doi:10.1016/j.matlet.2017.01.102

51. Park, J.-M.; Gu, G.-Y.; Wang, Z.-J.; Kwon, D.-J.; Shin, P.-S.; Choi, J.-Y.; DeVries, K. L. *Adv. Compos. Mater.* **2016,** *25,* 305–316. doi:10.1080/09243046.2015.1082714

52. Sahay, R.; Thavasi, V.; Ramakrishna, S. *J. Nanomater.* **2011,** *2011,* No. 317673. doi:10.1155/2011/317673

53. Sperling, L. E.; Reis, K. P.; Pozzobon, L. G.; Girardi, C. S.; Pranke, P. *J. Biomed. Mater. Res., Part A* **2017,** *105,* 1333–1345. doi:10.1002/jbm.a.36012

54. Liu, Y.; Lu, J.; Xu, G.; Wei, J.; Zhang, Z.; Li, X. *Mat. Sci. Eng. C* **2016,** *69,* 865–874. doi:10.1016/j.msec.2016.07.069

55. Chew, S. Y.; Wen, J.; Yim, E. K. F.; Leong, K. W. *Biomacromolecules* **2005,** *6,* 2017–2024. doi:10.1021/bm0501149

56. Li, D.; Wang, Y.; Xia, Y. *Nano Lett.* **2003,** *3,* 1167–1171. doi:10.1021/nl0344256

57. Katta, P.; Alessandro, M.; Ramsier, R. D.; Chase, G. G. *Nano Lett.* **2004,** *4,* 2215–2218. doi:10.1021/nl0486158

58. Li, M.; He, Y.; Xin, C.; Wei, X.; Li, Q.; Lu, C.; Juang, Y.-J. *Appl. Phys. Lett.* **2008,** *92,* 213114. doi:10.1063/1.2937400

59. Xu, H.; Li, H.; Ke, Q.; Chang, J. *ACS Appl. Mater. Interfaces* **2015,** *7,* 8706–8718. doi:10.1021/acsami.5b00996

60. Xie, J.; MacEwan, M. R.; Ray, W. Z.; Liu, W.; Siewe, D. Y.; Xia, Y. *ACS Nano* **2010,** *4,* 5027–5036. doi:10.1021/nn101554u

61. Inai, R.; Kotaki, M.; Ramakrishna, S. *Nanotechnology* **2005,** *16,* 208. doi:10.1088/0957-4484/16/2/005

62. Chen, D.; Liu, T.; Zhou, X.; Tjiu, W. C.; Hou, H. *J. Phys. Chem. B* **2009,** *113,* 9741–9748. doi:10.1021/jp9025128

63. Carnell, L. S.; Siochi, E. J.; Holloway, N. M.; Stephens, R. M.; Rhim, C.; Niklason, L. E.; Clark, R. L. *Macromolecules* **2008,** *41,* 5345–5349. doi:10.1021/ma8000143

64. Sundaray, B.; Subramanian, V.; Natarajan, T. S.; Xiang, R.-Z.; Chang, C.-C.; Fann, W.-S. *Appl. Phys. Lett.* **2004,** *84,* 1222–1224. doi:10.1063/1.1647685

65. Shin, M. K.; Kim, S. I.; Kim, S. J. *Appl. Phys. Lett.* **2006,** *88,* 223109. doi:10.1063/1.2208689

66. Zhang, L.; Aboagye, A.; Kelkar, A.; Lai, C.; Fong, H. *J. Mater. Sci.* **2014,** *49,* 463–480. doi:10.1007/s10853-013-7705-y

67. Panthi, G.; Park, M.; Kim, H.-Y.; Park, S.-J. *J. Ind. Eng. Chem.* **2015,** *24,* 1–13. doi:10.1016/j.jiec.2014.09.011

68. Mercante, L. A.; Pavinatto, A.; Iwaki, L. E. O.; Scagion, V. P.; Zucolotto, V.; Oliveira, O. N., Jr.; Mattoso, L. H. C.; Correa, D. S. *ACS Appl. Mater. Interfaces* **2015,** *7,* 4784–4790. doi:10.1021/am508709c

69. Huang, Z.-M.; Zhang, Y.-Z.; Kotaki, M.; Ramakrishna, S. *Compos. Sci. Technol.* **2003,** *63,* 2223–2253. doi:10.1016/S0266-3538(03)00178-7

70. Vigolo, B.; Pénicaud, A.; Coulon, C.; Sauder, C.; Pailler, R.; Journet, C.; Bernier, P.; Poulin, P. *Science* **2000,** *290,* 1331–1334. doi:10.1126/science.290.5495.1331

71. Alemán, B.; Reguero, V.; Mas, B.; Vilatela, J. J. *ACS Nano* **2015,** *9,* 7392–7398. doi:10.1021/acsnano.5b02408

72. Reguero, V.; Alemán, B. N.; Mas, B.; Vilatela, J. J. *Chem. Mater.* **2014,** *26,* 3550–3557. doi:10.1021/cm501187x

73. Wang, X.; Bradford, P. D.; Liu, W.; Zhao, H.; Inoue, Y.; Maria, J.-P.; Li, Q.; Yuan, F.-G.; Zhu, Y. *Compos. Sci. Technol.* **2011,** *71,* 1677–1683. doi:10.1016/j.compscitech.2011.07.023

74. Liu, W.; Zhao, H.; Inoue, Y.; Wang, X.; Bradford, P. D.; Kim, H.; Qiu, Y.; Zhu, Y. *Composites, Part A* **2012,** *43,* 587–592. doi:10.1016/j.compositesa.2011.12.029

75. Liu, W.; Zhang, X.; Xu, G.; Bradford, P. D.; Wang, X.; Zhao, H.; Zhang, Y.; Jia, Q.; Yuan, F.-G.; Li, Q. *Carbon* **2011,** *49,* 4786–4791. doi:10.1016/j.carbon.2011.06.089

76. Jiang, Q.; Wang, X.; Zhu, Y.; Hui, D.; Qiu, Y. *Composites, Part B* **2014,** *56,* 408–412. doi:10.1016/j.compositesb.2013.08.064

77. Zhang, Y.; Arugula, M. A.; Kirsch, J. S.; Yang, X.; Olsen, E.; Simonian, A. L. *Langmuir* **2015,** *31,* 1462–1468. doi:10.1021/la503474w

78. Zhang, L.; Xu, W.; Luo, X. G.; Wang, J. N. *Carbon* **2015,** *90,* 215–221. doi:10.1016/j.carbon.2015.04.026

79. Yu, B.; Liu, X.; Cong, H.; Wang, Z.; Lian, Y.; Tang, J. *Fullerenes, Nanotubes, Carbon Nanostruct.* **2015,** *23,* 320–325. doi:10.1080/1536383X.2013.826197

80. Wang, B.; Liu, L.; Huang, L.; Chi, L.; Liang, G.; Yuan, L.; Gu, A. *Carbon* **2015,** *85,* 28–37. doi:10.1016/j.carbon.2014.12.062

81. Liu, Y.; Liu, Y.; Feng, H.; Wu, Y.; Joshi, L.; Zeng, X.; Li, J. *Biosens. Bioelectron.* **2012,** *35,* 63–68. doi:10.1016/j.bios.2012.02.007

82. Liu, L.; Son, M.; Chakraborty, S.; Bhattacharjee, C.; Choi, H. *Desalin. Water Treat.* **2013,** *51,* 6194–6200. doi:10.1080/19443994.2013.780767

83. Hyder, M. N.; Lee, S. W.; Cebeci, F. Ç.; Schmidt, D. J.; Shao-Horn, Y.; Hammond, P. T. *ACS Nano* **2011,** *5,* 8552–8561. doi:10.1021/nn2029617

84. Staudinger, U.; Thoma, P.; Lüttich, F.; Janke, A.; Kobsch, O.; Gordan, O. D.; Pötschke, P.; Voit, B.; Zahn, D. R. T. *Compos. Sci. Technol.* **2017,** *138,* 134–143. doi:10.1016/j.compscitech.2016.11.015

85. Nag, S.; Sachan, A.; Castro, M.; Choudhary, V.; Feller, J. F. *Sens. Actuators, B* **2016,** *222,* 362–373. doi:10.1016/j.snb.2015.08.038

86. Loghin, F.; Colasanti, S.; Weise, A.; Falco, A.; Abdelhalim, A.; Lugli, P.; Abdellah, A. *Flexible Printed Electron.* **2016,** *1,* 045002. doi:10.1088/2058-8585/1/4/045002

87. Samimi, A.; Ghadiri, M. *Iran. J. Chem. Chem. Eng.* **2008,** *2008,* 27.

88. Moghadam, H.; Samimi, M.; Samimi, A.; Khorram, M. *Iran. J. Chem. Eng.* **2009,** *6,* 88–98.

89. Li, Q.; Kartikowati, C. W.; Ogi, T.; Iwaki, T.; Okuyama, K. *Carbon* **2017,** *115,* 116–119. doi:10.1016/j.carbon.2016.12.095

90. Khorram, M.; Samimi, M.; Samimi, A.; Moghadam, H. *J. Appl. Polym. Sci.* **2015,** *132.* doi:10.1002/app.41334

91. Moghadam, H.; Samimil, A. *Iran. J. Chem. Eng.* **2012,** *10,* 14–23.

92. Moghadam, H.; Samimi, M.; Samimi, A.; Khorram, M. *J. Appl. Polym. Sci.* **2010,** *118,* 1288–1296. doi:10.1002/app.32302

93. Yildiz, O.; Bradford, P. D. *Carbon* **2013,** *64,* 295–304. doi:10.1016/j.carbon.2013.07.066

94. Wang, X.; Yong, Z. Z.; Li, Q. W.; Bradford, P. D.; Liu, W.; Tucker, D. S.; Cai, W.; Wang, H.; Yuan, F. G.; Zhu, Y. T. *Mater. Res. Lett.* **2013,** *1,* 19–25. doi:10.1080/21663831.2012.686586

95. Hedberg, J.; Dong, L.; Jiao, J. *Appl. Phys. Lett.* **2005,** *86,* 143111. doi:10.1063/1.1897435

96. Lisetski, L.; Soskin, M.; Lebovka, N. Carbon nanotubes in liquid crystals: fundamental properties and applications. *Physics of liquid matter: modern problems;* Springer: Berlin, Germany, 2015; pp 243–297. doi:10.1007/978-3-319-20875-6_10

97. Lagerwall, J. P. F.; Scalia, G.; Haluska, M.; Dettlaff-Weglikowska, U.; Giesselmann, F.; Roth, S. *Phys. Status Solidi B* **2006,** *243,* 3046–3049. doi:10.1002/pssb.200669146

98. Ko, H.; Tsukruk, V. V. *Nano Lett.* **2006,** *6,* 1443–1448. doi:10.1021/nl060608r

99. He, X.; Gao, W.; Xie, L.; Li, B.; Zhang, Q.; Lei, S.; Robinson, J. M.; Hároz, E. H.; Doorn, S. K.; Wang, W.; Vajtai, R.; Ajayan, P. M.; Adams, W. W.; Hauge, R. H.; Kono, J. *Nat. Nanotechnol.* **2016,** *11,* 633–638. doi:10.1038/nnano.2016.44

100. deHeer, W. A.; Bacsa, W. S.; Châtelain, A.; Gerfin, T.; Humphrey-Baker, R.; Forro, L.; Ugarte, D. *Science* **1995,** *268,* 845–847. doi:10.1126/science.268.5212.845

101. King, B.; Panchapakesan, B. *Nanotechnology* **2014,** *25,* 175201. doi:10.1088/0957-4484/25/17/175201

102. Kędzierski, K.; Barszcz, B.; Biadasz, A.; Matczak, M.; Wróbel, D. *Prog. Org. Coat.* **2015,** *86,* 86–95. doi:10.1016/j.porgcoat.2015.04.017

103. Giancane, G.; Bettini, S.; Valli, L. *Colloids Surf., A* **2010,** *354,* 81–90. doi:10.1016/j.colsurfa.2009.09.047

104. Fu, Y.-R.; Zhang, S.; Chen, M.; Qian, D.-J. *Thin Solid Films* **2012,** *520,* 6994–7001. doi:10.1016/j.tsf.2012.07.103

105. Li, X.; Zhang, L.; Wang, X.; Shimoyama, I.; Sun, X.; Seo, W.-S.; Dai, H. *J. Am. Chem. Soc.* **2007,** *129,* 4890–4891. doi:10.1021/ja071114e

106. Zeng, Q.; Li, L.; Ma, H. L.; Xu, J.; Fan, Y.; Wang, H. *Appl. Phys. Lett.* **2013,** *102,* 213106. doi:10.1063/1.4807677

107. Ding, X.; Li, P.; Lin, S.-C. S.; Stratton, Z. S.; Nama, N.; Guo, F.; Slotcavage, D.; Mao, X.; Shi, J.; Costanzo, F.; Huang, T. J. *Lab Chip* **2013,** *13,* 3626–3649. doi:10.1039/c3lc50361e

108. Tsuda, K.; Sakka, Y. *Sci. Technol. Adv. Mater.* **2009,** *10,* 014603. doi:10.1088/1468-6996/10/1/014603

109. Steinert, B. W.; Dean, D. R. *Polymer* **2009,** *50,* 898–904. doi:10.1016/j.polymer.2008.11.053

110. Mei, L.-Y.; Song, P.; Liu, Y.-Q. *J. Appl. Polym. Sci.* **2015,** *132,* 1–9. doi:10.1002/app.41995

111. Alemán, B.; Ranchal, R.; Reguero, V.; Mas, B.; Vilatela, J. J. *J. Mater. Chem. C* **2017,** *5,* 5544–5550. doi:10.1039/C7TC01199G

112. Ubrig, N.; Shaver, J.; Parra-Vasquez, A. N. G.; Pasquali, M.; Kono, J.; Fagan, J. A.; Portugall, O. *J. Low Temp. Phys.* **2010,** *159,* 262–266. doi:10.1007/s10909-009-0112-8

113. Sengezer, E. C.; Seidel, G. D.; Bodnar, R. J. *Polym. Compos.* **2015,** *36,* 1266–1279. doi:10.1002/pc.23031

114. LeMieux, M. C.; Roberts, M.; Barman, S.; Jin, Y. W.; Kim, J. M.; Bao, Z. *Science* **2008,** *321,* 101–104. doi:10.1126/science.1156588

115. Shekhar, S.; Stokes, P.; Khondaker, S. I. *ACS Nano* **2011,** *5,* 1739–1746. doi:10.1021/nn102305z

116. Lee, J.-H.; Najeeb, C. K.; Nam, G.-H.; Shin, Y.; Lim, J.-H.; Kim, J.-H. *Chem. Mater.* **2016,** *28,* 6471–6476. doi:10.1021/acs.chemmater.6b01075

117. Lance, M. J.; Hsueh, C.-H.; Ivanov, I. N.; Geohegan, D. B. *J. Mater. Res.* **2005,** *20,* 1026–1032. doi:10.1557/JMR.2005.0139

118. Bendiab, N.; Almairac, R.; Sauvajol, J.-L.; Rols, S.; Elkaim, E. *J. Appl. Phys.* **2003,** *93,* 1769–1773. doi:10.1063/1.1534905

119. Choi, S. B.; Byeon, C. C.; Park, D. J.; Jeong, M. S. *J. Korean Phys. Soc.* **2016,** *68,* 210–214. doi:10.3938/jkps.68.210

120. Zakri, C.; Poulin, P. Nematic phase formation in suspensions of carbon nanotubes. *Liquid Crystals with Nano and Microparticles;* World Scientific Publishing Co. Pte. Ltd.: Singapore, 2017; pp 775–796.

121. Watt, I. M. *The principles and practice of electron microscopy;* Cambridge University Press: Cambridge, United Kingdom, 1997.

122. Lawes, G. *Scanning electron microscopy and X-ray microanalysis;* John Wiley & Sons, Inc.: New York, NY, U.S.A., 1987.

123. Goldstein, J.; Newbury, D. E.; Echlin, P.; Joy, D. C.; Romig, A. D.; Lyman, C. E.; Fiori, C.; Lifshin, E. *Scanning electron microscopy and X-ray microanalysis: a text for biologists, materials scientists, and geologists;* Springer Science & Business Media: Berlin, Germany, 2012.

124. Egerton, R. *Physical principles of electron microscopy: an introduction to TEM, SEM, and AEM;* Springer Science & Business Media: Berlin, Germany, 2006.

125. Lehman, J. H.; Terrones, M.; Mansfield, E.; Hurst, K. E.; Meunier, V. *Carbon* **2011,** *49,* 2581–2602. doi:10.1016/j.carbon.2011.03.028

126. Ali, A. A.; Joshua, W. K.; Rachel, M. B.; Tristan, D.; Ethan, D. M. *Nanotechnology* **2011,** *22,* 275717. doi:10.1088/0957-4484/22/27/275717

127. Young, R. *The Rietveld Method;* Oxford University Press: Oxford, United Kingdom, 1995.

128. Pecharsky, V. K.; Zavalij, P. Y. *Fundamentals of powder diffraction and structural characterization of materials;* Springer: Berlin, Germany, 2009; Vol. 69.

129. Cullity, B.; stock, S. *Elements of X-ray diffraction,* 3rd ed.; Prentice-Hall: Upper Saddle River, NJ, U.S.A., 2001.

130. Cao, A.; Xu, C.; Liang, J.; Wu, D.; Wei, B. *Chem. Phys. Lett.* **2001,** *344,* 13–17. doi:10.1016/S0009-2614(01)00671-6

131. Launois, P.; Marucci, A.; Vigolo, B.; Bernier, P.; Derré, A.; Poulin, P.
*J. Nanosci. Nanotechnol.* **2001**, *1,* 125–128. doi:10.1166/jnn.2001.025

132. Wang, B. N.; Bennett, R. D.; Verploegen, E.; Hart, A. J.; Cohen, R. E.
*J. Phys. Chem. C* **2007**, *111,* 5859–5865. doi:10.1021/jp068895a

133. Ch Das, N.; Yang, K.; Liu, Y.; Sokol, P. E.; Wang, Z.; Wang, H.
*J. Nanosci. Nanotechnol.* **2011**, *11,* 4995–5000.
doi:10.1166/jnn.2011.4110

134. Schaefer, D. W.; Zhao, J.; Brown, J. M.; Anderson, D. P.;
Tomlin, D. W. *Chem. Phys. Lett.* **2003**, *375,* 369–375.
doi:10.1016/S0009-2614(03)00867-4

135. Hough, L. A.; Islam, M. F.; Hammouda, B.; Yodh, A. G.; Heiney, P. A.
*Nano Lett.* **2006**, *6,* 313–317. doi:10.1021/nl051871f

136. Chen, B.; Li, S.; Imai, H.; Jia, L.; Umeda, J.; Takahashi, M.;
Kondoh, K. *Mater. Des.* **2015**, *72,* 1–8.
doi:10.1016/j.matdes.2015.02.003

137. Prusty, R. K.; Rathore, D. K.; Ray, B. C. *Adv. Colloid Interface Sci.*
**2017**, *240,* 77–106. doi:10.1016/j.cis.2016.12.008

138. Fatemi, S. M.; Foroutan, M. *J. Iran. Chem. Soc.* **2017**, *14,* 269–283.
doi:10.1007/s13738-016-0976-x

139. Huang, S.; Fan, W.; Guo, X.; Meng, F.; Liu, X.
*ACS Appl. Mater. Interfaces* **2014**, *6,* 21567–21575.
doi:10.1021/am506564n

140. Yang, Y.; Ramirez, C.; Wang, X.; Guo, Z.; Tokranov, A.; Zhao, R.;
Szlufarska, I.; Lou, J.; Sheldon, B. W. *Carbon* **2017**, *115,* 402–408.
doi:10.1016/j.carbon.2017.01.029

141. Ohnishi, M.; Shiga, T.; Shiomi, J. *Phys. Rev. B* **2017**, *95,* 155405.
doi:10.1103/PhysRevB.95.155405

142. Nam, T. H.; Goto, K.; Yamaguchi, Y.; Premalal, E. V. A.;
Shimamura, Y.; Inoue, Y.; Arikawa, S.; Yoneyama, S.; Ogihara, S.
*Composites, Part B* **2016**, *85,* 15–23.
doi:10.1016/j.compositesb.2015.09.012

143. Song, Y.; Sun, Z.; Xu, L.; Shao, Z. *Polymers (Basel, Switz.)* **2017**, *9,*
1. doi:10.3390/polym9010001

144. Belin, T.; Epron, F. *J. Mater. Sci. Eng. B* **2005**, *119,* 105–118.
doi:10.1016/j.mseb.2005.02.046

145. Varga, M.; Izak, T.; Vretenar, V.; Kozak, H.; Holovsky, J.;
Artemenko, A.; Hulman, M.; Skakalova, V.; Lee, D. S.; Kromka, A.
*Carbon* **2017**, *111,* 54–61. doi:10.1016/j.carbon.2016.09.064

146. Feng, W.; Bai, X.; Lian, Y.; Liang, J.; Wang, X.; Yoshino, K. *Carbon*
**2003**, *41,* 1551–1557. doi:10.1016/S0008-6223(03)00078-2

147. Xiong, L.; Shuai, J.; Hou, Z.; Zhu, L.; Li, W. *J. Colloid Interface Sci.*
**2017**, *498,* 405–412. doi:10.1016/j.jcis.2017.03.082

# Graphene composites with dental and biomedical applicability

Sharali Malik[*1], Felicite M. Ruddock[2], Adam H. Dowling[3], Kevin Byrne[4],
Wolfgang Schmitt[4], Ivan Khalakhan[5], Yoshihiro Nemoto[6], Hongxuan Guo[6],
Lok Kumar Shrestha[6], Katsuhiko Ariga[6,7] and Jonathan P. Hill[6]

## Full Research Paper

Address:
[1]Institute of Nanotechnology, Karlsruhe Institute of Technology (KIT), D-76131 Karlsruhe, Germany, [2]Department of Civil Engineering, Liverpool John Moores University, Byrom Street, Liverpool, L3 3AF, United Kingdom, [3]Materials Science Unit, Division of Oral Biosciences, Dublin Dental University Hospital, Trinity College Dublin, Lincoln Place, Dublin 2, Ireland, [4]School of Chemistry and CRANN Institute, University of Dublin, Trinity College, Dublin 2, Ireland, [5]Charles University, Faculty of Mathematics and Physics, Department of Surface and Plasma Science, V Holešovičkách 2, 18000 Prague 8, Czech Republic, [6]International Center for Materials Nanoarchitectonics (WPI-MANA), National Institute for Materials Science (NIMS), Namiki 1-1, Tsukuba, Japan and [7]Department of Advanced Materials Science, Graduate School of Frontier Sciences, The University of Tokyo, 5-1-5 Kashiwanoha, Kashiwa, Chiba 277-8561, Japan

Email:
Sharali Malik[*] - sharali.malik@kit.edu

* Corresponding author

Keywords:
biocompatibility; bioglass; graphene; mechanical properties; nanocomposite

## Abstract

Pure graphene in the form of few-layer graphene (FLG) – 1 to 6 layers – is biocompatible and non-cytotoxic. This makes FLG an ideal material to incorporate into dental polymers to increase their strength and durability. It is well known that graphene has high mechanical strength and has been shown to enhance the mechanical, physical and chemical properties of biomaterials. However, for commercial applicability, methods to produce larger than lab-scale quantities of graphene are required. Here, we present a simple method to make large quantities of FLG starting with commercially available multi-layer graphene (MLG). This FLG material was then used to fabricate graphene dental-polymer composites. The resultant graphene-modified composites show that low concentrations of graphene (ca. 0.2 wt %) lead to enhanced performance improvement in physio-mechanical properties – the mean compressive strength increased by 27% and the mean compressive modulus increased by 22%. Herein we report a new, cheap and simple method to make large quantities of few-layer graphene which was then incorporated into a common dental polymer to fabricate graphene-composites which shows very promising mechanical properties.

## Introduction

Now that much of the world's population are living beyond their "threescore years and ten" [1], that is to say, on average, into their 80s [2], there has been an increase in the need for minimal intervention dentistry [3]. This practice of a complete management solution for tooth decay has benefited from the extensive use of dental polymers. However, current dental polymers have a relatively short operational lifetime resulting from their lack of sufficient strength and durability. Therefore, the aim was to assess the use of graphene with a common dental polymer to form a composite material with improved mechanical properties.

One of the main problems facing dental-polymers is that of location. They are situated within the mouth which is an extremely demanding setting – exposure to moisture, high temperatures, and abrasion from toothbrushes plus a variety of foodstuffs all have to be dealt with. These conditions can lead to problems of mechanical failures cancelling out initial clinical success and over time requiring further work for restoration with the associated inconvenience and extra cost. Then there is the issue of biocompatibility to consider.

Biocompatibility is a prerequisite for all dental materials. They must be compatible with oral fluids, must not release toxic products into the oral location and must have sufficient strength and durability to be fit for purpose [4]. Most other studies of graphene-dental polymer materials have used graphene oxide (GO) [5] which may be cytotoxic [6,7]. Therefore, in these tests glass-ionomers (GIs) prepared with poly(acrylic acid), a common dental polymer [8], were used with the addition of few-layer graphene (FLG). Graphene has the advantages of having a high fracture and mechanical strength, a large surface area, flexibility and is also biocompatible and thought to be

non-cytotoxic [9-13], but as toxicity depends on many factors such as size, shape, concentration and dose further studies with regard to specific applications are needed. Therefore, the aim of these experiments was to assess the use of graphene with a glass-ionomer (GI) prepared with poly(acrylic acid) to form a biocompatible composite material with improved mechanical properties.

## Results and Discussion
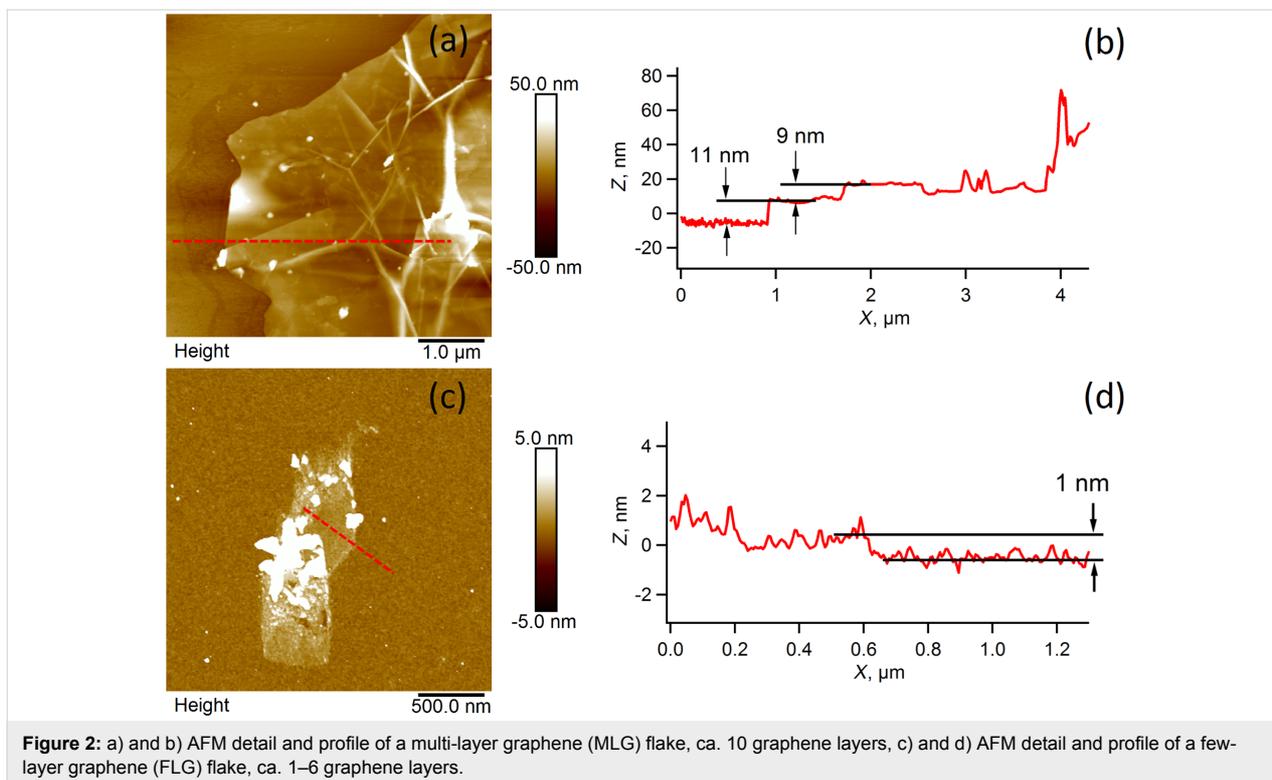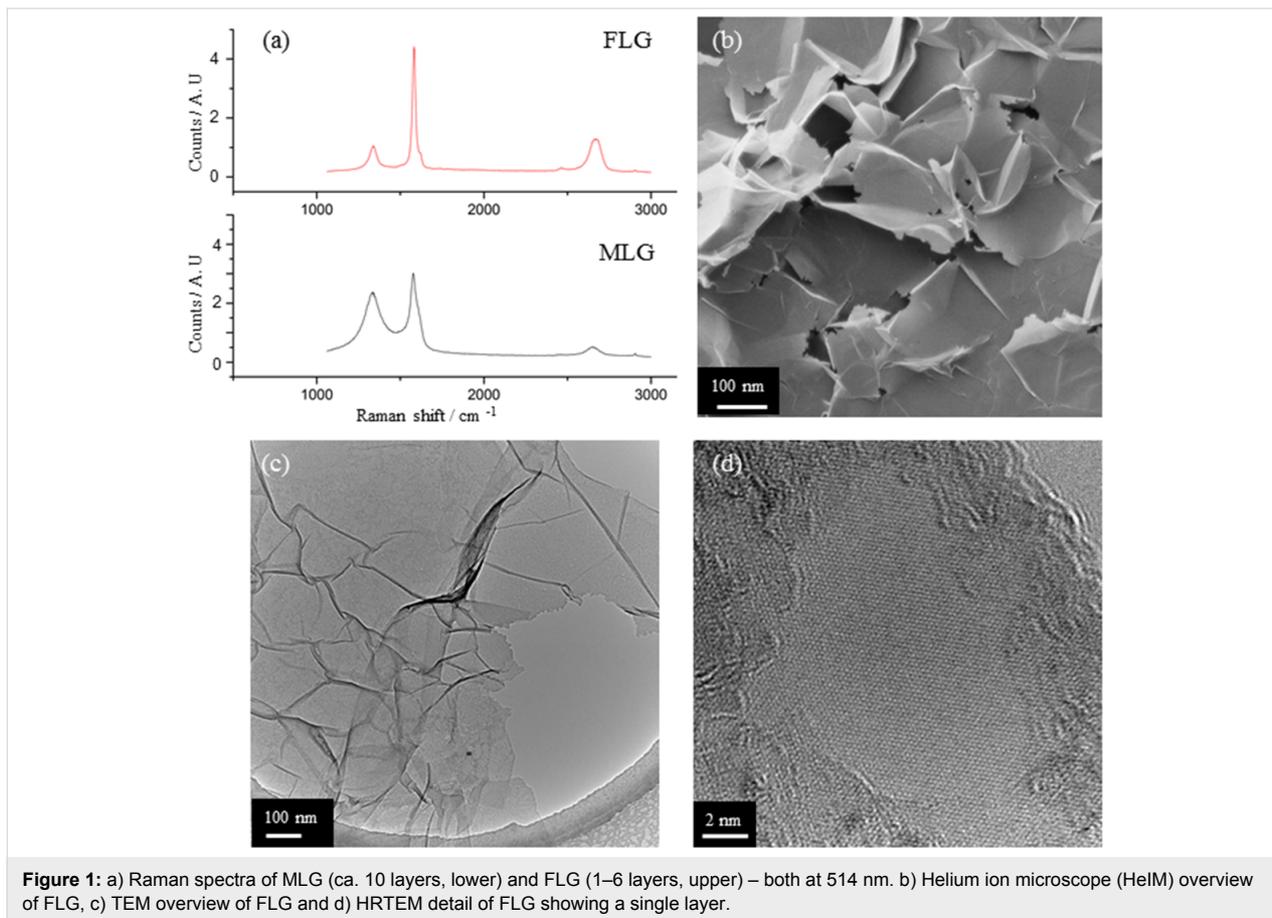### Few-layer graphene

For the graphene material it was decided to use commercially available multi-layer graphene (MLG) from Graphit Kropfmühl GmbH (EXGR98350 - batch 08.10.2012). The shape and position of the Raman 2D band ($\approx$2700 cm$^{-1}$) provides a useful analysis for assessing the quality and number of layers in graphene materials [14,15]. As the FLG material is composed of "flakes" the edges of the flakes give rise to a D band. The shape and position of the 2D band in the MLG material is indicative of multi-layer graphene rather than graphite and the 2D band in the FLG material is indicative of few-layer graphene [14]. This allows us to see the conversion of commercial MLG material (Figure 1a, lower) to FLG (Figure 1a, upper, 1b–d).

Figure 2 shows AFM (detail and profile) of the graphene material (MLG) before and (FLG) after heat-treatment in air at 500 °C for 2 h (ca. 10% volume loss of starting mass during heat-treatment). This resulted in the FLG material used in these experiments.

The XPS analysis (Table 1) shows that the MLG and FLG materials have similar oxygen content as the O 1s/C 1s ratios are very similar. The binding energies ($E_b$) $\approx$284.6 eV corresponds

**Table 1:** Chemical composition of MLG and FLG from XPS analysis.

|     | Component | $E_b$ (eV) | FWHM (eV) | Area (eV) | Fraction (%) | O 1s/C 1s |
|-----|-----------|-----------|-----------|-----------|--------------|-----------|
| MLG | C 1s | 284.01 | 1.83 | 8649.91 | 60.00 | 0.130 |
|     | C 1s | 285.39 | 3.09 | 3151.94 | 21.87 | |
|     | C 1s | 289.44 | 3.37 | 736.77 | 5.12 | |
|     | O 1s | 532.39 | 2.36 | 4202.32 | 10.61 | |
|     | O 1s | 530.44 | 2.07 | 188.13 | 0.75 | |
|     | N 1s | 399.36 | 2.07 | 188.13 | 0.75 | |
| FLG | C 1s | 283.67 | 1.58 | 8588.15 | 56.18 | 0.170 |
|     | C 1s | 284.83 | 1.94 | 3097.75 | 20.27 | |
|     | C 1s | 285.62 | 3.01 | 1254.09 | 8.21 | |
|     | O 1s | 532.43 | 1.58 | 1384.56 | 3.30 | |
|     | O 1s | 531.86 | 2.86 | 4686.88 | 11.15 | |
|     | N 1s | 399.35 | 2.48 | 238.66 | 0.89 | |

**Figure 1:** a) Raman spectra of MLG (ca. 10 layers, lower) and FLG (1–6 layers, upper) – both at 514 nm. b) Helium ion microscope (HeIM) overview of FLG, c) TEM overview of FLG and d) HRTEM detail of FLG showing a single layer.



**Figure 2:** a) and b) AFM detail and profile of a multi-layer graphene (MLG) flake, ca. 10 graphene layers, c) and d) AFM detail and profile of a few-layer graphene (FLG) flake, ca. 1–6 graphene layers.

to C–H, C–C, $(CH_2)_n$ and C=C bonds that are characteristic of graphite/graphene, ≈286 eV corresponds to C–O–C, ≈288.5 eV corresponds to O–C=O, ≈531.5–532 eV corresponds to C–O and ≈533 eV corresponds to C=O [16]. Therefore, it is reasonable to assume that the loss of carbon and oxygen from the MLG material compared to the FLG material can be attributed to the formation of CO and $CO_2$ during the heat-treatment. This is in accord with the Raman data which shows a clear "fingerprint" for graphene rather than graphene oxide [14,15].

## FLG-dental polymers

Six types of FLG-dental polymers were made up; one control plus five with different loadings of graphene. Figure 3 shows FLG-polymer A (lowest concentration of FLG) and FLG-polymer E (highest concentration of FLG used), hence E appears much darker than A (Figure 3a,b).

The Raman spectra of both FLG-dental polymers show a 2D band (≈2700 $cm^{-1}$) which is indicative of FLG [14,15] although in the higher graphene loaded polymer this band is more pronounced. The fracture sections of both polymers were conducting enough to need no coating to be examined by SEM. This is indicative of a good percolation network of the FLG material in the dental polymer (Figure 3d and 3e). The SEMs were obtained using an energy selective backscatter (EsB) detector which gives clear compositional contrast. In these micrographs

the white patches correspond to graphene in the fracture surface of the polymer matrix.

The mean dynamic viscosity, compressive fracture strength and compressive modulus and associated standard deviations for the control group and the groups prepared with poly(acrylic acid) solutions containing graphene are shown in Table 2.

There was a progressive significant increase in the dynamic viscosity of the poly(acrylic acid) solutions as the concentration of graphene added to the poly(acrylic acid) solutions was increased. This increase in viscosity with increasing nano-carbon concentration is consistent with that found by other researchers [17,18]. Further increases in the amount of graphene added to the poly(acrylic acid) solutions – 2.0 mg, 5.0 mg and 10.0 mg all resulted in significant increases in dynamic viscosity compared with the control group as illustrated in Table 2.

There was no significant trend in the compressive fracture strength data with increasing concentration of graphene added to the poly(acrylic acid) solutions as shown in Figure 4. The group prepared using a poly(acrylic acid) solution containing 0.5 mg of graphene produced the highest mean compressive fracture strength (118.2 ± 8.3 MPa) which was a 27% increase compared with the control group (93.3 ± 4.6 MPa).
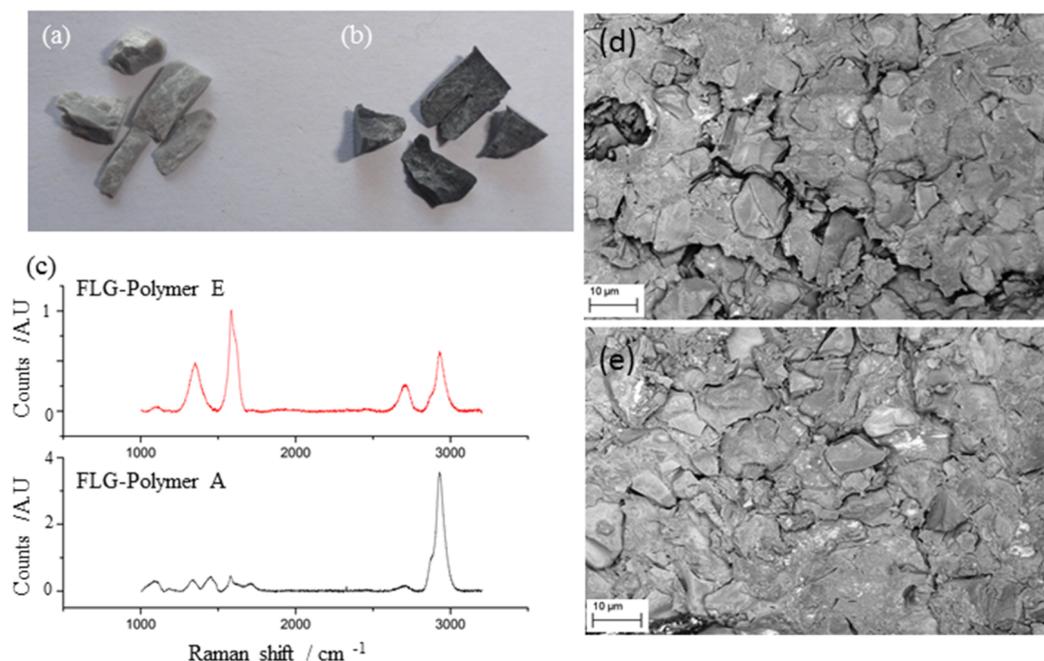


**Figure 3:** a) GI composite after strength testing made from FLG-polymer A, b) GI composite after strength testing made from FLG-polymer E, c) Raman spectra of GI composite made from FLG-polymer E and GI composite made from FLG-polymer A – both at 514 nm, d) SEM overview of fracture surface of GI composite made from FLG-polymer A, e) SEM overview of fracture surface of GI composite made from FLG-polymer E.

**Table 2:** The mean dynamic viscosity, compressive fracture strength and compressive modulus ± standard deviation for the control group and the groups prepared with poly(acrylic acid) solutions containing graphene.

| Group | Dynamic viscosity (mPa·s) | Compressive fracture strength (MPa) | Compressive modulus (GPa) |
|---|---|---|---|
| Control | 610 ± 0 | 93.3 ± 4.6 | 2.91 ± 0.12 |
| A – 0.5 mg | 617 ± 6 | 118.2 ± 8.3 | 3.56 ± 0.32 |
| B – 1.0 mg | 623 ± 6 | 111.3 ± 5.2 | 3.32 ± 0.11 |
| C – 2.0 mg | 653 ± 6 | 116.5 ± 7.8 | 3.49 ± 0.10 |
| D – 5.0 mg | 680 ± 10 | 111.0 ± 5.8 | 3.16 ± 0.15 |
| E – 10.0 mg | 713 ± 6 | 105.3 ± 7.1 | 3.18 ± 0.09 |
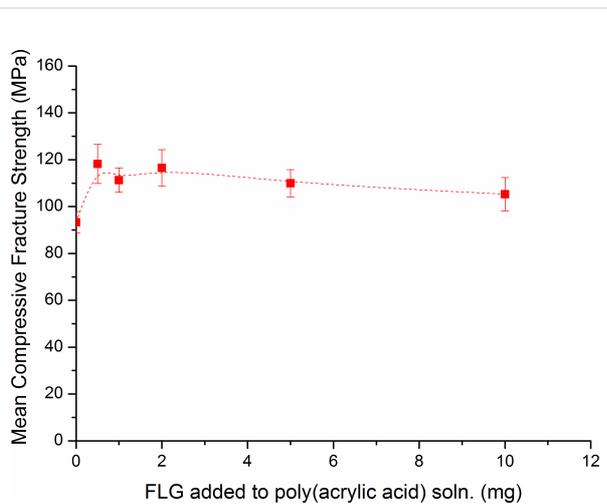


**Figure 4:** Change in mean compressive fracture strength with increasing graphene concentration.
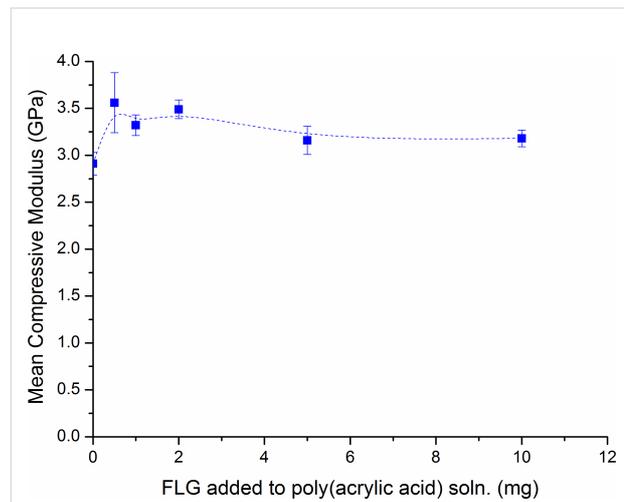


**Figure 5:** Change in mean compressive modulus with increasing graphene concentration.

For the compressive modulus data, there was no significant trend as the concentration of graphene added to the poly(acrylic acid) solutions was increased as shown in Figure 5. Significant increases in the compressive modulus data were reported for all groups prepared with poly(acrylic acid) solutions containing graphene compared with the control group as shown in Table 2. Similarly to the results from the compressive fracture strength data, the group which produced the highest mean compressive modulus (3.56 ± 0.32 GPa) was the group containing 0.5 mg of graphene, which showed a 22% increase compared with the control group (2.91 ± 0.12 GPa).

From the results of the mechanical testing it is clear that a small addition of FLG gives a large increase in the FLG-dental polymer fracture strength and compressive modulus. The latter is significant as it shows the capacity of the FLG-dental polymer to withstand loads tending to reduce in size – e.g., biting and chewing. The decrease in these enhanced properties with increasing FLG loading is probably due to aggregation of

the FLG in the polymer matrix. Further optimisation tests are ongoing.

## Conclusion

In summary, we have described herein a new, simple and cheap method to make large quantities of FLG starting with commercially available multi-layer graphene (MLG) and also the incorporation of this graphene into dental polymer composites. We have demonstrated that the fabricated graphene-dental polymer composites have significantly enhanced mechanical properties as compared with the plain dental-polymer material (control group). The mean compressive strength of the graphene-dental polymer showed a 27% increase and the mean compressive modulus showed a 22% increase compared with the control group – this is a significant increase. A recent review [8] concluded that despite the developments in GI powder and poly(acrylic acid) constituents they still had inferior mechanical properties compared with dental amalgam and resin based composites. They go on to say that major improvements have

yet to be made so that GIs can see real clinical usage. Therefore, these studies could well be the "major improvements" sought for as they show that GIs with a low concentration of graphene lead to major performance improvement in physio-mechanical properties. This represents a major advance in GI materials reinforcement strategy and will breathe a new lease of life into this research area. These in vitro studies are continuing and cell-line studies are also planned.

# Experimental
## Materials
The multi-layer graphene (MLG) material used in this research was commercially available MLG - EXGR98350 (batch 08.10.2012) supplied by Graphit Kropfmühl GmbH (Hauzenberg, Germany). The MLG material was heated in air at 500 °C for 2 h to give the FLG material.

## Graphene-polymer composite preparation
Poly(acrylic acid) powder, 1.0 g, with an average molecular weight of 40000 was mixed with 2.5 mL of distilled water to give a concentration of 40%. Then five concentrations of FLG and these poly(acrylic acid) solutions were made up containing 0.5, 1.0, 2.0, 5.0 or 10.0 mg of FLG (Table 2, group A–E). A control poly(acrylic acid) solution was also prepared without graphene by dissolving 1.0 g of the poly(acrylic acid) powder in 2.5 mL of distilled water (Table 2, group control). All the solutions were sonicated for 15 min and then stirred for 24 h.

All the poly(acrylic acid) solutions (A–E and control) were hand-mixed with a commercial glass-ionomer (GI) restorative powder (Ionofil Molar; Voco GmbH, Cuxhaven, Germany) using a powder to liquid mixing ratio of 4:1 (g/g) as recommended by Voco GmbH. In each case 0.188 g of the poly(acrylic acid) solution was pipetted onto one end of a glass slab while 0.75 g of the Ionofil Molar powder was placed onto the opposite end. The GI powder was divided into two halves, the first half was hand-mixed with all the poly(acrylic acid) solution for 20 s using a stainless steel spatula, and then the remaining GI powder was added and mixed for a further 20 s.

## Dynamic viscosity measurements
The viscosity of all the poly(acrylic acid) solutions was measured with a digital viscometer (Brookfield DV-E Viscometer; Brookfield Engineering Laboratories Inc., Middleboro, MA, USA). The poly(acrylic acid) solution was pipetted into the inner chamber of a small sample adaptor attached to the viscometer and a spindle was inserted slowly into the chamber to avoid entrapping air bubbles in the poly(acrylic acid) solution. The spindle was rotated in the poly(acrylic acid) solution at 100 rpm until a constant viscosity reading was obtained and the dynamic viscosity (mPa·s) was recorded. In total, three

viscosity measurements were taken for each of the poly(acrylic acid) solutions and the mean dynamic viscosity calculated.

## Compressive fracture strength tests
The compressive fracture strength was determined by preparing cylindrical specimens of 6.0 ± 0.1 mm height and 4.0 ± 0.1 mm diameter in accordance with ISO 9917-1 [19] using a Teflon split-mould [20]. The split-mould was placed on a Teflon base covered with an acetate strip and aligned using nylon wedges and a locating pin. The hand-mixed GI restorative plastic mass was applied to one side of the split-mould immediately after mixing using the stainless steel spatula and allowed to flow into the mould to minimise air bubble incorporation in the set cylindrical specimens. A second acetate strip was placed on top of the filled mould and the whole mould assembly was isolated from the surrounding atmosphere using a glass-slab and a G-clamp before transfer to a water-bath maintained at 37 ± 1 °C. After 1 h in the water bath, the specimens were removed from the mould, inspected and specimens containing visual defects were discarded. The flat ends of the specimens were hand-lapped on P600 silicon carbide paper (Beuhler, Lake Bluff, Illinois, USA) under water lubrication to ensure parallel specimen ends for uniform contact with the platens of the testing apparatus [21]. The specimens were stored in glass containers filled with 50 mL of distilled water in an incubator at 37 ± 1 °C for a further 23 h prior to testing. Ten nominally identical cylindrical GI restorative specimens were manufactured for each group investigated.

The mean diameter of each specimen was determined from three measurements taken using a digital micrometer accurate to 10 μm (Mitutoyo, Kawasaki, Japan). The compressive fracture strength of each specimen was made by applying a compressive load to the long axis of the specimen at a cross-head speed of 1 mm/min using a tensile testing apparatus (Instron Model 5565, High Wycombe, England). In order to mimic the oral environment, wet filter paper was placed on the flat ends of the specimen prior to testing [19]. The compressive fracture strength P (MPa) was calculated using Equation 1 [19],

$$P = \frac{F_f}{\pi r^2} \qquad (1)$$

where $F_f$ was the load at fracture (N) and $r$ the mean radius of the specimen (mm). The change in stress $\Delta\sigma$ (MPa) and strain $\Delta\varepsilon$ generated in each specimen during compression testing was quantified using Equation 2 and Equation 3, respectively.

$$\Delta\sigma = \frac{F}{\pi r^2} \qquad (2)$$

$$\Delta\varepsilon = \frac{D}{h} \qquad (3)$$

where *F* was the load (N), *r* the original mean radius of the specimen (mm), *D* the deflection undertaken by the specimen during testing (mm) and *h* the original height of the specimen (mm). Stress/strain plots were derived for each individual specimen and the compressive modulus (the ratio of stress to strain below the fracture limit) was determined by calculating the slope of the initial straight portion of the stress/strain plot prior to fracture [20].

## Statistics

All data in Table 1 are presented as means ± SD and were derived from ten independent samples at each FLG concentration. The one-way ANOVA ($p < 0.0001$) and Tukey's post-hoc tests of the compressive fracture strength data identified significant increases for all the groups containing FLG compared with the control group ($p = 0.003$). For the compressive modulus data, the one-way ANOVA ($p = 0.0001$) and Tukey's post hoc tests also identified significant increases for all the groups containing FLG compared with the control group ($p = 0.003$).

## Characterization

The MLG and FLG material was characterized by Raman spectroscopy (Renishaw at 514 nm) and the AFM measurements were performed on a MultiMode V AFM (Veeco) in tapping mode under ambient conditions. RTESP silicon probes (Veeco) were used with a nominal tip radius of 10 nm and nominal spring constant of 40 N/m. Image processing was carried out using the Nanoscope software. The X-ray photoelectron spectroscopy (XPS) measurements were performed on a Theta Probe spectrometer (Thermo Electron Co., Germany) using monochromatic Al Kα radiation (photon energy of 15 keV with maximum energy resolution of 0.47 eV). High resolution spectra for the core level C 1s and O 1s were recorded in 0.05 eV steps. An electron flood gun was used during the measurements to prevent sample charging. The FLG material was also characterized by TEM, HRTEM (Jeol ARM at 80 kV) and helium ion microscopy (HeIM, Zeiss Orion at 30 kV). In addition, FLG-polymer A and E were characterized by Raman Spectroscopy (JY T6400 at 514 nm) and SEM (Zeiss Ultra-Plus at 3 kV, EsB grid at 503 V).

## Acknowledgements

## ORCID® iDs

Sharali Malik - https://orcid.org/0000-0003-1057-529X
Felicite M. Ruddock - https://orcid.org/0000-0001-8512-1327
Yoshihiro Nemoto - https://orcid.org/0000-0001-8547-4990
Lok Kumar Shrestha - https://orcid.org/0000-0003-2680-6291
Katsuhiko Ariga - https://orcid.org/0000-0002-2445-2955
Jonathan P. Hill - https://orcid.org/0000-0002-4229-5842

## References

1. Moses. Psalm 90,10. *King James Bible;* 1611.
2. WHO *World health statistics* 2016, Ch. 6 Life Expectancy, ISBN 978 92 4 156526 4.
3. Mount, G. J.; Hume, R. W. *Preservation and Restoration of Tooth Structure,* 2nd ed.; 2005. ISBN 1-920824-74-X.
4. Anusavice, K. J.; Shen, C.; Rawls, H. R. *Phillips' Science of Dent. Mater,* 12th ed.; 2012; pp 48–68, 367–395, 474–498.
5. Sarosi, C.; Biris, A. R.; Antoniac, A.; Boboia, S.; Alb, C.; Antoniac, I.; Moldovan, M. *J. Adhes. Sci. Technol.* **2016**, *30,* 1779–1794.
6. Xie, H.; Cao, T.; Rodríguez-Lozano, F. J.; Luong-Van, E. K.; Rosa, V. *Dent. Mater.* **2017**, *33,* 765–774. doi:10.1016/j.dental.2017.04.008
7. Zhou, Y.; Jing, X.; Chen, Y. *J. Mater. Chem. B* **2017**, *5,* 6451–6470. doi:10.1039/C7TB00680B
8. Baig, M. S.; Fleming, G. J. P. *J. Dent. (Oxford, U. K.)* **2015**, *43,* 897–912. doi:10.1016/j.jdent.2015.04.004
9. Kang, J.; Shin, D.; Bae, S.; Hong, B. H. *Nanoscale* **2012**, *4,* 5527–5537. doi:10.1039/c2nr31317k
10. Huang, X.; Yin, Z.; Wu, S.; Qi, X.; He, Q.; Zhang, Q.; Yan, Q.; Boey, F.; Zhang, H. *Small* **2011**, *7,* 1876–1902. doi:10.1002/smll.201002009
11. Bonaccorso, F.; Lombardo, A.; Hasan, T.; Sun, Z.; Colombo, L.; Ferrari, A. *Mater. Today* **2012**, *15,* 564–589. doi:10.1016/S1369-7021(13)70014-2
12. Syama, S.; Mohanan, P. V. *Int. J. Biol. Macromol.* **2016**, *86,* 546–555. doi:10.1016/j.ijbiomac.2016.01.116
13. Sayyar, S.; Officer, D. L.; Wallace, G. G. *J. Mater. Chem. B* **2017**, *5,* 3462–3482. doi:10.1039/C6TB02442D
14. Graf, D.; Molitor, F.; Ensslin, K.; Stampfer, C.; Jungen, A.; Hierold, C.; Wirtz, L. *Nano Lett.* **2007**, *7,* 238–242. doi:10.1021/nl061702a
15. Dresselhaus, M. S.; Jorio, A.; Hofmann, M.; Dresselhaus, G.; Saito, R. *Nano Lett.* **2010**, *10,* 751–758. doi:10.1021/nl904286r
16. Thermo Scientific. XPS simplified. https://xpssimplified.com/periodictable.php.
17. Iliut, M.; Silva, C.; Herrick, S.; McGlothlin, M.; Vijayaraghavan, A. *Carbon* **2016**, *106,* 228–232. doi:10.1016/j.carbon.2016.05.032

18. Boland, C. S.; Khan, U.; Ryan, G.; Barwich, S.; Charifou, R.; Harvey, A.; Backes, C.; Li, Z.; Ferreira, M. S.; Möbius, M. E.; Young, R. J.; Coleman, J. N. *Science* **2016,** *354,* 1257–1260. doi:10.1126/science.aag2879

19. International Organisation for Standardization. *ISO 9917-1,* 2nd ed.; 2007.

20. Fleming, G. J. P.; Marquis, P. M.; Shortall, A. C. C. *Dent. Mater.* **1999,** *15,* 87–97. doi:10.1016/S0109-5641(99)00018-4

21. Lloyd, C. H.; Mitchell, L. *J. Oral Rehabil.* **1984,** *11,* 257–272. doi:10.1111/j.1365-2842.1984.tb00575.x